Mouvements de fluides et processus de déstabilisation des versants alpins : Apport de l'étude de l'instabilité de Séchilienne

Aurélien Vallet

UNIVERSITÉ DE FRANCHE-COMTÉ

UFR DES SCIENCES ET TECHNIQUES

LABORATOIRE CHRONO-ENVIRONNEMENT (UMR CNRS/UFC 6249, USC INRA)

THÈSE

Présentée en vue de l'obtention du titre de

DOCTEUR DE L'UNIVERSITÉ DE FRANCHE-COMTÉ

Spécialité - Sciences de la vie et de l'Environnement

Ecole doctorale - Environnement Santé

MOUVEMENTS DE FLUIDES ET PROCESSUS DE DÉSTABILISATION DES VERSANTS ALPINS

Apport de l'étude de l'instabilité de Séchilienne

Présentée et soutenue publiquement par

Aurélien VALLET

Le 26 novembre 2014 devant le jury composé de :

Catherine BERTRAND (MCF (HDR), Université de Franche-Comté, Besançon)	Directrice
Yves GUGLIELMI (Pr., CEREGE, Marseille)	Rapporteur
Michel JABOYEDOFF (Pr., Université de Lausanne)	Rapporteur
Olivier FABBRI (Pr., Université de Franche-Comté, Besançon)	Examinateur
Jean-Philippe MALET (CR (HDR), Université de Strasbourg)	Examinateur
Jacques MUDRY (Pr.)	Invité

SOMMAIRE

LISTE DES FIGURES

LISTE DES TABLEAUX

INTRODUCTION GÉNÉRALE

Dans de nombreuses régions du monde, la population a occupé et continue d'occuper des territoires exposés aux risques gravitaires. Les mouvements de terrain engendrent des catastrophes sociétales impliquant des pertes humaines associées à des dégâts matériels importants. Pour les sites où la stabilisation des mouvements de terrain n'est pas envisageable (coût, volume mobilisé trop important…), la protection des biens et des personnes passe par la conception de systèmes d'alerte précoces (early warning system) qui sont des dispositifs de contrôle visant à éviter, ou tout au moins à minimiser, l'impact d'un aléa gravitaire sur les populations et leurs activités. Ces dispositifs, pour être pertinents et efficaces, nécessitent la compréhension des mécanismes qui contrôlent la déstabilisation.

Les mouvements de terrain profonds présentent généralement une masse instable de plusieurs milliers de mètres cubes et une épaisseur de plusieurs dizaines de mètres (Dramis and Sorriso-Valvo, 1994). Les importants volumes mobilisés font peser des risques considérables sur les populations et les infrastructures. De plus, leur stabilisation est le plus souvent impossible et les moyens de mitigation sont limités par l'importance de la masse en mouvement. Les couplages hydro-mécaniques sont généralement complexes et leur compréhension constitue un axe de recherche majeur (Cappa et al., 2004). **C'est dans ce cadre que cette thèse s'intéresse à l'impact de l'écoulement souterrain sur la déstabilisation des mouvements de terrain profonds avec pour objectif de mieux comprendre et de caractériser la relation précipitations-déplacement**.

1 Causes et mécanismes des mouvements de terrain

La principale force responsable des **mouvements de terrain** est la force de gravité. Le poids d'un objet sur un plan incliné peut être exprimé en deux composantes. Une composante perpendiculaire, la composante normale (P_n), qui maintient l'objet en place sur la pente, et une composante tangentielle (P_t) parallèle, qui tire l'objet vers le bas (Fig. 1). Ces deux composantes sont généralement rapportées à l'aire de contact : la contrainte normale (σ_n) et la contrainte tangentielle ou cisaillante (σ). Plus la pente est élevée, plus la contrainte cisaillante augmente au détriment de la contrainte normale, et un mouvement s'initie quand le ratio contrainte cisaillante/normale atteint une valeur critique appelée le coefficient de friction (μ). Les forces de réaction d'un objet au mouvement ou à la déformation sont regroupées sous le terme de résistance au cisaillement (R_c) et comprennent la cohésion (C) et la friction (Eq. (1)). La friction est la force de résistance qui s'oppose au mouvement. Elle est proportionnelle à la force normale du poids par l'intermédiaire du coefficient de friction alors que la force de cohésion est la force de résistance à la déformation d'un objet.

$$R_c = C + \mu\, \sigma_n \qquad (1)$$

Un versant est stable si et seulement si la contrainte de cisaillement qui l'entraine vers le bas est compensée par la résistance au cisaillement du versant. La stabilité d'un versant est souvent exprimée par le facteur de sécurité (Fs), le rapport entre la résistance au cisaillement et la contrainte de cisaillement. Si le coefficient de sécurité est inférieur à 1, une rupture de pente est probable.

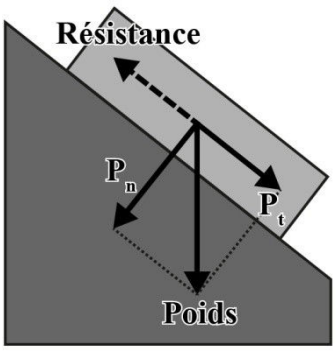

Fig. 1: Les forces impliquées dans la déstabilisation des mouvements de terrain

Les mécanismes de déformation des versants instables peuvent prendre des formes diverses et variées (Fig. 2). Différents **systèmes de classification** des glissements de terrain ont été proposés. Les systèmes de Varnes (1978) et Hutchinson (1988) sont cependant les plus largement utilisés. En

1993, un système de classification adapté aux mouvements de terrain européens (projet EPOCH) a été proposé. Le système EPOCH reconnait sept types de mouvements (*fall, topple, translational slide, rotational slide (slump), lateral spreading, flow and complex*) et trois types de matériaux (*rock, debris, soil/earth*). L'éboulement (*fall*) se caractérise par le mouvement en chute libre d'un matériau à partir d'un versant abrupt. Le basculement (*topple*) implique une action de pivotement d'unités rocheuses (dont le point de pivot est à la base de l'unité) et ne fait pas intervenir de surface de rupture/cisaillement basale (*slide*). Selon la géométrie de la surface de rupture, la cinématique des 'slides' se produit soit en rotation (*rotational slide*) soit en translation (*translational slide*) sur une masse cohérente. La diffusion latérale (*lateral spreading*) est caractérisée par une extension latérale, conséquence d'une perte de cohésion d'une unité sous-jacente. L'écoulement (*flow*) correspond au mouvement continu d'une masse de matériaux se comportant comme un fluide visqueux. L'écoulement pour un matériel rocheux (*rock flow)* est appelé *sackung*. Les mouvements complexes correspondent à une évolution du mécanisme de déformation au cours du temps. Plus récemment, Dikau et al. (1996) ont produit une classification des mécanismes de glissements de terrain en accord avec Hutchinson (1988) et EPOCH (1993).

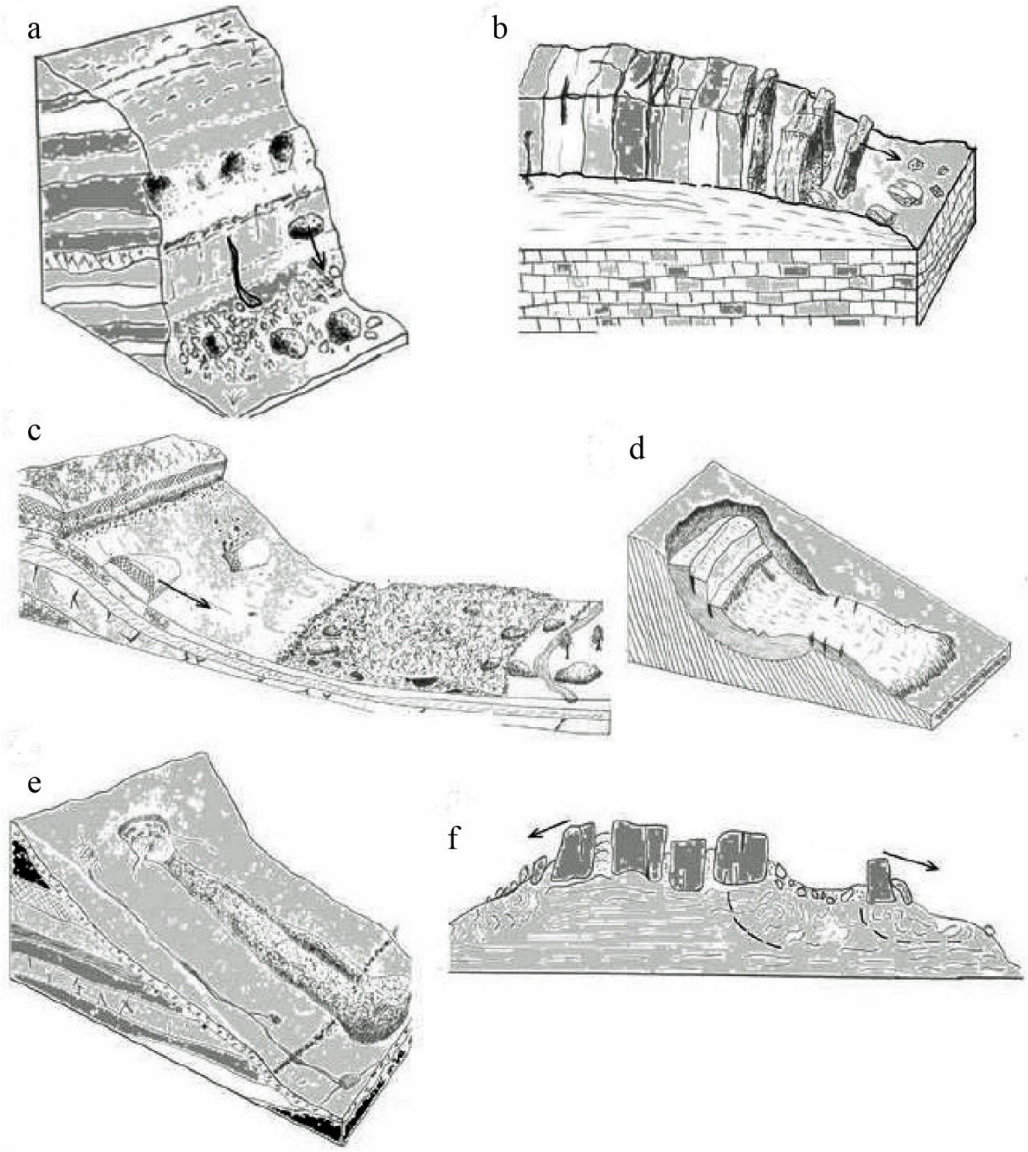

Fig. 2: Illustration de six types de mouvement de terrain : (a) l'éboulement ou chute de blocs, (b) basculement, (c) glissement translationnel, (d) glissement rotationnel, (e) écoulement et (f) la diffusion latérale (Blasio, 2011)

La diversité des mouvements de terrain s'explique par le fait que leur initiation ou leur déclenchement sont régis par l'effet de différents facteurs qui peuvent se combiner et évoluer au cours du temps **: les facteurs de prédisposition, les facteurs préparatoires et les facteurs déclencheurs** (Statham and Finlayson, 1980). Les facteurs de prédisposition correspondent aux conditions intrinsèques du mouvement et sont déterminés par l'héritage géologique (lithologique, structural, processus glaciaires et fluviatiles…) sur le long terme (10^4 à 10^6 années). Les facteurs préparatoires correspondent aux processus géomorphologiques à moyen terme (10 à 10^4 années) induits par le climat (érosion, altération, gélifraction, conditions hydrologiques, pergélisol) et l'utilisation des sols (anthropisation des cours d'eau, déforestation…). Les facteurs déclencheurs correspondent aux sollicitations extrêmes ponctuelles ou à court terme (<10 ans) qui initient ou

amplifient la déstabilisation d'un versant. Ces sollicitations peuvent prendre la forme de séismes, d'événements pluvieux extrêmes, de crues de rivière exceptionnelles ainsi que d'actions anthropiques affectant la stabilité d'un versant.

Les **précipitations**, par l'intermédiaire de la pression de fluides interstitielle, sont considérées comme le facteur déclencheur majeur de la déstabilisation des mouvements de terrain (Van Asch et al., 1999; Wieczorek and Guzzetti, 1999; Iverson, 2000; Bogaard et al., 2007; Bonzanigo et al., 2007). La contrainte effective (σ') est définie comme étant égale à la contrainte normale (σ_n) du milieu moins la pression de fluides interstitielle (u) : $\sigma' = \sigma_n - u$. Une augmentation de la pression de fluides entraine une diminution de la contrainte effective ce qui peut ensuite engendrer une déstabilisation du versant si un seuil d'instabilité est atteint (par exemple le critère de Coulomb). En effet une diminution de la contrainte effective, donc de la composante normale du poids, diminue la friction dont la résistance au cisaillement est dépendante ($R_c = c + \sigma'\mu$).

Cette augmentation de pression interstitielle prend différentes formes selon la profondeur des mouvements de terrain (Van Asch et al., 1999). Pour les mouvements de terrain superficiels (<2 m), c'est le taux d'humidité dans le sol proche de l'état de saturation, alors que pour les mouvements de terrain profonds (>5m), ce sont les variations du niveau piézométrique de l'eau souterraine. La corrélation des phases d'accélérations ou de ruptures avec des événements pluvieux est la conséquence un couplage hydro-mécanique direct fluide vers solide. Cependant, les processus hydrauliques et mécaniques peuvent s'influencer mutuellement en modifiant les propriétés intrinsèques du milieu, conséquence des couplages hydro-mécaniques indirects (Rutqvist and Stephansson, 2003). Les couplages directs constituent des facteurs déclencheurs (court terme) alors que les couplages indirects constituent des facteurs préparatoires (moyen/long terme). En conséquence, la relation précipitations-déplacement peut évoluer au cours du temps, induisant des mécanismes de déformation tel le fluage à long-terme (Saito, 1969; Brückl, 2001; Federico et al., 2012). La figure 3 résume schématiquement les interactions en processus hydrauliques et mécaniques. Les mouvements de terrain nécessitent donc une analyse «dynamique» au lieu d'un modèle classique «statique», en introduisant des composantes dépendantes du temps (Brunsden, 2001; Corominas et al., 2005; Du et al., 2013). Enfin, l'accumulation d'eau dans le mouvement de terrain peut aussi entraîner une accélération ou rupture du mouvement de terrain par augmentation de poids de la zone instable (Brunsden, 1999).

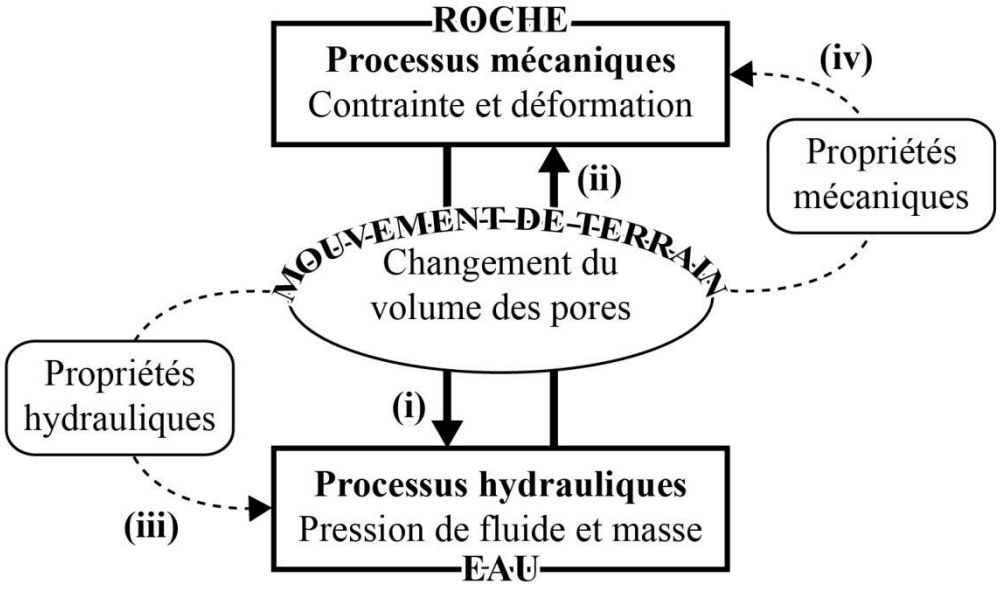

Fig. 3: Couplages hydromécaniques dans un milieu fracturé, (i) et (ii) correspondent aux couplages directs liés à la variation du volume des pores (court terme), (iii) et (iv) correspondent aux couplages indirects liés aux changements de propriétés des matériaux (moyen/long terme), modifiée d'après Rutqvist et Stephansson (2003)

2 Hydrogéologie des mouvements de terrain profonds en milieu fissuré

Dans la chaîne alpine, **les mouvements de terrain profonds** se rencontrent le plus fréquemment dans les massifs cristallins (Barla and Chiriotti, 1995; Agliardi et al., 2001). Dans les environnements montagneux, l'initiation de nombreux mouvements de terrain profonds succède à la dernière période glaciaire (Julian and Anthony, 1996; Vengeon, 1998; Lebrouc et al., 2013). Le creusement des vallées en U (fortes pentes) par les glaciers et l'héritage géologique structural constituent les facteurs de prédisposition majeurs contribuant à l'initiation de la déstabilisation. L'activité tectonique qui a pu être amplifiée par le rebond glaciaire, l'évolution du pergélisol qui persiste après le retrait du glacier, l'altération des matériaux par le changement climatique (climat froid et sec vers un climat chaud et humide) constituent par la suite les principaux facteurs préparatoires de la déstabilisation (Sanchez et al., 2010; Lebrouc et al., 2013). Les mouvements de terrain profonds sont généralement de taille hectométrique et se produisent sur des versants à pente élevée. Les déplacements totaux sont faibles (seulement quelques mètres par an en moyenne) par rapport à la masse mobilisée (Agliardi et al., 2001). La déformation des mouvements de terrain profonds est souvent complexe et implique généralement des mécanismes de déformation de type translationnel, rotationnel, basculement, sackung ou fluage. La zone en mouvement est généralement caractérisée par un déplacement à composante horizontale dominante accommodée par une zone en extension à l'amont ayant un déplacement à composante verticale dominante. Ces mouvements montrent des caractéristiques géomorpho-structurales communes : double crêtes, escarpements, zones en contre pente et tranchées/fissures (Fig. 4).

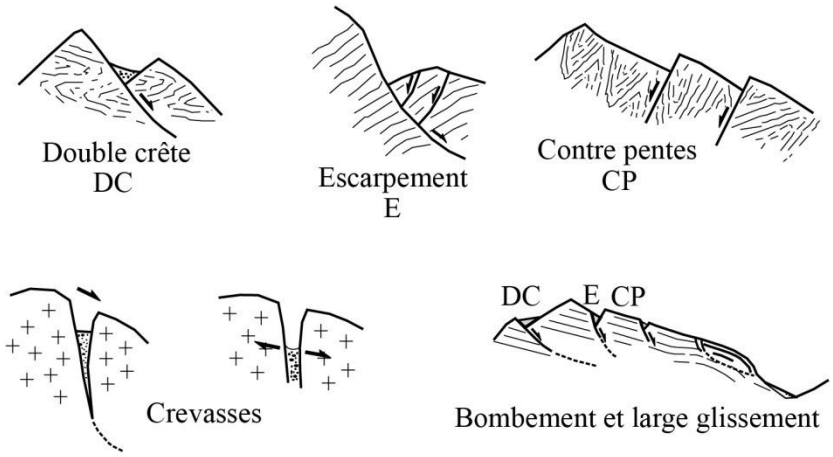

Fig. 4: Structures géomorphologiques typiques des déformations gravitaires profondes (Agliardi et al., 2001)

L'hydrogéologie en milieu fissuré est caractérisée par des milieux hétérogènes, anisotropes et discontinus, avec un écoulement préférentiel dans les discontinuités (Maréchal, 1998; Bogaard et al., 2007). L'intensité des écoulements dépend du degré d'ouverture des fractures, de leur connectivité et de leur densité. En conséquence, les mesures hydrogéologiques sont très dépendantes de l'échelle d'observation (Clauser, 1992) et une mesure locale est rarement représentative du comportement global de l'aquifère. **L'hydrogéologie en milieu fissuré en contexte montagneux** ajoute des spécificités dans l'organisation de l'écoulement par rapport aux propriétés mentionnées dans le paragraphe précédent. En outre, dans les contextes montagneux, il existe un gradient de conductivité hydraulique verticale avec des valeurs allant de 10^{-11} à 10^{-5} m/s en direction des zones décomprimées de surface (Maréchal and Etcheverry, 2003). Les couches sédimentaires recouvrant le substratum cristallin peuvent également conduire à un contraste de perméabilité hydraulique. Ces contrastes de perméabilité peuvent être suffisants pour supporter des aquifères perchés (Vengeon, 1998; Tullen, 2002; Cappa et al., 2004; Binet, 2006). Le relief montagneux est aussi à l'origine de gradients hydrauliques élevés par rapport aux conditions de plaine (Maréchal, 1998) et peut contraindre les écoulements (par exemple les lignes de sources créées par une rupture de pente). Enfin, le climat montagnard engendre une grande variabilité spatiale et temporelle des précipitations. De plus, en hiver les précipitations sont sous forme de pluie ou de neige, ce qui entraine un déphasage en fonction de l'altitude de la recharge, selon la position de l'isograde 0°C.

L'hydrogéologie des mouvements de terrain profonds montre généralement un gradient de conductivité hydraulique élevé entre la zone instable déstructurée et la roche fissurée profonde. Cette organisation conduit généralement à un système à deux couches aquifères constitué par un aquifère perché, porté par le mouvement de terrain qui est déconnecté d'une zone profonde saturée (Van Asch et al., 1999; Guglielmi et al., 2002; Binet et al., 2007a; Pisani et al., 2010; Huang et al., 2012). La recharge de l'aquifère perché est fortement influencée par le contexte géomorphologique (Fig. 5). En effet, l'ouverture des fractures et les zones en contre-pentes facilitent l'infiltration de l'eau et limitent le ruissellement sur la zone instable (Binet et al., 2007a). L'extension des fractures en profondeur favorise des écoulements souterrains préférentiels qui peuvent devenir perpendiculaires à la pente. Cependant, le bassin d'alimentation de l'aquifère perché peut ne pas être seulement limité à l'extension du mouvement de terrain et concerner des zones éloignées (Guglielmi et al., 2002). Les propriétés hétérogènes, anisotropes et discontinues des milieux fissurés sont accentuées par la déstructuration engendrée par le mouvement de terrain et par la présence de matériaux altérés (colluvions, argile) qui peuvent remplir les fractures de la zone en décompression.

Finalement, les couplages hydromécaniques indirects ont pour conséquence une évolution spatio-temporelle des propriétés hydrauliques et de la relation entre les pressions de fluides et la déformation (Chigira, 1992), ce qui complexifie la compréhension du fonctionnement hydrogéologique des mouvements de terrain.

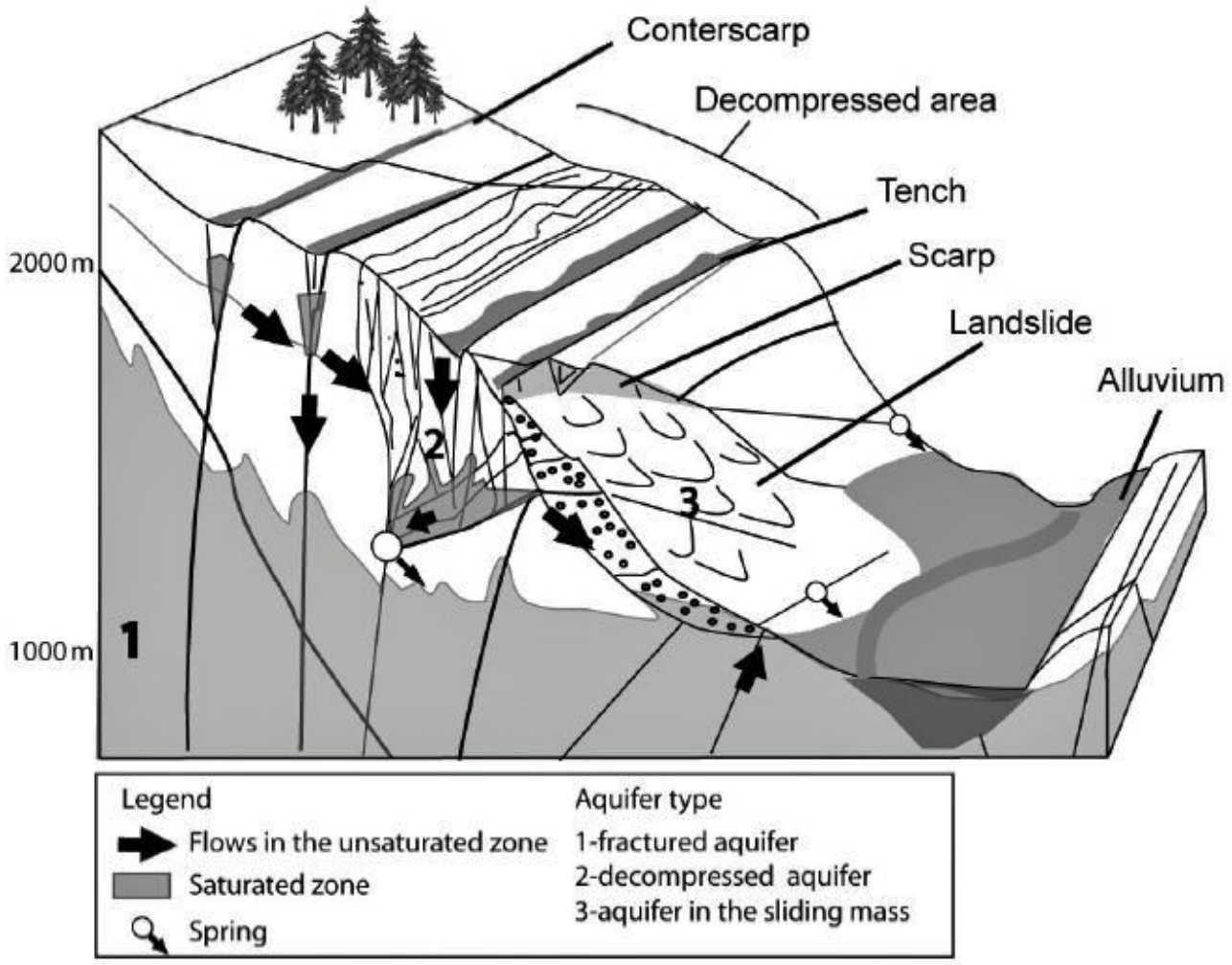

Fig. 5: Modèle conceptuel des écoulements d'eau dans les versants rocheux instables, établi selon les informations acquises pour les versants de la Haute Vallée de la Tinée (sud-est des Alpes Françaises, Binet et al., 2007a)

3 Méthodes d'investigation hydrogéologique des mouvements de terrain

Afin de bien appréhender l'impact de l'écoulement souterrain sur la déstabilisation des mouvements de terrain, il est nécessaire de conduire des études hydrogéologiques permettant de déterminer un schéma conceptuel de fonctionnement hydrogéologique. Les études hydrogéologiques sont rendues difficiles par la faible densité de points naturels ou artificiels d'accès à la nappe souterraine déclenchant le mouvement. En effet, dans les zones instables, les piézomètres ont une courte durée de vie en raison de leur inexorable endommagement. De plus, l'hétérogénéité des milieux fissurés, accentué par la désorganisation de la zone instable, rends difficile l'interprétation de mesures locales qui peuvent être peu représentatives du milieu. Les méthodes classiques d'investigation hydrogéologique ne sont pas toujours appropriées, et les études récentes se portent sur des méthodes indirectes non intrusives dont les deux principales sont le suivi de traceurs naturels ou artificiels (Guglielmi et al., 2002; Binet et al., 2007a; Bogaard et al., 2007; Charlier et al., 2010; Cervi et al., 2012; Debieche et al., 2012; Lin and Tsai, 2012) et la géophysique appliquée à l'hydrogéologie (Lebourg et al., 2005; Meric et al., 2005; Jomard et al., 2007; Grandjean et al., 2009; Bièvre et al., 2012).

Les méthodes de traçages artificiels ou naturels permettent une intégration spatiale des processus et fournissent donc des informations générales à l'échelle du système étudié (Guglielmi et al., 2002; Bogaard et al., 2007; Cervi et al., 2012). Les signaux hydrogéochimiques des sources sont influencés par les types de lithologie rencontrés par l'eau souterraine, et par le comportement hydrodynamique de l'aquifère (Binet, 2006). En périodes de basses-eaux, le signal des eaux souterraines est caractéristique de l'interaction-eau-roche (origine de l'eau, chemin d'écoulement) et du temps de résidence, car l'aquifère est alors peu influencé par la recharge qui est très faible. D'un autre coté, l'analyse des variations saisonnières (tendance saisonnière, dispersion, amplitude...) permet de caractériser le comportement hydrodynamique de l'aquifère (dilution, réactivité...). Parallèlement, l'utilisation de modèles à base thermodynamique permet de valider des hypothèses de circulation des eaux souterraines (Guglielmi et al., 2002; Binet et al., 2009; Cervi et al., 2012). La chimie des eaux souterraines peut également être modifiée par les processus hydromécaniques (Binet et al., 2009), ce qui permet d'identifier les eaux qui ont circulé dans les zones instables. Généralement, les études sur les mouvements de terrain se limitent aux éléments majeurs (Binet et al., 2007a). Cependant, des éléments complémentaires peuvent être intégrés dans les études hydrogéologiques pour cibler et quantifier des processus particuliers (aire de recharge,

temps de transit, calcul de bilan, interaction eau-roche) tels que les isotopes de l'hydrogène et de l'oxygène (Guglielmi et al., 2002), la fluorescence naturelle (Charlier et al., 2010) et les éléments traces (Cervi et al., 2012). Finalement, les traceurs artificiels permettent de tester des hypothèses ciblées de circulation des eaux souterraines en déterminant des directions, des chemins et des vitesses d'écoulement, ainsi que de quantifier des propriétés hydrauliques (Binet et al., 2007b).

Les méthodes géophysiques traditionnelles d'exploration se fondent sur l'analyse d'anomalies de paramètres physiques qui ne sont pas nécessairement liés de façon univoque à la présence d'eau dans le milieu étudié (Jongmans and Garambois, 2007). Ces méthodes apportent néanmoins des informations précieuses sur la géométrie des structures impliquées dans les écoulements et sont très souvent couplées avec des études hydrogéologiques complémentaires telles que des analyses hydrogéochimiques (Lebourg et al., 2005), des essais d'infiltration (Jomard et al., 2007; Grandjean et al., 2009) ou le suivi de la nappe/taux d'humidité (Bièvre et al., 2012). La polarisation spontanée se distingue des méthodes traditionnelles par un couplage hydro-électrique fort. Cette méthode a été utilisée récemment pour caractériser l'écoulement des eaux souterraines dans des mouvements de terrain (Bruno and Martillier, 2000; Giano et al., 2000; Meric et al., 2005).

4 Cadre de la thèse : le mouvement de terrain de Séchilienne

Cette thèse a été effectuée dans **le cadre du projet SLAMS,** dont elle constitue le volet hydrogéologique. Ce projet, financé par l'Agence Nationale pour la Recherche, a pour intitulé "Etudes Multidisciplinaires du Mouvement de Séchilienne: aléa, risques associés et conséquences socio-économiques". L'instabilité de Séchilienne est un des mouvements de terrain métropolitains qui montrait un des plus fort risques socio-économiques dans les années qui ont suivi la réactivation du mouvement (1980). Le scénario le plus défavorable consistait en la rupture d'une partie du mouvement dont les éboulis constituaient un risque majeur pour le hameau de l'Ile Falcon, ainsi que pour l'axe de communication Grenoble-Briançon. De plus, cet éboulement pouvait engendrer la formation d'un barrage naturel concomitant avec une crue de la Romanche, dont la rupture brutale pouvait provoquer une importante vague et affecter les infrastructures chimiques de Jarrie situées en aval (infrastructures classées SEVESO).

Face à ce risque majeur, un investissement sociétal considérable a été consenti après les années 1980 et a privilégié la gestion du risque (Decrop, 2012), notamment *via* un système de surveillance et la mise en place de parades (déviation de la route nationale, expropriations…). A l'inverse, ce site a souffert du manque de projets de recherche fondamentale véritablement interdisciplinaires. Bien qu'actuellement le dernier rapport du collège d'experts (Panet et al., 2009) et l'étude de la Compagnie Nationale du Rhône (Durville et al., 2011) montrent que le risque peut être considéré comme faible (éboulements polyphasées, impact du barrage faible et existence d'une galerie de dérivation de la Romanche, crue centennale révisée à la baisse, expulsion des derniers habitants de l'Ile Falcon en 2011, nouvelle déviation de la RD1091 prévue pour 2017), l'aléa gravitaire est toujours présent et l'instabilité de Séchilienne constitue un objet d'investigation scientifique de premier ordre du fait de la complexité de la cinématique de la déformation et des couplages hydro-mécaniques. La recherche fondamentale peut désormais s'appuyer sur un réseau dense et performant (mesures de déplacements, données météorologiques, données de forages/galeries, balises sismiques, suivi hydrochimique) développé depuis près de 30 ans par le CEREMA (anciennement CETE) et complété depuis peu par l'observatoire OMIV (Observatoire Multidisciplinaire des Instabilités de Versant). Ce réseau de surveillance et l'abondance des données collectées sur le long-terme font de Séchilienne un terrain d'investigation idéal pour les scientifiques.

Le versant instable de Séchilienne est situé dans les Alpes, sur le massif cristallin externe de Belledonne. Il est situé à 20 km au sud-est de Grenoble (France), sur la rive droite de la rivière Romanche, sur le versant sud du massif du Mont-Sec (Fig. 6). Le substratum est composé de micaschistes recouverts en discordance par des roches sédimentaires essentiellement carbonatées datées du Carbonifère au Lias. Localement, des dépôts fluvio-glaciaires quaternaires recouvrent ces deux ensembles.

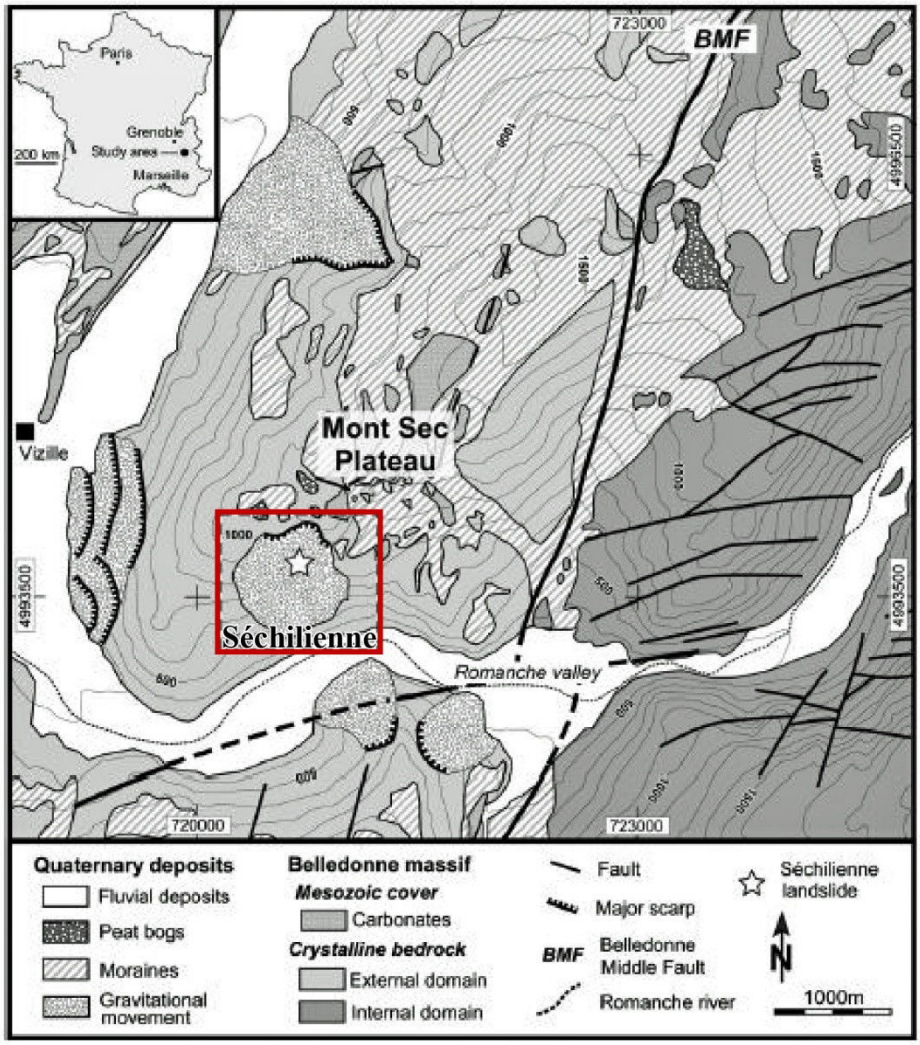

Fig. 6: Carte géologique du massif de Belledonne, modifiée d'après Lebrouc et al. (2013)

Le mouvement de terrain est délimité à l'est par une zone de failles majeures de direction N20 et au nord par un escarpement de plusieurs centaines de mètres de long et plusieurs dizaines de mètres de haut, en contrebas du Mont-Sec (Fig. 7a). Peu d'indices géomorphologiques permettent de délimiter précisément la zone instable sur les parties sud et ouest. En contrebas de l'escarpement majeur, entre 1100 et 950 m, une zone dite en affaissement présente une géomorphologie en dépression alors que plus bas, entre 950 et 450 m, la pente du versant devient raide (> 40°) et est interprétée

comme une zone en accumulation (Vengeon 1998; Le Roux et al 2011; Fig. 7b). L'ensemble de la masse instable est estimé entre 48 et 63 millions de m^3 (Le Roux et al., 2011). Le versant est découpé par un réseau dense de deux ensembles de fractures sub-verticales de direction N110-120 et N70, hérités de la tectonique régionale (Le Roux et al., 2010). Dans la zone d'accumulation, le réseau dense de fractures ouvertes N70 délimite de nombreux compartiments verticaux de largeur pluri-décamétrique (Vengeon, 1998; Lebrouc et al., 2013). Ces fractures ont été progressivement remplies par des colluvions en surface et passent en profondeur à des zones broyées riches en matériaux argileux. De plus, un grand nombre de fractures pluri-métriques de direction N50-70, avec un pendage parallèle au versant, est présent dans la zone d'accumulation. Les fractures de direction N110-120 sont dominantes dans la zone en affaissement.

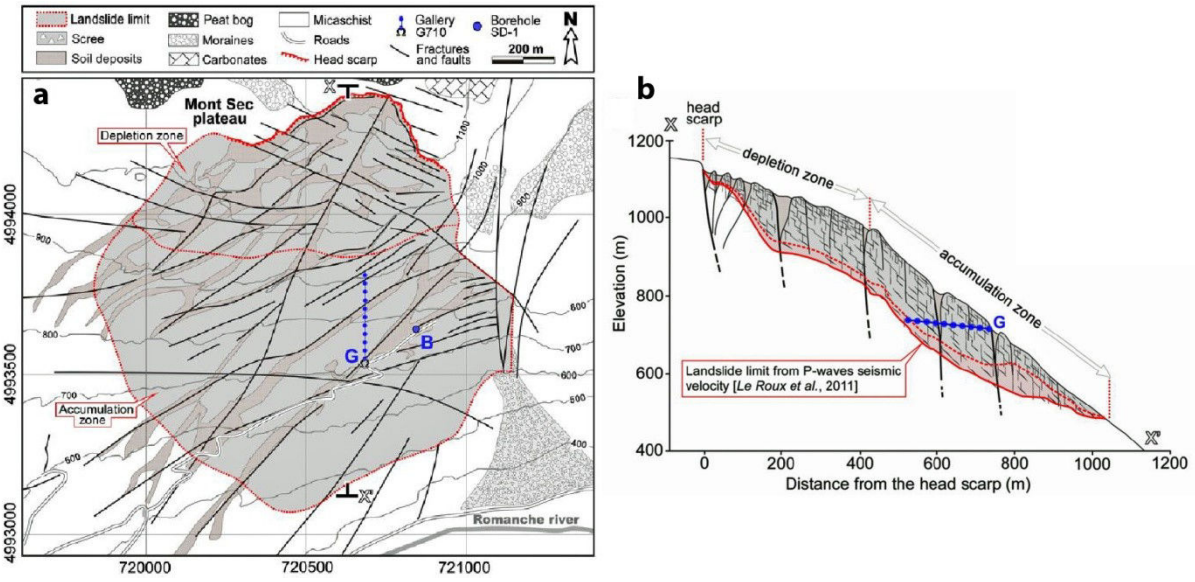

Fig. 7: Géologie et géomorphologie du mouvement de terrain de Séchilienne avec (a) carte et (b) coupe, modifiée d'après Lebrouc et al. (2013)

Des datations récentes (Le Roux et al., 2009) par la méthode des isotopes cosmogéniques (^{10}Be), effectuées le long de l'escarpement nord, ont révélé que la rupture du versant date de 6.4±1.4 ka, c'est-à-dire plus de 5400 ans après la dernière déglaciation totale de la vallée (13.3 ka). L'initiation de la déstabilisation du mouvement de terrain ne serait donc pas directement générée par la fonte des glaciers. Les résultats de modélisation numérique thermique en 2D, effectuée par Lebrouc et al. (2013), montrent que ce décalage temporel peut être expliqué par la persistance du pergélisol, qui aurait renforcé temporairement la résistance du versant. Cependant, le développement du pergélisol aurait aussi endommagé (*ice segregation mechanism*) le versant et influencé la géométrie de l'instabilité.

Le mouvement de terrain de Séchilienne est caractérisé par une déformation progressive profonde contrôlée par le réseau de fractures ainsi que par l'absence d'une surface de glissement basale nette. Le versant est affecté par un mouvement de basculement profond des blocs N50-70° vers la vallée (zone en accumulation), couplé à l'affaissement de la partie supérieure du versant de Mont Sec (Vengeon, 1998; Durville et al., 2009; Lebrouc et al., 2013).

Le suivi des mesures de déplacement (Fig. 8) montre des vecteurs de déplacement relativement homogènes aussi bien pour la direction (N140) que pour les pentes (10 à 20°) pour les deux zones (affaissement et accumulation) avec une vitesse de déplacement faible de 2 à 15 cm/an (Le Roux et al., 2011). Ces vitesses diminuent progressivement vers l'ouest et le sud ce qui permet d'estimer les limites de la zone instable. Une zone très active (zone dite des Ruines de Séchilienne) se démarque de cet ensemble. Cette zone est responsable de nombreux éboulements rocheux, avec des vitesses élevées de déplacement de l'ordre de 150 cm/an affectant un volume estimé à 3 millions de mètres cube.

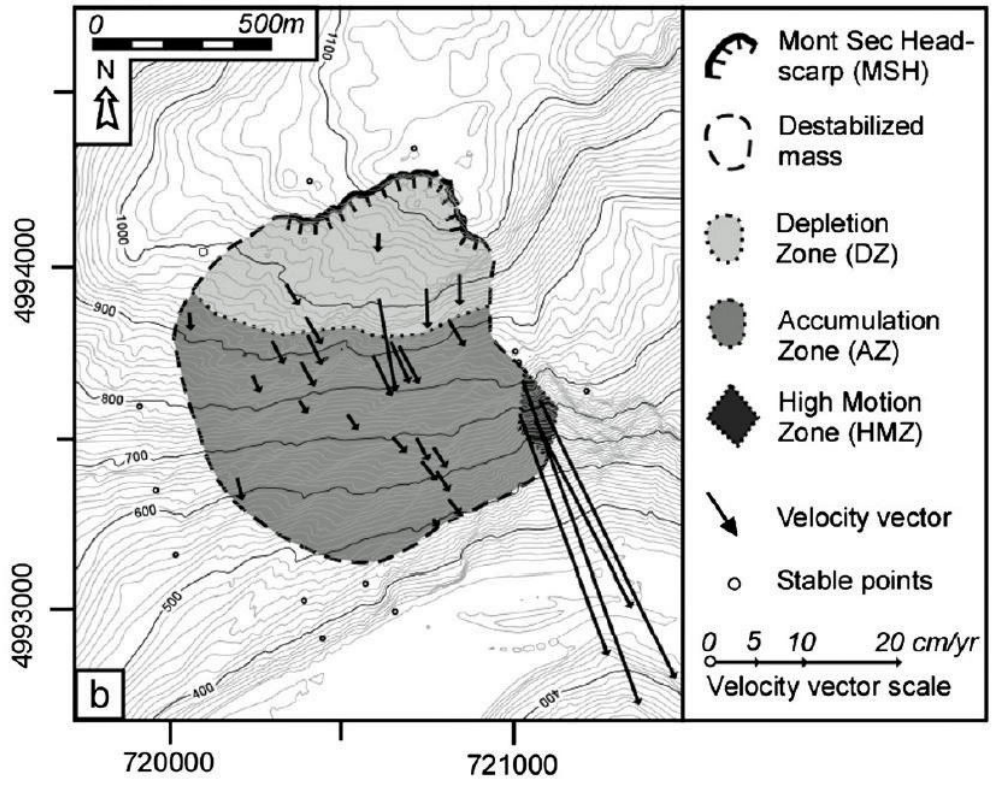

Fig. 8: Carte cinématique avec les vecteurs de déplacement et la délimitation des zones en accumulation et affaissement (Le Roux et al., 2011)

La zone instable très fracturée, d'une profondeur de 150-200 m environ, montre une conductivité hydraulique beaucoup plus élevée que le socle intact sous-jacent (Vengeon, 1998; Meric et al.,

2005; Le Roux et al., 2011), et constitue un aquifère perché (Guglielmi et al., 2002). Sur l'ensemble du massif, une zone profonde saturée est située à la base du versant surmontée par une zone non saturée. L'écoulement des eaux souterraines est principalement contrôlé par le réseau étendu de fractures, avec des vitesses relativement élevées de l'ordre du km/jour (Mudry and Etievant, 2007). Le mouvement de terrain de Séchilienne est caractérisé par une bonne corrélation entre les précipitations et les vitesses de déplacement qui montrent toutes les deux des variations saisonnières significatives (Rochet et al., 1994; Alfonsi, 1997; Durville et al., 2009; Chanut et al., 2013). De plus, Helmstetter et Garambois (2010) ont montré une corrélation faible mais significative entre les signaux des précipitations et de la micro-sismicité associée aux éboulements.

Bien que l'instabilité de Séchilienne ait déjà été investiguée par deux études hydrochimiques ponctuelles de Vengeon (1998) et Guglielmi et al. (2002), le schéma conceptuel d'écoulement des eaux souterraines présente encore de nombreuses incertitudes. Vengeon (1998) a montré que l'aquifère perché du mouvement de terrain est rechargé par l'élévation du niveau d'eau de la zone saturée profonde (Fig. 9a), alors que pour Guglielmi et al. (2002) la recharge provient essentiellement d'un aquifère perché présent dans la couverture sédimentaire (Fig. 9b). Pour Vengeon (1998), la déstabilisation est contrôlée par l'aquifère perché du versant instable alors que pour Guglielmi et al. (2002), le comportement hydromécanique du versant dépend de la circulation de l'eau entre la zone saturée perchée et la zone profonde. Récemment, une étude hydromécanique de Cappa et al. (2014) a montré que la déstabilisation du mouvement de terrain de Séchilienne peut être contrôlée en parti par les fluctuations de la zone saturée profonde. Afin de mieux caractériser les processus hydromécaniques contrôlant la déstabilisation, il est nécessaire d'améliorer la compréhension du fonctionnement hydrogéologique du versant instable et du massif, en se basant sur des investigations hydrogéologiques approfondies.

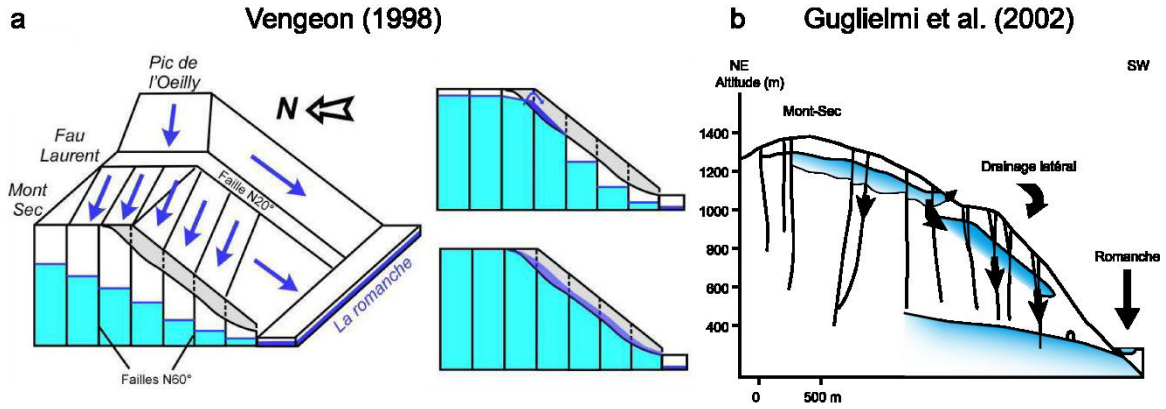

Fig. 9: Schéma conceptuel du fonctionnement hydrogéologique du versant instable de Séchilienne, (a) modèle de Vengeon modifié d'après Le Roux (2009) et (b) modèle de Guglielmi modifié d'après Guglielmi et al. (2002)

5 Objectif et structure de la thèse

L'objectif de cette thèse est de déterminer le fonctionnement hydrogéologique du versant de Séchilienne et de caractériser les couplages hydro-mécaniques associés afin de mieux comprendre l'impact de l'écoulement souterrain sur la déstabilisation du mouvement de terrain de Séchilienne. Cette thèse s'attache, au travers de ses quatre chapitres, à répondre aux questions scientifiques suivantes :

➔ Quel est le fonctionnement hydrogéologique du versant instable de Séchilienne ?

➔ Quel est le signal hydrogéologique le plus adapté pour l'étude des mouvements de terrain profonds ?

➔ Quel est l'impact des écoulements souterrains sur la déstabilisation du versant de Séchilienne ?

➔ Quel outil est adapté pour la prévention de la déstabilisation des mouvements de terrain profonds ?

Le **chapitre I** s'intéresse à l'établissement d'un **schéma conceptuel hydrogéologique** du mouvement de terrain de Séchilienne, ainsi que du massif fissuré environnant. Une méthode de suivi de l'eau des sources est proposée. Elle combine trois approches complémentaires : (1) un multi-traçage artificiel au cours d'une période de hautes eaux, (2) un suivi saisonnier des isotopes stables et de la conductivité électrique de l'eau et (3) un suivi hydrogéochimique pendant les périodes de basses eaux. Ce suivi des sources est complété par une étude des venues d'eau dans les galeries souterraines présentes sur le site de Séchilienne.

Le **chapitre II** s'attache à quantifier le **signal de recharge** (pluie efficace) qui alimente l'hydrosystème de Séchilienne. Les milieux instables rendent difficile l'acquisition de données piézométriques et les données de pression de fluides sont donc rarement mesurées. La recharge est généralement l'unique paramètre qui permet de caractériser et de quantifier l'impact des écoulements souterrains sur la déstabilisation. Cependant, dans la plupart des études, soit les précipitations brutes sont utilisées au lieu de la recharge soit les méthodes utilisées pour déterminer la recharge sont basées sur des simplifications excessives. Ce chapitre propose une nouvelle méthode pour estimer simplement et avec précision la recharge.

Le **chapitre III** analyse et caractérise la **relation entre les précipitations et le déplacement** d'un mouvement de terrain sujet au fluage. Une analyse «dynamique» sur le long-terme en introduisant des facteurs dépendant du temps a été effectuée pour caractériser le processus de déformation par fluage. Cette étude combine une analyse en séries chronologiques et en ondelettes, couplée à un modèle empirique hydro-mécanique. L'objectif sous-jacent est d'évaluer si la déformation par fluage du versant instable de Séchilienne peut être expliquée et modélisée avec les seules données de précipitations.

Le **chapitre IV** développe une méthode objective de détermination d'un **seuil pluviométrique d'activation (rainfall threshold)** adapté aux mouvements de terrain profonds**.** Cette méthode est basée sur l'estimation de la recharge et sur la définition d'un seuil pluviométrique multi-dimensionnel. Elle a été conçue pour être semi-automatique, assurant une intégration facilitée dans un système d'alerte. La méthode est constituée de deux parties indépendantes : (1) l'identification d'événements stables/instables basée sur les séries chronologiques de déplacement et (2) la détermination d'un seuil pluviométrique d'activation grâce à un classificateur mathématique (Machines à Vecteur de Support : SVM).

Ces quatre chapitres sont écrits sous forme de manuscrits d'article en langue anglaise. Le chapitre I a été soumis à *Hydrogeology journal*. Le chapitre II a été soumis dans la revue *Hydrology and Earth System Sciences.* Les chapitres III et IV ont été soumis respectivement *à Landslides* et *Journal of Hydrology*.

CHAPITRE I : SCHÉMA CONCEPTUEL D'ÉCOULEMENT POUR LES MOUVEMENTS DE TERRAIN PROFONDS: CONTRIBUTION D'UN SUIVI SAISONNIER DE TRACEURS NATURELS ET ARTIFICIELS

GROUNDWATER CONCEPTUAL MODEL OF LARGE LANDSLIDES: CONTRIBUTION OF TIME-RELATED ENVIRONNEMENTAL TRACING COMBINED WITH TRACER TESTS (SÉCHILIENNE, WESTERN ALPS)

Vallet A.[1], Bertrand C.[1], Mudry J.[1], Bogaard T.[2], Fabbri O.[1], Baudement C.[3], Régent B.[1]

[1] UMR6249 Chrono-Environnement - Université de Franche-Comté - 16 route de Gray - F-25030 Besançon cedex - France

[2]. Water Resources Section, Delft University of Technology, Stevinweg 1, 2628 CN, Delft, The Netherlands

[3]. CEREGE (UMR7330), Aix-Marseille University, CNRS-IRD, Europôle Méditerranéen de l'Arbois - Avenue Louis Philibert - BP 80 - 13545 Aix-en-Provence cedex 04, France

1 Résumé du chapitre I

Les variations du niveau de l'eau souterraine jouent un rôle important dans l'activation ou la réactivation des mouvements de terrain profonds. Les études hydro-mécaniques des mouvements de terrain, notamment les modèles numériques, nécessitent une bonne compréhension du fonctionnement hydrogéologique. Toutefois, ces milieux présentent de grandes hétérogénéités (dense réseau de fractures, milieu altéré et remanié…), où les méthodes hydrogéologiques classiques, telles que la piézométrie, ne sont pas appropriées.

Les études hydrogéologiques récentes se sont portées sur des méthodes indirectes, telles que le suivi de traceurs naturels ou artificiels aux exutoires des aquifères. Ce type d'études, appliquées aux mouvements de terrain, varie entre deux extrêmes : (i) un nombre limité de campagnes d'échantillonnages permettant un aperçu des conditions hydrogéologiques et (ii) des études hydrogéologiques dédiées, mesurant un large éventail de paramètres sur le long terme, incluant le niveau de l'eau. Ce chapitre propose une méthode intermédiaire d'investigation qui permet de déterminer avec précision un modèle conceptuel des eaux souterraines. Cette méthode combine trois approches complémentaires de suivi des eaux des sources :

- un essai ponctuel multi-traceurs artificiels au cours d'une période de hautes eaux (Fig. 12),
- un suivi saisonnier des isotopes stables et de la conductivité électrique de l'eau (Fig. 14),
- un suivi hydrochimique au cours des périodes de basses eaux (Fig. 15).

Ces trois méthodes permettent de déterminer pour chaque exutoire le chemin d'écoulement, le temps de séjour de l'eau souterraine, l'altitude moyenne du bassin versant, le comportement hydrodynamique de l'aquifère qui les alimente, et l'origine des écoulements. La caractérisation du schéma conceptuel est complétée par une analyse en série temporelle des chroniques journalières de précipitations, de recharge et de vitesse de déplacement.

Pour le mouvement de terrain de Séchilienne, cette étude met en évidence un écoulement préférentiel et rapide de l'eau souterraine dans les fractures et un écoulement plus inertiel dans la roche moins fracturée (Fig. 17). Les principales failles/fractures jouent un rôle de premier plan dans le drainage de l'ensemble du massif et peuvent avoir une influence spatiale

significative. La galerie EDF, située à la base du versant, agit également comme un axe d'écoulement majeur dans le massif, en drainant les eaux souterraines vers l'ouest.

Un contraste des propriétés hydrauliques de la zone instable par rapport à la masse de roche stable à l'extérieur du mouvement de terrain est aussi mis en évidence. Cette hétérogénéité verticale conduit à un hydrosystème composé d'un double aquifère, avec un aquifère perché peu profond, localisé dans la zone instable, et un aquifère profond, localisé dans l'ensemble du massif (Fig. 17).

L'aquifère perché est temporaire, discontinu, et son étendue, ainsi que sa connectivité fluctuent en fonction des variations journalières à saisonnières de la recharge. L'eau souterraine s'écoule principalement à travers un réseau dense de fractures largement ouvertes. L'aquifère perché est presque sec durant les périodes de basses-eaux. La zone de recharge de cet aquifère est essentiellement locale, bien qu'au cours des périodes de hautes eaux, la zone de recharge puisse s'étendre au delà de la surface du mouvement de terrain, et mobiliser alors des écoulements en provenance de la couverture sédimentaire.

Une analyse des séries chronologiques de précipitations/recharges, ainsi que des vitesses de déplacement, montre qu'il est très probable que l'aquifère perché et l'aquifère profond déclenchent tous les deux la déstabilisation du mouvement de terrain de Séchilienne (Fig. 17).

2 Introduction

If gravity is known as the main factor in landslide motion, water plays a prominent triggering role. An increase of groundwater level plays an important role in the (re)activation of deep-seated slope movements (Van Asch et al., 1999; Iverson, 2000; Rutqvist and Stephansson, 2003) and many studies attempted to characterize the relationships between the water infiltration and landslide destabilisation (Alfonsi, 1997; Hong et al., 2005; Helmstetter and Garambois, 2010; Belle et al., 2013; Chanut et al., 2013) or to model hydro-mechanical coupling (Cappa et al., 2004; Corominas et al., 2005; Guglielmi et al., 2005; Cappa et al., 2006; Bonzanigo et al., 2007; Sun et al., 2009). However, to be accurate and to reflect field conditions, such approaches must be based on a relevant and realistic groundwater conceptual model.

In the Alps, most deep-seated landslides occur in crystalline bedrocks (Barla and Chiriotti, 1995; Agliardi et al., 2001). Hydrogeology of fractured rocks is characterized by heterogeneous, anisotropic and discontinuous properties (Maréchal, 1998; Cappa et al., 2004; Bogaard et al., 2007). In addition, vertical gradients of the hydraulic conductivity can occur with values ranging from 10^{-11} to 10^{-5} m/s towards the decompressed surface areas (Maréchal and Etcheverry, 2003). These permeability contrasts may be sufficient to support perched aquifers (Vengeon, 1998; Tullen, 2002; Cappa et al., 2004; Binet, 2006). Heterogeneous, anisotropic and discontinuous properties are accentuated by the landslide deformation and by presence of weathering product (colluvium, clay) filling the open fractures. Consequently, hydrogeological data are highly dependent on the scale of observation (Clauser, 1992) and local measurements are rarely representative of the overall behaviour of the landslide aquifer.

Most deep-seated landslides have a well-developed destabilization monitoring network with numerous stations and various technologies involved (extensometer, radar, LIDAR, geodesy…). Hydrogeological studies of landslides are however difficult to carry out because of the scarcity of natural or artificial access points to the aquifer triggering the movement. Indeed, in the unstable area piezometers have short lifespans. In addition, direct and local measures of the groundwater levels may be not representative of the whole moving rockmass. Classical methods of hydrogeological investigation are not appropriate and recent studies focus on indirect methods such as hydrochemistry surveys by monitoring springs for artificial

and natural tracers (Guglielmi et al., 2002; Cappa et al., 2004; Binet et al., 2007a; Bogaard et al., 2007; Charlier et al., 2010; Cervi et al., 2012; Debieche et al., 2012; Lin and Tsai, 2012). Hydrochemistry surveys enable a spatial integration of the groundwater processes and thus provide general information at the scale of the studied system (Guglielmi et al., 2002; Bogaard et al., 2007). However, indirect information of landslide groundwater provided by spring monitoring is often difficult to obtain as most deep-seated unstable zones are highly unstructured favouring infiltration rather than spring outflows (Binet et al., 2007a). In addition, unstable-slope groundwater outflows commonly flow through the scree cone at the landslide foot toward an alluvial aquifer at the valley bottom what limits surface spring occurrence. Therefore, generally few springs are located in the unstable zone and hydrogeological investigations have to be focused on springs surrounding the landslide. Generally, hydrochemical studies of landslides are limited to major element (Binet et al., 2007a). However, additional parameters can be included in hydrogeological studies to identify and quantify specific processes (recharge area, transit times, balance calculation, water-rock interaction) such as isotope of hydrogen and oxygen contents (Guglielmi et al., 2002), trace elements (Cervi et al., 2012), and the natural fluorescence (Charlier et al., 2010).

Because hydrochemistry surveys are time-consuming, expensive and require specific expertise, many landslide studies are based on a few field visits, in order to have a snapshot survey of the hydrogeological conditions (Vengeon, 1998; Guglielmi et al., 2002; Binet et al., 2007a). On the contrary, a dedicated hydrogeological study monitors a wide range of parameters, including water-level, on the long term, enabling extensive analysis (Cervi et al., 2012). This study aims at showing that an intermediate level of investigation allows to accurately and efficiently determine or to refine a groundwater model. The proposed method combines three complementary approaches: (1) a one-time multi-tracer test survey during a high flow period, (2) a seasonal monitoring of the water stable isotope content and the water electrical conductivity, and (3) a hydrochemical survey during a low flow periods, in order to determine: (i) flow path and residence time of the groundwater, (ii) average recharge elevation and hydrodynamic behaviour of springs, and (iii) spring chemical clusters and water origin.

3 Materials and methods

3.1 Method and strategy

It is crucial to characterize the groundwater flow pattern functioning during high flow period since it is during such a period that the landslide destabilisation triggered by high recharge amount is the worst. Moreover, during high groundwater level conditions, fracture connectivity is maximal, resulting in flow paths not existing in the drier seasons. Fluorescent tracers are used in this study as they show a high sensitivity analysis, low detection limits, and low toxicity level (Leibundgut et al., 2011). Tracer test settings can be used to characterize (1) the extension of the recharge area of the unstable slope, (2) groundwater flow path hypotheses by investigating the contribution of a spatially constrained area, (3) the presence or not of a perched drainage in the disturbed zone, (4) the role of the main fractures in the slope groundwater flow and (5) groundwater flow velocities. The recovery rate of the tracer can further help quantifying the hydraulic properties of the aquifer (Cappa et al., 2004; Binet et al., 2007b).

The dual-permeability of fractured reservoirs involves complex hydraulic connections between few conductive fractures and numerous poorly conductive fractures (Cappa et al., 2004). The numerous poorly conductive fractures are hereafter referred to as micro-fissured matrix. The seasonal fluctuations of the springs chemistry inform to which proportion the spring is recharged through the conductive fractures (sensitive to dilution by recharge variations) of the aquifer and/or the micro-fissured matrix (inertia of the aquifer promoting water-rock interaction) (Pili et al., 2004). In addition, the fluctuations of the saturated zone depth, controlled by the seasonal recharge variability, can modify the hydraulic connections and the groundwater flowpaths of the fractured reservoir. Springs supplied by a well-developed and well-connected network of conductive fractures will show a significant seasonal variation of the elevation of their average recharge area whereas the springs supplied by the micro-fissured matrix will show less seasonal variations. Therefore the analysis of seasonal variations of chemistry and of recharge-area elevation of springs (seasonal pattern, dispersion, amplitude ...) can be used to qualitatively characterize the hydrodynamic behaviour of the aquifer. In this study, the water chemistry of springs is investigated with the water electrical conductivity which is representative of the water total mineralization.

Recharge-area elevation is evaluated using water stable isotope ($\delta^{18}O$). Water stable isotope fractionation is thermo-dependent, leading to a series of effects on the isotope fractionation (Clark and Fritz, 1997). At the scale of a landslide site, only the elevation effect and seasonal effects have a non-negligible impact on the isotope fractionation (Leibundgut et al., 2011). The determination of the local elevation effect (elevation = a * $\delta^{18}O$ + b) enables the determination of the average recharge elevation of the sampled springs. Generally, the seasonal effect, which can significantly influence the elevation effect, makes it necessary to characterize the local elevation effect for each sampling campaign.

During low flow periods, the groundwater flow is mainly driven by the aquifer drainage, with low external disturbance (low recharge). As a consequence, the chemical content of the groundwater is controlled by the mineral dissolution rates and the water-rock interaction duration, and is independent from the recharge influence (Hilley et al., 2010). The hydrochemistry analysis enables to distinguish various water chemical groups and to compare them with the massif lithology. This comparison provides information about water origin, residence time and flow paths. The groundwater chemistry can also be influenced by the landslide hydromechanical processes, thus allowing to distinguish water which flowed through the unstable zone from the water which did not flow through the unstable zone (Binet et al., 2009). In addition, geochemical inverse modelling allows to characterize solid phases involved in the water-rock interaction processes, to estimate the mass transfers and to confirm the flow path hypotheses with the results of tracer tests and $\delta^{18}O$ values (Cervi et al., 2012).

3.2 Study area

The Séchilienne landslide is located to the south-east of Grenoble (France), on the right bank of the Romanche River, on the southern slope of the Mont-Sec massif (Fig. 10). The landslide is located in the Belledonne crystalline range and is composed of micaschists. The micaschists are characterized by a N-S trending vertical foliation. Carboniferous to Liassic sedimentary deposits unconformably cover the micaschists along the massif ridge line, above the unstable zone. Locally, glacio-fluvial deposits overlie both the micaschists and the sedimentary deposits. Micaschists mainly consist of quartz, biotite, phengite and chlorite, with occurrences of quartz-albite granoblasts, carbonate veins, and disseminated pyrite. Liassic deposits consist of limestones with intercalation of breccia-rich layers containing pebbles of coal, micaschists and dolomites, while Triassic deposits are represented by sandstone, quartzite, dolomite and

minor intercalation of black shales and argilites. Carboniferous deposits are characterized by micaceous black shales, sandstones and conglomerates with intercalations of anthracite (Barféty et al., 1972; Vengeon, 1998). Fluvio-glacial and colluvial deposits contain reworked materials from the previously cited formations.

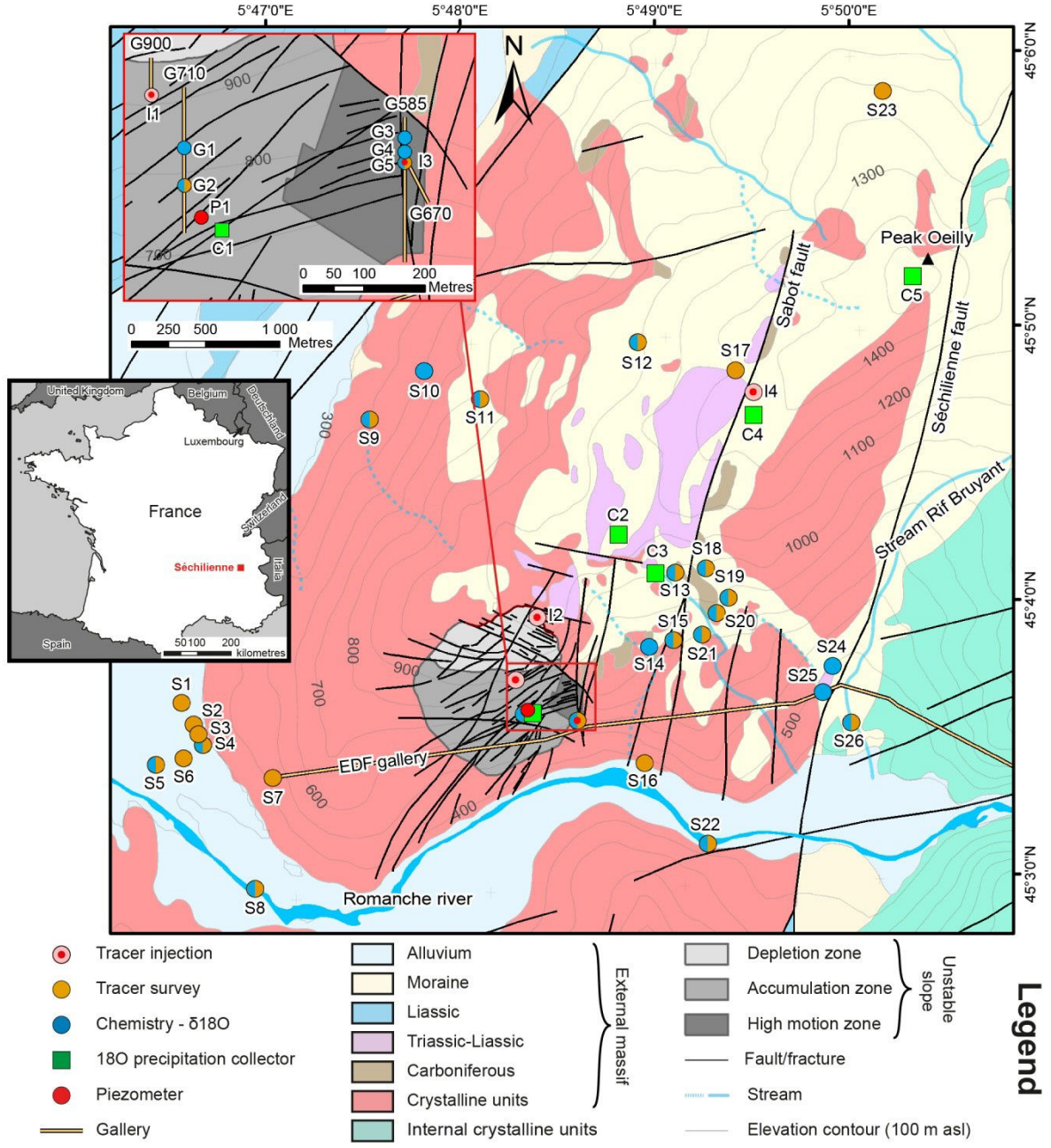

Fig. 10: Séchilienne landslide site map and monitoring network. The unstable slope boundary is defined according to the geophysical survey of Leroux et al. (2011)

The Séchilienne landslide is limited eastwards by a N-S fault scarp and northwards by a major head scarp of several hundred meters wide and tens of meters high below the Mont Sec. Rare

geomorphological evidence allows to define precisely the western and southern boundaries of the unstable area. The landslide Séchilienne is characterized by a deep progressive deformation controlled by the network of faults and fractures. A particularity of the Séchilienne landslide is the absence of a well-defined basal sliding surface. The landslide is affected by a deeply rooted (about 100-150 m) toppling movement of the N50-70° slabs to the valley (accumulation zone) coupled with the sagging of the upper slope (depletion zone) beneath the Mont Sec (Vengeon, 1998; Durville et al., 2009; Lebrouc et al., 2013). Lastly, a very actively moving zone, where high displacement velocities are measured, is distinguishable from the unstable slope. The Séchilienne landslide is characterized by a good correlation between antecedent cumulative precipitation and average displacement velocities (Rochet et al., 1994; Alfonsi, 1997; Durville et al., 2009; Chanut et al., 2013). Helmstetter and Garambois (2010) showed a weak but significant correlation between rainfall signals and rockfall micro-seismicity. Vallet et al. (2014) showed that the Séchilienne displacement rates are better correlated to the recharge than to the precipitation, reinforcing the significant role of groundwater flow in the Séchilienne destabilization.

3.3 Application to the Séchilienne site

The landslide is highly fractured and shows a much higher hydraulic conductivity than the intact underlying bedrock (Vengeon, 1998; Meric et al., 2005; Le Roux et al., 2011), thus leading to a landslide perched aquifer (Guglielmi et al., 2002). Besides, a deep saturated zone at the base of the slope is hosted by the fractured metamorphic bedrock over the whole massif bearing the landslide, with a thick vadose zone at its top. Although the Séchilienne landslide has already been investigated by two distinct hydrochemistry snapshot surveys (Vengeon, 1998; Guglielmi et al., 2002), groundwater flow mechanisms that are responsible for recharge of the landslide perched aquifer are still in debate.

Vengeon (1998) showed that the landslide perched aquifer is recharged by water-level rises of the deep saturated zone, whereas Guglielmi et al. (2002) showed that the main recharge originates from the sedimentary perched aquifer. Conclusions are mainly based on rough water-balance estimation, geological observations and limited hydrogeology data. Indeed, the Séchilienne site presents a spatially sparse hydrogeological network. First, no springs are located in the unstable zone. Second, surrounding springs of the massif are subject to high

anthropic pressure (water diversion) which makes springs flow measurements impossible and so hinders the analyses.

The monitoring network implemented in this study is described in figure 10 and Appendix A. Water sample analyses are described in Appendix B. Tracer test surveys were performed in two campaigns during April 2001 and March 2002. The March 2002 survey was coupled with a hydrochemical survey of the water inflows in the EDF gallery (Appendix A). Seasonal analysis and hydrochemical surveys spread from September 2010 to September 2012. They include (1) four isotopic campaigns (26 spots) performed quarterly coupled with 12 water electrical conductivity (EC) surveys, (2) 5 hydrochemistry surveys (21 spots) performed in low flow periods, from early June to late September. The four isotopic campaigns were performed every three months: December 2011, March 2012, June 2012 and September 2012. Hydrochemical data of the G585 gallery (Vengeon, 1998), were also integrated in this study. Lastly, water inflows and fracture data observed in the five galleries and their 3D spatialization were compiled in order to approximate the depth to the water level within the unstable slope (Vengeon, 1998). The seasonal variations of the recharge area (and also of EC) are estimated for each spring by estimating the standard deviation (SD) based on the samples of the seasonal campaigns. An average elevation of the recharge area for each spring is also estimated based on the seasonal samples.

3.3.1 Tracer test injection points

A 4-tracer test survey was implemented in April 2001 in the Séchilienne unstable slope recharge area. Four different fluorescent tracers were injected at four strategic locations (Fig. 10 and Table 1).

Table 1: Settings of the multi-tracer test of April 2001

Injection location	Tracer	Date	Tracer (kg)	Water (m^3)
I2	Rhodamine	10-April-2001 10:00	5	8
I1	Sodium napthionate	10-April-2001 13:00	6	30
I4	Uranin	10-April-2001 17:00	8	3
I3	Eosin	11-April-2001 12:00	5	●

A sinkhole (I4) located along the Sabot fault (Fig. 10) was selected as a representative infiltration location of the top sedimentary cover to evaluate the extent of the recharge area. A crack located in the depletion zone (I2) was chosen to represent the infiltration on the

summital landslide area. A depression zone (I1) located in the accumulation zone near the mine gallery G900 was chosen to test the hydraulic conductivity of the N70 near-vertical fractures. A sink in the mine gallery G585 (I3) was chosen as an injection spot to test the infiltration on the N-S fault zone bordering the rapidly moving landslide zone. Since the EDF gallery was flooded at the time of the survey, a detailed monitoring of the water inflow points was not possible. A second tracer test was performed in March 2002 when the gallery was emptied for maintenance. Due to the impossibility to measure the flow of springs, only the shortest transit times are deduced from the tracer test survey.

3.3.2 Estimation of the elevation of the spring recharge area from $\delta^{18}O$ measurements

In mountainous areas, a local calibration of the isotopic gradient is generally possible, using springs with well defined recharge areas. In the case of the Séchilienne landslide, no such springs allow to estimate the isotope elevation gradient. Instead, five rainfall collectors were settled to characterize the $\delta^{18}O$ signal (Fig. 10, appendix A). The infiltration isotopic signals can be modified from the precipitation initial signal through the soil layers by evaporation processes, leading to a $\delta^{18}O$ enrichment (Gat, 1996). Two rainfall collectors were therefore coupled with a lysimeter in order to evaluate the evaporation impact on the actual $\delta^{18}O$ infiltration signal.

Because the hydrodynamic properties of the aquifers can delay and buffer the infiltration signal, the water which comes out of springs does not generally correspond to the last rainfall period. Therefore, a $\delta^{18}O$ synchronic instantaneous water sampling for both springs and rainfall collectors would not be relevant. To take into account the transit through the aquifer, the spring water $\delta^{18}O$ signal will be compared with the $\delta^{18}O$ signal of a cumulated amount of precipitation which fell during the period between two consecutive spring sampling campaigns (about three months). Thus, the isotopic signal of the rain collectors corresponds to the precipitation $\delta^{18}O$ signal weighted by the three-month rainfall amount. The isotope elevation gradient of precipitation is determined with the $\delta^{18}O$ data of the five rain collectors. The isotope elevation gradient of infiltration will be considered identical to the slope of the isotope elevation gradient of precipitation and only the intercept is adjusted to fit to the lysimeter $\delta^{18}O$ measurements, assuming that evaporation is homogeneous (Fig. 11a). The elevation of the spring recharge area is estimated from the *infiltration* isotope gradients for the

April-June and July-September sampling campaigns, for which actual evaporation is significant, and from the *precipitation* isotope gradient for the October-December and January-March sampling campaigns.

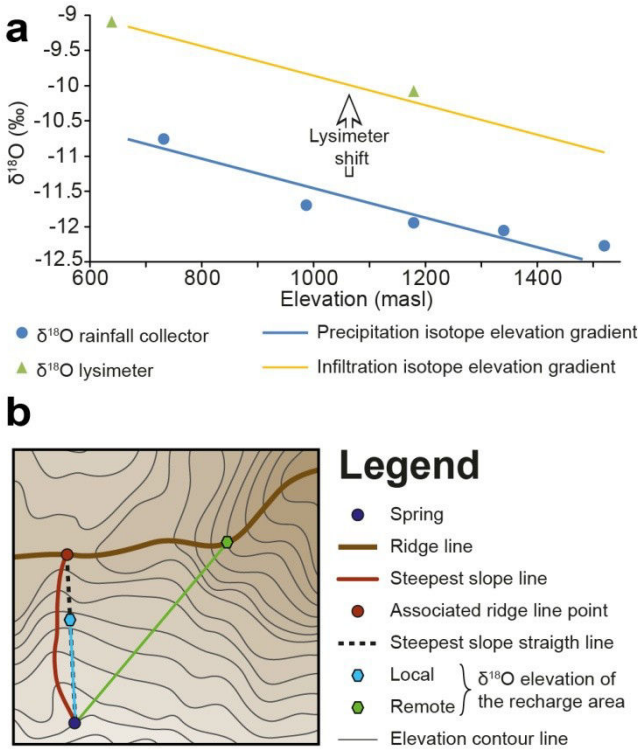

Fig. 11: Illustration of the methods implemented for the $\delta^{18}O$ analysis. (a) Determination of the isotope elevation gradient for precipitation and infiltration. (b) Spatial analysis of the $\delta^{18}O$ elevation of the spring recharge area

In order to locate the recharge area of the springs, the steepest slope line is drawn for each spring, up to the ridge line, based on a digital elevation model of a 25 meters resolution (Fig. 11b). This allows to define a ridge line point associated to each spring. If the $\delta^{18}O$ elevation of a spring recharge area falls within or close to the spring elevation-associated ridge line point elevation interval (materialized by the steepest slope straight line, Fig. 11b), then the recharge area will be considered as local. In this case, the groundwater flow is thought to follow the topographical gradient without any influence or disturbance linked to geological features such as fractures or faults. Otherwise, the $\delta^{18}O$ elevation of the spring recharge area will be placed along the ridge line, at the corresponding elevation, and the recharge area of the springs will be considered as remote. In this case, the groundwater flow is thought to be controlled by geological features. An average elevation of the recharge area for each spring is estimated from the elevation values of the four water sampling campaigns. The difference between this

average elevation and the elevation of the associated ridge line point, expressed in function of the percentage, will allow to discriminate groups of springs.

3.3.3 Hydrochemistry analysis

Groundwater chemistry is discussed using major ion concentrations. The nature and origin of the various springs is established by using a Durov diagram, which allows characterizing the relationships between the chemical type (function of encountered rock types) and the electrical conductivity (degree of mineralization). Hydrochemistry is complex as the alteration of each of the three distinct rocks (moraines, carbonates and micaschists) produces the same ions (Table 2).

Table 2: Origin of minerals according to rock types (B: bedrock, SC: Sedimentary cover) and stoichiometric formulae

Lithology	Minerals	Stoichiometric formulae	Water ion release
B	Albite	$NaAlSi_3O_8$	Na, HCO_3
B	Muscovite	$KAl_3Si_3O_{10}(OH)_2$	K, HCO_3
B	Clinochlore-14A	$Mg_5Al_2Si_3O_{10}(OH)_8$	Mg
B	Phlogopite	$KAlMg_3Si_3O_{10}(OH)_2$	Mg, K
B	Phengite	$K_{0.6}Mg_{0.25}Al_{1.8}Al_{0.5}Si_{3.5}O_{10}(OH)_2$	K, Mg
B (veins)/SC	Calcite	$CaCO_3$	Ca, HCO_3
SC	Dolomite	$CaMg(CO_3)_2$	Ca, Mg, HCO_3
B	Goethite	FeOOH	Fe
B	Pyrite	FeS_2	Fe, SO_4, H^+

Major ion combinations are used to characterize the water origin and the flow paths: Ca *vs*. HCO_3 for the sedimentary cover and Na *vs.* Cl to distinguish a precipitation origin from alteration of the micaschist (albite). In addition, the water content variations for each identified hydrochemical facies are investigated with Stiff diagrams. The hydrochemical facies deduced from the previous analyses are then spatially compared with the distribution of the geological formations. A geochemical inverse model is performed on the spring chemical contents and rock mineral phases, using PHREEQC code (version 3.1.1). The initial water chemistry (Table 3) matches with the average composition of Alpine rain water (Atteia, 1994). Minerals representative of the sedimentary cover and micaschist bedrock (Table 3) were chosen based on the work of Vengeon (1998).

Table 3: Inverse model conditions: mineral phases and initial water rain water composition from Atteia (1994)

Phases	Rain water	
Albite	Temp (°C)	20
Muscovite	pH	6
Clinochlore-14A	pe	4
Phlogopite	Ca (meq/L)	$3.85E^{-02}$
Phengite	Mg(meq/L)	$4.42E^{-02}$
Calcite	Na(meq/L)	$7.39E^{-03}$
Dolomite	K(meq/L)	$1.25E^{-03}$
Goethite	Fe(meq/L)	$5.45E^{-05}$
Pyrite	Al(meq/L)	$1.15E^{-04}$
$O_2(g)$	S(6) (meq/L)	$1.50E^{-02}$
$CO_2(g)$	Cl(meq/L)	equilibrate
	HCO_3(meq/L)	$2.41E^{-02}$
	SiO_2(mmol/L)	$5.30E^{-01}$

4 Results and discussion

4.1 High flow periods: Tracer test survey

Among the I4 test (Fig. 12a), the G1 water inflow displays the highest tracer velocity (3 km/day). Besides, numerous springs (S13, S16, S20 and S21) located along the N20 Sabot fault are positive, with velocities ranging from 0.45 to 0.84 km/day. The same is observed for the outlet S7 of the EDF gallery (0.88 km/day). The velocity contrast between G1 and the other positive springs indicates that the drainage by the unstable slope bypasses the N20 faults and is supported by near-surface drainage between the sedimentary cover and the unstable slope perched aquifers. This test also demonstrates the prominent role of the Sabot fault and the EDF gallery in the drainage of the slope.

For the I2 test, only G1 and S13 are positive (Fig. 12b). A high velocity difference can be observed between the down-slope flow, 7-fold faster than the lateral flow towards the N20 fault (0.55 *vs.* 0.08 km/day). This difference can be attributed to the dense opened fractures network and to the highest hydraulic gradient alongside the steepest slope. This test demonstrates the significant drainage role of the unstable slope and also the role of the N20 Sabot fault.

The I1 test highlights a main westward drainage component, except for S16 and G5 springs (Fig. 12c). In this part of the unstable zone, the groundwater flow is very likely supported by the dense network of N70 fractures and by the EDF gallery. On the contrary, the southeast drainage seems to be supported the Sabot fault. The average velocities range between 0.06 and 0.16 km/day. The first test in the gallery 585 (I3- A test, Fig. 12d) is detected at the EDF gallery outlet (S7), confirming the drainage role of the EDF gallery. High velocities (0.49 to 2.36 km/day) are observed for the western springs contrary to the eastern S16 spring (0.14 km/day).

The second G585 test (I3-B test, Fig. 12e) is positive at four kilometric points: 5.28 and 5.50 to the east, demonstrating the influence of the N20 Sabot fault, and 6.32 and 6.40 to the west, confirming the role of the EDF gallery in the collection of a part of the water flowing from the N70 fractures.

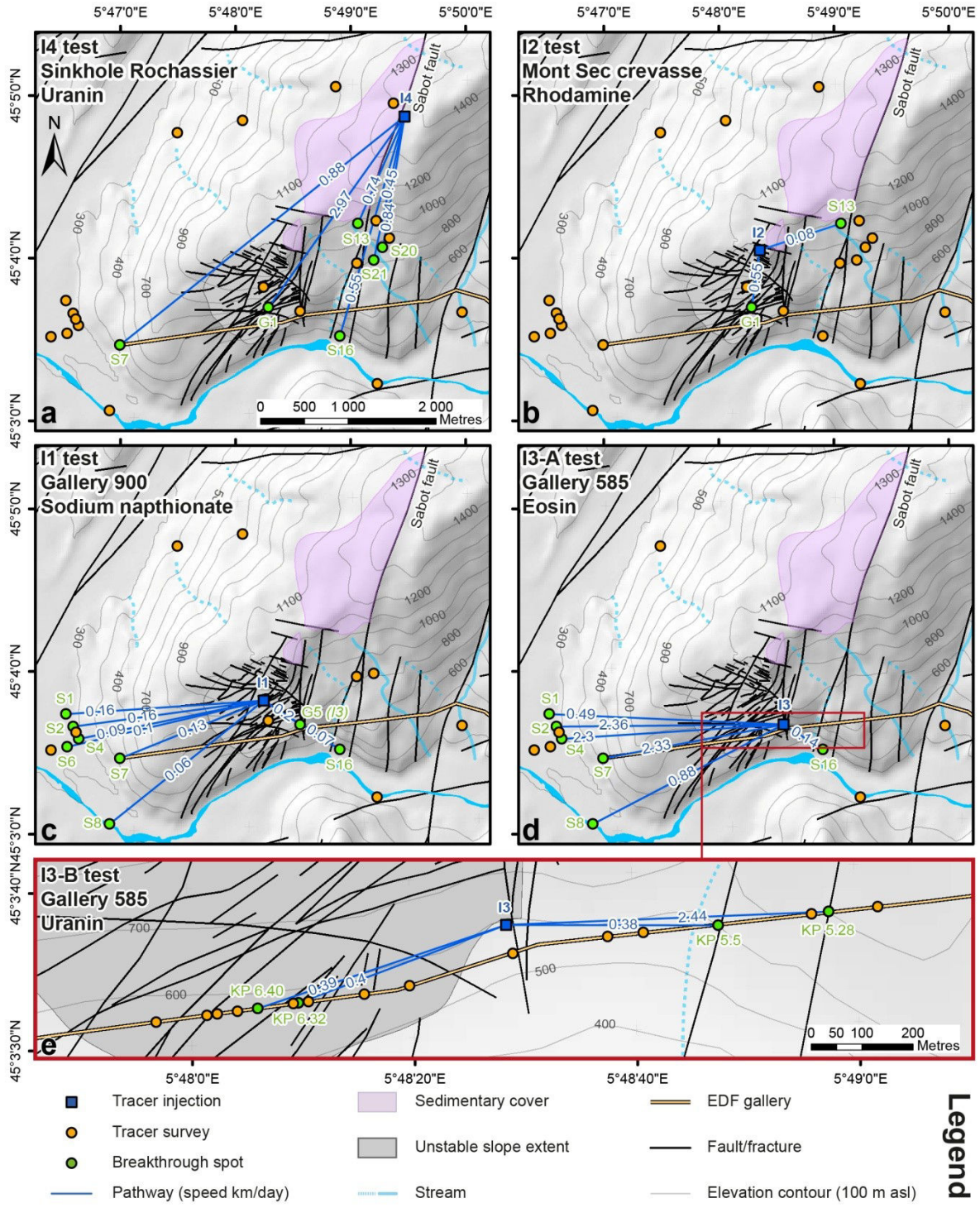

Fig. 12: Tracer-tests analysis of April 2001 and March 2002 campaigns with (a) I4 test, (b) I2 test, (c) I1 test, (d) I3-A test and (e) I3-B test

A comparative analysis of the four tracer tests allows a better characterization of groundwater flow in the massif. The same velocity range, about 0.13 and 2.3 km/day, is observed for the eastern springs and for the EDF gallery outlet (S7) for both the I1 and I3-A tests, respectively, suggesting that the eastern springs are partly recharged by water from the EDF gallery. S7

showed high velocities (2.3 km/day) during I3-A test (Fig. 12d) and the EDF gallery water inflows show low velocities (0.4 km/day) during I3-B test, but breakthrough times are similar (about one day). This velocity contrast can be explained by the quasi-instantaneous transit through the EDF gallery which overestimates groundwater velocities to the EDF gallery. S7 flow velocity for I3-A tests can be estimated at 0.4 km/day instead of 2.33 km/day, similar to the EDF gallery tracer speeds observed during the I3-B test. The high speeds of the western springs (S2 and S4) during the I3-A test, similar to the S7 outflow, show that these springs are likely influenced by the EDF gallery outflow. The I2 test show a high velocity toward G1 (0.55 km/day) as well as the I1 test toward G5 (0.2 km/day). These high velocities reveal a high hydraulic connectivity of the unstable zone promoted by a dense fracture network. The Romanche River (S8) is positive for two tracer tests (I1 and I3-A) meaning that the EDF gallery collects only a part of the slope groundwater, the remaining reaching the river through the alluvium aquifer. Among the three tracer tests (I2, I1, I3-A), a rather homogeneous velocity (0.07 to 0.14 km/day) is observed for S16 and S13. These slow flows, compared to the one observed during the I4 test, demonstrate flow through micro-fissured matrix drained toward the east by N20 faults.

4.2 Seasonal analysis

The isotopic abundance ratio of a water sample is expressed as $\delta^{18}O$ in ‰ *vs.* V-SMOW. The determination of the isotopic elevation gradients for the four seasons show significant seasonal variations (with values of -0.12‰/100m for November-December , -0.25‰/100m for January-March, -0.21‰/100m for April-June and -0.18‰/100m for July-September, Fig. 13). These values confirm the seasonal effect on the isotope fractionation and are in accordance with commonly observed values from -0.1‰/100m to -0.36‰/100m (Leibundgut et al., 2011). S25, S24, S13, S18, S5, S9, S11 and G1 show either unrealistic values (disregarded) or lack of data.

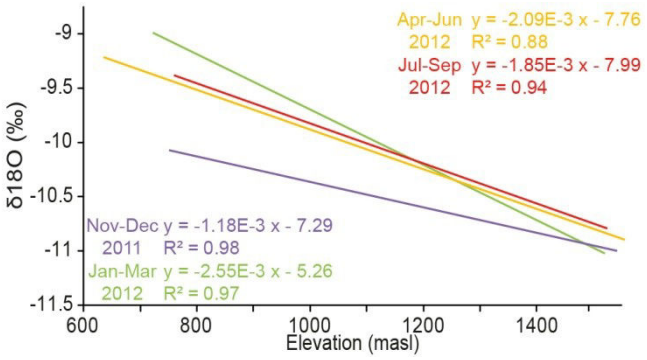

Fig. 13: Isotope elevation gradients for the four seasonal water sampling campaigns

The elevation of the recharge area of the S5 and S4 springs are similar and are about 1800 m above the highest massif peak (Peak Oeilly) and below the Romanche river (Fig. 14a), but a distinct seasonal variability (SD of 32 for S5 and 315 m for S4). In addition, is also observed these springs show low values and a low variability of EC (340 µS/cm with SD of 14 µS/cm; Fig. 14c). These two springs seem to be influenced by both the massif slope groundwater and the Romanche water. The Romanche water smoothes the amplitude and the variations of the EC and increases the elevation of the recharge area and its seasonal variability (high sensitivity of drainage surface network from seasonal variations). S4 cannot be recharged by the Romanche alluvium aquifer, thus indicating that the open EDF gallery, which withdraws water from the Romanche River, recharges the slope aquifer at its western part. S25 and S24 springs show a behaviour similar to that S4 with low values and a low variability of EC (370 and 200 µS/cm with SD of 5 µS/cm). The S25 and S24 hydrodynamic behaviours of S25 and S24 are probably due to the recharge of the slope aquifer by the Rif Bruyant stream. The dilution by Rif Bruyant (recharge-area elevation of 1010 m asl) certainly caused an underestimation elevation of the recharge area of the slope aquifer water recharging the springs. Therefore the elevation of the recharge area is assumed to be near the Peak Oeilly from which groundwater is drained by the main Séchilienne fault (Fig. 14d)

S21, S15, S14, S20, and S13 springs show mean elevations higher than the elevation of their associated ridge line points (16 % higher on average, Fig. 14b). These springs further show high seasonal variabilities (SD of 100 m and 22 µS/cm on average) with the lowest EC values and recharge areas elevations observed during the high flow period and the reverse for the low flow periods (Fig. 14a and 14c). These springs are supplied by rapid water flow through fractures during high flow periods (dilution) and drainage through the micro-fissured matrix

during low flow periods mobilizing remote recharge area. On the contrary, S9, S10, and S11 springs show mean recharge area elevation close to their associated ridge line points (at most 4 % higher) with low seasonal variations. These springs show moderate EC variability (SD: 15 µS/cm) with no clear seasonal patterns. These results show that their recharge areas are mainly local and little sensitive to the seasonal variations (Fig. 14a, 14b and 14c), meaning that the springs flow is controlled by the micro-fissured matrix component. S18 spring presents an intermediate hydrodynamic behaviour between the two previous groups.

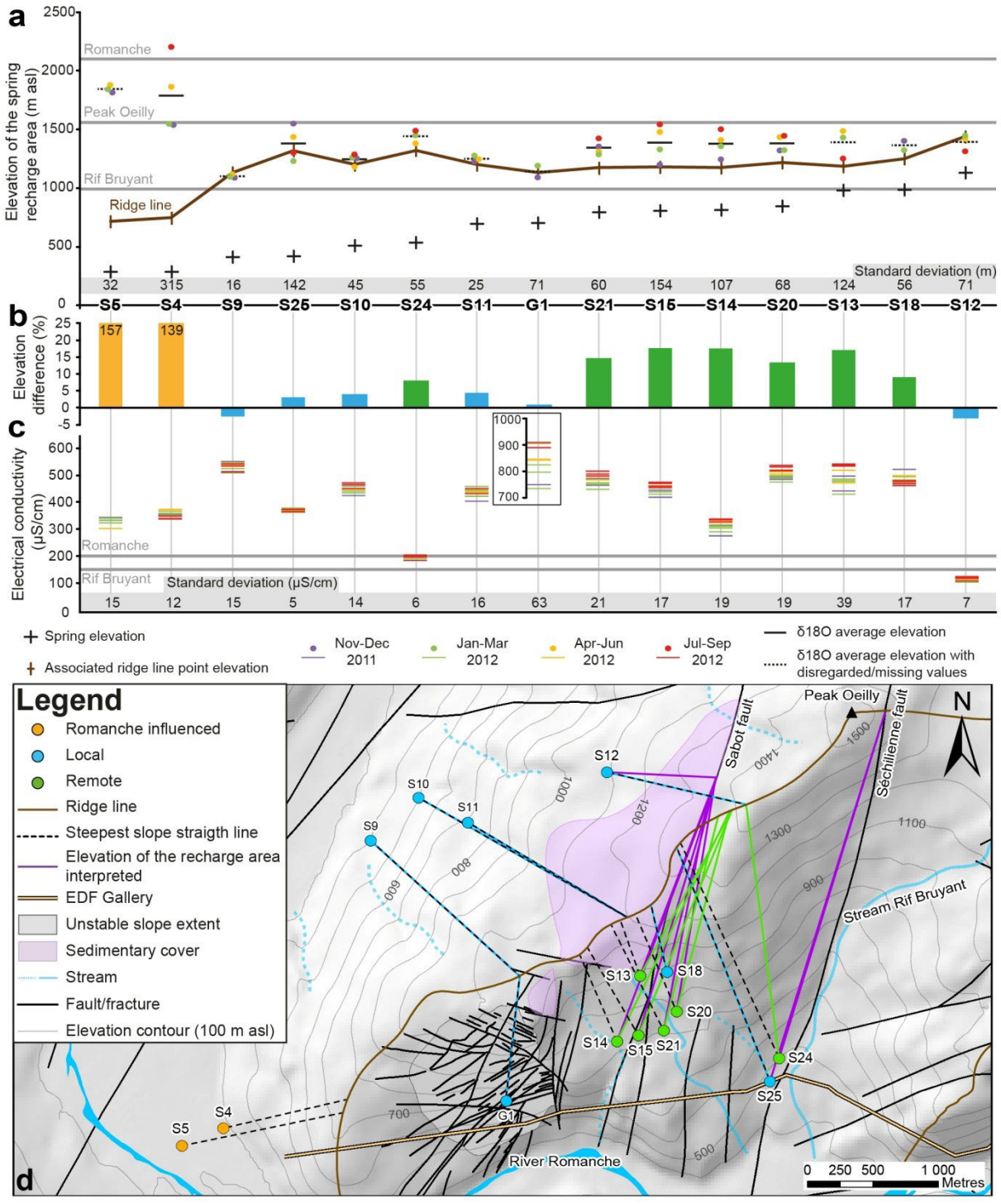

Fig. 14: Seasonal analysis of $\delta^{18}O$ and electrical conductivity of springs. (a) Seasonal $\delta^{18}O$ estimated elevation of springs plotted relatively to spring elevation, associated ridge line elevation, and $\delta^{18}O$ estimated elevation of surface network (Romanche and Rif Bruyant). (b) Difference between the average spring recharge area elevation and the associated ridge line point elevation. (c) Seasonal analysis of electrical conductivity plotted relatively to surface network signal (Romanche and Rif Bruyant). (d) Spatial analysis of the $\delta^{18}O$ elevation of the spring recharge area

Spring G1 was only sampled twice and it is not possible to assess clearly the seasonal variations. However, the recharge area seems mainly local as the two high flow period surveys show a mean recharge area (1143 m asl) closed to the elevation of the associated ridge line point. G1 shows the highest EC values (840 µS/cm) and the highest EC seasonal variability (SD: 63 µS/cm). These results are interpreted as enhanced water-rock interaction between groundwater and the unstable slope rocks (section 4.3.2, Binet et al. 2009). Spring S12 has a very low conductivity (155 µS/cm), probably due to low water-rock interaction time. It also shows a scattered $\delta^{18}O$ signal. One possible explanation is that this spring is recharged by rapid water flow through sedimentary cover.

4.3 Low flow periods: hydrochemistry survey

The chemical composition of the monitored springs is detailed in Table 4. The Durov and Stiff diagrams (Fig. 15a and 15b) highlight four distinct water chemical groups reflecting groundwater flow through various geological media. Group 1 corresponds to Ca-HCO_3-rich waters (S12) with low EC values (about 100 µS/cm). Group 2 corresponds to Mg-Ca-HCO_3-rich waters (S24, S25, S11, S10 and S9) where Ca and Mg are in the same proportions and EC are from 200 µS/cm (S24) to 540 µS/cm (S9). Water composition of group 3 varies from Mg-Ca-HCO_3-SO_4-rich waters (G4 and G3), with intermediate Mg-Ca-SO_4-HCO_3-rich water (G5 and G1), to Mg-Ca-SO_4-rich waters (G2). The EC values vary from 300 µS/cm (G4 and G3) to 850 µS/cm (G1). Group 4 corresponds to Ca-Mg-HCO_3-SO_4-rich waters (S4, S14, S15, S18, S21, S20 and S13) with EC values varying from 350 µS/cm (S4 and S14) to 520 µS/cm (S21, S20 and S13). In this study, the inverse model is tested for four springs: S11, S10, S9 representative of the stable zone and G1 representative of the unstable zone.

Table 4: Physico-chemical parameters and major ions of the monitoring springs. Values are the average from the number of gather samples. SN: sample number. HF: Hydrochemical facies, Temp.: temperature (°C), EC: electrical conductivity (µS/cm), ionic concentrations in meq/L, n.a. = non-analysed

HF	Station ID	Water Type	SN	Temp. (field)	pH (field)	EC (field)	Ca meq/l	Mg meq/l	Na meq/l	K meq/l	Cl meq/l	HCO_3 meq/l	SO_4 meq/l	SiO_2 mmol/l
1	S12	Ca-HCO_3	5	10.22	7.72	120.0	0.88	0.21	0.09	0.01	0.03	0.86	0.16	0.14
2	S24	Mg-Ca- HCO_3	5	10.30	7.57	202.8	1.05	0.93	0.15	0.01	0.06	1.59	0.41	0.17
	S9	Mg-Ca- HCO_3	4	12.10	7.52	538.8	2.69	3.16	0.19	0.02	0.06	4.28	1.62	0.16
	S10	Mg-Ca- HCO_3	4	11.47	7.94	455.8	2.59	2.32	0.16	0.02	0.04	3.84	1.12	0.16
	S11	Mg-Ca- HCO_3	2	9.90	7.75	440.5	2.50	2.32	0.14	0.02	0.04	3.75	1.06	0.15
	S25	Mg-Ca- HCO_3	5	13.66	7.86	367.0	1.95	1.87	0.18	0.02	0.08	3.04	0.75	0.16
3	G1	Mg-Ca-SO_4- HCO_3	4	11.75	8.08	872.5	5.10	4.79	0.26	0.04	0.05	3.43	5.88	0.12
	G2	Mg-Ca-SO_4	4	12.10	7.67	384.3	1.98	1.80	0.21	0.05	0.05	0.61	3.18	0.23
	G3	Mg-Ca- HCO_3-SO_4	1	10.10	7.05	314.0	1.55	2.09	n.a.	n.a.	0.33	2.64	1.03	n.a
	G4	Mg-Ca- HCO_3-SO_4	2	10.55	7.44	446.0	2.03	3.04	n.a.	n.a	0.07	2.92	2.29	n.a
	G5	Mg-Ca-SO_4- HCO_3	3	10.10	7.37	629.7	2.22	5.07	n.a.	n.a	0.06	3.47	3.92	0.14
4	S4	Ca Mg-HCO_3-SO_4	5	11.22	7.56	354.8	2.88	0.68	0.21	0.02	0.18	2.05	1.36	0.12
	S13	Ca Mg-HCO_3-SO_4	5	8.62	7.85	522.4	4.20	1.46	0.10	0.02	0.03	3.30	2.30	0.12
	S14	Ca Mg-HCO_3-SO_4	5	11.50	7.77	332.2	2.31	1.07	0.15	0.01	0.09	2.51	0.80	0.13
	S15	Ca Mg-HCO_3-SO_4	5	11.24	7.54	465.2	3.53	1.42	0.13	0.02	0.09	3.25	1.58	0.12
	S18	Ca Mg-HCO_3-SO_4	5	8.92	7.63	481.8	4.06	1.21	0.10	0.01	0.13	3.87	1.36	0.12
	S20	Ca Mg-HCO_3-SO_4	5	10.66	7.50	521.2	4.25	1.41	0.12	0.02	0.06	3.58	1.97	0.12
	S21	Ca Mg-HCO_3-SO_4	3	12.00	7.70	499.7	3.99	1.33	0.12	0.01	0.06	3.40	1.93	0.12

4.3.1 Stable zone (Group 1 and 2)

The low concentrations of Ca and HCO_3 of Group 1, located on the calcite equilibrium line, is representative of water circulating in a carbonate or calcite dominant cover (limestone or moraines) with a short residence time (Fig. 15c). For Group 2 (S24, S25, S11, S10, S9), inverse modelling shows that the Mg concentrations come from 89 % of dolomite and 11 % of phlogopite. 86 % of the Ca is derived from the dolomite and the remaining 14 % from the calcite. Therefore, the high Mg concentrations are explained by water transit through the carbonate materials. However, these spring compositions are above the dolomite equilibrium line (Fig. 15c). This can be explained by the alteration of pyrite which releases protons (Eq. (2)) which can consume afterwards the HCO_3 produced by dissolution of carbonate minerals (Eq. (3)), releasing CO_2 and H_2O (Eq. (4)). The δS^{34} analyzes performed by Vengeon (1998) show that SO_4 has a sulfurized origin, due to alteration of pyrite, present only in the micaschist bedrock.

$$FeS_2 + \frac{15}{4} * O_2 + \frac{7}{2} * H_2O \leftrightarrow Fe(OH)_3 + 2SO_4^{2-} + 4H^+ \quad (2)$$

$$(Ca, Mg)(CO_3)_2 + 2H_2O + 2CO_2 \leftrightarrow Ca^{2+} + Mg^{2+} + 4HCO_3^- \quad (3)$$

$$HCO_3^- + H^+ \leftrightarrow H_2O + CO_2 \quad (4)$$

This succession of chemical reactions explains the range of pH (between 7 and 8) measured in the Séchilienne waters, despite the production of protons, and results in a depletion of HCO_3 ions with respect to Ca and Mg, the latter being balanced by SO_4 (Table 4). The springs of Group 2 are therefore recharged by water which circulated through carbonates and basement formations. The low conductivity of S24 and S25 are explained by the influence of the Rif Bruyant stream, highlighted by the seasonal analysis (see section 4.2).

4.3.2 Unstable zone (Group 3)

Group 3 (G5, G4, G3, G2, G1) is characterized by the highest SO_4 concentrations (Fig. 15 and Table 4) which can be explained by two mechanisms related to the slope deformation. First, the opening and/or closing of fractures and cracks lead to a new flowpath through unaltered pyrite zones (Calmels et al., 2007) and, second, the friction and grinding along fractures due to the movement of rock masses cause a refreshment of pyrite reactive surfaces increasing the weathering rate (Binet et al., 2009). Lastly, the alteration of the pyrite promotes the alteration of carbonate and minerals in silicate veins or in colluvial deposits (Dongarrà et al., 2009; Gaillardet et al., 1999), as shown by the high Ca concentrations in G1 (Fig. 15c), and Na in the G710 gallery (G1 and G2, Fig. 15d). The acquisition of mineralization occurs mainly with the interaction of the basement minerals and SO_4 is clearly the marker of the unstable zone. The difference of the mineralization among the various gallery points is due to heterogeneities in mineral distribution within the basement and fracture network of the unstable zone. The inverse model calculation shows two solutions of mineral assemblage which can explain the Mg content of G1. Mg contents is either explained by water-rock interactions mainly in the basement with a Mg origin of 37 % from dolomite and 63 % from chlorite or explained by water-rock interactions in carbonate materials with a Mg origin of 91 % from dolomite and 9 % from phlogopite. The last scenario can be explained either by major tension cracks filled with colluvial deposits rich in limestone fragments or by water flowing from the sedimentary cover as suggested by the I4 tracer test (Fig. 12a).

4.3.3 Mixing zone (Group 4)

The group 4 (S4, S14, S15, S18, S21, S20 and S13) is distinguishable from other springs by concentrations of Ca, Na and SO_4. The Ca concentrations fall near the calcite equilibrium line (Fig. 15c), reflecting a significant transit in carbonate materials. The SO_4 concentrations which are up to 25 % higher than the springs of the stable zone (group 2) can be explained by groundwater flow through the stable bedrock. A mixing test was performed with water of carbonate pole (S12) and with water of the unstable zone (G1) to quantify the contribution of each component. The water composition of group 3 is explained by a water mixing 30 % of the unstable zone water and 70 % of the sedimentary cover water, which is consistent with tracer tests (Fig. 12). However, the mixing computation requires four times more mineralized water than S12 water, meaning that the carbonate component of the mixture has a longer residence time in the sedimentary cover. Lastly, S4 water is also a water mixture from the Romanche river water, the stable zone water and the unstable zone through drainage of the EDF gallery.

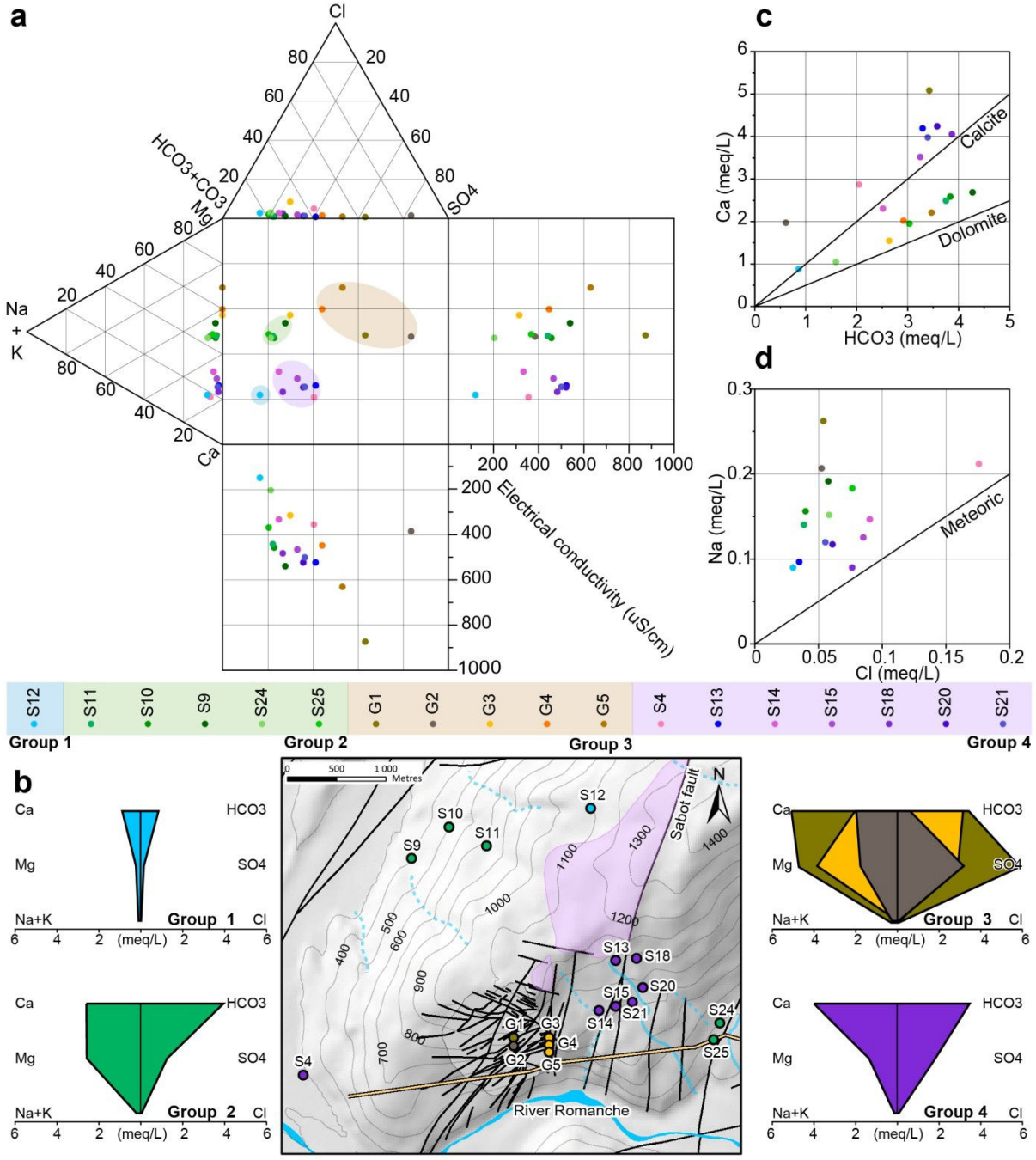

Fig. 15: Hydrochemistry analysis with (a) Durov diagram, (b) spatial analysis and Stiff diagrams and scatter plots of chemical concentrations: (c) Ca vs. HCO_3 and (d) Na vs. Cl

4.4 Gallery water inflows survey

Five galleries and one piezometer (P1) were surveyed (Fig. 16a). The highest gallery (G900) is always dry and no water inflows could be identified. The G710 gallery shows two leakages, one quasi-permanent almost dry in summer (G1), at 150 m from the entrance and one temporary (G2) at 80 m from the entrance. Two leakage zones were also identified for the

G670 gallery at 25 m and 70 m from the entrance. G585 gallery shows a temporary water inflow (202 m, G3) and a permanent water inflow (160 m, G5), and a localized leakage area (170 m, G4). Water inflows of the galleries are localized near fracture damaged zones (Vengeon, 1998), reinforcing the prominent role of fracture network in the groundwater flow path bypassing the less pervious matrix. Although the piezometer P1 is currently clogged, the water level fluctuations were recorded between 590 and 602 m asl from November 2009 to April 2010. These water-levels are considered as representative of high groundwater conditions (Fig. 16c).

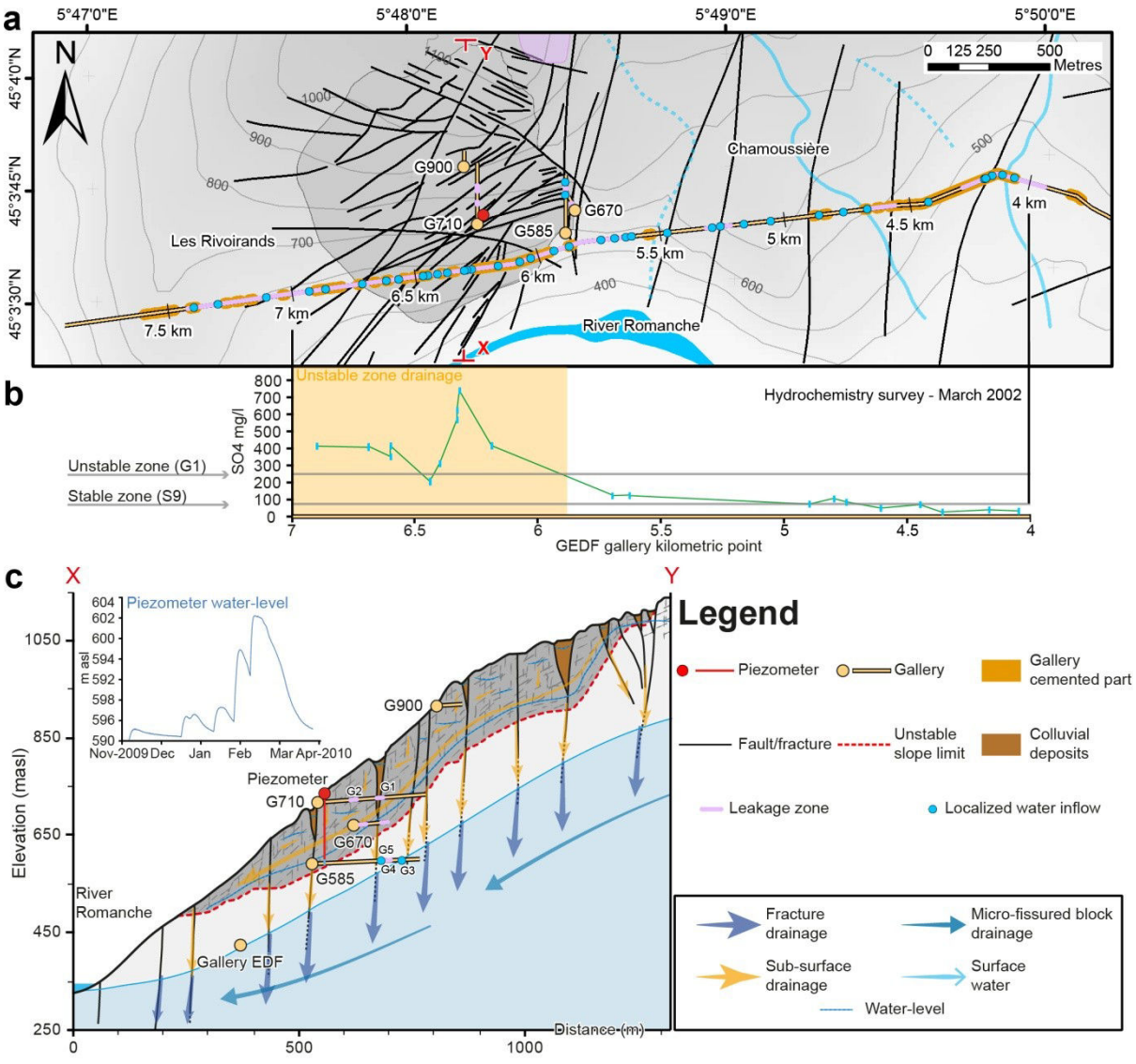

Fig. 16: Gallery survey. (a) Spatial analysis of water inflows. (b) SO_4 concentration of the EDF gallery water inflows. (c) Cross-section analysis of water inflows. The cross-section of the unstable zone is modified after Lebrouc et al. (2013). The unstable slope boundary is defined according to the geophysical survey of Leroux et al. (2011)

The EDF gallery has the particularity to show bare rock with limited cemented sections (revealing high fractured zones) with water flowing unconfined by gravity from an upriver Romanche withdrawing point. During the excavation of the EDF gallery, perennial springs located at Les Rivoirands and Chamoussière villages were permanently dried up (Fig. 16a). Numerous and scattered water inflows and leakages occur in the EDF gallery between 5.5 km and 7 km, matching with the dense fractures network of the landslide (Fig. 16a). Between 3.9 km and 4.5 km, the Séchilienne fault completely damaged the zone and many water inflows occur, revealing the prominent drainage role of the fault. To a lesser extent, the Sabot fault seems to have a more localized impact on the EDF gallery water inflows. The hydrochemistry survey shows that SO_4 is the marker of the unstable slope (see section 4.3.2). From kilometric points 4 to 5.80, SO_4 signal is similar to S9 representative of the stable zone, whereas from kilometric points 6 to 7, the SO_4 signal increases and even exceeds the concentration of G1 representative of the unstable zone (Fig. 16b). The SO_4 signal confirms the prominent drainage role of the unstable slope by the EDF gallery.

4.5 Groundwater conceptual model

4.5.1 Stable zone: Fractures vs. micro-fissured matrix

Two main groundwater flow types are identified: rapid and reactive water flow in fractures (S4, S13, S14, S15, S20, S21, S24 and S25) which bypass the bulk of the less pervious and inertial micro-fissured matrix on which S9, S10 and S11 depend (seasonal analysis, Fig. 14). These groundwater flows are characteristic of the dual-permeability of fractured reservoirs (Maréchal, 1998; Cappa et al., 2004). The main N20 Sabot fault plays a major role in the massif drainage, with a rapid transfer from the sedimentary cover, but this fault also drains the unstable zone with much lower velocities (tracer test and seasonal analysis, Fig. 12 and 14). This is confirmed by the hydrochemistry survey which show that the springs located along the Sabot fault match with a mixing of water which flowed through the sedimentary cover and the unstable slope (Fig. 15, group 4). Therefore, the Sabot fault has a significant spatial influence, draining out the deep aquifer below the unstable slope, likely because of a lowering of groundwater level which causes a west to east hydraulic gradient (tracer test, Fig. 12). Flow velocities (tracer test, Fig. 12), water mixing (hydrochemistry, Fig. 15) and the lack of fractures indicate that the unstable slope drainage is done mainly through the micro-fissured matrix and is minor relatively to the Sabot fault drainage axis (Fig. 17a).

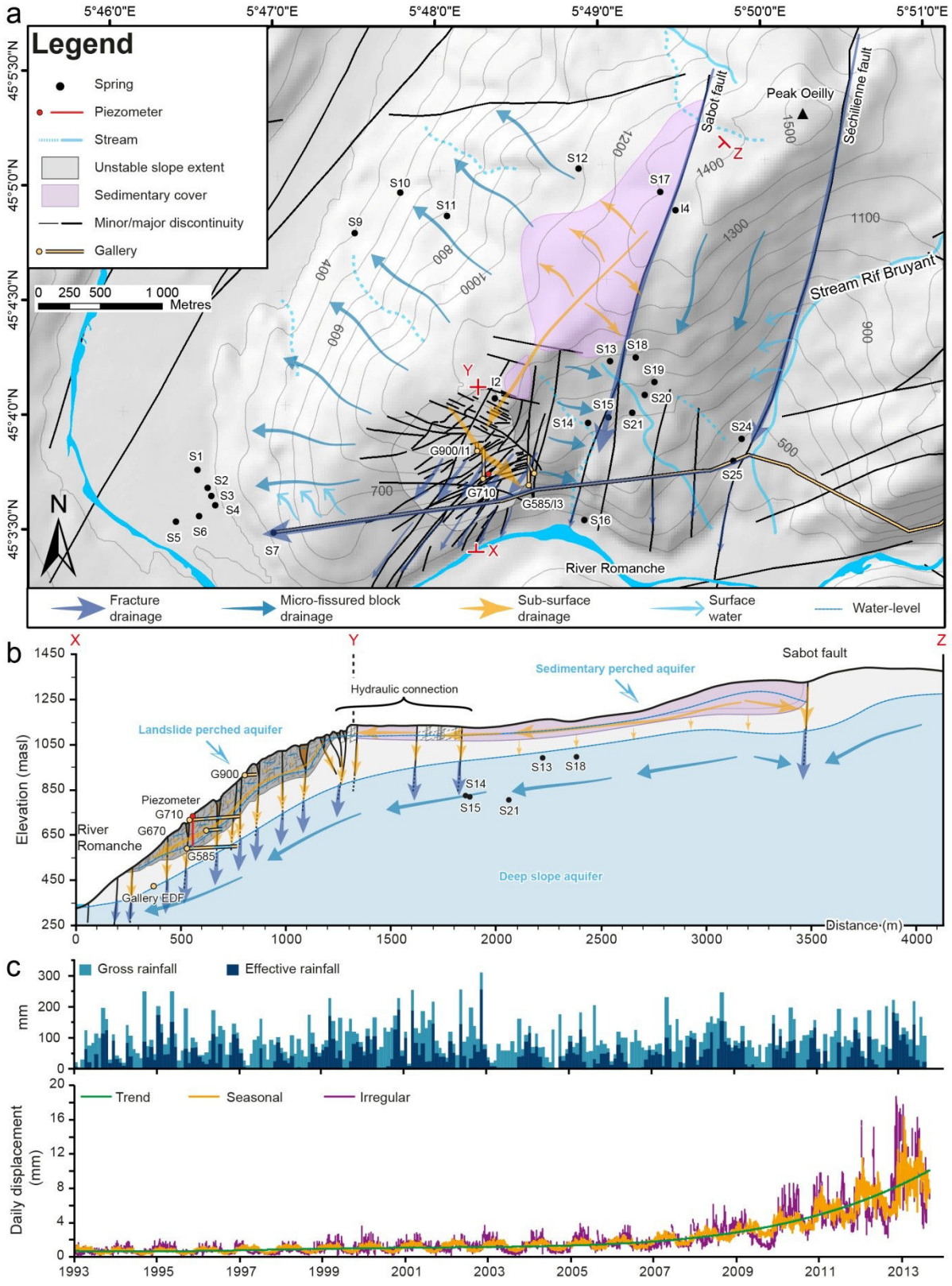

Fig. 17: Sketch of the groundwater conceptual model. (a) Spatial sketch. (b) Cross-section sketch. (c) Time series analysis of A13 extensometer displacement. The cross-section of the unstable zone is modified after Lebrouc et al. (2013). The unstable slope boundary is defined according to the geophysical survey of Leroux et al. (2011)

The Séchilienne fault also acts as a major drainage axis and even promotes the water infiltration from Rif Bruyant stream (seasonal analysis, Fig. 14). Outside of the major fault or fracture zones, the groundwater behaviour is more inertial, being characterized by a longer residence time. This is testified by the hydrodynamical behaviour of the springs of the northern slope of the Mont Sec massif. S18 shows probably an intermediate recharge mechanism, partly by the fractured network and partly by the micro-fissured matrix.

4.5.2 Unstable zone: Landslide perched aquifer

During the low flow period, the water-level of the piezometer P1 drops below 590 m asl and therefore below the boundary of the unstable zone and the no saturated zone has been observed in the galleries (gallery survey, Fig. 16). On the contrary, during almost all the high flow periods, the water-level of P1 (about 600 m asl) suggests a satured zone at the base of the unstable zone below the G710 gallery. Moreover, during high flow periods, a shallow continuous drainage (tracer tests, Fig. 12) occurs through the landslide, draining water from the sedimentary cover (I4 tracer test, Fig. 12a). This recharge mechanism involves a hydraulic connection of the unstable zone with the sedimentary perched aquifer which bypasses the deep aquifer (Fig. 17). This indicates that, in high flow periods, the recharge area is much larger than the landslide surface (Guglielmi et al., 2002; Cappa et al., 2004). However, the water from the G710 gallery has mainly a local origin (seasonal analysis, Fig. 14) with a characteristic SO_4 concentration explained by mechanical weathering rather than by variations of residence time (hydrochemistry, Fig. 15). This shows that the recharge of the unstable perched aquifer is mainly local and that the contribution of the remote groundwater from the sedimentary cover is minority (Fig. 17).

Heterogeneous, anisotropic and discontinuous properties of the landslide (Binet, 2006) lead to a perched discontinuous fractured reservoir slope which is better described by numerous disconnected saturated zones rather than by a single one (Cappa et al. 2004, Fig. 16c and 17b). This discontinuous reservoir is temporary since it is rapidly drained by the dense fracture network as demonstrated by intra-annual variability of the leakage flow and chemistry signal of the landslide galleries (seasonal analysis and gallery survey, Fig. 14 and 16). The recharge is essentially local, enhanced by the trenches and the counterscarps which tend to limit the runoff and to facilitate groundwater infiltration in the landslide area (Binet et al., 2007a). During high flow periods, the waters infiltrated in the landslide flow

perpendicularly to the slope through the dense network of near-vertical N70 conductive fractures down to a basal continuous perched aquifer (vertical drainage) maintained saturated by the high recharge amount. When the recharge amount is sufficient, the numerous disconnected saturated zones can become temporarily connected, leading to a groundwater flow parallel to the slope down to the landslide (horizontal drainage). This near-surface drainage, above the basal perched aquifer, occurs in the unsaturated zone and is controlled by the N70 fractures near-parallel to the slope. On the contrary, during the dry season, the recharge amount is not sufficient to maintain a continuous perched aquifer in the landslide and only temporarily disconnected saturated zones can occur after storm events. The numerous disconnected saturated zones likely results from the high vertical gradient of the hydraulic conductivity (Maréchal, 1998) and the heterogeneity of the landslide, particularly the tension cracks filled by colluvial deposits and altered materials (Cappa et al., 2004). An interpretative position water level of the perched aquifer during the high flow periods is suggested along the cross-section XYZ (Fig. 16c and 17b).

4.5.3 Unstable zone: slope deep aquifer

The EDF gallery acts as a main drainage structure for the slope (tracer test, Fig. 12), and especially beneath the unstable zone, where the fracture network is very dense (gallery survey, Fig. 16b). The EDF gallery imposes a constant head of the deep aquifer at about 425 m asl (Fig. 16c). The deep aquifer water-level is also controlled by the constant water head of the Romanche alluvium. The EDF gallery, on its eastern side recharges the deep aquifer with mixed water from the Romanche River and water inflow from the unstable zone. (seasonal analysis and hydrochemistry, Fig. 14 and 15). The EDF gallery operates as major east-west drain, whose rate and effect are mainly controlled by the N70 crossing fractures (Fig. 17a) Groundwater which is not collected by the EDF gallery flows toward the Romanche alluvium aquifer or to the springs located westward (tracer-test, Fig. 12c and 12d). All these informations allow to draw an interpretative position of the deep aquifer water-level (Fig. 16c and 17b).

4.5.4 Relationship between groundwater and landslide destabilisation

The Séchilienne landslide shows a two-layer aquifer system constituted by a perched aquifer, hosted by the near-surface reworked rockmass, disconnected from a deep saturated zone. This

organization is commonly observed on deep-seated landslide sites (Van Asch et al., 1999; Guglielmi et al., 2002; Cappa et al., 2004; Binet et al., 2007a; Pisani et al., 2010; Huang et al., 2012) Although the Séchilienne landslide destabilization is mainly triggered by the (short-term) precipitation, time-dependent (long term) factors such as rock weakening and modification of unstable slope hydraulic field pressure are significant at Séchilienne. Indeed, the long-term displacement velocity monitoring shows that the displacement rates and amplitudes significantly increased with time (exponential trend, Fig. 17c), independently of the recharge amount. The trend is the consequence of a creep deformation process (Chigira, 1992; Federico et al., 2012) which has progressively decreased the rock strength. The detrended time series, which is clearly linked to the hydrocycle (Vallet et al., 2014), can be decomposed into seasonal and irregular statistical components, which may be associated to the unstable slope deep aquifer and to the perched aquifer water-level fluctuations, respectively. Indeed, the perched aquifer, characterized by a limited pore water pressure building (Cappa et al., 2014) and a high infiltration rate (Binet et al., 2007a), is more sensitive to rainfall events. On the contrary, the deep aquifer, characterised by a low-permeability and a larger recharge area with a significant evapotranspiration potential (due to its extensive vegetation cover), is more sensitive to seasonal recharge variations. The signal similarity between irregular component and gross rainfall, and seasonal component and recharge (Fig. 17c) demonstrates the possible double influence of the two identified layers aquifer on the unstable slope destabilisation, of which the deep aquifer impact has been recently confirmed by Cappa et al. (2014).

5 Conclusion

This study highlights the dual-permeability properties of fractured rock reservoirs with preferential water flow in fractures bypassing most of the less pervious and inertial micro-fissured matrix. The major faults/fractures play a foremost role in the massif drainage. The EDF gallery also acts as a major drain in the massif. This survey highlights the hydraulic properties contrast between the unstable zone and the intact rock mass outside the landslide. This vertical heterogeneity leads to a two-layer aquifer, with a shallow perched aquifer localized in the unstable zone and a deep aquifer on the whole massif. The landslide perched aquifer is temporary, mainly discontinuous and its extent and connectivity fluctuate according to short-term recharge amount variations. The perched aquifer is almost dry during the low flow periods. The groundwater flows mainly through a dense network of widely opened fractures. The recharge area of the landslide perched aquifer is mainly local although in high flow periods, the recharge area can become much larger than the landslide surface and includes the remote sedimentary cover perched aquifer. A time series analysis shows that both the perched aquifer and the deep aquifer likely trigger the landslide destabilisation.

Seasonal monitoring of natural and artificial tracers allows to characterize the groundwater scheme the unstable slope and the surrounding stable massif. Stable isotopes of strontium survey could better constrain the water-rock interaction processes (sedimentary cover vs. basement). The results obtained in the Séchilienne landslide show that this method is able to solve various important issues for hydromechanical studies (Cappa et al., 2014). Due to the general scarcity of hydrogeological monitoring networks in landslide sites, the proposed method is suitable to conceive outstanding flow schemes for all landslide types in contexts as well as in soft materials.

Acknowledgments

This research was funded by SLAMS (Séchilienne Land movement: Multidisciplinary Studies) the program of the Agence Nationale de la Recherche. The meteorological and displacement data were supplied by CEREMA Lyon. The authors gratefully acknowledge the support of Jean-Pierre Duranthon and Marie-Aurélie Chanut (CEREMA Lyon). The authors are also very grateful to Christophe Loup (UMR Chrono-Environnement) for the chemical

analyses. The implementation of the monitoring network would not have been possible without the cooperation of Mrs. and Mr. Aymoz, Patrick Boyer from the Office National des Forêts and Gérard Cret, mayor of Séchilienne.

6 Appendix A: monitoring network

Hydrochemistry data and the conceptual models of Vengeon (1998) and Guglielmi et al. (2002) were used as a baseline to design the monitoring network and to select the injection locations of the artificial tracers. For each point of the monitoring network the Table 5 details, the location name and the type. The Séchilienne studied site has a strong anthropic pressure, with many public and private water supply springs, making spring flow estimation difficult. Most of the monitored spring (Fig. 10) flows are (i) the overflow leftover from water withdraws (S5, S6, S9, S11, S13, S15, S18, S19, S20, S21, S25), (ii) single points in areas with multiple resurgences, (S1, S2, S3, S4, S10, S12, S14, S24, G5) and (ii) water leakage/inflow collected with the mean of vinyl sheets in galleries (G1, G2, G3, G4).

Table 5: List of the points of the monitoring network with their location name and type

Location code	Location name	Type	Location code	Location name	Type
S1	Vizille	Spring	S22	Romanche	Stream
S2	Vizille	Spring	S23	Mulet	Spring
S3	Vizille	Spring	S24	Les Aillouds	Spring
S4	Vizille	Spring	S25	Mounier	Spring
S5	Dhuy	Spring	S26	Rif-Bruyant	Stream
S6	Reine	Spring	C1	Gallery 710	rain collector lysimeter
S7	Gallery EDF	Gallery outlet	C2	Madeleine	rain collector lysimeter
S8	Romanche	Stream	C3	Fonafrey	rain collector
S9	Cornier	Spring	C4	Rochassier	rain collector
S10	Chemin Mont-Jean	Spring	C5	Pic-Oeilly	rain collector
S11	Mont-Jean	Spring	G1	Gallery 710-1	Water inflow
S12	Pleney	Spring	G2	Gallery 710-2	Water inflow
S13	Fonafrey	Spring	G3	Gallery 585-1	Water inflow
S14	Thiebaud-EDF	Spring	G4	Gallery 585-2	Water inflow
S15	Thiebaud-Lavoir	Spring	G5	Gallery 585-3	Water inflow
S16	Noyer-Chute	Spring	I1	Gallery 900	Fractures
S17	Clobasse	Spring	I2	Crevasse	Rock crevasse
S18	Clos-Bénit	Spring	I3	Gallery 585	Fractures
S19	Finet	Spring	I4	Rochassier	Sinkhole
S20	Les Mathieux	Spring	P1	Gallery 710	Piezometer
S21	La Bathie	Spring			

Among the 30 springs identified across the Séchilienne massif, none is located in the unstable zone. However, three former mining galleries, situated at 900, 670 and 585 m asl (G900,

G670, G585), and a gallery excavated to survey the landslide at 710 m asl (G710) are located within the unstable zone, with lengths of 60 m, 88m, 240m and 240m, respectively (Fig. 10). All these galleries have a north-south orientation, except the G670 one which is oriented N155 and which intersect the unstable zone. G585 and G710, both located in the unstable zone, show water inflow and/or leakage suitable for monitoring. Unfortunately, the G585 is no longer accessible and was only sampled by Vengeon (1998) and monitored for tracer test surveys. Another gallery (EDF gallery, French Electricity Company) is also located at the foot of the landslide slope at an elevation of about 425 m asl. These galleries show bare rock, except the EDF gallery where some highly fractured zones were covered with concrete.

A piezometer (P1) is located near the G710 gallery. It recorded the water level from November 2009 to April 2010, before being clogged. For the water isotope survey, five hermetically closed rain collector tanks (C1, C2, C3, C4 and C5) were buried about one meter deep and wrapped with an isotherm cover to avoid isotope fractionation due to the fluctuations of the atmosphere temperature. Rain collector points were installed every 200 m in elevation from 640 to 1520 m asl, covering most of the massif hosting the landslide (Fig. 10). Two rain collector locations (C1 and C2), respectively installed in woodland and in grassland (the two main vegetation types of the landslide recharge area), were coupled with a lysimeter.

The EDF gallery outlet (S7), the Romanche river (S8 and S22) and the Rif Bruyant stream (S26) are occasionally added to the monitoring network. Additionally, the EDF gallery was also monitored for a unique water chemistry survey (March 2002) during maintenance of the EDF gallery. The G900 gallery was used only for tracer test survey. Demolition works of a hydropower plant, after tracing survey, modified the flow path of S16 which is now flowing directly to alluvial aquifer. S23 and S17 were only monitored for the tracer test survey.

Special instrumentations and sample rates were implemented for the two tracer tests in 2001 and 2002. For the multi-tracing survey performed in April 2001, the monitoring survey lasted for two months, and sample rate was adapted according to survey time by decreasing the sampling resolution (Fig. 10). G5, S5 and S6 springs were monitored with an automatic sampler. Activated charcoal packets and manual water sampling were implemented at S1, S4, S9, S11, S13, S15, S18, S19 and S20. Only charcoal monitoring was performed on the remaining springs. In the reiterated tracer test from gallery G585 (I3-B test), only hand

samplings were performed in all water inflows of the EDF gallery, between kilometric points 5 and 7 during the 2 days following the injection day (Fig. 12e).

7 Appendix B: Sample analysis

7.1 Survey of the tracer tests

Artificial tracers (Uranin, Eosin, Rhodamin B and Sodium naphtionate) were extracted from charcoal adsorbents using an eluent (ethanol mixed with ammonia) by a *fluorescence spectrometer* (Perkin-Elmer *LS 30* UV-Spectrometer Model). Accuracy depends on the natural organic matter content, which is highly variable through precipitations events. Analyses by fluorescence spectrometry were performed at the Chrono-Environnement laboratory at the University of Franche-Comté.

7.2 Oxygen stable isotope

Water samples were collected in glass vials with caps with an additional parafilm to prevent from any possible evaporation. Oxygen stable isotope were analyzed with the Liquid Water Isotope Analyzers method (LWIA) using off-axis integrated cavity output spectroscopy analyzer (OA-ICOS), model DLT-100, manufactured by Los Gatos Research Inc. For more details about method accuracy, precision and repeatability, see Penna et al. (2010) and Lis et al. (2008). Isotopic analyses were performed at the Faculty of Civil Engineering and Geosciences at the Delft University of Technology in the Netherlands.

7.3 Field measurement

The pH, water electrical conductivity and temperature were measured on site with a WTW apparatus model LF30 (a Xylem Inc. branch). The probes were calibrated before each campaign with standard buffer solutions. Measurements are reduced to the standard temperature of 25 °C with a respective accuracy of 0.1 pH units and 0.1 µ S/cm.

7.4 Water chemistry analysis

Water samples were collected in polyethylene bottles and were filtered at 0.45µm. Analyses of Na^+, Ca^{2+}, K^+, Mg^{2+} were performed by atomic absorption spectrometry (AA 100 Perkin–Elmer) with detection limits of 0.01; 0.5; 0.1 and 0.1 mg/L, respectively. Analyses of SO_4^{2-}, NO^{3-} and Cl^- were performed by high pressure ion chromatography (Dionex DX 100) with detection limits of 0.1; 0.05 and 0.1 mg/L, respectively. The concentrations in HCO_3^- were

measured by acid titration with a N/50 H_2SO_4, within at most 48 hours after sampling, with 1 % accuracy. For the Séchilienne hydrochemical conditions (pH between 6 and 8.5), total and carbonate alkalinity can be considered as equalling to HCO_3^- concentration. Only analyses which have a charge balance lower than 10 % were taken into account. Silica was analyzed with a spectrophotometer (Spectroquant, Pharo 300, Merck) using a silica-test kit (Merck) with 3 % accuracy. Chemistry analyses were performed at the Chrono-Environnement laboratory at the University of Franche-Comté.

CHAPITRE II : UNE NOUVELLE MÉTHODE POUR CALCULER LA RECHARGE POUR L'ÉTUDE DES MOUVEMENTS DE TERRAIN PROFONDS

A NEW WORKFLOW TO COMPUTE GROUNDWATER RECHARGE FOR THE STUDY OF RAINFALL TRIGGERED DEEP-SEATED LANDSLIDES, APPLICATION TO THE SÉCHILIENNE UNSTABLE SLOPE (WESTERN ALPS)

Vallet A.[1], Bertrand C.[1], Fabbri O.[1], Mudry J.[1]

[1] UMR6249 Chrono-Environnement - Université de Franche-Comté - 16 route de Gray - F-25030 Besançon cedex - France

1 Résumé du Chapitre II

Le chapitre précédent a montré qu'un système à double aquifère, perché et profond, contrôle probablement la déstabilisation du mouvement de terrain de Séchilienne. La compréhension des couplages hydro-mécaniques responsables de la déstabilisation nécessite d'estimer les pressions de fluides dans le massif. L'anisotropie et l'hétérogénéité des mouvements de terrain profonds, combinées avec une déformation du milieu, font que les études hydrogéologiques traditionnelles, essentiellement basées sur les forages, sont inadaptées (faibles représentativités, endommagement du matériel). Les données de pression de fluides sont donc rarement mesurées (cas de Séchilienne) et les paramètres indirects, tels que la recharge, sont les seules données hydrogéologiques qui permettent de caractériser la relation pluie-déplacement.

Dans la plupart des études, les méthodes utilisées pour déterminer la recharge sont basées sur des simplifications excessives, où les équations utilisées sont rarement calibrées. De plus, de nombreuses études utilisent encore les précipitations brutes au lieu de la recharge pour caractériser la relation pluie-déplacement. Actuellement, aucune méthode n'a été proposée pour estimer simplement et avec précision la recharge des eaux souterraines dans le cadre des études sur les mouvements de terrain.

Ce chapitre propose une méthode de calcul quotidien de la recharge, basée sur un bilan hydrique au niveau du sol impliquant l'évapotranspiration et le coefficient de végétation associé, le ruissellement et la réserve en eau utile du sol. Cette méthode comprend quatre étapes (Fig. 18).

La première étape s'attache à calibrer des équations réduites d'évapotranspiration (nécessitant un nombre limité de paramètres métrologiques). La deuxième étape s'applique à estimer les paramètres requis pour le bilan hydrique de la zone de recharge. Ces paramètres sont estimés avec une méthode SIG basée sur l'analyse de photographies aériennes, d'un modèle numérique de terrain, de cartes géologiques et d'observations de terrain (végétation, profil de sol…). La troisième étape se base sur un bilan hydrique au niveau du sol pour calculer la recharge (Fig. 19). L'estimation des paramètres de la zone d'alimentation est ensuite ajustée grâce à une analyse de sensibilité basée sur la corrélation recharge-déplacement (quatrième étape).

Cette méthode est testée sur le site du mouvement de terrain de Séchilienne. Afin de démontrer la pertinence de la méthode proposée, une corrélation signal d'entrée-déplacement a été effectuée sur quatre stations mesurant la vitesse de déplacement avec trois signaux caractérisant le signal d'entrée : (1) les précipitations brutes, (2) une estimation de la recharge simplifiée communément utilisée (recharge = précipitations moins l'evapotranspiration) et (3) la recharge calculée avec la méthode développée dans ce chapitre. La significativité des corrélations est évaluée avec un test de bootstrap.

Pour le mouvement de terrain de Séchilienne, une zone de recharge unique est délimitée pour le système à double aquifère d'après le modèle conceptuel d'écoulement établi dans le Chapitre I. Parmi les cinq équations d'évapotranspiration testées, l'équation réduite de Penman-Monteith montre les meilleures performances. Une analyse de sensibilité permet de définir une gamme de valeurs pour les paramètres de réserve utile en eau du sol (75-115 mm) et de coefficient de ruissellement (9-13.9%). Un coefficient de végétation est estimé à 0.777 en hiver et à 0.955 en été. L'analyse de sensibilité s'avère être une alternative appropriée pour estimer ou affiner les paramètres de la zone de recharge, en particulier dans le cas où les données de terrain sont insuffisantes (Fig. 24).

Les résultats obtenus montrent que pour l'ensemble des stations (Fig. 27), le déplacement est significativement mieux corrélé au signal de recharge calculé avec la méthode développée dans ce chapitre (R^2 moyen de 0.46) qu'au signal de précipitations brutes (R^2 moyen de 0.23) ou qu'au signal de recharge estimé par simple retranchement de l'évapotranspiration (R^2 moyen de 0.31).

2 Introduction

Pore water pressure build-up by recharge of aquifers is one of the main triggering factors of destabilisation of deep-seated landslides (Noverraz et al., 1998; Van Asch et al., 1999; Guglielmi et al., 2005; Bogaard et al., 2007; Bonzanigo et al., 2007). In most deep-seated landslides, pore water pressure data are not available since piezometers, if any, have a very short lifespan because of slope movements. In addition, landslides show heterogeneous, anisotropic and discontinuous properties (Cappa et al., 2004; Binet et al., 2007a) and local measurements are rarely representative of the overall behaviour of the landslide aquifers. In the absence of piezometric measurements, the groundwater recharge is used as the most relevant parameter to characterize the pore water pressure of the landslide aquifers. Groundwater recharge (hereafter recharge), also referred to as deep percolation, is the part of the precipitation which recharges the saturated zones (aquifers).

Landslide studies involve a wide range of specialities (sub-surface geophysics, structural geology, modelling, geotechnics, and geomechanics). Scientists or engineers in charge of landslides may not have the required hydrology knowledge to accurately estimate the recharge. In most cases, deep-seated landslide studies devoted to characterise the rainfall-destabilisation relationships do not take into account recharge with enough accuracy. In particular, some studies estimate the recharge without calibration of the evapotranspiration estimation methods and without soil-water balance (Canuti et al., 1985; Alfonsi, 1997; Hong et al., 2005; Binet et al., 2007c; Durville et al., 2009; Pisani et al., 2010; Prokešová et al., 2013). Lastly, several studies use precipitation data instead of the recharge (Rochet et al., 1994; Zêzere et al., 2005; Meric et al., 2006; Helmstetter and Garambois, 2010; Belle et al., 2013). These approaches can over-estimate the groundwater recharge and can thus bias the characterisation of the relationship between rainfall and destabilisation. A more accurate estimation of the groundwater recharge signal can improve the accuracy of these studies. So far, no computation workflow has been proposed to estimate simply and accurately the recharge in the context of landslide studies.

Patwardhan et al. (1990) showed that the soil-water balance method is an accurate way to estimate groundwater recharge. Recharge computation with a soil-water balance depends mainly on the surface runoff, the soil-available water-capacity (SAWC) and the specific vegetation (so-called crop) evapotranspiration (ET_c, also referred to as potential

evapotranspiration) which is deduced from reference vegetation evapotranspiration (ET_0). The Penman-Monteith method (Eq. (16)), hereafter referred to as the ET_0 standard equation or FAO-56 PM,) developed in the paper FAO-56 (Food and Agriculture Organization of the United Nations) is considered by the scientific community as a global standard method to estimate ET_0 worldwide (Jensen et al., 1990; Allen et al., 1998). This method requires the knowledge of the air relative humidity, the air temperature, the wind speed and the solar radiation. However, most weather stations in landslide areas record only air temperature and rainfall. Unlike the FAO-56 PM method, methods based only on air temperature and/or solar radiation (R_s) allow a simpler expression of ET_0 (Tabari et al., 2013). The R_s can also be estimated only from air temperature (Almorox, 2011), thus allowing ET_0 to be obtained only from air temperature records. These reduced-set methods are developed under specific site conditions and must be calibrated in order to improve accuracy (Allen et al., 1994; Shahidian et al., 2012).

The objective of this study is to develop a parsimonious, yet robust, guideline workflow to calculate time series of groundwater recharge that can be used as a deterministic variable in landslide studies. To maximize accessibility to diverse user groups, we strive to develop an efficient method, balancing technical accuracy with operational simplicity. The proposed workflow is applied on the deep-seated Séchilienne landslide. To test the utility of the proposed workflow, correlation analysis is used to evaluate whether the calculated groundwater recharge is more strongly correlated with measured land mass displacement velocities than with precipitation or with recharge estimated with a common simplification in landslide studies (recharge = precipitation minus non-calibrated ET_0; Canuti et al., 1985; Binet et al., 2007; Pisani et al., 2010; Prokešová et al., 2013). The significance of the correlations is assessed with bootstrap tests. The proposed study aims at showing that an accurate estimation of the recharge can significantly improve the results of rainfall-displacement studies.

3 Method

3.1 General workflow

The computation workflow of the recharge (Fig. 18), hereafter referred to as LRIW (Landslide Recharge Input Workflow), includes four steps. The first step consists of a regional calibration of ET_0 and R_S equations (detailed in section 3.2, equations detailed in appendix A). The calibrated methods then allow to estimate evapotranspiration at the landslide site equipped with a weather station measuring only temperature. In the case of a landslide having a weather station recording the full set of parameters (relative humidity, temperature, wind speed and solar radiation), the first step can be skipped and the FAO-56 PM method can be used to estimate ET_0. The second step consists in estimating the recharge-area parameters using a GIS (Geographic Information Systems) composite method (detailed in section 3.3). The third step uses a soil-water balance to estimate the recharge with the calibrated ET_0 and R_S methods, and the estimation of the recharge-area parameters (detailed in section 3.4). The fourth step consists of a sensitivity analysis based on a recharge-displacement velocity correlation and is performed in order to refine the SAWC and runoff coefficient estimations (detailed in section 3.5). For deep-seated landslides triggered by deep water-saturated zones, the impact of a multi-day cumulative rainfall is far more significant than rainfall duration or intensity (Van Asch et al., 1999; Guzzetti et al., 2008). For these reasons, this study is based on displacement and weather data recorded at a daily time-step. For the sake of simplicity, the daily displacement, equivalent to a velocity measurement in mm/day, is hereafter named displacement.

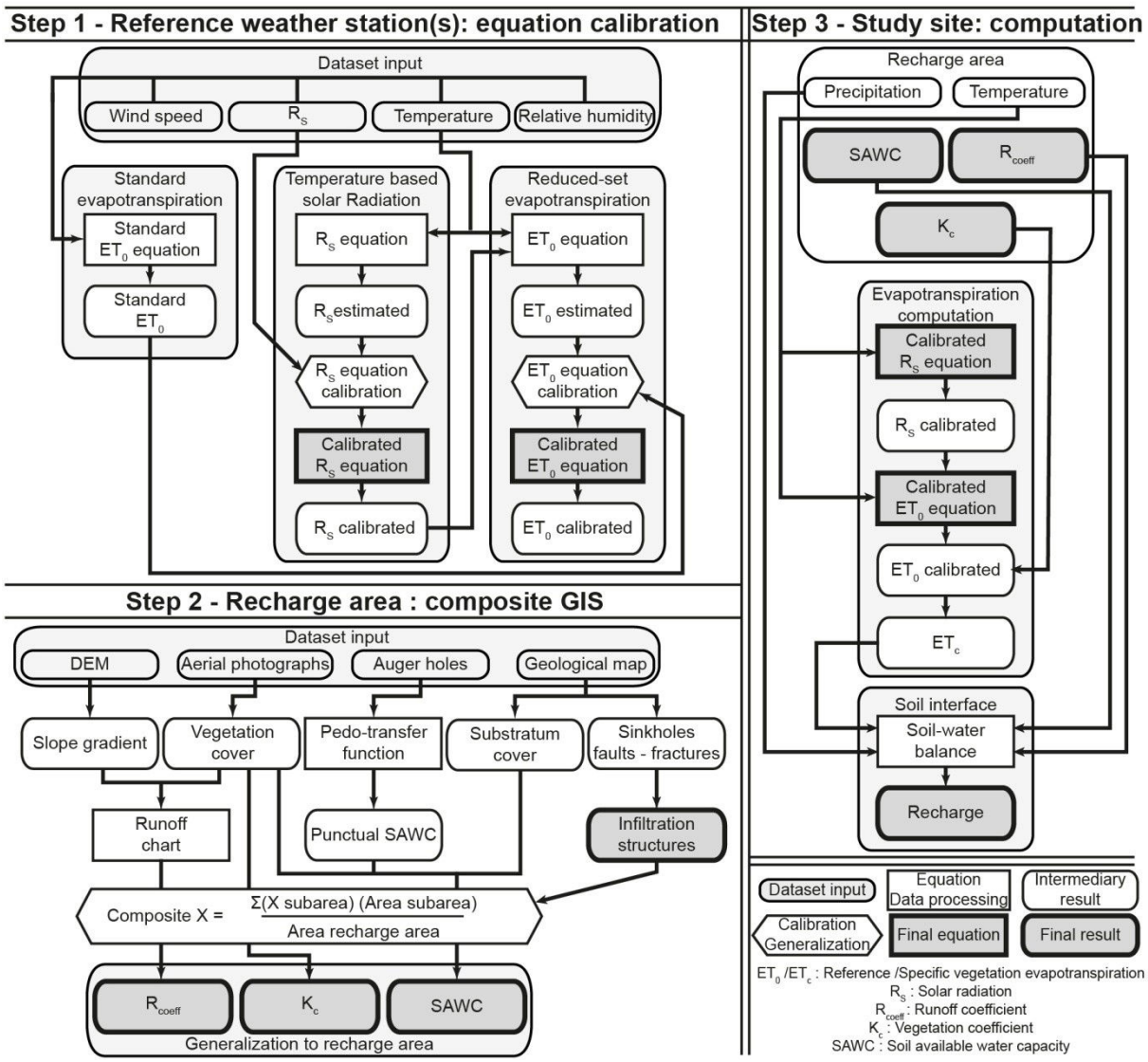

Fig. 18: Landslide Recharge Input Workflow (LRIW) diagram. Step 1: calibration of standard ET_0 and R_S methods. Step 2: estimation of recharge-area parameters required for the soil-water balance (R_{coeff}, K_c and SAWC) and the infiltration structures. Step 3: computation of the recharge with the soil-water balance

3.2 Step 1: Regional calibration of ET_0 and R_S methods

ET_0 reduced-set and R_S temperature methods were developed for given regions or sites with their own climatic conditions and must be calibrated to take into account the weather conditions of the study site. Details about calibration can be found in the literature (Allen et al., 1994; Itenfisu et al., 2003; Lu et al., 2005; Alkaeed et al., 2006; Alexandris et al., 2008; Shahidian et al., 2012; Tabari et al., 2013).

The regional calibration method (Fig. 18– Step 1) is performed using the records of nearby weather stations (hereafter referred to as reference weather stations) having similar climatic

conditions as the study site and recording the required meteorological parameters. The calibration of R_S and ET_0 methods are performed for each reference weather station (local scale). The local adjustment coefficients of the reference stations are then averaged in order to define a regional calibration. The reference weather stations should be representative of the climatic conditions of the studied landslide. The user has to maintain a balance between the number of selected reference stations and the necessity for these stations to be located in areas with climatic conditions similar to those of the study site. For sites with a sparse weather station network, one reference station can be sufficient for the calibration, provided that this station has the same weather conditions as those of the studied site.

The performance assessment of regional-scale calibrated methods is based on the comparison between observed measurements and calibrated estimates for R_s and between FAO-56 PM estimates and calibrated estimates for ET_0. Performance indicators are the coefficient of determination (R^2), the slope and the intercept from linear regression (independent variable: estimated parameter; dependant variable: reference parameter), and the root mean square error (RMSE).

3.2.1 Solar radiation methods

Bristow and Campbell (1984) and Hargreaves and Samani (1985) proposed methods to compute R_S based on solely the air temperature measurement (Eq. (11) and Eq. (12) in appendix A). Castellvi (2001) demonstrated that both methods show good results for daily frequencies. The coefficients of the Bristow-Campbell method have to be evaluated. The coefficients of the Hargreaves-Samani method have default values. However, Trajkovic (2007) showed that the regional calibration of the Hargreaves-Samani method is significantly improved by coefficient adjustments rather than by linear regression. Therefore, all the HS_{mod} R_s coefficients are adjusted. In this study, modified forms of the Bristow-Campbell method (Eq. (13)) and Hargreaves-Samani method (Eq. (14)) are used. For the R_S equations, the adjustment of the regional calibration coefficients is non-linear. To adjust the calibration coefficients, a grid search iterative algorithm is used to maximise the value of R_S performance (Eq. (5)).

$$R_S\,performance = \frac{\sum_{i=1}^{m}\left(R_m^2 - RMSE_m\right)}{m} \quad (5)$$

where m is the number of weather stations used for the calibration. R^2 and RMSE are computed with measured and estimated values of R_S at each reference weather station.

3.2.2 Evapotranspiration methods

ET_0 is the evapotranspiration from a reference grass surface and is used as a standard from which ET_c is deduced as follows (Allen et al., 1998):

$$ET_c = ET_0 \times K_c \quad (6)$$

where K_c is the vegetation coefficient.

Several ET_0 methods using a reduced dataset in comparison to the FAO-56 PM method, have been developed worldwide. Only a few methods are commonly used. This is the case with the five ET_0 methods selected for this study, which have shown good performance when using daily to weekly frequencies (Trajkovic, 2005; Yoder et al., 2005; Alexandris et al., 2008; Shahidian et al., 2012; Tabari et al., 2013). The five ET_0 methods Eq. (17) to Eq. (22) in appendix A) include one temperature-based method, that is the Hargreaves-Samani method (1985), four solar radiation/temperature-based methods, the methods of Makkink (1957), Turc (1961), Priestley and Taylor (1972), and the Penman-Monteith reduced-set method (Allen et al., 1998).

ET_0 is calculated using data collected from each of the reference weather stations (independent ET_0 estimates). These calculations follow FAO-56 PM method outlined in the FAO-56 document (Allen et al., 1998). These independent ET_0 estimates are then used as pseudo-standards for the purpose of calibrating the regional-scale ET_0 estimates that are based solely on air temperature measurements. A linear regression is performed for each of the evapotranspiration methods and for each reference weather station (Eq. (7)). The slope a and the intercept b of the best-fit regression line are used as local calibration coefficients.

$$ET_{0\,FAO-56\,PM} = a\,ET_{0\,method} + b \quad (7)$$

where $ET_{0\ FAO\text{-}56\ PM}$ is the standard ET_0 method and $ET_{0\ method}$ is obtained by any of the five methods tested in this study. The linear regression method has been widely used to calibrate ET_0 methods (Allen et al., 1994; Trajkovic, 2005; Shahidian et al., 2012).

3.3 Step 2: Estimation of the parameters of the recharge area

The estimation of the recharge with the soil-water balance (Step 3) requires the calculation, at the scale of the recharge area, of three parameters which are SAWC, runoff coefficient R_{coeff}, and K_c. These three parameters are controlled by one or several factors which are, in this study, the slope gradient, the geological nature of the substratum and the type of vegetation cover. Besides, at the scale of the recharge area, the controlling factors are commonly heterogeneous and thus cannot be readily computed. For each of the controlling factors, the recharge area is divided into sub-areas (hereafter referred to as factor sub-areas) characterized by homogenous factors. Factor sub-areas can be either continuous or discontinuous, and their number and shape can differ, depending of the spatial distribution of the factors. Relevant factor sub-areas are in turn used to define parameter sub-areas. For a given parameter sub-area, the value of the parameter is estimated from either field measurements or from the literature. The parameter values at the scale of the recharge area are then calculated by taking into account the relative surface of the parameter sub-areas (Fig. 18 – Step 2). Lastly, if preferential infiltration structures (hereafter referred to as infiltration structures) such as sinkholes, cracks, reverse slope areas, bare ground or any topographical depressions which can collect the surface runoff are present in the recharge area, the above-mentioned parameters have to be adjusted. For such areas, the SAWC and R_{coeff}, being very low, will be set at zero in the calculations. Similarly, for such areas, ET_0 is negligible and therefore the surface of these areas is disregarded for the K_c computation. The parameter values are then refined by a sensitivity analysis (see section 3.5) in order to find the optimal set of recharge-area parameters.

The K_c parameter takes into account four key characteristics (vegetation height, albedo, canopy resistance and evaporation from soil) that distinguish the vegetation type of a given sub-area from the reference grass used to estimate the ET_0 (Allen et al., 1998). The K_c sub-areas are defined according to the type of vegetation (e.g., meadow, forest…) obtained from

aerial photographs. The dominant vegetation species assigned to each vegetation type can be obtained from literature (e.g., forest agency data) or field observations. Since the K_c parameter depends on the stage of development of the vegetation, it varies from a minimum value during winter to a maximum value during summer. The minimum and maximum K_c values are estimated from the literature and are assigned respectively to the 4th of February (middle of winter) and the 6th of August (middle of summer) of each year. A daily linear interpolation is performed for K_c between these two dates (Verstraeten et al., 2005).

The SAWC parameter refers to the difference between a maximum water content above which all free water is drained through gravity (field capacity) and a minimum moisture content below which plant roots cannot extract any water (permanent wilting point). The SAWC is mainly affected by soil texture and thickness, both depending primarily on the geological substratum and the vegetation. The SAWC sub-areas are defined according to the type of vegetation (obtained from aerial photographs) and to the geological substratum (obtained from geological maps). SAWC values are calculated with pedotransfer functions (Bruand et al., 2004; Pachepsky and Rawls, 2004) from soil properties (type of horizon, texture and bulk density) and thickness. Soil properties and thickness can be obtained from the literature (e.g., pedological maps) or from laboratory measurements of auger hole cores. SAWC values can be also obtained directly from the literature.

The method used to estimate the surface runoff is similar to the commonly used 'runoff rational method'. The R_{coeff} parameter depends mainly on topography and vegetation. The R_{coeff} sub-areas are defined according to the vegetation (obtained from aerial photographs). An average slope gradient obtained from the DEM is assigned to each sub-area. The R_{coeff} values can then be calculated from vegetation cover and slope gradient through the use of charts such as the Sautier chart (Musy and Higy, 2011).

Infiltration structures are first located through inspection of aerial photographs (lineaments analysis) and geological maps and are then inspected in the field.

3.4 Step 3: Recharge computation with soil-water balance

The soil-water balance workflow used to estimate the recharge at a daily frequency is detailed in figure 19. All terms required for the soil-water balance estimation are expressed in water amount (millimetres), except for R_{coeff} expressed in %. The soil-water balance is based on

ET_c, SAWC, K_c and R_{coeff}. The precipitation (P) is the amount of liquid (rain) or solid (snow) water which falls on the recharge area. The precipitation will be taken here as the sum of snow melt and rainfall. A part of this water amount is intercepted by the vegetative canopy (interception; Fig. 19A). The remainder of precipitation reaches the ground surface and forms: (1) the runoff (Rf), which is the water joining the surface drainage network; and (2) the infiltration (I) into the soil layer which supplies the SAWC. The remaining part of the precipitation not uptaken by evapotranspiration and runoff and not stored in the SAWC is called the recharge (R). It corresponds to deep percolation and is the component of the precipitation which recharges the saturated zone (Fig. 19A).

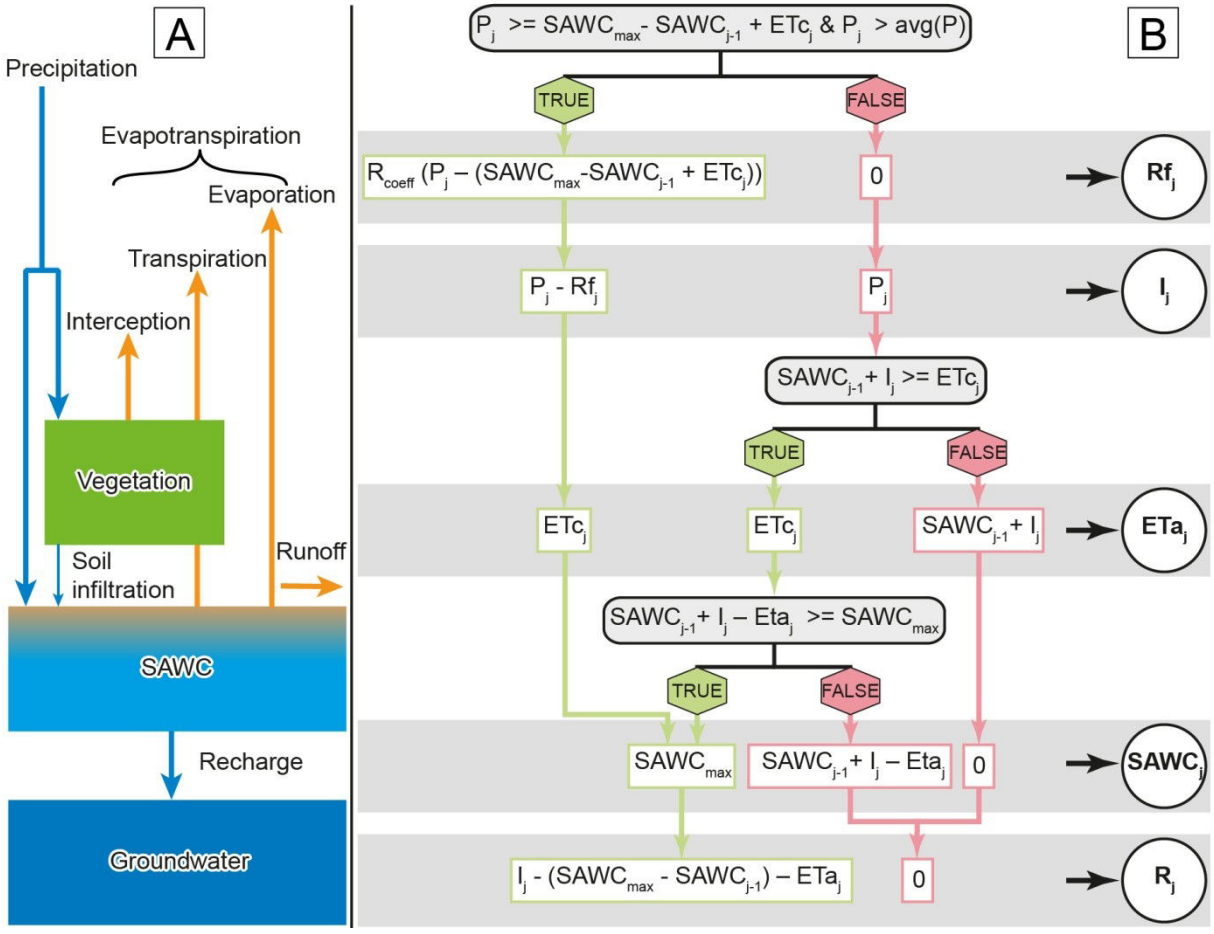

Fig. 19: Soil-water balance: (A) soil-water balance conceptual representation and (B) soil-water balance diagram used for recharge computation on a daily frequency. SAWC: soil-available water-capacity, $SAWC_{max}$: SAWC threshold (possible maximum), P: precipitation (rainfall + snow melt), avg (P): precipitation average of the entire record, I: part of precipitation which infiltrate the soil, Rf: surface runoff, R_{coeff}: runoff coefficient, ET_c: specific vegetation evapotranspiration, ET_a: actual vegetation evapotranspiration, and R: recharge. Units: mm of water, except R_{coeff} in percent. J is the computation day and j-1 is the day before. TRUE and FALSE are the answers of the conditional inequality statements

The ET_c is a lumped parameter including potential transpiration, potential soil evaporation and canopy interception evaporation (Verstraeten et al., 2005). In the proposed diagram workflow (Fig. 19B) the interception component is integrated in the ET_c component. The ET_c is the water evapotranspired without any other restrictions than the atmospheric demand (assuming unlimited soil water availability). However, field conditions do not always fulfil these requirements, particularly during low rainfall periods, when water supplies are inadequate to support vegetation uptakes. The actual evapotranspiration (ET_a) corresponds to the actual amount of evapotranspired water.

Runoff takes place when the intensity of a precipitation event exceeds the soil infiltration capacity. The use of a daily measurement frequency for precipitation does not allow an accurate estimation of rainfall intensity. Instead, a R_{coeff} is applied only for days when precipitation is greater than the average. Such days are considered as high intensity rainfall days. The R_{coeff} is applied only to excess precipitation, after the demands of evapotranspiration and SAWC are met, i.e., when SAWC is fulfilled (Fig. 19B).

3.5 Step 4: Sensitivity analysis of the recharge-area parameters

In the landslide recharge area, recharge can be considered as spatially heterogeneous. Indeed, in fractured rocks, the groundwater flow is mainly driven by an anisotropic fracture network. The proportion of infiltrated water which flows toward the landslide aquifer can be significantly different between two zones of the recharge area. Nevertheless, the GIS composite method considers that any part of the recharge area has the same weight with respect to the groundwater which flows toward the landslide aquifer. This homogeneous recharge assumption can lead to biased estimations of the recharge-area parameters. On the other hand, uncertainties in the delimitation of the recharge area can also lead to biased estimations.

A sensitivity analysis evaluates the possible over-estimation or under-estimation of the set of recharge-area parameters. The infiltration-structure sub-areas is used as a fitting factor (varying from 0 to 100% of the recharge area surface) to adjust the estimation of the set of recharge-area parameters. A variation of the infiltration structure percentage corresponds to a variation of the infiltration structures contribution weight to the recharge of the landslide aquifer. As a consequence, a variation of the infiltration structure percentage does not affect

the relative proportion of the other sub-area surfaces but only their weights. The sensitivity analysis is based on the performance of a linear correlation between daily time series of recharge and displacement. The landslide displacement triggered by pore water pressure is therefore related to the hydrodynamic variations of the landslide aquifers. For this reason, the performance of the correlation between recharge and displacement informs whether the recharge-area parameters are satisfactorily estimated. The sensitivity analysis allows to determine the optimal set of recharge-area parameters which maximize the performance of the correlation.

3.6 Correlation between water input and displacement

3.6.1 Antecedent cumulative sum

The correlation between water input and displacement requires measurements of landslide displacements at the same temporal frequency (daily frequency in this study) as the measurements of water input (precipitation or recharge). The groundwater hydrodynamic processes in aquifers are non-linear. A former rainfall event displays less impact (though not negligible) than a recent one on the aquifer hydrodynamic fluctuations (Canuti et al., 1985; Crozier, 1986; Diodato et al., 2014). The daily precipitation/recharge time series cannot therefore be used without appropriate corrections. An antecedent cumulative sum of precipitation/recharge weighted by a factor α is applied as a moving window to the daily precipitation/recharge time series (Eq. (8)). The antecedent cumulative sum allows to approximate the daily triggering impact of the aquifer *ATI* on the landslide destabilisation. In order to take into account the groundwater transit time, a β time-lag factor is introduced. This factor can shift the moving window from the target date *t*.

$$ATI_t = \sum_{i=t+\beta}^{t+\beta+n} \frac{W_i}{1+\alpha\ (\mathrm{i}-(\mathrm{t}+\beta))} \quad (8)$$

where:

ATI_t Aquifer Triggering Impact at the date t (in mm)

t target date

β time shift of the moving window (in days)

i i^{th} day from the date t (i=t+β: start of the moving window and i= t+β +n: end of the moving window)

n length of the moving window of the cumulative period (in days)

W_i water input, i.e., precipitation or recharge at the i^{th} day (in mm)

α weighting factor

An iterative grid search algorithm is used to find the optimal set of parameters of the antecedent cumulative sum. The optimal set of parameters is the set that maximizes the correlation performance itself based on the R^2 indicator. The grid search algorithm investigates the following parameter ranges: n from 1 to 250 days (increment: 1 day), α from 0 to 0.5 (increment: 0.001) and β from 1 to 10 days (increment: 1 day).

3.6.2 Significance of the water input-displacement correlation

The bootstrap method, which is an inference statistical resampling method, is used to estimate the confidence interval (CI) of estimated parameters and to perform statistical hypothesis tests (Chernick, 2008). The bootstrap method uses resampling with replacement and preserves the pair-wise relationship. However, for inter-dependent data (such as time series), the structure of the dataset has to be preserved during the resampling. The moving block bootstrap is a variant of the bootstrap method. It divides data into blocks for which the structure is kept (Cordeiro and Neves, 2006). The moving block bootstrap method is performed with a 90-day block size (season) and 50,000 iterations for each run.

To estimate the significance of the linear regression, the lower bound of the confidence interval (LBCI) of R^2 is used at the level of confidence of 95%. An LBCI value greater than 0 means that the relationship is significant. Particular to statistical hypothesis tests is the definition of the tested null hypothesis which is often a default position opposite to the aim of the test, i.e. "there is no relationship between two quantities". The null hypothesis is assumed to be true until it is rejected by statistical evidence in favour of the alternative opposite

hypothesis. The recharge estimated with the LRIW workflow is hereafter called R_{LRIW} and the recharge estimated by subtracting a non-calibrated ET_0 from precipitation is hereafter called R_{PMNE} (PMNE standing for Precipitation Minus Non-calibrated ET_0).

To estimate whether the R_{PMNE}/displacement correlation R^2 is significantly better than the precipitation/displacement correlation R^2 value, the Null Hypothesis 1 (NH1) is tested. The NH1 states that the R_{PMNE}/displacement correlation R^2 value is not significantly greater than the R^2 value obtained from precipitation. In other words, the NH1 statistic test is the difference between the R_{PMNE} R^2 value and the precipitation R^2 value, expected to be 0 if no difference. Similarly, the Null Hypothesis 2 (NH2) and the Null Hypothesis 3 (NH3) are tested. NH2 estimates whether the R_{LRIW}/displacement correlation R^2 is significantly better than the precipitation/displacement correlation R^2 value. NH3 estimates whether the R_{LRIW}/displacement correlation R^2 is significantly better than the R_{PMNE}/displacement correlation R^2 value.

To estimate whether the best rainfall/displacement correlation R^2 value computed from the sensitivity analysis is significantly better than the other R^2 values obtained, the Null Hypothesis 4 (NH4) is tested. The NH4 states that the best R^2 value is not significantly greater than the ones obtained with all the remaining combinations. In other words, the NH4 statistic test is the difference between the best R^2 value and the R^2 values obtained with the remaining combinations, expected to be 0 if no differences.

For all null hypotheses, the decision to reject the null hypothesis is made by determining how much of the bootstrap distribution (among 50,000 iterations) falls below zero by using the lower bound of the confidence interval (LBCI) at the level of confidence of 95%. An LBCI value greater than 0 allows to reject the null hypotheses.

4 Application to the Séchilienne landslide

4.1 Geological settings and rainfall triggering

The Séchilienne landslide is located in the French Alps on the right bank of the Romanche river, on the southern slope of the Mont-Sec Massif (Fig. 20). The climate is mountainous with a mean annual precipitation height of 1200 mm. The geological nature of the area is composed of vertical N-S foliated micaschists unconformably covered by Carboniferous to Liassic sedimentary deposits along the massif ridge line above the unstable zone. Quaternary glacio-fluvial deposits are also present. The Séchilienne landslide is limited eastwards by a N-S fault scarp and northwards by a major head scarp of several hundred meters wide and tens of meters high below the Mont Sec. The slope is cut by a dense network of two sets of near-vertical open fractures trending N110 to N120 and N70 (Le Roux et al., 2011).

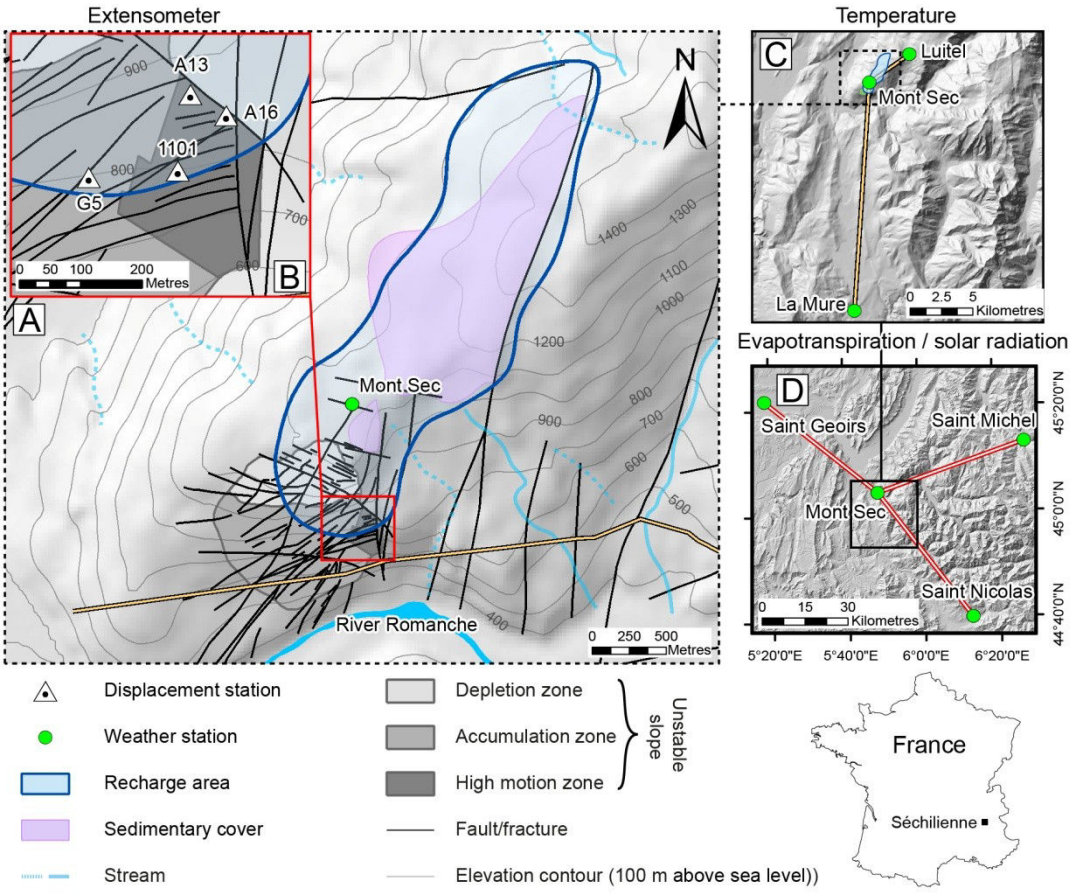

Fig. 20: Location map of the Séchilienne landslide. A: Map of the Séchilienne unstable slope and recharge area showing the Mont-Sec weather station. B: Enlarged map of the most active area showing displacement stations. C: Map showing the weather stations used for the temperature estimation at Mont-Sec. D: Map showing the weather stations used for evapotranspiration and solar radiation method calibration

The Séchilienne landslide is characterized by a deep progressive deformation controlled by the network of faults and fractures. A particularity of the Séchilienne landslide is the absence of a well-defined basal sliding surface. The landslide is affected by a deeply rooted (about 100-150 m) toppling movement of the N50-70° slabs to the valley (accumulation zone) coupled with the sagging of the upper slope (depletion zone) beneath the Mont Sec (Vengeon, 1998; Durville et al., 2009; Lebrouc et al., 2013). A very active moving zone is distinguishable from the unstable slope where high displacement velocities can be 10-time higher than the rest of the landslide.

The landslide shows a higher hydraulic conductivity than the underlying stable bedrock (Vengeon, 1998; Meric et al., 2005; Le Roux et al., 2011), thus leading to a landslide perched aquifer (Guglielmi et al., 2002). The recharge of the landslide perched aquifer is essentially local, enhanced by the trenches and the counterscarps which tend to limit the runoff and to facilitate groundwater infiltration in the landslide area. However, the hydrochemical analyses of Guglielmi et al. (2002) shows that the sedimentary deposits distributed above the landslide hold a perched aquifer which can recharge the landslide perched aquifer. The fractured metamorphic bedrock beneath the landslide contains a deep satured zone at the base of the slope and an overlying vadose zone. The groundwater flow of the entire massif is mainly controlled by the network of fractures with high flow velocities (up to a few kilometres per day; Mudry and Etievant, 2007). The hydromechanical study of Cappa et al. (2014) shows that the deep aquifer can also trigger the Séchilienne landslide destabilization as a result of stress transfer and frictional weakening. Thus, the Séchilienne landslide destabilisation is likely triggered by a two-layer aquifer: the landslide perched aquifer and the deep aquifer. The Séchilienne landslide is characterized by a good correlation between precipitations and displacement velocities (Rochet et al., 1994; Alfonsi, 1997; Durville et al., 2009; Chanut et al., 2013).The seasonal variations of the daily displacement are clearly linked to the seasonal variations of the recharge (high displacements during high flow periods and low displacements during low flow periods).

4.2 Method implementation

Three weather stations located at less than 60 kilometres from the studied site are used as reference weather stations: Grenoble-Saint-Geoirs, Saint-Jean-Saint-Nicolas and Saint-Michel-Maur (Table 6 and Fig. 20). The Saint-Michel-Maur weather station does not measure

R_S, which is estimated with the Angström formula (Eq. (15) in Appendix A) using sunshine duration data recorded at the station. The Angström formula empirical default coefficients are tuned with the two others weather stations ($a_S = 0.232$ and $b_S = 0.574$).

Table 6: Summary of weather datasets with parameters used (●) at the various locations. Distance is the measured from the Séchilienne landslide, R_S is the solar radiation, N is the sunshine duration, W is the wind speed, H is the humidity, T is the temperature and P is the precipitation depth

Station Name	Elevation (m asl)	Distance (km)	From	To	R_S	N	W	H	T	P	Number of days with data
Saint-Jean-Saint-Nicolas	1210	55	01 Jan. 2004	01 Jan. 2012	●	●	●	●	●		2876
Saint-Michel-Maur	698	54	01 Jan. 2004	01 Jan. 2012		●	●	●	●		2864
Grenoble-Saint-Geoirs	384	51	08 Jul. 2009	01 Jan. 2012	●	●	●	●	●		907
Chamrousse	1730	9	12 Sep. 2002	01 Mar. 2012			●	●			3261
La Mure	881	18	9 Sep. 1992	01 Jan. 2012					●		7517
Luitel	1277	4	06 Jul. 2006	23 Jul. 2012					●		2193
Mont-Sec	1148	0.2	9 Sep. 1992	01 Jan. 2012						●	7517

The recharge computation uses the daily rainfall recorded at the weather station located at Mont-Sec, a few hundred meters above the top of the landslide (Table 6 and Fig. 20). This station is equipped with rain and snow gauges. Although this study aims at estimating recharge using only temperature and precipitation datasets, temperature measurements at the Mont-Sec station are considered unreliable because of a non-standard setting of the temperature sensor and numerous missing data. The estimation of the Mont-Sec temperature is detailed in appendix B.

The delimitation of the recharge area of the two-layer hydrosystem (Fig. 20) of the Séchilienne landslide is based on the geological and hydrochemical studies of Vengeon (1998), Guglielmi et al. (2002) and Mudry and Etievant (2007). The recharge area is delimited by the spatial extent of the sedimentary cover of which the hosting perched aquifer recharges the two-layer hydrosystem. Groundwater flow of the entire Mont-Sec massif is controlled by faults and fractures. The N20 fault bordering the sedimentary cover to the east as well as the N-S fault zone bordering the landslide to the east are structures which delimitate the recharge area. The scarcity of information does not allow to accurately define the actual extent of the recharge area. The sensitivity analysis mentioned in Section 3.5 allows to compensate for the possible biases introduced by this uncertainty.

The following spatial datasets are used for the estimation of the parameters of the recharge area. The aerial photographs (0.5 m resolution) and a DEM of 25 m resolution are provided by the "Institut National de l'Information Géographique et Forestière" (IGN) and geological maps are provided by the French Geological Survey (BRGM). The Séchilienne landslide is permanently monitored by a dense network of displacement stations managed by the CEREMA Lyon (Duranthon et al., 2003). In this study, one infra-red station (1101) and three extensometer stations (A16, A13 and G5) are used. Stations 1101, A13 and A16 are representative of the most active zone (median displacement of 2.5, 1.75 and 2.98 mm/day, respectively), while G5 is located on a much less active zone (median displacement of 0.05 mm/day, Fig. 20 and Table 7).

Table 7: Statistics of the displacement records and results of the best linear correlation between precipitation/R_{LRIW} and displacement records for 4 displacement stations (1101, A13, A16 and G5). The displacement column indicates basic statistics of the displacement records: 1st quartile (Q1), median and 3rd quartile (Q3). Cumulative period (n), shift factor (β) and weighting factor (α) are the terms of the equation (8). P stands for precipitation

Station	Displacement mm/day	Cumulative period (n)			Shift factor (β)			Weighting factor (α)			R^2		
	Q1/median/Q3	P	R_1	R_2	P	R_1	R_2	P	R_1	R_2	P	R_{PMNE}	R_{LRIW}
1101	1.75 / 2.50 / 3.84	42	54	68	2	2	2	0.071	0.065	0.091	0.28	0.35	0.50
A13	1.18 / 1.75 / 3.41	52	80	82	3	2	2	0.102	0.070	0.091	0.28	0.37	0.52
A16	1.94 / 2.98 / 4.39	64	71	76	2	2	2	0.163	0.125	0.168	0.34	0.44	0.59
G5	0.02 / 0.05 / 0.08	8	169	132	0	6	6	0.039	0.003	0.011	0.001	0.08	0.24

The sensitivity analysis is performed on the A16 extensometer on the period from 01 May 1994 to 01 January 2012, period during which both A16 extensometer and recharge datasets are available. The performance test of the LRIW workflow against precipitation and R_{PMNE} is performed on the four displacements stations on the period from 01 January 2001 to 01 January 2012, period during which the four stations and recharge datasets are available. The R_{PMNE} is estimated with the non-calibrated Turc equation (Eq. (18)) which is the most appropriate ET_0 reduced-set equation for the Séchilienne site. Indeed, the Turc equation was developed initially for the French climate. The Turc equation requires the estimation of R_s which is performed with the non-calibrated Hargreave-Samani equation (Eq. (12)).

4.3 Displacement data detrending

The long-term displacement monitoring shows that displacement rate and amplitude exponentially increased with time as illustrated by the records of extensometer A16 (Fig.

21A). The rainfall data series does not show any trend over the year, meaning that the displacement trend is independent of the recharge amount. Consequently, on the Séchilienne landslide, for the same amount of rainfall, the displacement rate and magnitude responses increase steadily with time. The observed trend is the consequence of a progressive weakening of the landslide due to long-term repetitive stresses. The accumulating deformation can be assimilated to long-term creep (Brückl, 2001; Bonzanigo et al., 2007) and can be explained by a decrease of the slope shear strength and/or to a modification of hydraulic properties (Rutqvist and Stephansson, 2003). In addition to the trend, the Séchilienne landslide is constantly moving and shows large daily to seasonal variations which seem to be the landslide response from the rainfall trigger. Consequently, the rainfall-displacement correlation is performed on the detrended displacement which is the landslide response from the precipitation trigger.

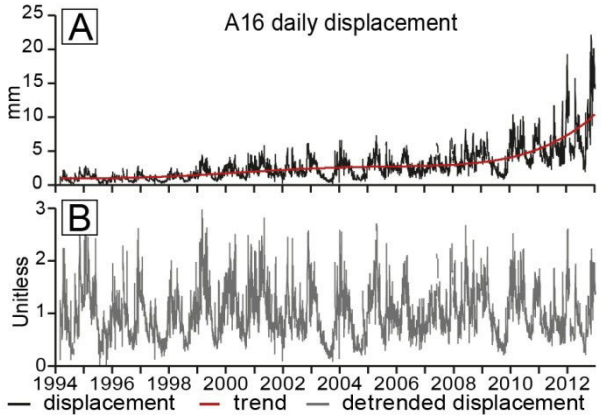

Fig. 21: Trend removal of A16 extensometer displacement data. A: A16 displacement data and the fourth order polynomial curve fitting considered as the displacement trend; B: A16 detrended data (unitless) corresponding to A16 displacement data for which the trend is removed by a multiplicative method

The exponential trend is removed with the statistical multiplicative method ($y_t = T_t S_t I_t$) where the time series (y_t) is composed of three components (Madsen, 2007; Cowpertwait and Metcalfe, 2009; Aragon, 2011): trend (T_t), seasonal (S_t) and irregular (I_t). In this study, the irregular and seasonal components are both assumed to be linked to the rainfall triggering factor ($y_t = T_t D_t \ with \ D_t = S_t I_t$). The trend is determined by curve fitting of a fourth-order polynomial (parametric detrending). The result is a detrended unitless time series (D_t) with both variance and mean trend removed. The time series decomposition process is illustrated with the A16 extensometer in figure 21.

5 Results of the recharge estimation with the LRIW method

5.1 Calibration of methods

The two calibrated R_S methods show good results with respect to R_S measured at the weather stations. The BC_{mod} R_s method is selected as it shows a better performance (R^2 = 0.864; RMSE = 1.567) than the HS_{mod} R_s method (R^2 = 0.847; RMSE = 1.625). The equation (9) presents the calibrated BC R_s method with all the calibrated coefficients.

$$BC_{mod}\ R_s = 0.669\ Ra\left[1-\exp\left(-0.010\ (\alpha\Delta T)^{2.053}\right)\right]+1.733 \quad (9)$$

The cloud cover adjustment factor α is either equal to 0.79 (cloud impact) or to 1. All the equation terms are described in the Appendix A. The BC_{mod} R_s calibrated method is used to compute R_s input data of the five ET_0 methods.

Overall, all of the ET_0 methods tested show good results for regional calibration and are all suitable for the Séchilienne site (Table 8). Among the ET_0 methods tested, the PM_{red} ET_0 method shows the best performance (R^2 = 0.932; RMSE=0.505) and requires only a low regional adjustment. Therefore, the PM_{red} ET_0 method is selected to compute ET_0 for the Séchilienne site (hereafter referred to as ET_0 Séch). The figure 22 displays the estimated ET_0 Séch versus the FAO-56 PM computation for each reference weather station.

Table 8: Calibration and performance of the five tested ET_0 methods relatively to the FAO-56 PM ET_0 standard (Penman-Monteith method defined in the FAO-56 paper). All the ET_0 methods are detailed in the appendix A. a, b and R^2 are the results of linear regression between FAO-56 PM ET_0 and ET_0. RMSE is the root mean square error

Method	a	b	R^2	RMSE
HS Et_0	0.920	0.130	0.917	0.548
Turc ET_0	0.880	0.434	0.900	0.588
PS ET_0	0.352	0.365	0.919	0.533
M ET_0	1.107	-0.018	0.910	0.565
PM_{red} ET_0	0.994	0.013	0.932	0.505

The equation (10) is the final calibrated PM_{red} ET_0 method with all the calibrated coefficients. The input R_n term is deduced from the calibrated BC_{mod} R_S method (Eq. (9)).

$$ET_{0\ Séch} = 0.994\frac{0.408\Delta\left(R_n-0\right)+\gamma\frac{900}{T_{avg}+273}1.5\left(e_s-e_a\right)}{\Delta+\gamma\left(1+0.34\ 1.5\right)}+0.013 \quad (10)$$

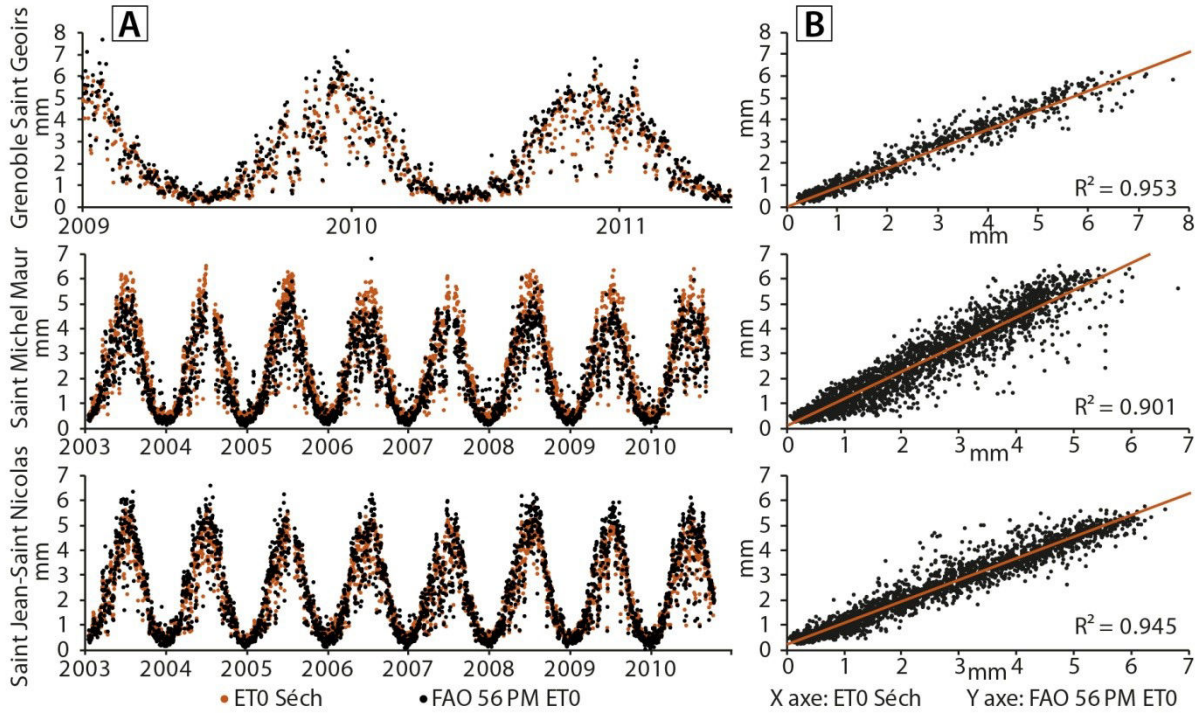

Fig. 22: ET_0 regional calibration results at the three reference weather stations (Grenoble-Saint-Geoirs, Saint-Jean-Saint-Nicolas and Saint-Michel-Maur). A: $ET_{0\ Séch}$ and FAO-56 PM ET_0 as a function of time. B: linear regression between $ET_{0\ Séch}$ (X axis) and FAO-56 PM ET_0 (Y axis). $ET_{0\ Séch}$ stands for ET_0 computed with the combination of calibrated ET_0 Penman-Monteith reduced-set method and calibrated R_S modified Bristow-Campbell method

5.2 Recharge-area parameters

Sub-areas are expressed in percentages of the whole recharge area (Table 9 and Fig. 23). Two types of vegetation cover, pasture and forest, are defined using aerial photographs, with proportions of 23% and 53%, respectively. Three main geology sub-areas, micaschist bedrock (15%), sedimentary cover (20%) and superficial formations (41%), are defined through examination of the geological map and field investigations. Infiltration structures are centered on the major faults identified on the geological map, on lineaments deduced from aerial-photograph analysis and on geomorphological features (sinkholes, cracks...) A 50-meter wide influence zone is added to the identified objects, leading to an infiltration-structure sub-area representing 24% of the recharge area. The Séchilienne forest is mainly composed of beeches (*Fagus sylvatica*) and conifers (*Picea excelsa*), which are associated occasionally with ashes (*Fraxinus*) and sweet chestnuts (*Castanea sativa*).

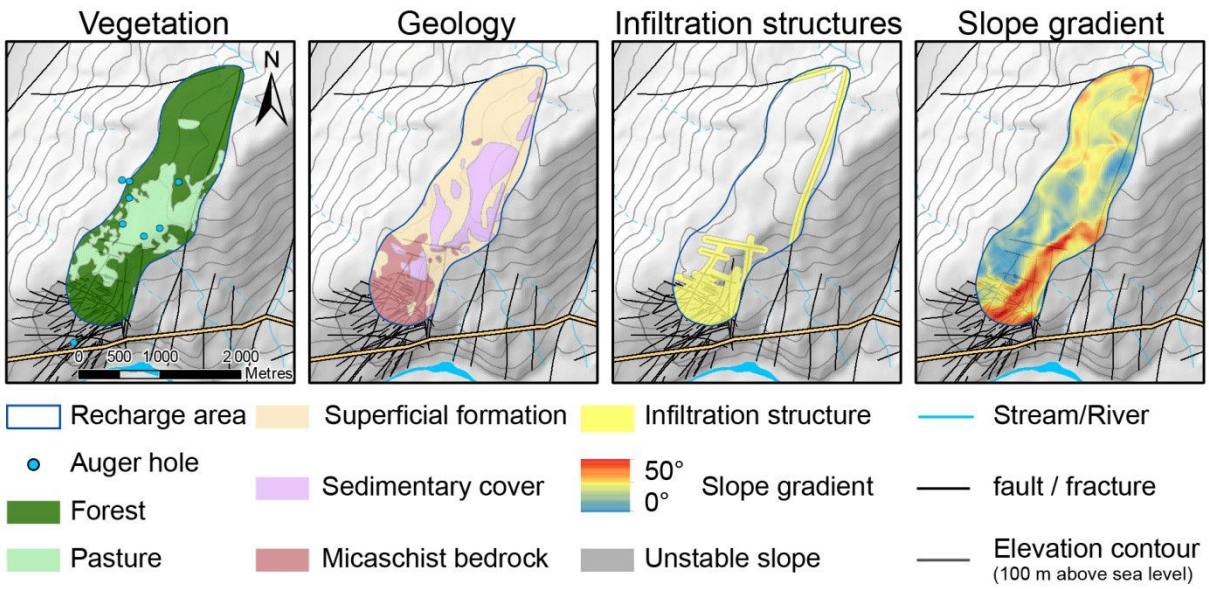

Fig. 23: Factor sub-areas, auger hole and slope gradient used for the estimation of recharge-area parameters

For K_c estimation, the proportion of beeches and conifers is assumed to be identical for the Séchilienne forest (each 50% of forest sub-area) and other species are ignored. K_c are set to 0.71 and 0.97 for conifers, and to 0.78 and 0.9 for beeches according to Verstraeten et al. (2005). Most pastures are anthropogenic and consist of grass. K_c are set to 0.85 and 1 according to Allen et al. (1998). Infiltration structure sub-areas are not taken into account in the K_c estimation, so the relative proportions of pasture and forest become 30% and 70%, respectively. The contribution of each sub-area (Table 9, column "K_c RA") allows the determination of the recharge area K_c values at the scale of the recharge area (0.777 to 0.955).

The combination of geology and vegetation sub-areas results in six types of SAWC sub-areas (Table 9). For each SAWC sub-area, at least one auger hole was drilled. For each soil auger core, the soil texture, the stoniness and the organic-matter content are estimated by morphological description (Jabiol and Baize, 2011). Based on these estimations, the SAWC is then computed using the pedotransfer functions of Jamagne et al. (1977) and Bruand et al. (2004). The average estimation of SAWC at the recharge area scale is 106 ±10 mm (rounded to 105 mm).

To estimate the R_{coeff}, an average slope gradient is computed from slope gradient analysis and is assigned to each vegetation sub-area. Pasture and forest sub-areas show an average slope gradient of 14° and of 20.6° respectively. R_{coeff} values of 22% for pasture and 15% for forest are deduced from Sautier chart (Musy and Higy, 2011). This chart was developed for

Switzerland where environmental conditions are similar to the French Alps. A 12.8% runoff coefficient is then estimated at the recharge area scale, according to the respective proportions of sub-areas in the recharge area (Table 9).

Table 9: Estimation of Kc (vegetation coefficient), SAWC (soil available water capacity) and runoff for the recharge area of the Séchilienne landslide. Geology and vegetation are the sub-area factors identified and expressed in proportion of the recharge area. The average slope gradient is the slope gradient for each identified vegetation sub-area factor. Kc, runoff and SAWC columns are the estimated values for each sub-area factor. Kc RA, SAWC RA and runoff RA columns are the contribution of each sub-area parameter. The recharge-area bottom-row stands for the estimation at the scale of the recharge area

Geology sub-area (%)		Vegetation sub-area (%)	Average slope gradient (°)	Kc min. max.	Kc RA min. max.	Runoff (%)	Runoff RA (%)	SAWC (mm)	SAWC RA (mm)
Micaschist	3	Pasture	14.0	0.85 1	0.256 0.301	22	5.1	173	5
Sedimentary	9							100	9
Superficial formations	11	23						112	12
Micaschist	12	Forest	20.6	0.745 0.935	0.521 0.654	15	7.7	254	30
Sedimentary	11							81	9
Superficial formations	30	53						133	41
Outcrop no soil	24	24	-	-	-	0	0	0	0
Recharge area	100	100	-	-	0.777 0.955	-	12.8	-	106

5.3 Sensitivity analysis of the parameters of the recharge area

Sensitivity analysis is performed for SAWC ranging from 0 (100% of infiltration structures corresponding to precipitation) to 145 mm of SAWC (0% infiltration structures +10 mm of SAWC uncertainties measurement) with increments of 10 mm. The coupled surface R_{coeff} ranges from 0 to 16.3% (with increments of about 1%). For each combination, recharge is computed according to the soil-water balance (Fig. 18 – Step 3 and Fig. 19) with: (i) the temperature estimated for the recharge area (Appendix B), (ii) the precipitation recorded at Mont-Sec weather station, and (iii) the parameters of the recharge area.

All the best computations have a one-day lag, with periods ranging from 56 to 104 days (Fig. 24A and Table 10). The best R^2 obtained from recharge is obtained with both the estimated recharge-area parameters (SAWC = 105 mm, $R^2 = 0.618$) and the recharge-area parameters for SAWC adjusted from 85 ($R^2 = 0.618$) to 115 mm ($R^2 = 0.617$, Fig. 24B and Table 10). For all the recharge combinations tested, the LBCI values from bootstrap testing of NH2 are

greater than 0, allowing to reject the null hypothesis NH2 (Fig. 24C). In other words, it shows that the R^2 obtained with recharge is always significantly higher than the one computed with precipitation ($R^2 = 0.311$) even for a SAWC of 5 mm ($R^2 = 0.426$, Table 10).

Table 10: Sensitivity analysis results of the best correlation between precipitation/R_{LRIW} and A16 extensometer detrended displacement. IS is for infiltration structures. SAWC is the soil-available water-capacity. LBCI is the lower bound of the confidence interval. R^2 row is the R^2 computed from recharge-area parameters indicated in each table row. Cumulative period (n), shift factor (β) and weighting factor (α) are the terms of the equation (8). Null hypothesis NH2 test: R^2_{row}-$R^2_{precipitation}$. Null hypothesis NH4 test: $R^2_{SAWC\ 105}$-R^2_{row}

SAWC mm	Runoff coeff. %	IS %	Cumulative Period (n) day	Shift factor (β) day	Weighting factor (α)	R^2	LBCI of R^2	LBCI of NH2	LBCI of NH4
0	0.0	100	56	1	0.1697	0.311	0.230	0	0.241
5	0.6	96	92	1	0.1362	0.426	0.335	0.073	0.139
15	1.8	89	101	1	0.1226	0.522	0.435	0.158	0.055
25	3.0	82	104	1	0.1259	0.563	0.481	0.194	0.022
35	4.2	75	104	1	0.1317	0.585	0.508	0.214	0.005
45	5.4	68	103	1	0.1374	0.599	0.525	0.227	-0.004
55	6.6	61	102	1	0.143	0.608	0.537	0.234	-0.008
65	7.8	53	101	1	0.1484	0.613	0.544	0.238	-0.009
75	9.0	46	100	1	0.155	0.616	0.548	0.240	-0.009
85	10.3	39	98	1	0.1609	0.618	0.551	0.242	-0.007
95	11.5	32	94	1	0.1648	0.618	0.552	0.242	-0.004
105	12.8	24	92	1	0.1689	0.618	0.552	0.241	0.000
115	13.9	18	89	1	0.1727	0.617	0.551	0.240	-0.002
125	15.1	10	86	1	0.1745	0.614	0.549	0.237	-0.003
135	16.3	3	82	1	0.1746	0.611	0.545	0.235	-0.003
145	16.3	-	77	1	0.1731	0.609	0.543	0.234	-0.003

One of the best correlation performances is obtained for the estimated recharge-area parameters. This reveals that the delimitation of the recharge area reflects properly the Séchilienne landslide groundwater contributing recharge area. For the adjusted recharge-area parameters scenarios having SAWC values above 45 mm, the LBCI values from bootstrap testing of NH4 from are lower than 0, not allowing to reject the null hypothesis NH4 (Table 10 and Fig. 24D). In other words, it shows that the R^2 obtained with a SAWC of 105 mm is not significantly higher than the ones obtained from SAWC above 45 mm. Recharge-displacement correlations for SAWC values ranging from 75 (runoff = 9%) to 115 mm (runoff = 13.9%) show (i) a cumulative period computation (n) below 101 days, that is within the third quartile, (ii) an R^2 greater than 0.616, that is within the third quartile, (iii) LBCI

values of NH2 greater than 0 and (iv) LBCI values of NH4 lower than 0 (Table 10 and Fig. 24). These SAWC and runoff values seem to statistically reflect the recharge area properties of the landslide and are suggested for further work on the Séchilienne landslide.

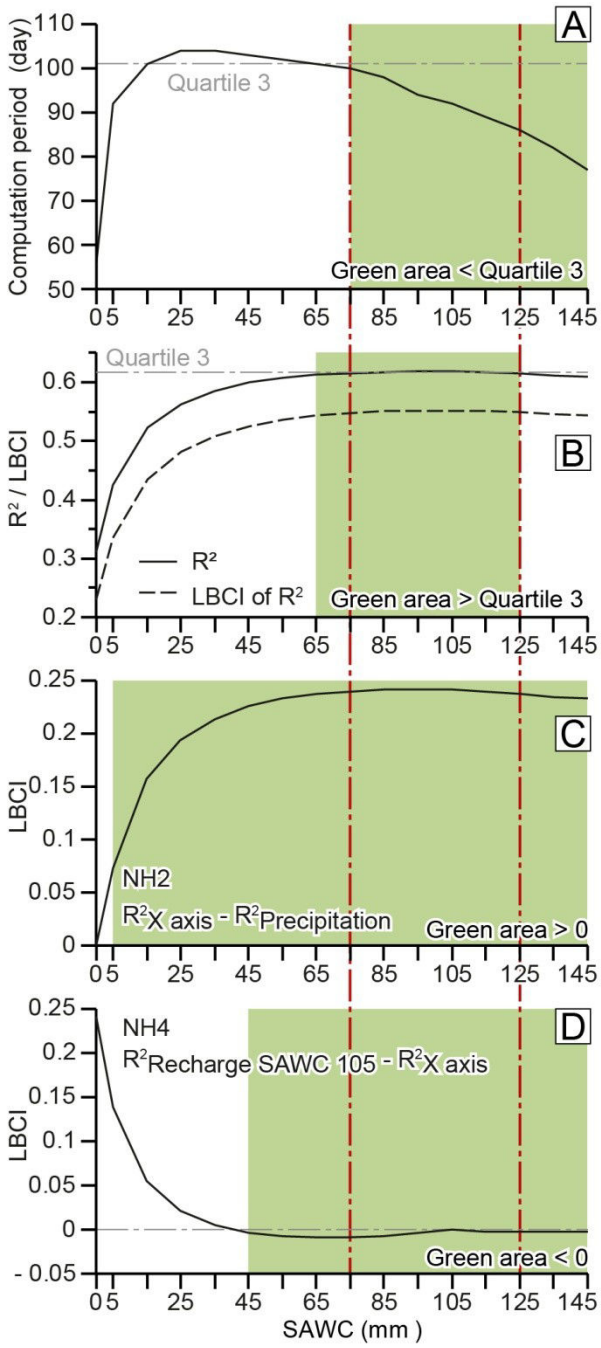

Fig. 24: Results of the sensitivity analysis relative to SAWC (soil-available water-capacity) for (A) the computation period, (B) the R^2 and the LBCI of R^2, (C) the LBCI of the null hypothesis NH2 and (D) the LBCI of the null hypothesis NH4. LBCI is the lower bound of the confidence interval

5.4 Estimation of the recharge for the Séchilienne landslide

For the remaining part of this paper, the R_{LRIW} is based on the estimated recharge-area parameters (infiltration structures = 24%, SAWC = 105 mm, and R_{coeff} = 12.8%). Indeed, among all solutions giving satisfying performances in the sensitivity analysis, these parameters arise from actual field data. The R_{LRIW} is compared with the precipitation signal in the figure 25.

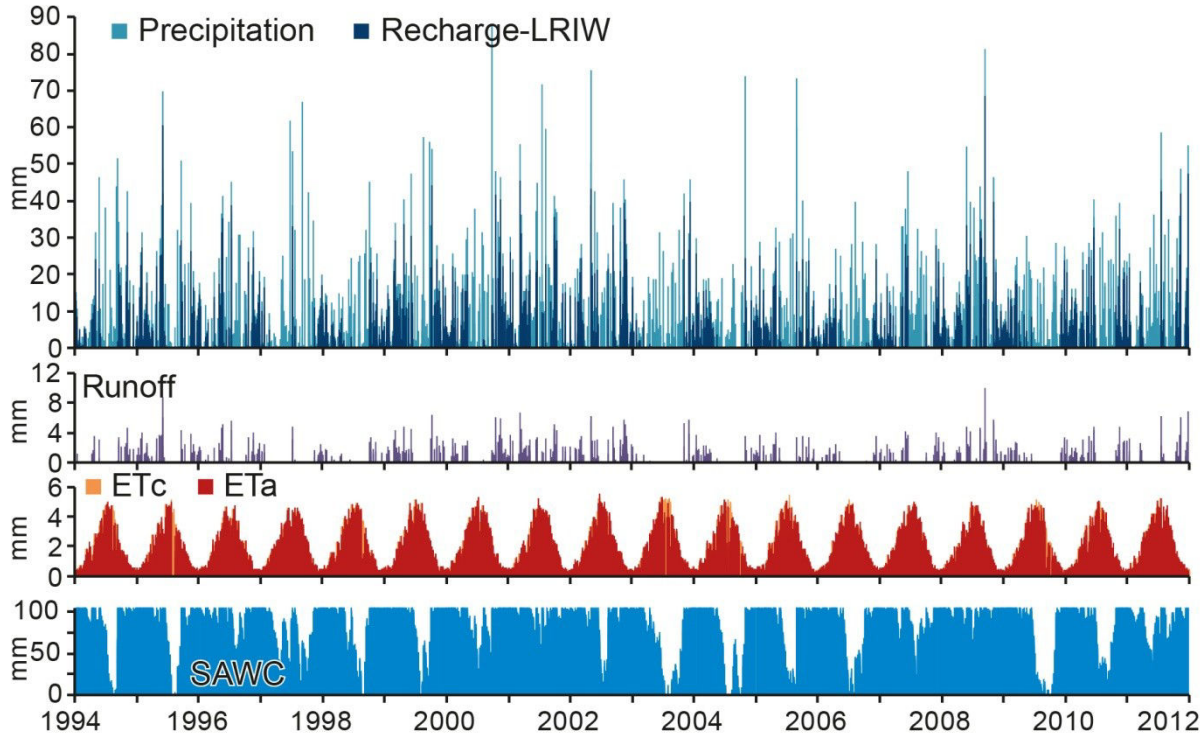

Fig. 25: Recharge computation with the LRIW method at Séchilienne with an SAWC of 105 mm and a runoff coefficient of 12.8%. ET_c: specific vegetation evapotranspiration; ET_a: actual vegetation evapotranspiration, SAWC: soil-available water-capacity

The R_{LRIW} signal differs significantly from the precipitation signals, marked by a high seasonal contrast. This is especially true, during summer when ET_c is important. Indeed, the first rainfall events after a dry period do not reach the aquifer until the SAWC is exceeded. The figure 26 shows the best correlation results for precipitation and R_{LRIW}, together with A16 detrended daily displacement. The cumulative recharge signal reproduces well the displacement acceleration and deceleration phases, and especially the dry summers where displacement dramatically dropped (summers 1997, 1998, 2003, 2004 and 2009, Fig. 26B). On the contrary, the cumulative precipitation signal is more contrasted and more noisy, and does not manage to reproduce several peaks (in width as well as in intensity) of the detrended

displacement signal (winters 1997, 2000, 2004, 2005 and 2010). In addition, the cumulative precipitation signal shows a weak correlation with displacement deceleration phases (summers 1998, 1999, 2000 2006, 2009 and 2010).

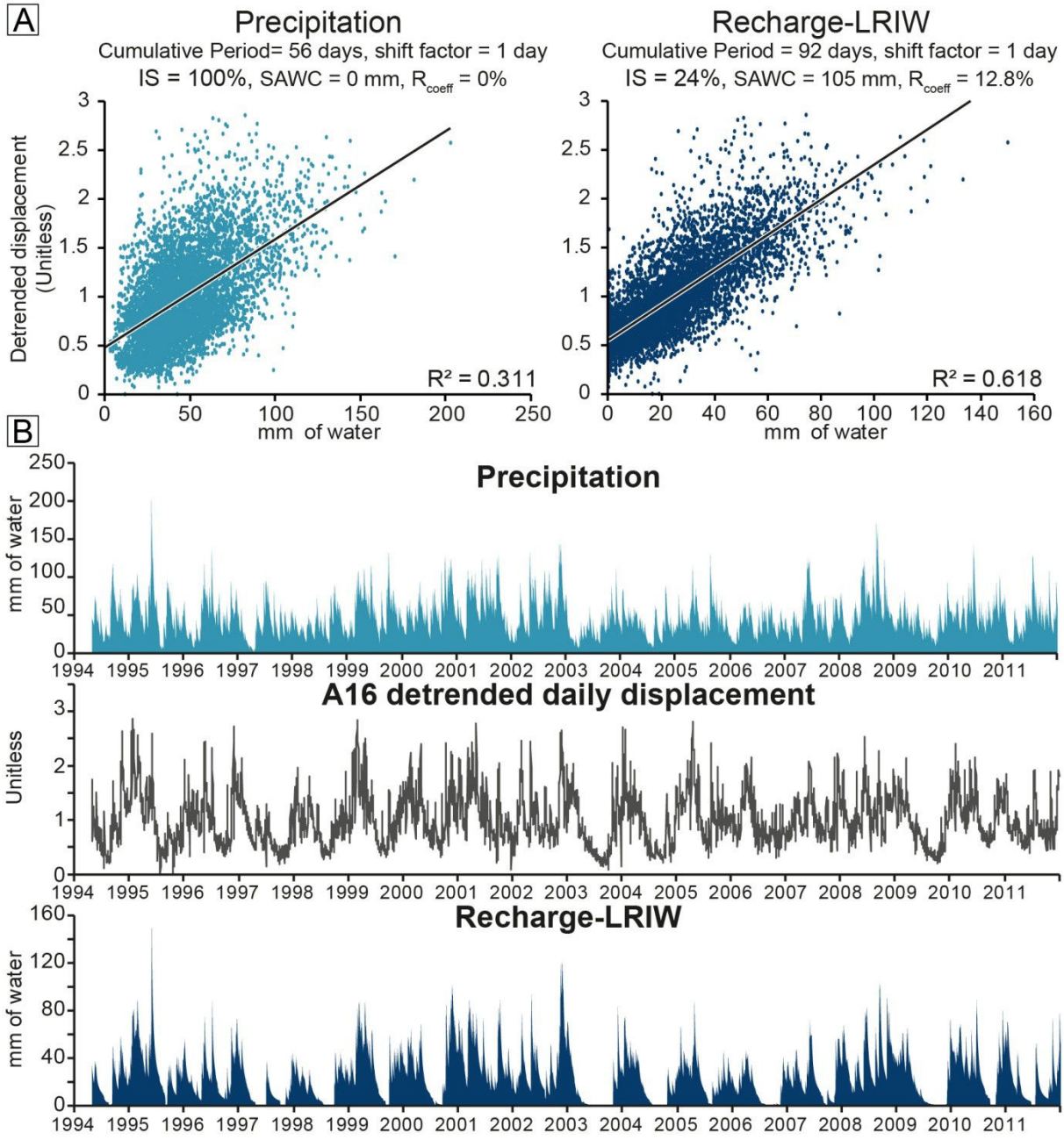

Fig. 26: Best linear correlation for precipitation and recharge computed with the LRIW method. IS is for infiltration structures. SAWC is soil-available water-capacity. Cumulative period (n) and shift factor (β) are the terms of the equation (8). A: Linear regression between precipitation/R_{LRIW} and A16 detrended displacement. B: Correlation between precipitation/R_{LRIW} and A16 detrended displacement as a function of time

6 Discussion

6.1 Relevance of the LRIW method

The figure 24 summarizes the comparison of the performances between the precipitation, the R_{PMNE} and the R_{LRIW} based on the NH1, NH2 and NH3 tests. All LBCI values from bootstrap testing of NH1, NH2 and NH3 are greater than zero, allowing to reject the three null hypotheses for the four stations (Fig. 27A). Rejection of the NH1 null hypothesis shows that the R^2 obtained with R_{PMNE} are significantly higher than those computed with precipitation. Rejection of the NH2 null hypothesis shows that the R^2 obtained with R_{LRIW} are significantly higher than those computed with precipitation. Similarly, rejection of the NH3 null hypothesis shows that the R^2 obtained with R_{LRIW} are significantly higher than those computed with R_{PMNE}. R^2 values vary from 0.0006 to 0.343 for precipitation, from 0.076 to 0.444 for R_{PMNE} and from 0.243 to 0.586 for R_{LRIW}, for G5 and A16 extensometer respectively (Table 7). On average, R_{PMNE} allows to increase the R^2 value by 29% relatively to precipitation, while R_{LRIW} allows to increase the R^2 by 78% (Fig. 27B). The R^2 obtained with R_{LRIW} are 38% higher on average than those obtained with R_{PMNE}. These results are confirmed by the LBCI and by the observed values of the NH2 test which are always greater than those from the NH1 test as well as by the positive LBCI values of the NH3 test (Fig. 27). The correlation performance for the recharge estimated with the LRIW method significantly exceeds the performances of the two other signals, making the LRIW method particularly appropriate to be used in landslide studies. A discussion about the benefit of this study for the understanding of the rainfall-displacement relationship in the case of the Séchilienne landslide can be found in appendix C.

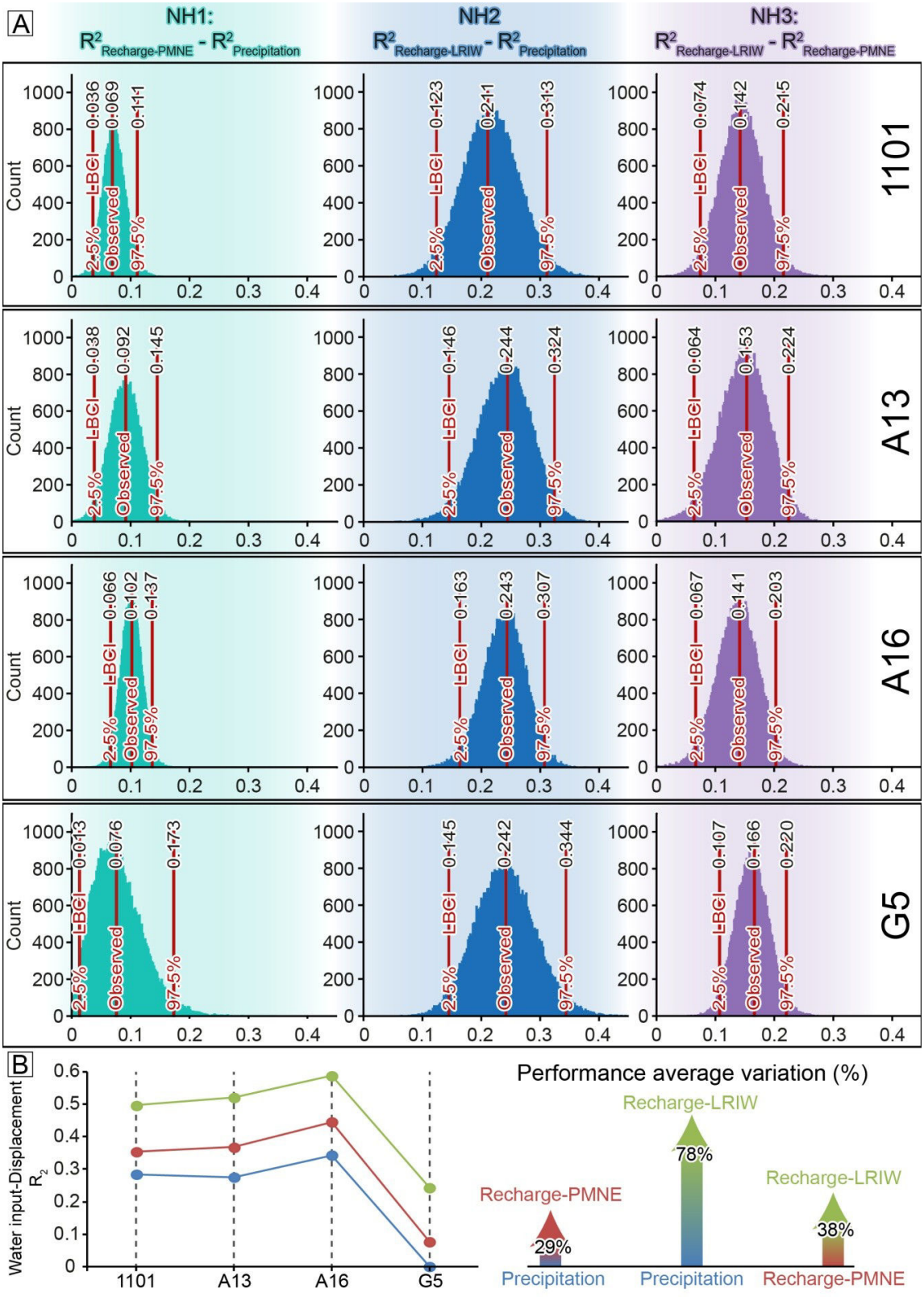

Fig. 27: Performance of the LRIW workflow. A: Bootstrap distribution of null hypothesis NH1, NH2 and NH3 tests for four displacement recording stations. LBCI is the lower bound of the confidence interval. B: R^2 values for the four displacement recording stations obtained with the precipitation, recharge-PMNE, and recharge-LRIW. LBCI is the lower bound of the confidence interval. G5 station is disregarded in the performance average variation calculation as G5 R^2 value obtained with precipitation is close to 0 leading to non representative variation.

6.2 Applicability of the LRIW method to other landslides

Several studies have shown the relevance of recharge for coastal landslides (Maquaire, 2000; Bogaard et al., 2013), unstable embankment slope landslides (Cartier and Pouget, 1987; Delmas et al., 1987; Matichard and Pouget, 1988) and deep-seated earth flow landslides (Malet et al., 2003; Godt et al., 2006). In addition, destabilization of shallow landslides is known to be influenced by antecedent soil moisture and precipitation (Brocca et al., 2012; Garel et al., 2012; Ponziani et al., 2012). Recharge, which implicitly gathers together antecedent soil moisture and precipitation, can be a significant parameter to consider.

Although the method proposed in this study has not been yet tested at other sites, there are several arguments which suggest its applicability elsewhere. First, the FAO Penman-Monteith method used in this study is considered worldwide as the evapotranspiration method standard (Allen et al., 1998; Shahidian et al., 2012). Several evapotranspiration methods were developed locally and many of them can be calibrated against reference methods in other contexts (Hargreaves and Allen, 2003; Yoder et al., 2005; Alkaeed et al., 2006; Igbadun et al., 2006; Trajkovic, 2007; Alexandris et al., 2008; López-Moreno et al., 2009; Sivaprakasam et al., 2011; Tabari and Talaee, 2011; Shahidian et al., 2012; Tabari et al., 2013). Otherwise, Penman-Monteith or Hargreaves-Samani methods are recommended (Allen et al., 1998). A number of solar radiation methods were developed and can be applied worldwide if locally calibrated, allowing estimation of vegetation evapotranspiration with temperature alone (Allen et al., 1998; Almorox, 2011). Recharge-area parameters can be estimated locally or with local or global literature reference values . The use of global values will increase recharge estimation uncertainties. However, the implementation of a sensitivity analysis allows a refinement of recharge-area parameters in order to compensate for the lack of site-specific data. Pachepsky and Rawls (2004) developed pedotransfer functions to estimate SAWC for various regions of the world. R_{coeff} values from the widely used rational method can be applied, as well as most of the runoff coefficients from the literature (McCuen, 2005; Musy and Higy, 2011). In addition, pedotransfer functions can also be used for runoff estimation. Lastly, vegetation coefficients are available from local surveys (Gochis and Cuenca, 2000; Verstraeten et al., 2005; Hou et al., 2010), but can also be found in the literature for many species (Allen et al., 1998).

7 Conclusion and perspectives

A method based on a soil-water balance, named LRIW, is developed to compute recharge on a daily interval, requiring the characterization of evapotranspiration and parameters characterising the recharge area (soil-available water-capacity and runoff). A workflow is developed to compute daily groundwater recharge and requires the records of precipitation, air temperature, relative humidity, solar radiation and wind speed within or close to the landslide. The determination of the parameters of the recharge area is based on a spatial analysis requiring field observations and spatial datasets (digital elevation models, aerial photographs and geological maps). Once determined, the parameters are refined with a sensitivity analysis.

The method has been tested on the Séchilienne landslide. This test demonstrates that the performance of the correlation with landslide displacement velocity data is significantly enhanced using the LRIW estimated recharge. The R^2 obtained with the LRIW recharge are 78% higher on average than those obtained with precipitation and are 38% higher on average than those obtained with recharge computed with a commonly used simplification in several landslide studies (recharge = precipitation minus non-calibrated ET_0). The sensitivity analysis of the LRIW workflow appears to be an appropriate alternative to estimate or to refine soil-water balance parameters of the recharge area, especially in the case of insufficient field investigations or in the absence of the necessary spatial dataset.

The LRIW workflow is developed to be as universal as possible in order to be applied to other landslides. The workflow is developed in order to be sufficiently simple to guide any non-hydro specialist who intends to estimate the recharge signal in the case of rainfall-landslide displacement studies. Within this scope, a software is planned to be developed in the near future in order to provide a user-friendly tool for recharge estimation. In addition, the LRIW workflow also enables the reconstruction of retrospective time series for sites recently equipped with weather stations designed to measure a full set of parameters. A further step will be to account for the spatial and temporal variability of precipitation and recharge area properties, thus providing a better estimation of the recharge. In addition, taking recharge into account can assist in determining a warning rainfall threshold for Séchilienne slope movements.

Acknowledgments

This research was funded by the SLAMS program (Séchilienne Land movement: Multidisciplinary Studies) of the National Research Agency (ANR). The meteorological data were provided by MétéoFrance, LTHE, ONF and CEREMA Lyon. Aerial photographs and the digital elevation model were provided by IGN. Displacement data were supplied by CEREMA Lyon. The authors acknowledge the support of Jean-Pierre Duranthon and Marie-Aurélie Chanut from the CEREMA Lyon and Jean-Paul Laurent from the LTHE. Appreciation is also given to Eric Lucot of Chrono-Environnement for his kind advices for soil log interpretation and to Patrick Giraudoux for his support to implement bootstrap tests. Lastly, the authors thank Peter Milmo for English and technical proof reading.

8 Appendix A: Equations for evapotranspiration and solar radiation methods

8.1 Equation parameters terms for all equations

R_a	extraterrestrial solar radiation [MJ m^{-2} day^{-1}]
R_s	solar radiation [MJ m^{-2} day^{-1}]
R_n	net solar radiation [MJ m^{-2} day^{-1}]
N	maximum possible duration of sunshine [hour]
n	actual daily duration of sunshine [hour]
T_{avg}	average air temperature at 2 m height [°C]
T_{min}	minimum air temperature at 2 m height [°C]
T_{max}	maximum air temperature at 2 m height [°C]
G	soil heat flux density [MJ m^{-2} day^{-1}]
γ	psychrometric constant [kPa $°C^{-1}$]
u_2	wind speed at 2 m height [m s^{-1}]
e_s	mean saturation vapour pressure [kPa]
e_a	actual vapour pressure [kPa]
e^o	saturation vapour pressure at the air temperature T [kPa]
Δ	slope of vapour pressure curve [kPa $°C^{-1}$]
RH	relative humidity [%]
α	cloud cover adjustment factor [unitless]

The procedure for calculating these equation terms are given in the FAO-56 guidelines for computing crop water requirements (Allen et al., 1998).

8.2 Solar radiation (R_S)

The solar radiation $BC\ R_s$ is obtained from the Bristow-Campbell method (Bristow and Campbell, 1984):

$$BC\ R_s = A_{BC}\ Ra\left[1 - exp\left(-B_{BC}\left(\alpha\ \Delta T_{BC}\right)^{C_{BC}}\right)\right] \text{with } \Delta T_{BC} = T_{max(j)} - \frac{T_{\min(j)} + T_{\min(j+1)}}{2} \quad (11)$$

The solar radiation $HS\ R_s$ obtained from the Hargreaves-Samani method (Hargreaves and Samani, 1985):

$$HS\ R_s = A_{HS} Ra\left(\Delta T_{HS}\right)^{B_{HS}} \text{ with } \Delta T_{HS} = T_{max(j)} - T_{\min(j)} \quad (12)$$

where:

j is for the current target day and j+1 is for the following day

A_{BC}, B_{BC}, C_{BC} are the Bristow-Campbell empirical coefficients (no default values)

A_{HS}, B_{HS} are the Hargreaves-Samani empirical coefficients ($A_{HS} = 0.16$ *and* $B_{HS} = 0.5$)

In this study, modified forms of R_S equation of Bristow-Campbell and Hargreaves-Samani are implemented: (i) a constant is added to take into account the possibility of a R_S estimation shift, (ii) the ΔT from the Bristow-Campbell method is used in both equations. and (iii) a cloud cover adjustment factor α is applied to ΔT since, for cloudy conditions, ΔT can produce an estimate larger than the incoming solar radiation (Bristow and Campbell, 1984).

Bristow-Campbell modified equation ($BC_{mod}\ R_s$):

$$BC_{mod}\,R_s = A_{BC}\,Ra\left[1 - exp\left(-B_{BC}\ (\alpha\,\Delta T)^{C_{BC}}\right)\right] + D_{BC} \tag{13}$$

Hargreaves-Samani modified equation (s):

$$HS_{mod}\,R_s = A_{HS}\,Ra\,(\alpha\,\Delta T)^{B_{HS}} + C_{HS} \tag{14}$$

with $\Delta T = T_{max(j)} - \frac{T_{\min(j)} + T_{\min(j+1)}}{2}$;

Where:

j is for the current day and j+1 is for the following day

$A_{BC}, B_{BC}, C_{BC}, D_{BC}$ are the Bristow-Campbell regional calibration coefficients

$A_{HS},\ B_{HS},\ C_{HS}$ are the Hargreaves-Samani regional calibration coefficients

The α coefficient is applied for the two first rain-event days since, for a rain period longer than two days, the value of the Rs estimated from ΔT and the actual R_s value become almost identical. If ΔT on the day before a rain event (ΔT_{j-1}) is less than ΔT_{j-2} by more than 2°C, the coefficient α is also applied assuming that cloud cover was already significantly present. For the remaining days, α is not applied (α = 1). A 2°C threshold and a 2-day period is used (Bristow and Campbell, 1984). In this study, the calibration of α is based on the principle that if this adjustment is not relevant, a calibrated α coefficient would be equal to 1 (no effect).

R_S can also be calculated with the Angström formula using sunshine duration data recorded at a weather station (FAO-56 guidelines, Allen et al., 1998):

$$R_s = \left(a_s + b_s \frac{n}{N}\right) R_a \tag{15}$$

where: $a_s + b_s$ is the fraction of extraterrestrial solar radiation reaching the earth on clear days (default values, a_s=0.25 and b_s = 0.5).

8.3 Reference vegetation evapotranspiration (ET_0)

The reference vegetation evapotranspiration $FAO-56\,PM\;ET_0$ obtained from the Penman-Monteith method modified form from the FAO paper number 56 (Allen et al., 1998) is:

$$FAO-56\,PM\;ET_0=\frac{0.408\Delta\left(R_n-G\right)+\gamma\dfrac{900}{T_{avg}+273}u_2\left(e_s-e_a\right)}{\Delta+\gamma\left(1+0.34u_2\right)} \tag{16}$$

The reference vegetation evapotranspiration $HS\,ET_0$ obtained from the Hargreaves-Samani method (Hargreaves and Samani, 1985) is:

$$HS\,ET_0=0.0135\;0.408\,Rs\left(T_{avg}+17.8\right) \tag{17}$$

The unit conversion factor 0.408 was added to the original formula in order to compute ET_0 in mm day^{-1} with R_S in MJ m^{-2} day^{-1}.

The reference vegetation evapotranspiration $Turc\,ET_0$ obtained from the Turc method (Turc, 1961) is:

$$For\;RH>50\%,\quad Turc\,ET_0=0.01333\frac{T_{avg}}{T_{avg}+15}\left(23.9001\,Rs+50\right) \tag{18}$$

$$For\;RH<50\%,\quad Turc\,ET_0=0.01333\frac{T_{avg}}{T_{avg}+15}\left(23.9001\,Rs+50\right)\left(1+\frac{50-RH}{70}\right) \tag{19}$$

For the Séchilienne landslide, the equation (18) is preferred to the equation (19) because of an average relative humidity (RH) of the nearby mountain weather stations greater than 50% (Chamrousse, 70%; Saint-Michel-Maur, 66 %; Saint-Jean-Saint-Nicolas, 66 %).

The reference vegetation evapotranspiration $PT\,ET_0$ obtained from the Priestley-Taylor method (Priestley and Taylor, 1972) is:

$$PT\;ET_0=1.26\frac{\Delta}{\Delta+\gamma}\left(R_n-G\right) \tag{20}$$

The reference vegetation evapotranspiration $M\,ET_0$ obtained from the Makkink method (Makkink, 1957) is:

$$M\ ET_0 = 0.61 \frac{\Delta}{(\Delta + \gamma)} \frac{R_s}{2.45} - 0.012 \tag{21}$$

The Penman-Monteith reduced-set method which allows to calculate the reference vegetation evapotranspiration $PM_{red}\,ET_0$ is identical to the PM FAO-56 method (Eq. (16)) but humidity and wind speed are estimated according to FAO-56 guidelines (Allen et al., 1998). The actual vapour pressure is estimated with the equation (22):

$$e_a = e^0(T_{min}) = 0.611\ exp\left(\frac{17.27\ T_{min}}{T_{min} + 237.3}\right) \tag{22}$$

In the case of the Séchilienne landslide, the wind speed was fixed at 1.5 m/s at a 2-meter height (2 m/s by default), which is the daily average of the nearby mountain weather stations (Chamrousse, 2.33 m/s; Saint-Michel-Maur, 0.95 m/s; Saint-Jean-Saint-Nicolas, 1.26 m/s).

8.4 Practical informations

The ET_0 methods used in this study were developed for irrigation scheduling, for which the scope of application involves positive temperatures (plant water supply during the spring-summer growing period). However, in mountainous sites, winter temperatures are often below 0°C, and ET_0 empirical methods can compute negative ET_0 values. Negative ET_0 computed values do not have any physical meaning and are therefore set to zero for this study. The Priestley-Taylor and Penman-Monteith ET_0 methods use net solar radiation (R_n) instead of R_S, which can be deduced from R_S following the FAO-56 guideline (Allen et al., 1998). ET_0 reduce-set methods do not take into account the wind speed variations. By removing saturated air from the boundary layer, wind increases evapotranspiration (Shahidian et al., 2012). Several studies show the influence of the wind speed on ET_0 method performance and therefore on calibration (Itenfisu et al., 2003; Trajkovic, 2005; Trajkovic and Stojnic, 2007). For this study, the days with average wind speed above the 95th percentile of the dataset (extreme values) are disregarded for the calibration.

9 Appendix B: Temperature estimation at the Mont-Sec weather station

9.1 Method

The temperatures at the Mont-Sec weather station are estimated thanks to the characterisation of the local air temperature gradient using two surrounding weather stations recording the temperatures at a daily rate (Luitel et La Mure weather stations). Once, the local air temperature gradient is characterized, one of the station is used to estimate the Mont-Sec temperatures.

The decrease in air density with elevation leads to a decrease in air temperature known as the lapse rate (Jacobson, 2005). A commonly used value of this rate is -6.5 °C / 1000 m. The air temperature can thus be related to elevation. In order to compute a local air temperature gradient, two weather stations surrounding the Séchilienne site were used (weather stations of Luitel and La Mure). The Luitel station is located on the Séchilienne massif whereas the La Mure station is located about 18 km from the landslide. Both stations have weather conditions similar to the Séchilienne recharge area. Although temperature estimation from the Luitel station would probably be more accurate, in order to maximize common interval lengths of temperature with displacement records from 1994 to 2012, the La Mure station with records from 1992 to 2012 is preferred to estimate temperatures at Mont-Sec.

The local air temperature gradient in relation to elevation is defined by the equation (23). The La Mure station temperatures (minimum and maximum) are used to estimate the temperatures at Luitel in relation to elevation, over their common recording period. A linear regression between temperature measured at La Mure and Luitel is performed to determine the a and b coefficients. The b coefficient, which gathers the lapse rate (λ) and the elevation difference, is then divided by the elevation difference of the two stations used for the calibration.

$$T_{(Station)} = a\,T_{(Mure)} + b = a\,T_{(Mure)} + \lambda\,Diff_{elevation} \tag{23}$$

with $Diff_{elevation} = Elevation_{Mure} - Elevation_{Station}$

where:

a and b	regional calibration coefficients
T	temperature minimum or maximum [°C]

λ	temperature lapse rate [°C m^{-1}]
$Diff_{elevation}$	difference of elevation between two weather stations [m]
Elevation	weather station elevation [m asl]
Station	target station (Luitel for calibration, Mont-Sec for computation)

9.2 Results

The estimation of the local air temperature gradient shows a very good performance with R^2 equal to 0.895 (LBCI at 5% level = 0.826) and 0.916 (LBCI at 5% level = 0.850), and RMSE equal to 2.12 and 2.48 respectively for minimum and maximum daily temperature calibration. The equations (24) and (25) are used to estimate temperatures at Mont-Sec with temperatures measured at La Mure. Instead of taking the elevation of the Mont-Sec weather station (1147 m), the average elevation of recharge area (1200 m) is used, resulting in a difference of elevation with La Mure of 319 m. The recording period used for temperature calibration is from 06 July 2006 to 23 July 2012 (2193 records). This is a common data interval for the two weather stations used (La Mure, Luitel). The estimated local air temperature gradient is 0.7°C per 100 meters of elevation (the average of the λ of the two following equations).

$$T_{min(Mont\ Sec)} = 0.911\ T_{min(Mure)} - 0.0056 \times 319 \quad (24)$$

$$T_{max(Mont\ Sec)} = 0.928\ T_{max(Mure)} - 0.0087 \times 319 \quad (25)$$

The absence of reliable temperature records at the Mont-Sec weather station increases the estimation of R_S and ET_0 uncertainties.

10 Appendix C: Rainfall-displacement relationship in the case of the Séchilienne landslide

The rainfall-displacement relationship is hereafter discussed for the precipitation and the R_{LRIW} signals. Although the R^2 values are significantly variable from one station to another, the 2.5th and 97.5th percentiles and the observed value of the NH2 test are rather constant for the four displacement stations (respectively about 0.145, 0.250 and 0.325, Fig. 27A). The improvement of the correlation performance by using recharge rather than precipitation has the same order of magnitude for the four stations, whereas R^2 values vary considerably between the four stations. This may be explained by the fact that groundwater hydrodynamics probably triggers the entire Séchilienne landslide while the displacement velocity response depends on the damage level of the rock at the location of the displacement station. This interpretation is supported by the variability of the cumulative period, the shift factor, the weighting factor and the R^2 value, especially between G5 and the three others stations (Table 7). Lastly, regarding the A16 extensometer, R^2 is better on the recent short testing interval (0.343) than the former one from the sensitivity analysis (0.311) for precipitation and inversely for the recharge (0.586 for the recent interval instead of 0.618 for the former interval). This could be the consequence of a degradation of the near-surface rock mechanical properties of the Séchilienne landslide (as suggested by the displacement trend, Fig. 21), which makes the landslide more sensitive to precipitation events in the recent period.

The best correlations from the sensitivity analysis suggest that infiltration structures could gather a large proportion of the flow (up to 61% for SAWC = 55 mm) with respect to their recharge surface area (24%, Table 10). If so, fractures can play an important role in the groundwater drainage from the massif towards the landslide aquifers. The cumulative period and the shift factor deduced from the antecedent cumulative sum allow to determine the response-time of the Séchilienne landslide to rainfall events. Displacement stations located in the high motion zone show homogenous time delays with shift factors of 2 to 3 days. The average cumulative periods beyond which precipitation or R_{LRIW} have no longer any influence on the landslide destabilisation are estimated at about 50 days for precipitation and 75 days for R_{LRIW}. The station G5 shows significantly different time delays and cumulative periods, whatever the precipitation or R_{LRIW} data used. This difference can be explained by the low signal-to-noise ratio which makes the correlations difficult to interpret.

CHAPITRE III : FONCTIONNEMENT ET MODÉLISATION DE LA RELATION PRÉCIPITATIONS-DÉSTABILISATION DES MOUVEMENTS DE TERRAIN PROFONDS SUJETS AU FLUAGE

FUNCTIONNING AND PRECIPITATION-DISPLACEMENT MODELLING OF DEEP-SEATED LANDSLIDES SUBJECT TO CREEP DEFORMATION

Vallet A.[1], Charlier J.-B.[2], Fabbri O.[1], Bertrand C.[1], Carry N.[1], Mudry J.[1]

[1] UMR6249 Chrono-Environnement - Université de Franche-Comté - 16 route de Gray - F-25030 Besançon cedex - France

[2] BRGM - 1039 Rue de Pinville - 34000 Montpellier - France

1 Résumé du chapitre III

Peu d'études mettent l'accent sur la caractérisation des mécanismes de déformation par fluage des mouvements de terrain, car de telles approches nécessitent d'effectuer des analyses sur le long terme et donc sur de longues séries chronologiques. En conséquence, il existe un réel besoin d'améliorer la compréhension conceptuelle de ces mécanismes. L'étude des relations pluie-déplacement permet de caractériser ces processus hydro-mécaniques et est adaptée aux données disponibles, généralement limitées à la pluviométrie et aux déplacements. L'instabilité de Séchilienne est un terrain d'investigation idéal pour étudier de tels mécanismes, les précipitations et les vitesses de déplacement étant mesurées quotidiennement depuis près de deux décennies.

Pour caractériser le fonctionnement hydro-mécanique des mouvements de terrain sujets au fluage, une analyse en ondelettes est combinée à un nouveau modèle numérique, appelé GLIDE (**G**roundwater **L**andsl**I**de **D**isplacement Cr**E**ep). Le modèle GLIDE se compose d'un modèle hydrogéologique et d'un modèle sollicitation-déformation (Fig. 28). La structure du modèle hydrogéologique est basée sur un double aquifère, un aquifère perché dans la zone instable et un aquifère profond à la base du versant intact mis en évidence dans le chapitre I. Le fonctionnement du réservoir sol, qui permet de calculer la recharge à partir des précipitations, est basé sur la méthode développée dans le chapitre II. La déformation par fluage sur le long terme, nécessite une analyse «dynamique» en introduisant des paramètres en fonction du temps. Le modèle sollicitation-déformation permet de prendre en compte empiriquement des paramètres dépendants du temps, tels que l'endommagement et la consolidation du versant.

Dans un premier temps, une analyse en ondelettes (Fig. 32 et 33) est appliquée sur les précipitations et la recharge, ainsi que sur les vitesses de déplacement, avec et sans la tendance de fluage. Sur la base des analyses en ondelettes, le modèle GLIDE est appliqué aux chroniques de précipitations afin de simuler les vitesses de déplacement de trois extensomètres (Fig. 35). Les résultats montrent que le déplacement sans la tendance (variations périodiques) est mieux corrélé au signal de recharge qu'au signal de précipitations. Les variations infra-annuelles du déplacement sans la tendance sont engendrées par des événements pluvieux instantanés, alors que les variations annuelles et pluriannuelles, où la

plus grande part de la variance est observée, sont majoritairement corrélées à la recharge, et donc à des processus hydrogéologiques. Le modèle GLIDE montre de bonnes performances et établit que les précipitations comme seules données d'entrées peuvent expliquer les variations périodiques ainsi que la tendance exponentielle du fluage à long terme du mouvement de terrain de Séchilienne. Les variations périodiques de la vitesse de déplacement sont contrôlées par un hydrosystème constitué d'un aquifère perché (aquifère réactif responsable des variations hautes fréquences des vitesses de déplacements) et d'un aquifère profond (aquifère inertiel responsable des variations annuelles des vitesses de déplacements). Le mécanisme de fluage, matérialisé par la tendance exponentielle des vitesses de déplacement, ne peut être directement lié aux chroniques de précipitations. Cependant, cette déformation est la conséquence de l'endommagement des propriétés mécaniques du versant, en raison des actions répétées des variations des pressions de fluides.

2 Introduction

By decreasing the resistance of materials due to pore water pressure variations (Van Asch et al., 1999; Iverson, 2000; Cappa et al., 2004; Corominas et al., 2005; Bogaard et al., 2007), groundwater recharge is a key triggering factor for landslide destabilisation. Hydro-mechanical processes which lead to slope failure of deep-seated landslides are complex and are influenced by the evolution of the landslide deformation through time (Iverson, 2000; Brunsden, 2001; Rutqvist and Stephansson, 2003; Binet et al., 2007a; Prokešová et al., 2013). This is especially true in the case of deep-seated landslides, subject to long-term creep deformation (Saito, 1969; Chigira, 1992; Brückl, 2001; Bonzanigo et al., 2007; Blasio, 2011; Federico et al., 2012). Long-term creep mechanism is characterized by time-dependent deformation of rock masses under stress (Federico et al., 2012). The deformation reduces the whole landslide strength through the weakening of the slope material (Chigira, 1992). Besides, in the case of landslides with irregular displacement patterns, a strength increase by consolidation may occur during periods at rest (Nieuwenhuis, 1991; Angeli et al., 2004). For landslides experiencing such deformation processes, the modelling of landslide deformation requires the use of a “dynamic” model instead of classical “static” models, by introducing time-dependent components (Brunsden, 2001; Corominas et al., 2005; Du et al., 2013).

Few studies focussed on landslide creep deformation since such approaches require to perform long-term analyses and thus require multi-annual records of time series (Corominas et al., 2005). There is indeed a need to improve the understanding of landslide creep deformation for which generally only sparse data limited to rainfall and displacement are available. For that, investigating rainfall-displacement relationships can help to characterize hydro-mechanical processes (Matsuura et al., 2008). However, the landslide behaviour which is non-linear with respect to precipitation requires to use adapted signal processing methods such as wavelet analysis. This method is a powerful technique frequently used in geosciences (Kumar and Foufoula-Georgiou, 1997; Torrence and Compo, 1998; Labat et al., 2000; Jevrejeva et al., 2003; Grinsted et al., 2004; Maraun and Kurths, 2004). By decomposing a time series into time-scale space, this method can identify power variations of the signal. It is ideal for analysing non-stationary signals and for identifying short- to large-scale periodic phenomena. Wavelet analysis has recently been used with success in hydrogeology to study rainfall-groundwater and rainfall-runoff relationships of karst springs (Labat et al., 2000;

Massei et al., 2006). To our knowledge, no application on rainfall-displacement data has been carried out in order to characterize the hydro-mechanical response of landslides to rainfall.

Two types of numerical models for displacement simulation or prediction are generally used: (1) black-box models which quantify the rainfall-displacement relationships, and (2) physically-based models which integrate hydrogeological and mechanical landslide properties. Black-box (or input-output) models are generally lumped, considering the landslide area as one entity, whereas physical-based models can be spatially distributed. Various black-box models can be used: the transfer function model (Belle et al., 2013; Abellán et al., 2014), the neural network model (Liu et al., 2005; Du et al., 2013) and the inverse function model (Li et al., 1996). Such modelling methods are simple and parsimonious. However, few of these models take into account time-dependent factors which exert significant controls on landslide creep deformation (Li et al., 1996; Du et al., 2013). Although black-box models show accurate performance and simplicity to be integrated in a warning system, they do not emphasize on physical process and therefore can be limited in the understanding of the landslide-control mechanisms. Conversely, physically-based models (Cappa et al., 2004; Corominas et al., 2005; Guglielmi et al., 2005; Malet et al., 2005; Tacher et al., 2005; van Asch et al., 2007; Cappa et al., 2014) provide a good understanding of the failure mechanisms and integrate time-dependent factors. These models require numerous in-situ geophysical, geotechnical or hydrodynamic measurements. The acquisition of these data is complex (even impossible) because of the continuously moving landslide mass. Moreover, these data are often poorly representative of the spatial variations of the landslide properties, especially in the case of scattered measurements. Consequently, the necessary parameters are often seldom monitored. Lastly, these models are far from routine and their operational applicability in a warning system is limited (Corominas et al., 2005). Hybrid models combining black-box groundwater models with physically based mechanical models (Angeli et al., 1998; Bernardie et al., 2014) allow an intermediary level of investigation and are more appropriated for landslide prediction. Nevertheless, these models still require in-situ measurements.

Reservoir lumped models can be used to decipher the complexity of the hydrogeological systems by considering each reservoir (e.g. soil, perched aquifer, deep aquifer) as a storage element of the hydrosystem (Angeli et al., 1998; Charlier et al., 2012). This kind of model

may be an acceptable compromise between empirical black-box models and distributed models which are physically consistent but are difficult to implement. A reliable model needs precisely characterized hydrogeological and hydromechanical systems, in order to relate model parameters to physically meaningful concepts. Using time-series decomposition, Du et al. (2013) showed that both long-term trend and residual short-term periodic components can be modelled separately since their hydro-mechanical mechanisms have various origins. This suggests that preliminary time series decomposition is a promising approach for a new reservoir modelling methods accounting for the main hydrogeological processes, and their corresponding role on landslide displacement.

This paper aims at characterizing hydro-mechanical processes by investigating rainfall-displacement relationships using wavelet analysis, and at developing a reservoir model to simulate displacement for landslides subject to creep deformation. The approach combines two steps. First, a wavelet analysis carried out on decomposed time series is performed in order to separate the effects on the landslide displacement velocities of precipitation, or recharge from the effects of long-term creep deformation. Considering the hydrogeological context, this analysis allows to build a landslide conceptual model. Second, a new time-dependent lumped reservoir hydro-mechanical model is developed to simulate the short-term periodic displacement variations as well as the long-term creep trend. The proposed method is applied to the Séchilienne landslide in the French Alps where precipitations and displacement have been monitored for twenty years.

3 Signal processing method

3.1 Statistical time-series decomposition

The decomposition of time-series is a statistical method that separates a time series into several distinct components. Three components are of interest: a deterministic non-seasonal secular trend component T_t, a deterministic seasonal component S_t with a known periodicity, a stochastic irregular component I_t (or "noise") that describes irregular influences. The seasonal component refers here to a statistical term which includes all periodic variations of a time series. The irregular component represents the residuals of the time series after the extraction of the two first components (Madsen, 2008; Cowpertwait, 2009; Aragon, 2011). The two S_t and I_t, components represent the detrended component D_t.

Two statistical decomposition methods are generally used for representing a time-series y_t as a function of its trend, seasonal, and irregular components: the additive decomposition method and the multiplicative decomposition method. The additive decomposition method (Eq. (26)) is appropriate when there is no exponential growth in the time series and when the amplitude of the seasonal component remains constant over time.

$$y_t = T_t + S_t + I_t \text{ with } D_t = S_t + I_t \tag{26}$$

On the contrary, the multiplicative decomposition method (Eq. (27)) is appropriated when the time-series shows an exponential growth and when the amplitude of the seasonal component grows with the mean of the series.

$$y_t = T_t S_t I_t \text{ with } D_t = S_t I_t \tag{27}$$

S_t and I_t fluctuate around 0 or around 1 for the additive and multiplicative decomposition, respectively. In some cases, and notably when the sampling time step is within the same range as the high signal frequencies, we may assume that I_t is negligible, leading to decompose y_t into a trend component T_t and a detrended D_t component.

3.2 Wavelet analysis

The wavelet analysis method used in this paper is briefly presented on the basis of definitions put forward by several authors in geosciences (Kumar and Foufoula-Georgiou, 1997;

Torrence and Compo, 1998; Labat et al., 2000; Jevrejeva et al., 2003; Grinsted et al., 2004; Maraun and Kurths, 2004). The wavelet analysis method allows to decompose a time series over a time-frequency space, thus providing a visualization of power distribution along time and frequency. The wavelet transform can be used for analysis of non-stationary processes that contain multi-scale features, for detection of singularities, or for transient phenomena (Kumar and Foufoula-Georgiou, 1997).

The continuous wavelet transform (CWT) can be regarded as successive bandpass filters applied to the time series of uniform shape and varying location and width (Torrence and Compo, 1998). As CWTs are applied to time series of finite length, edge effects may appear on the wavelet power spectrum (or scalogram), leading to the definition of a cone of influence (COI) for the region where such effects are significant (Torrence and Compo, 1998). The COI is computed at the 95% confidence level and is marked by attenuated colour intensities on the scalogram. Many geophysical time series have distinctive red noise characteristics (Grinsted et al., 2004). The 5% significance level of the wavelet power against red noise is shown as a thick contour on the scalogram. Only the identified patches within the thick contours and outside of the COI region can be reliably interpreted.

The covariance between two time-series x and y is estimated using a cross wavelet transform (XWT, also called a cross-scalogram) which is the convolution of the scalogram of both x and y signals. The XWT reveals patches area with a high common power value. Maraun and Kurths (2004) reported that XWT appears unsuitable for significance testing of the inter-relationship between two series. These authors recommend to use wavelet coherence (WTC) which is a measure of the covariance intensity of the two series in the time-frequency space. A causality relationship is interpreted for patches having synchronic common high power on XWT and WTC. In this study, the Morlet wavelet is used as it is fairly well localized in the time-frequency space (Torrence and Compo, 1998).

A multi-resolution analysis is used to decompose a signal into a progression of successive approximations and details in increasing order of resolution. In this study, a multi-resolution using ‘Daubechies-20’ wavelet is carried out to filter the times series, removing outliers by the isolation of the noisy component in the high frequencies.

Continuous wavelet analyses (CWT, XWT, and WTC) were carried out using a free Matlab software package (Mathworks, Natick, MA) provided by Grinsted et al. (2004) at http://noc.ac.uk/using-science/crosswavelet-wavelet-coherence. The package includes a code originally written by C. Torrence and G. Compo, available at: http://paos.colorado.edu/research/wavelets/, and by E. Breitenberger of the University of Alaska, adapted from the freeware SSA-MTM Toolkit: http://www.atmos.ucla.edu/tcd/ssa/. The multi-resolution analysis was carried out using a free Matlab software package provided by the WaveLab Development Team and available at http://statweb.stanford.edu/~wavelab/.

4 Numerical modelling of precipitation-displacement velocity

4.1 Model structure and governing equations

The GLIDE (**G**roundwater **L**andsl**I**de **D**isplacement Cr**E**ep) model aims at simulating the landslide displacement, using a reservoir hydro-mechanical model coupling a groundwater model and a landslide creep model. The structure and the parameters of the model are given in figure 28 and Table 11. In this study, the landslide displacement is decomposed into two components according to the multiplicative method detailed in section 3.1. The detrended component is assumed to be linked to the groundwater trigger effect. The trend is assumed to result from a long-term rock weakening of the landslide strength. The detrended displacement and the displacement trend are modelled separately using a groundwater model and a landslide creep model, respectively. After that, a re-composition of the global signal is done to simulate the displacement time series.

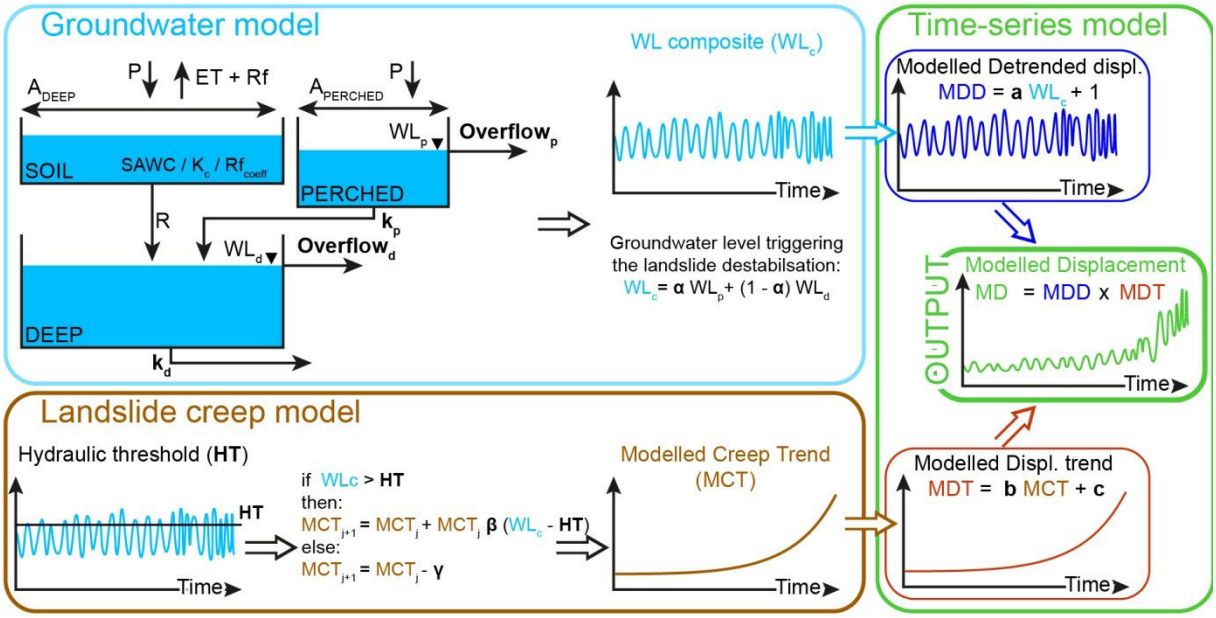

Fig. 28: Structure of the GLIDE model. Bold italic parameters correspond to the model parameters that are to be estimated

Table 11: Parameters of the numerical model: description and calibration results for the scenario 1 (S1) and the scenario 2 (S2). Estimation methods of the parameters: manual (M), calibrated (C) and regression (R)

Name	Model	Signification	Unit	Method	Station	S1	S2
A_{DEEP}	Groundwater	Surface of the recharge area	km^2	M	-	3	
SAWC		Soil available water capacity	mm	M	-	105	
K_c		Coefficient of vegetation	-	M	-	0.777 / 0.955	
Rf_{coeff}		Runoff coefficient	-	M	-	0.128	
$Overflow_d$		Maximum hydraulic head due to deep reservoir overflow	m	C	-	0.12	0.10
k_d		Reservoir recession coefficient	-	C	-	0.02	0.03
$A_{PERCHED}$		Surface of the recharge area	km^2	M	-	0.05	
$Overflow_p$		Maximum hydraulic head due to perched reservoir overflow	m	C	-	0.09	0.06
k_p		Reservoir recession coefficient	day^{-1}	C	-	0.06	0.11
α		Trigger coefficient between WL_p and WL_d expressed as the contribution of WL_p	-	C	-	0.30	0.23
HT	Landslide creep	Hydraulic threshold	-	C	-	-0.19	-0.20
β		Rock weakening coefficient	-	C	A13	$8.22\ 10^{-4}$	$1.20\ 10^{-3}$
					A16	$5.34\ 10^{-4}$	$7.01\ 10^{-4}$
					1101	$1.19\ 10^{-3}$	$1.51\ 10^{-3}$
γ		Rock strengthening coefficient	mm	C	A13	$5.71\ 10^{-4}$	$9.72\ 10^{-4}$
					A16	$1.65\ 10^{-8}$	$2.44\ 10^{-4}$
					1101	$1.09\ 10^{-3}$	$1.28\ 10^{-3}$
a	Time-series	Triggering coefficient of WL_C	-	R	A13	0.30	0.37
					A16	0.35	0.44
					1101	0.33	0.44
b		Rock weakening impact coefficient	-	R	-	1	1
c		Initial state of the modelled trend	mm	R	A13	-0.44	-0.28
					A16	-0.19	-0.21
					1101	0.02	0.27

4.1.1 Groundwater model: detrended displacement

Hydrogeology of deep-seated landslides generally shows a high hydraulic conductivity gradient between the near-surface unstable zone and the deep fractured rock. This organisation leads to a two-layer aquifer system constituted by a perched aquifer, hosted by

the near-surface unstructured rock mass, disconnected from a deep aquifer (Van Asch et al., 1999; Guglielmi et al., 2002; Binet et al., 2007a; Pisani et al., 2010; Huang et al., 2012) . The model structure presented in figure 28 is based on a two-layer-reservoir constituted of a perched aquifer and of a deep aquifer.

The deep aquifer is considered to be recharged by a large recharge area at the scale of the massif, whereas the recharge area of the perched aquifer is located on the landslide area (A_{DEEP} and $A_{PERCHED}$, [L^2] dimension). Input of the perched aquifer is considered as equal to raw precipitation, because the unstable area is characterized by a high infiltration rate of localised recharge in the collapse zone through bare ground, crevices or counter-slopes (Cappa et al., 2004; Charlier et al., 2010). The deep aquifer is recharged by percolation from the perched aquifer, and by diffuse infiltration from a soil reservoir. Lastly, since groundwater is drained by temporary streams and springs during high water periods, overflow processes are taken into account, adding overflow thresholds in both perched and deep aquifer reservoirs ($Overflow_p$ and $Overflow_d$, [L] dimension).

Each reservoir has one input H_{in} and one output H_{out}. The depth of water stored H, in the reservoir is obtained using the following equation:

$$\frac{dH}{dt} = H_{in} - H_{out} \text{ with } H_{out} = k.H \quad (28)$$

where k ([T^{-1}] dimension) is a constant characterizing the recession curve of the reservoir (k_p for perched reservoir and k_d for deep reservoirs).

The soil reservoir is a soil-water balance model accounting for evapotranspiration ET ([L] dimension) and surface runoff Rf_{coeff} (dimensionless) in order to simulate a diffuse recharge through soil cover. The ET is estimated with a calibrated temperature-based evapotranspiration equation (Penman-Monteith reduced-set, Allen et al., 1998) coupled with a vegetation coefficient K_c (dimensionless). The soil available water capacity $SAWC$ ([L] dimension), the K_c and the Rf_{coeff} are estimated with a geographic information systems method and field investigations (soil survey with auger holes, vegetation survey….). The soil-water balance computation and the estimation of the required parameters follow the method developed by Vallet et al. (2014).

The hydromechanical study of Cappa et al. (2014) showed that deep aquifer water pressure, beneath the unstable zone, can facilitate rupture of slow-moving landslides as a result of stress transfer and frictional weakening. In addition to the perched aquifer, the deep aquifer is assumed to trigger the displacement of the deep-seated landslide. A composite groundwater level WL_c (dimensionless), triggering the landside destabilisation, is estimated from both perched and deep reservoir water-levels (WL_p ([L] dimension and WL_d ([L] dimension) according to a triggering coefficient α varying from 1 to 0 (Fig. 28). WL_c is deduced from normalised water levels of the perched and the deep reservoirs in order to be independent of the water level amplitudes.

4.1.2 Landslide creep model: long-term displacement trend

The long-term displacement trend observed on creep deformation landslide is a direct consequence of the time evolution of the whole landslide strength. Thus, the modelled creep trend *MCT* ([L] dimension) increases with the whole landslide weakening whereas the *MCT* decreases with landslide consolidation. The water-level composite WL_c output from the groundwater model is considered as the water pressure input of the landslide creep model. The landslide creep model is based on a constant hydraulic threshold *HT* (dimensionless) which has to be exceeded ($WL_c > HT$) in order to increase the *MCT,* thus simulating rock weakening. Conversely, when the WL_c does not reach the hydraulic threshold, the *MCT* decreases, simulating rock consolidation. The weakening mechanism is assumed to be proportional to the water-level exceeding the hydraulic threshold (WL_c - *HT*) by adjusting a weakening coefficient β (dimensionless). The weakening process depends on the antecedent rock mass strength:

$$MCT_{j+1} = MCT_j + MCT_j \beta (WL_c - HT) \quad (29)$$

with MCT_j and MCT_{j+1} respectively stand for *MCT* at day *j* and day *j+1*. On the other hand, the landslide consolidation process is assumed to be independent of the landslide strength state and the groundwater level. The consolidation is estimated by subtracting a strengthening coefficient γ ([L] dimension) to *MCT*:

$$MCT_{j+1} = MCT_j - \gamma \quad (30)$$

4.1.3 Time-series model: displacement recomposition

The time-series model combines the results of both the groundwater model and the landslide creep model. First, the modelled detrended displacement *MDD* (dimensionless) is assumed to be linearly proportional to the WL_c output of the groundwater model:

$$MDD = a\,\boldsymbol{WL_c} + 1 \tag{31}$$

The *a* parameter (dimensionless) is considered as the triggering impact of the water level on the landslide destabilisation. A shifting intercept is set to 1 since the detrended component fluctuates around 1 whereas WL_c fluctuates around 0 as a consequence of the water-level normalization.

Second, the modelled displacement trend *MDT* ([L] dimension) is assumed to be proportional to the *MCT* state output of the landslide creep model (*b* parameter (dimensionless) of which a shifting *c* parameter ([L] dimension), accounting for the initial condition of the *MCT*, is added as follows

$$MDT = b\,\boldsymbol{MCT} + c \tag{32}$$

The modelled displacement *MD* ([L] dimension) is then reconstructed by multiplying *MDD* and *MDT* which gives:

$$MD = (b\,\boldsymbol{MCT} + c)(a\,\boldsymbol{WL_c} + 1) = ab\,\boldsymbol{MCT}\,\boldsymbol{WL_c} + b\,\boldsymbol{MCT} + ac\,\boldsymbol{WL_c} + c \tag{33}$$

Equation (33) can be simplified as follows:

$$MD = A\,\boldsymbol{MCT}\,\boldsymbol{WL_c} + B\,\boldsymbol{MCT} + C\,\boldsymbol{WL_c} + D \tag{34}$$

Equation (34) represents the governing equation of the time-series model.

4.2 Parameterization and calibration strategy of the model

4.2.1 Model parameters

Modelling the displacement at one station requires 16 parameters (5 being estimated, 8 being calibrated and 3 being deduced from multiple linear regression, Table 11). The groundwater

model needs a total of 10 parameters (A_{DEEP}, $SAWC$, K_c, Rf_{coeff}, $Overflow_d$, k_d, $A_{PERCHED}$, $overflow_p$, k_p, α) of which 5 (A_{DEEP}, $SAWC$, K_c, Rf_{coeff}, $A_{PERCHED}$) can be estimated from field investigations, and 5 are calibrated. Additionally, the groundwater model also needs 3 initial conditions of the soil, the perched reservoir and the deep reservoir. The landslide creep model needs a total of 3 parameters (HT, β, γ) which should be calibrated. The landslide creep model needs also an initial condition for the MCT. This initial condition is taken into account by the coefficient c from the time-series model and is therefore set to 1 in the landslide creep model. The 3 parameters (a, b, c) of the time-series model are determined with a constraint multiple linear regression between the three modelled inputs ($MCT \times WL_c$, MCT and WL_c) and the measured displacement output such that $AB^{-1}=CD^{-1}$ in equation (34). The use of a multiple linear regression allows to avoid the integration of a, b and c from equation (31) and (32) into the calibration process.

4.2.2 The case of modelling multiple displacement records

In case of modelling multiple stations displacement records, the modularity of the model allows adjustment in order to take into account spatial variability. Various strategies may be performed depending on the variability of the landslide behaviour.

With regard to the detrended component: in the case of homogeneous detrended displacement over various measurement sites, the groundwater model can then be assumed to be generic to the whole landslide, leading to use the groundwater model as lumped at the landslide scale. In the opposite case, the groundwater level triggering the landslide destabilisation should be considered to vary according to the station location. In this case, a shift lag has to be introduced in the groundwater model for each zone having a significant detrended component behaviour.

With regard to the trend component: in the case of a displacement trend following the same increasing pattern in various measurement sites, then the landslide creep model can be considered to be generic to the landslide and only the a, b and c parameters of the time-series model have to be estimated with a multiple regression. In the opposite case, then the parameters of the landslide creep model and of the time-series model have to be calibrated separately for each station (HT threshold remains the same for all stations since the location variability is taken into account by the β and γ parameters). In that case, the MCT output of

the landslide creep model is equal to the displacement trend of each station and only the c parameter has to be estimated. The *b* parameter is therefore equal to 1 and constraints of equation (34) become $B=1$ and $A=CD^{-1}$. Lastly, for landslides where no trend can be identified, only the groundwater model is necessary to simulate the displacement.

4.2.3 Calibration periods and optimization

Simulated annealing (Kirkpatrick et al., 1983; Černý, 1985), which is a global optimization method, is implemented to calibrate the model. The displacement trend accentuates the calibration at the end of the interval where amplitudes are higher than average, leading to an unbalanced calibration (under-calibration at the beginning of the interval). This has for consequences that the recent period of the time series is better simulated. In order to disregard the trend influence on the calibration process, the model is calibrated only on the detrended component by removing the modelled trend (Eq. (32)) from the measured and modelled displacements. Moreover, the classical partition into two continuous calibration and validation periods having similar ranges of values appears to be inappropriate. Thus, the definition of the calibration and validation periods is defined differently. The time series is split into constant length intervals which are alternatively assigned to the calibration and to the validation intervals. This set-up allows to have both the calibration and validation intervals spread on the entire variation range. Lastly, to limit the influence of such partitioning as well as to assess the model performance on the whole time series, a split sample test is conducted (Klemeš, 1986). This test considers that each set of calibration intervals should be used in turn for calibration (scenario 1) and validation (scenario 2).

4.2.4 Performance criteria

Three criteria were used to assess model performances: the Nash–Sutcliffe coefficient of efficiency NS (Nash and Sutcliffe, 1970), the Nash–Sutcliffe with logarithmic values NSL (Krause et al., 2005) and the Root Mean Square Error RMSE. The RMSE and the NS indicator are sensitive to extreme values, while the use of NSL allows to give more weight to low values. In the case of modelling multiple displacement stations, calibration with a unique composite performance indicator is required. A weighted mean of the performance criteria is calculated proportionally to the dataset length of each station (NS_m, NSL_m and $RMSE_m$). The NS_m, the NSL_m and the $RMSE_m$ indicators are used to assess the performance for the

detrended displacement (groundwater model) whereas only the $RMSE_m$ indicator is used for the two other components (landslide creep model and time-series model). Indeed, NS and NSL indicators values depend on the time-series mean, and are therefore biased by the long-term trend.

5 Study site

5.1 Geological context

The Séchilienne landslide is located in the French Alps on the right bank of the Romanche river, on the southern slope of the Mont-Sec Massif (Fig. 29). The site is characterized by a mountain climate with a mean annual precipitation depth of 1200 mm. The geological nature of the area consists in vertical N-S foliated micaschists unconformably covered by Carboniferous to Liassic sedimentary deposits. These deposits are distributed along the massif ridge line above the unstable zone. Quaternary glacio-fluvial deposits are also present.

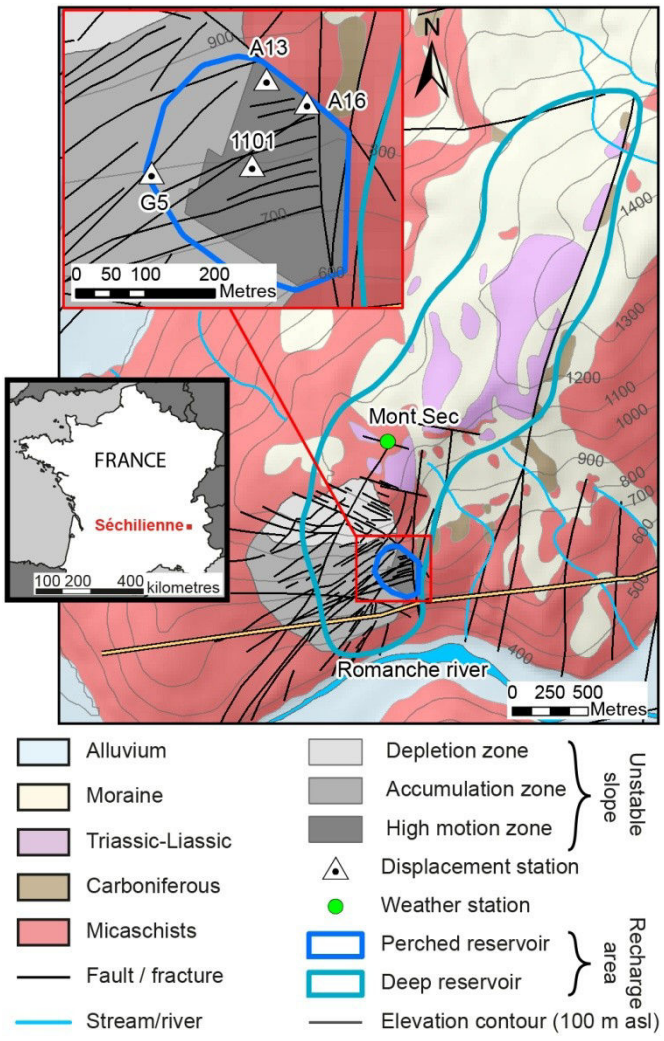

Fig. 29: Séchilienne landslide site map and monitoring network

The Séchilienne landslide is limited eastwards by a N-S fault scarp and northwards below the Mont Sec by a major head scarp of several hundred meters wide and tens of meters high. Rare

geomorphological evidence allows to define precisely the western and southern boundaries of the unstable area. Below the head scarp, between 1100m and 950m asl, a gentle slope zone is in depletion while, between 950m and 450m asl, the slope becomes steeper (>40°) and is interpreted as an accumulation zone (Vengeon, 1998; Le Roux et al., 2011). The area affected by the landslide is estimated to about 1 km^2 (Le Roux, 2009). The slope is cut by a dense network of two sets of near-vertical open fractures trending N110° to N120° and N70° (Le Roux et al., 2011). In the accumulation zone, the dense network of wide and open N70° fractures divides the slope into several vertical compartments. The fractures are filled by colluvium and by clayey material near surface, and change to crushed zones filled with clayed material in depth (Vengeon, 1998; Lebrouc et al., 2013). Additionally, a large number of N50°-N70° fractures dipping near-parallel to the slope are present in the accumulation zone (Vengeon, 1998). In the depletion zone, the N110° to N120° fractures are dominant (Lebrouc et al., 2013).

5.2 Hydro-mechanical background

The Séchilienne landslide is characterized by a deep progressive deformation controlled by the network of faults and fractures. A particularity of the Séchilienne landslide is the absence of a well-defined basal sliding surface. The landslide is affected by a deeply rooted (about 100-150m) toppling movement of the N50° to 70° slabs to the valley (accumulation zone) coupled with the sagging of the upper slope (depletion zone) beneath the Mont Sec (Vengeon, 1998; Durville et al., 2009; Lebrouc et al., 2013). The displacement monitoring shows displacement vectors relatively homogeneous in the direction (N140°) and in dip angles (10° to 20°). Low velocity displacements (2 to 15 cm/yr) are observed for both the depletion and the accumulation zones (Le Roux et al., 2011). These velocities gradually decrease towards the west and south, allowing to define the limits of the unstable area. The unstable mass is estimated between 48 and 63 million m^3 (Le Roux et al., 2011). A very active moving zone, where high displacement velocities about 150 cm/yr are measured, lies within the unstable slope. This zone is responsible for abundant rockfall and its volume is estimated at 3 million m^3.

The landslide shows a higher hydraulic conductivity than the underlying stable bedrock (Vengeon, 1998; Meric et al., 2005; Le Roux et al., 2011), thus leading to a landslide perched aquifer (Guglielmi et al., 2002). Heterogeneous, anisotropic and discontinuous properties of

the landslide lead to a discontinuous perched fractured reservoir. The recharge of the landslide perched aquifer is essentially local, enhanced by the trenches and the counterscarps which tend to limit the runoff and to facilitate groundwater infiltration in the landslide area. However, the hydrochemical analyses of Guglielmi et al. (2002) shows that the sedimentary deposits distributed above the landslide hold a perched aquifer which can recharge the landslide perched aquifer. The fractured metamorphic bedrock beneath the landslide contains a deep satured zone at the base of the slope and an overlying thick (about 100 m) vadose zone. The groundwater flow of the entire massif is mainly controlled by the well developed network of fractures with high flow velocities (up to a few kilometres per day; Mudry and Etievant 2007). The hydromechanical study of Cappa et al. (2014) shows that the deep aquifer can trigger the Séchilienne landslide destabilization. Thus, the Séchilienne landslide destabilisation is likely triggered by a dual-aquifer layer: the landslide perched aquifer and the deep aquifer. Consequently, the Séchilienne landslide is characterized by a good correlation between antecedent cumulative precipitation and average displacements (Rochet et al., 1994; Alfonsi, 1997; Durville et al., 2009; Chanut et al., 2013; Vallet et al., 2014).

5.3 Dataset

5.3.1 Measured meteorological and displacement data

Precipitations are recorded at the Mont-Sec weather station, located a few hundred meters above the top of the disturbed zone (Fig. 29). This station is equipped with rain and snow gauges and gives an estimate of snow melt in water depth using cosmic radiations. Hereafter, precipitation includes rainfall and snow melt.

The Séchilienne landslide is monitored by several displacement stations, managed by the CEREMA Lyon (Duranthon et al., 2003). A variety of techniques (extensometers, radar, infra-red, inclinometers, GPS) is used. In this study, one infra-red (referred to as 1101) and three extensometer (referred to as A16, A13 and G5) stations have been used. 1101, A16 and A13 are located within of the most active unstable zone (Fig. 29). Data are available from 1 September 1992 to 31 August 2013 with record percentages of 87% for A16, 94% for A13, 33% for 1101, 45% for G5 and 100% for the weather station (Table 12).

Table 12: Summary of the meteorological and displacement velocity dataset

Name	Type	From	To	Number of data (days)
A13	Extensometer	01 September 1992	31 August 2013	7182
A16	Extensometer	02 March 1994	30 June 2013	6685
1101	Infra-red	01 January 2006	30 June 2013	2519
G5	Extensometer	15 September 2000	8 July 2013	3614
Mont-Sec	Weather station	01 September 1992	31 August 2013	7671

5.3.2 Meteorological and displacement data processing

The groundwater recharge estimation from precipitation (see section 4.1.1) is based on a soil-water balance method proposed by Vallet et al. (2014) with a soil available water capacity (SAWC) of 105 mm, a runoff coefficient (Rf_{coeff}) of 12.8% and a vegetation coefficient (K_c) varying linearly from 0.777 in winter to 0.955 in summer.

Displacement time series show outliers attributed to instrumentation error or to noise. The outliers are removed if their values exceed a given threshold. The threshold is defined according to the standard deviation and the mean of a moving window and is adjusted manually according to the signal characteristics (threshold = mean +/- manual factor × standard deviation). Two successive windows are used: an annual window (365 days) and a seasonal window (90 days).

The multiplicative method is the more appropriate method to decompose the displacement time-series (detail in section 3.1). The displacement trend is defined by curve fitting of a fifth-order polynomial (parametric trend) for the four displacement stations. The result is a unitless time-series fluctuating around 1, named detrended displacement, with both variance and mean trend removed. The wavelet analysis is performed at a 8-day time step, and high frequencies corresponding to this 8-day period are filtered before applying the model. An example of data filtering using multi-resolution and outliers removing for the A13 extensometer is shown in figure 30.

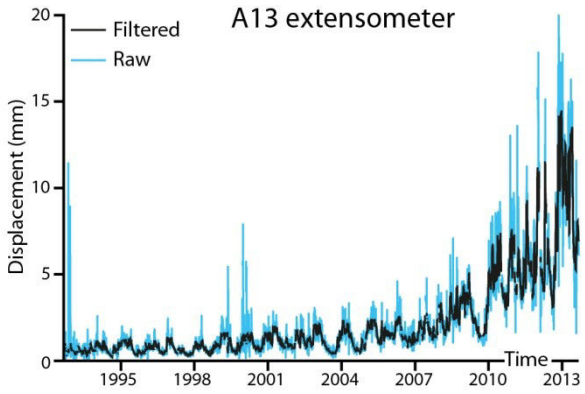

Fig. 30: Example of filtering and outlier removing on the A13 extensometer data

5.4 Model parameterization for the case study

The GLIDE model is calibrated against the displacement stations located on the most active zone (1101, A16 and A13). The data of the G5 extensometer are disregarded because they are characterized by a low signal-to-noise ratio (Fig. 31). The model calibration is implemented according to the results detailed in section 6.1.4. The similarity of the detrended displacements of the four stations leads to use the groundwater lumped model without introducing any shift lag. The different trends observed between the four stations lead to specifically calibrate the parameters of the landslide creep model and the time-series model for each station. For the groundwater model, the soil reservoir parameters are detailed in the section 5.3.2. The recharge area of the deep aquifer (identical to the one of the soil reservoir) and of the perched aquifer are estimated to 3 km^2 and 0.05 km^2, respectively (Fig. 29), according to Guglielmi et al. (2002) and Cappa et al. (2014). The recharge area of the perched aquifer is limited to the high motion zone of the landslide.

In this study, 3 displacement time-series are modelled, involving 23 parameters. 5 parameters are deduced from field measurements, 12 parameters are calibrated and 6 are deduced from multiple linear regressions. Among these parameters, 11 parameters are generic to the three stations (the 10 parameters of the groundwater model and 1 parameter (*HT*) of the landslide creep model) and 12 parameters are specific to the targeted station (4 parameters per station of which 2 are deduced from the multiple linear regression). A warm-up period of 1 year is applied in order to consider that the simulated results are independent from the initialization bias. Initial conditions of the warm-up period for the soil, perched and the deep reservoir are set by default at 50% of *SAWC* maximum, $Overflow_p$ and $Overflow_d$ respectively. The

groundwater model requires 5 parameters (k_p, k_c, $Overflow_p$, $Overflow_d$ and α) to be calibrated. The landslide creep model *HT* parameter remains the same for the three targeted stations while the β and γ parameters, accounting for local variabilities, are calibrated specifically. Similarly, the time-series model parameters (a, c) are deduced from the multiple linear regression for each target station. At Séchilienne, the b parameter is equal to 1 (see section 4.2.2).

The performances of the numerical model are analysed with a sensitivity analysis of the performance indicators from week (8 days, minimum imposed by the use of displacement data filtered at 8 days) to month (31 days) time-step windows. Two-year periods were alternatively assigned to the calibration and to the validation intervals.

6 Results and discussions

6.1 Hydro-mechanical processes

This section aims at characterizing the hydro-mechanical processes investigating input-output relationships using wavelet analysis on rainfall and displacement time series.

6.1.1 Input

Precipitation and recharge time series are plotted in figure 31. Precipitations show low seasonal variations with winter months drier than the rest of the year likely due to water storage in the form of snow cover. On the contrary, the recharge signal shows a high seasonal contrast (dry summer *vs.* wet winter). The recharge signal is clearly influenced by atmospheric temperature variations through evapotranspiration processes. The precipitation and the recharge signals do not show any trend and the amplitude of the seasonal variations remains constant over the whole time series.

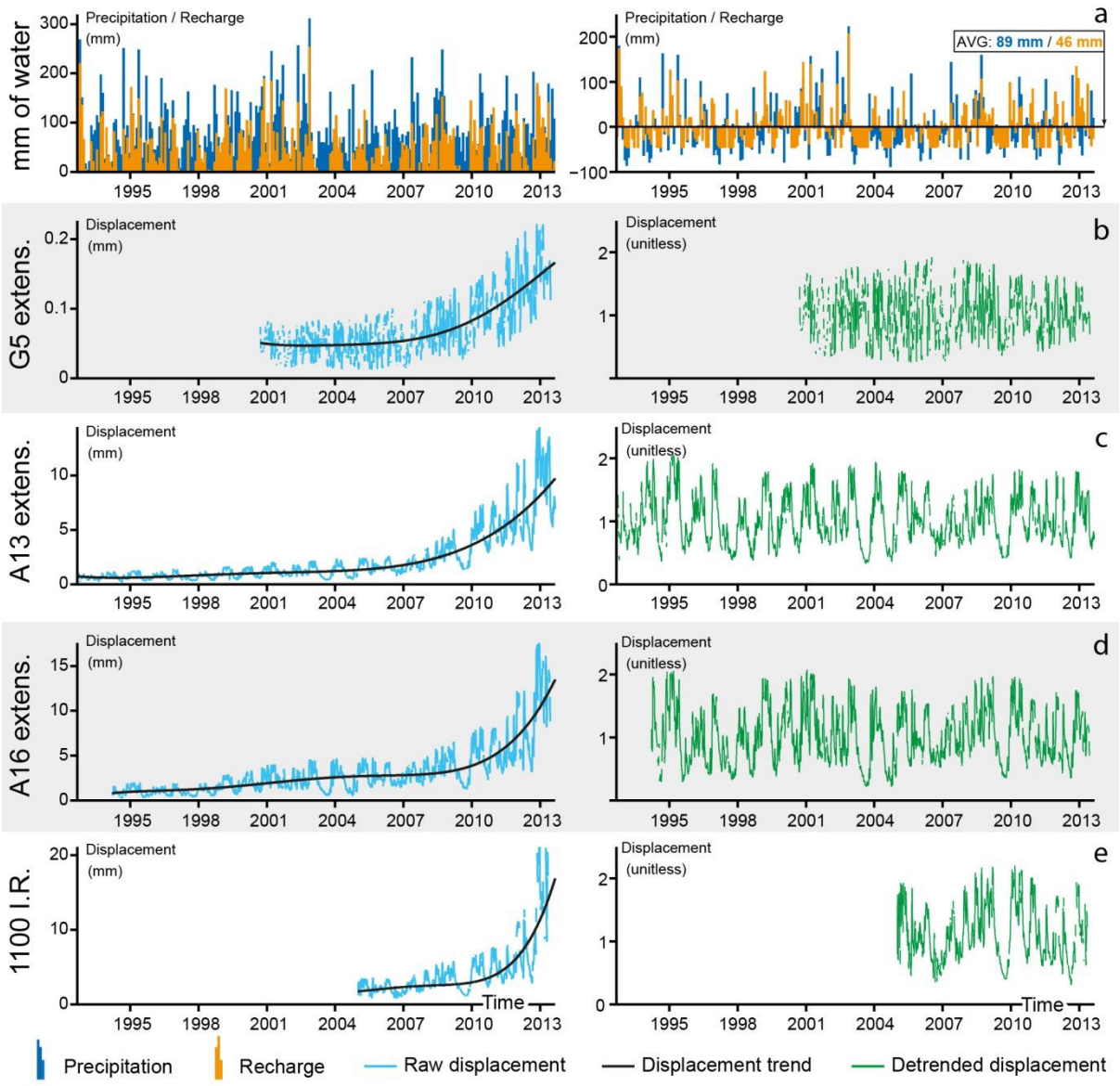

Fig. 31: Input and output dataset. (a) Input: monthly precipitation and monthly recharge. (b, c, d, e) Output: filtered displacement data with raw signal and trend and detrended signal

The CWT of precipitation plotted in figure 32a shows numerous high frequencies to monthly structures (less than 64 days) mostly during winter periods. Some abnormally wet years even show consistent seasonal structures (64-128 day period) during the 1994, 1995, 1999, 2002, 2005, 2008, 2011 and 2012 winters. One-year structures can be identified from 2002 to 2004 and from 2008 to 2010, which are the years with the highest monthly rainfall depth. Lastly, a 5-year component is observed, reflecting a clear variation in large-scale precipitation distribution. The CWT of recharge (Fig. 32b) is similar to that of precipitation, but structures are almost missing during summer months. It leads to a more pronounced power contrast in the scalogram, generating spread structures. Moreover, one-year structures for recharge,

matching with wetter years, are more developed and more regular over the time series than those for precipitation signal.

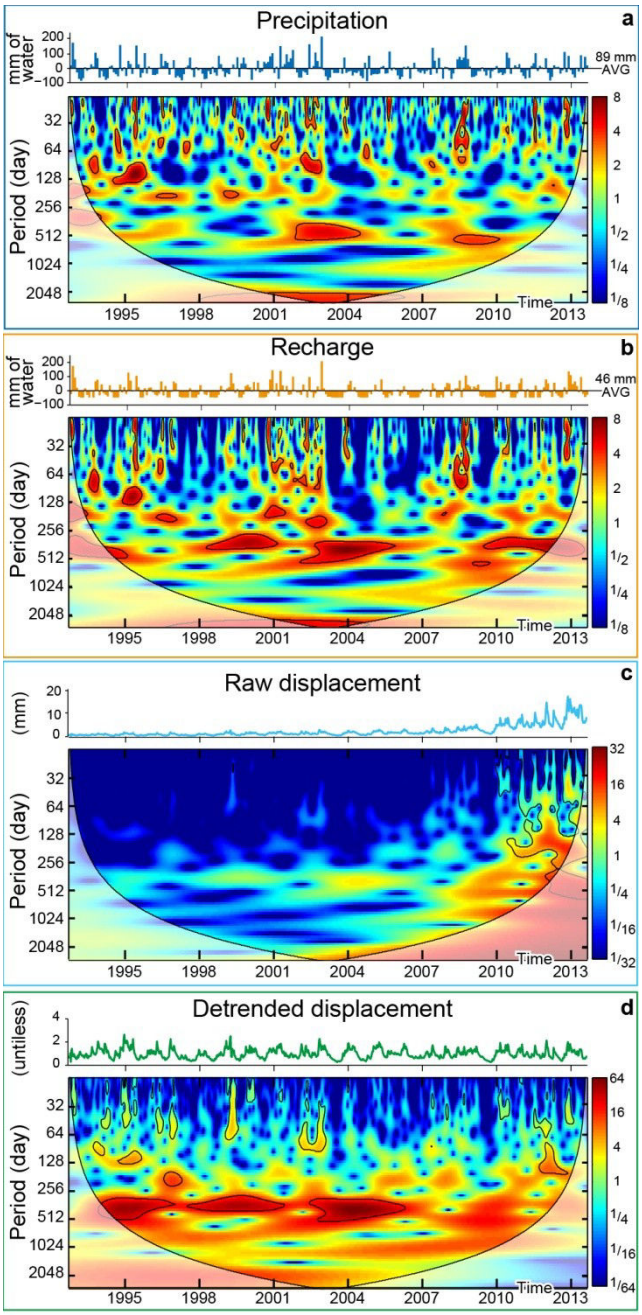

Fig. 32: Continuous wavelet power spectra of (a) precipitation, (b) recharge, (c) A13 raw displacement and (d) A13 detrended displacement. The thick black line designates the 5% significance level against red noise. The cone of influence, whose edge effects might distort the picture, is shown by using attenuated colour intensities

6.1.2 Output

Long-term displacement time series, plotted in figure 31, show that displacement rates and amplitudes increase significant with time from 2008 (Fig. 31). The displacement time series show an exponential growth, with the amplitude of the infra-annual variations growing with the mean of the series. Although the G5 extensometer is located in a less active zone, the trend is also observable, meaning that the creep process affects the whole landslide. However, the observed trends for the four displacement stations have a significantly different increasing pattern (Fig. 31). The detrended displacement time-series of the four displacement stations show sharp seasonal variations with the lowest values in summer and the highest values in winter (Fig. 31), within a relatively constant range of values over the years. The seasonal variations of the four stations show synchronous peaks and troughs, meaning that the hydro-mechanical response at the infra-annual scale is homogeneous over the most active zone of the landslide.

Since the four displacement data series show similar patterns and since A13 has the widest recording period, results of the wavelet analysis are only presented for the extensometer A13. The CWT for A13 is performed for the raw displacement and for the detrended displacement (Fig. 32c and 32d). The CWT of A13 raw displacement (Fig. 32c) shows a weak power until 2008. From 2010 to 2013, low-power high frequencies structures (<64 days period) gradually increase in number, in power and in period. A scale-dependent structure for a 8 day to 1-year period is observed, highlighting the multi-scale distribution of energy over the more recent years. This scale effect reveals that the landslide destabilisation becomes more sensitive to the triggering factor. The CWT of the detrended displacement of A13 (Fig. 32d) shows a very different scalogram. Low-power erratic structures are observed at the infra-annual scale, whereas most of the power is located at the annual scale through regular structures which appear concomitant with those highlighted in the recharge signal.

6.1.3 Input-output relationship

Relationships between the various signals are investigated using XWT and WTC. The figure 33 presents cross-scalograms between precipitations and recharge (input signals) and detrended displacements (output signal). The XWT between precipitation and detrended displacement (Fig. 33a) highlights numerous weekly to seasonal structures that are irregularly

connected and distributed (8-128 days). This pattern matches with one-time high water inputs during wet years. A discontinuous structure on the 1-year band (256-512 days period) is also displayed. Unlike for infra-seasonal structures, no significant coherence is observed for annual structures on the WTC although XWT shows high power. This analysis shows that precipitations and displacements are correlated in the infra-annual scale only, scale at which the power for the displacement signal is the lowest. XWT between recharge and detrended displacement (Fig. 33b) shows identical coherent structures in the infra-annual scale. However, structures in the 1-year band are more widespread and more connected. A significant coherence appears throughout the time-scale space, suggesting strong relationships between recharge and detrended displacement time series at all scales. It shows that the recharge signal is correlated to displacements over the whole time-frequency space.

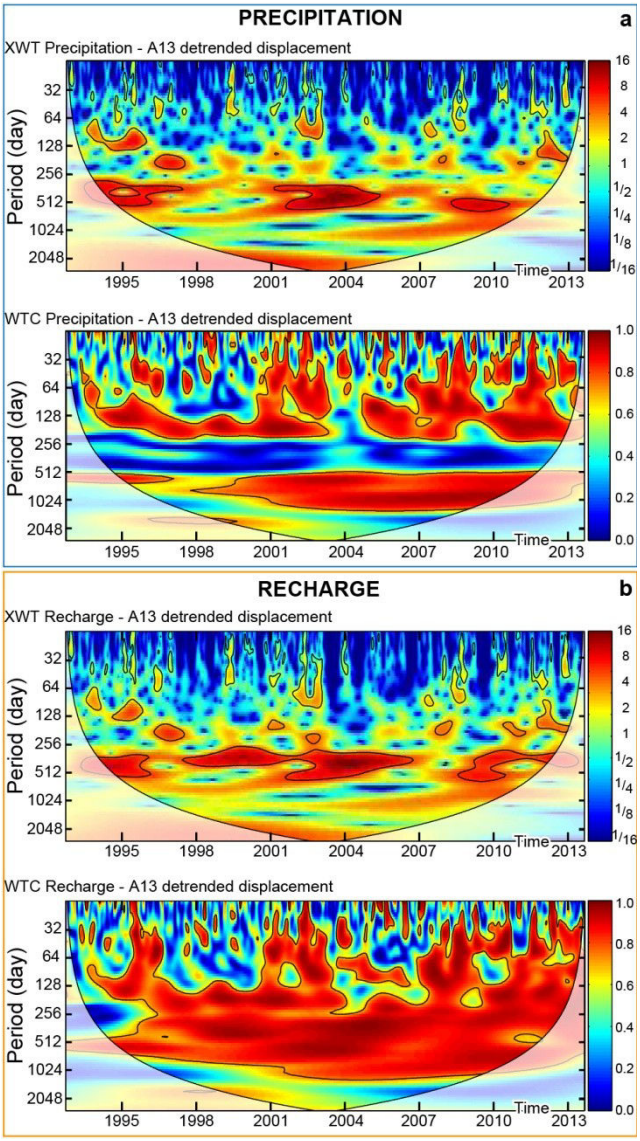

Fig. 33: Cross wavelet (XWT) and wavelet coherence (WTC) spectra with (a) precipitation and A13 detrended displacement and (b) recharge and A13 detrended displacement. The thick black line designates the 5% significance level against red noise. The cone of influence, whose edge effects might distort the picture, is shown by using attenuated colour intensities

6.1.4 Discussion of the groundwater functioning and modelling constraints

The analysis of the input-output relationships shows that annual variations of the detrended displacement are better explained by the recharge signal than by the precipitation signal. It appears that the infra-annual detrended displacement results of one-time high precipitation events (for both precipitation and recharge signals) whereas annual and multi-annual variations, for which most of the variability is observed, are rather linked to recharge and thus to groundwater processes. Consequently, we may assume that two recharge types occur. The periodic variations of the Séchilienne displacement seem to be triggered by a dual-

groundwater layer with a perched (reactive aquifer responsible of high frequency displacements) and a deep aquifer (inertial aquifer responsible of low frequencies of displacement).

Unlike the observed exponential trend on the amplitude and on the mean for the four displacement stations, the meteorological data series does not show any trend over the year. The trend on amplitude is the consequence of a sensitivity increase of the landslide to rainfall triggering impulses, whereas the trend in mean is not directly dependent on rainfall, accounting for the unstructured state of the landslide. The trend in mean is interpreted as a long-term modification of the landslide mechanical properties (rock weakening), consequence of a long-term creep deformation mechanism.

In order to verify the main hypotheses about the hydrological processes highlighted above, a new modelling approach adapted to the overall framework summarized hereafter is needed. The groundwater model should be a two-layer aquifer model with a reactive perched aquifer and an inertial deep aquifer is needed for Séchilienne. This pattern is coherent with the conceptual groundwater model of Guglielmi et al. (2002). In addition, the detrended displacements of the four stations show synchronous seasonal variations with regular amplitude, meaning that the groundwater process responsible of the destabilisation can be considered to be homogeneous at the Séchilienne landslide scale, leading to use the model as lumped for groundwater processes. The displacement trends indicate that the Séchilienne landslide is subject to a non-linear deformation, showing a standard creep deformation curve that cannot be directly related to the precipitation/recharge input. The four displacement stations show significantly different growing patterns on their trends. This spatial variability has to be taken into account in the model. To predict the Séchilienne displacement with only the precipitation time-series, the model must simulate the two identified components: seasonal variations and long-term creep trend. The GLIDE model fulfils these conditions and is applied for Séchilienne.

6.2 Results and implication of the GLIDE model

6.2.1 Modelling performance

The figure 34 shows the evolution of the performance criteria according to the computation step from 8 to 32 days. The figure 35 illustrates the ability of the model to reproduce observed

data for a computation step of 8 days. The model parameter values estimated for the scenario 1 (S1) and 2 (S2) are detailed in Table 11.

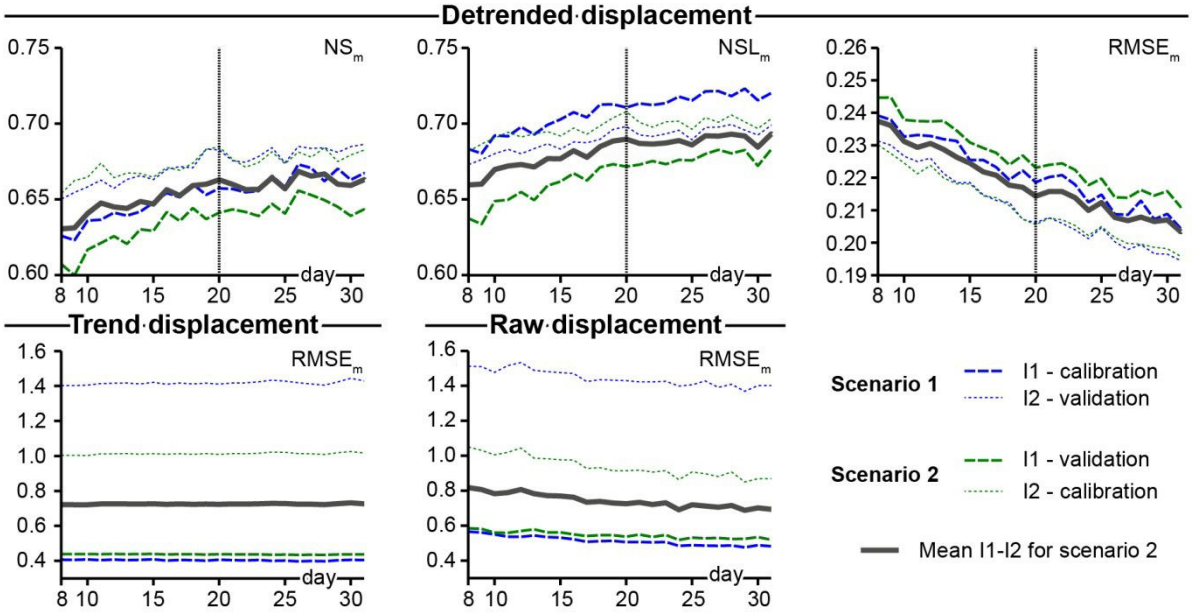

Fig. 34: Evolution of model performances according to a computation time from 8 to 30 days for the two scenarios S1 and S2

Regarding the detrended displacement, S1 shows a better performance than for S2 in taking into account the performance on both calibration and validation periods (Fig. 34). For the three performance criteria, a time-step above 20 days (average break point) does not improve significantly the model performances. Above this break point, NS_m and NSL_m are always larger than 0.65 and 0.67 respectively and $RMSE_m$ are lower than 0.23 (Fig. 34). The model shows similar performance for the displacement trend and for raw displacement. For the two scenarios, the performances are always significantly better on the interval I1 than on the interval I2 (Fig. 34), with the $RMSE_m$ indicator always lower than 1.5 mm/d for the displacement trend and raw displacement. The performance of S2 is distinguishable from S1 for the I2 interval with a $RMSE_m$ lower than 1 mm/d, meaning that the RMSE criterion is sensitive to the calibration interval. The I2 interval covers periods for which the detrended displacement shows higher values (peaks) than the interval covered by the I1 interval. Contrarily to the detrended displacement, the computation time step does not significantly influence the performance of the model for the trend and raw displacement and no average break points are observed.

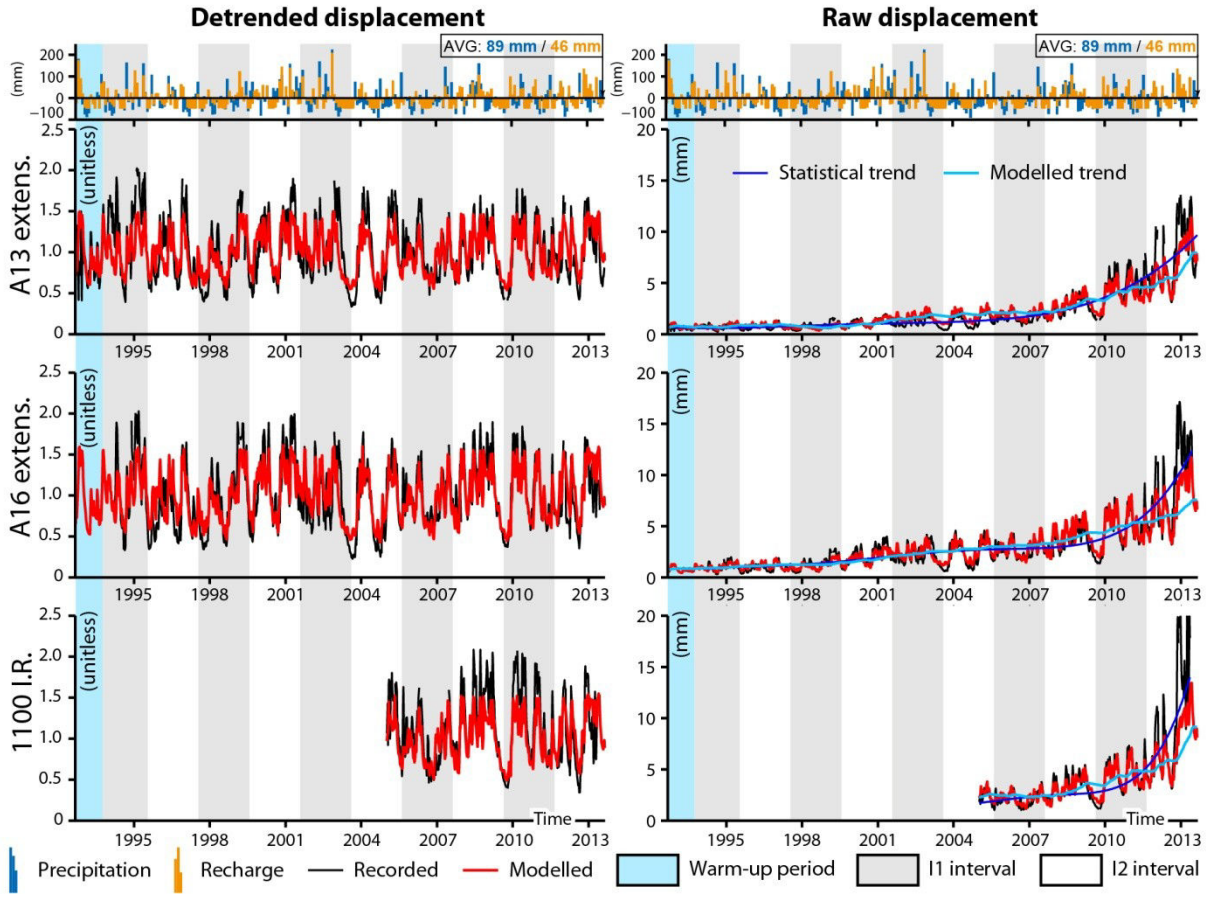

Fig. 35: Simulations of the three displacement recording stations and of the three displacement components (trend, detrended and raw signals) for an 8 days computation time

The following discussion is based on the results from the modelling for S2 which shows the best performance to model the raw displacements. According to figure 35, the modelled detrended displacements reproduce satisfactorily the dynamics of the displacement time-series variation. In particular, peaks and troughs are synchronously simulated, as well as their increasing and decreasing slopes. However, the model fails to reproduce several extreme values (as indicated by the better performance of the NSL_m indicator than that of the NS_m indicator, Fig. 34). The modelled raw displacement fits well the creep trend over most of the studied interval except the last part where the model underestimates the exponential increase (Fig. 35). The calibration process by the mean of the $RMSE_m$ values is significantly dependent on the creep trend (see section 4.2.3), meaning that the model in order to be accurate should be calibrated over the last part of the trend.

The failure of the model to reproduce the exponential trend part can be the consequence of two phenomena: (1) the control mechanism of the landslide destabilisation becomes mainly

driven by the landslide weight to the detriment of the groundwater pressure, or (2) the stress-strain relationship is deeply modified by the rearrangement of the landslide constitutive material. During the summers of 2012 and 2013, the Séchilienne landslide showed a sharp decrease of the displacement velocity (Fig. 35), meaning that the rainfall trigger is still required to accelerate the landslide. Nevertheless, for these two dry periods, the landslide velocities did not return to normal level (i.e., before the exponential growing). These observations support the second assumption involving indirect hydro-mechanical coupling, i.e. a mutual influence between mechanical and hydraulic processes through changes in landslide constitutive material properties (Rutqvist and Stephansson, 2003).

6.2.2 Relationship between groundwater pressure and creep deformation

Applied to the Séchilienne landslide, the GLIDE model is able to simulate displacement short-term periodic variations as well as the displacement long-term creep trend. Thus, the hydromechanical functioning hypotheses are validated. The model shows that the long-term creep deformation mechanism is mainly the consequence of groundwater pressure recurrent variations. Moreover, despite the exponential increase, the Séchilienne landslide destabilisation is not independent from the precipitation trigger. The creep trend is a consequence of an indirect hydro-mechanical coupling which modifies the stress-strain relationships.

Model parameter values can give insights about the hydromechanical mechanisms they account for and can improve the conceptual groundwater model. The hydraulic threshold *(HT)* corresponds to the 46% percentile of the water-level composite *(WL_c)*, meaning that the weakening of the Séchilienne landslide occurs over 46% of the studied interval time. The reservoir recession coefficients, representative of the aquifer permeability, show that the disturbed zone in the perched aquifer has a higher transmissive behaviour *(k_p* = 0.11) than the undamaged bedrock in the deep aquifer *(k_d* = 0.03). This contrast agrees with the occurrence of a reactive perched aquifer in the disturbed zone (Guglielmi et al., 2002). The α triggering coefficient, used to compute the WL_c from the perched *(WL_p)* and the deep *(WL_d)* water-levels, shows that the Séchilienne destabilisation is triggered at 77% by the deep aquifer and 23% by the perched aquifer, while the contribution areas are 98% and 2%, respectively. This result confirms the dual influence of the two-layer hydrosystem on the destabilisation. This result also shows that the perched aquifer, despite its small surface area, plays a significant role in

the destabilisation. However, the main destabilization triggering role still lies in the deep aquifer, in agreement with Cappa et al (2014).

The a parameter estimates the periodic groundwater triggering impact on the destabilisation for the three stations (A13: 0.37, A16: 0.44 and I1101: 0.44). The rock weakening coefficient β allows to estimate relatively the weakening amount for each station (A13: 1.20×10^{-3}, A16: 7.01×10^{-4} and I1101: 1.51×10^{-3}). The rock strengthening coefficient γ estimates the consolidation rate for each modelled station (A13: 9.72×10^{-4} mm/d, A16: 2.44×10^{-4} mm/d and I1101: 1.28×10^{-3} mm/d). Low γ values ($<10^{-3}$ mm/d) mean that periods at rest are better characterized by the absence of weakening processes rather than by physical consolidation. The A13 extensometer is the least influenced by the groundwater pressure whereas the 1101 infra-red station is the most influenced by the changes of the mechanical properties of the constitutive material showing the higher weakening and strengthening coefficients. The extensometer A16 shows the lowest strengthening coefficient γ but this station is reactive to the periodic groundwater stress since it shows the highest α coefficient. The differences between the three stations confirm that local mechanical properties affect significantly the surface deformation and the creep process.

6.2.3 Warning system ability

The GLIDE lumped model fulfils the requirement to adhere to the concept of requisite simplicity (Stirzaker et al., 2010), balancing technical accuracy with utility for operational implementation as a warning system. However, the ability of the model to be used in an operational early warning system has to be assessed by performing a forecasting procedure such as the one proposed by Bernardie et al. (2014). Although the model performances for the most recent intervals are not as good as those for the former intervals, it does not mean that the model is not reliable for displacement prediction. Indeed, this study models the precipitation/displacement relationship with the aim of improving the understanding of creep deep-seated landslide functioning. For this purpose, the calibration of the model is performed independently of the trend (see section 4.2.2). For prediction purpose, in the framework of an early warning system, it would be relevant to calibrate the model against the raw displacement, i.e. by taking into account the trend influence, which will considerably reduce the error on the prediction of future values.

7 Conclusion

The aims of this paper are (i) to characterize hydro-mechanical processes by investigating precipitation-displacement relationships using a wavelet analysis and, (ii) to develop a lumped model (GLIDE) to simulate displacement for landslides subject to creep deformation. First, the wavelet analysis applied on raw and detrended dataset allows to define a first conceptual model that shows that the infra-annual detrended displacement results from one-time high precipitation events. Conversely, annual and multi-annual variations, where most of the displacement variability is observed, are rather linked to recharge and thus to groundwater processes. Our approach demonstrates the relevancy of wavelet analysis in characterizing the non-linear creep processes for landslides. Second, the GLIDE model, coupling a groundwater model to a creep landslide model built on this preliminary model, shows good performances to simulate the decomposed displacement time series into trend and detrended displacement, validating the functioning hypothesis.

The main insights of this study are that (i) the Séchilienne landslide displacement periodic variations are triggered by a dual groundwater layer, with a perched reactive aquifer (responsible of high frequency displacements) and a deep inertial aquifer (responsible of low frequencies of displacement), and that (ii) although the displacement trend cannot be directly related to the precipitation input, the trend is the consequence of rock mechanical weakening due to recurrent groundwater pressure variations. These results show that the long-term creep deformation is mainly the consequence of the recharge input. As a perspective, the good performance of the GLIDE model shows that the model is suitable for predicting displacement in the framework of an operational early-warning system at the conditions that a forecasting procedure is implemented.

Acknowledgments

This research was fund by the program SLAMS (Séchilienne Land movement: Multidisciplinary Studies) of the Agence Nationale de la Recherche. The meteorological and displacement data were supplied by CEREMA Lyon. The authors acknowledge the support of Jean-Pierre Duranthon and Marie-Aurélie Chanut from the CEREMA Lyon.

CHAPITRE IV : DÉTERMINATION MULTI-DIMENSIONNELLE D'UN SEUIL STATISTIQUE D'ACTIVATION DE LA DÉSTABILSATION BASÉE SUR LA RECHARGE ET LES MACHINES À VECTEURS DE SUPPORT

DETERMINATION OF A MULTI-DIMENSIONNAL STATISTICAL RAINFALL THREHSOLD FOR CONTINUOUSLY MOVING DEEP-SEATED LANDSLIDES BASED ON GROUNDWATER RECHARGE AND SUPPORT VECTOR MACHINES

Vallet A.[1], Varron D.[2], Bertrand C.[1], Mudry J.[1], Fabbri O.[1]

[1] UMR6249 Chrono-Environnement - Université de Franche-Comté - 16 route de Gray - F-25030 Besançon cedex - France

[2] UMR6623 Laboratoire de Mathématiques de Besançon - Université de Franche-Comté - 16 route de Gray - F-25030 Besançon cedex - France

1 Résumé du chapitre IV

Les systèmes d'alerte des mouvements de terrain sont fondés sur la surveillance de diverses données relatives à la déstabilisation du versant. Cependant la prédiction des phases de déstabilisation dans le cadre d'un système d'alerte précoce nécessite un outil basé sur les précipitations. La capacité de prédiction est rendue possible grâce aux prévisions météorologiques. Le seuil d'activation pluviométrique (rainfall threshold) est une méthode largement utilisée pour les mouvements de terrain peu profonds. Cette méthode permet d'identifier les conditions pluviométriques qui ont causé une déstabilisation du versant. A notre connaissance, aucune tentative de définir un seuil d'activation pluviométrique à un mouvement de terrain profond n'a été entreprise avec succès, en raison de la relation complexe qui existe entre les précipitations et la déstabilisation. Le chapitre III a montré que les variations périodiques et la tendance pluriannuelle des vitesses de déplacement mesurées sur l'instabilité de Séchilienne peut s'expliquer uniquement avec les données de précipitations. La détermination d'un seuil d'activation pour l'instabilité de Séchilienne est donc particulièrement pertinente.

Le but de ce chapitre est de développer une approche objective pour la détermination d'un seuil d'activation pluviométrique pour les mouvements de terrain profonds. La nouvelle approche se base sur la recharge (calculée d'après la méthode du chapitre II) et sur une définition multi-dimensionnelle des conditions pluviométriques. Cette nouvelle approche est comparée à la méthode classique basée sur les précipitations et à une définition à "deux dimensions" des conditions pluviométriques (Fig. 36 et 37). La méthode est constituée de deux parties indépendantes qui peuvent être utilisées en association ou séparément, selon les exigences de l'utilisateur et en fonction des contraintes du site qui sont : (1) l'identification semi-automatique d'événements stables/instables basée sur les séries chronologiques de vitesses de déplacement (Fig. 38) et (2) la détermination d'un seuil d'activation multi-dimensionnelle basée sur un classificateur mathématique (machines à vecteurs de support SVM). La démarche semi-automatique adoptée pour la détermination du seuil d'activation permet une intégration opérationnelle facilitée dans un système d'alerte.

La combinaison du seuil d'activation multi-dimensionnelle (Fig. 43) avec la méthode semi-automatique de détection d'événement (Fig. 42) développée dans cette étude montre des

performances élevées et permet une définition objective et optimale du seuil. En plus d'optimiser les temps de calcul, de ne nécessiter aucune hypothèse préalable et d'avoir une mise en œuvre entièrement automatique, l'approche multi-dimensionnelle montre des performances similaires à l'approche bidimensionnelle classique (Fig. 44). L'approche multi-dimensionnelle permet aussi d'identifier la période qui maximise la discrimination des événements stables et instables. Enfin, cette étude montre que la recharge est un paramètre important à prendre en compte pour les mouvements de terrain profonds. En effet, l'utilisation de la recharge au lieu des précipitations permet d'améliorer significativement les performances du seuil d'activation (Fig. 45). Les performances et la simplicité du seuil multi-dimensionnel en font un outil opérationnel approprié pour un système d'alerte. Les probabilités estimées avec la méthode SVM permettent de concevoir un seuil de précipitations ajustable qui peut s'adapter aux critères spécifiques d'un système d'alerte multi-niveaux (Fig. 46).

2 Introduction

The determination of a rainfall threshold is a widely used method for estimating the minimum critical rainfall amount which may result in slope failure (Wilson and Wieczorek, 1995; Terlien, 1998; Vita et al., 1998; Wieczorek and Guzzetti, 1999; Iverson, 2000; Aleotti, 2004; Guzzetti et al., 2008; Frattini et al., 2009). This tool, first established by Caine (1980), is mainly used for shallow landslides. Rainfall thresholds can be defined either by an empirical (statistical) or by a deterministic (physical-based) approaches, at local or at regional scales. The rainfall threshold identifies the boundary which separates rainfall conditions which do or do not cause slope destabilization. Although landslide warning systems can be based on various data (landslide displacement velocity, microseismic activity monitoring, rockfall, etc), only rainfall thresholds allow predictions to be made, due to the availability of weather forecasts. This association reinforces the prominent role that rainfall thresholds play in slope failure alert system.

Elevated pore water pressure, induced by the recharge of groundwater hydrosystems, is one of the main triggering factors of deep-seated landslides (Iverson, 2000; Rutqvist and Stephansson, 2003; Bogaard et al., 2007; Bonzanigo et al., 2007). However, the relationship between groundwater level and destabilization rate is complex for deep-seated landslides (Rutqvist and Stephansson, 2003; Binet et al., 2007a; Berti et al., 2012). In addition, for deep-seated landslides involving groundwater flow, the groundwater recharge, rather than precipitation, is a relevant parameter to consider (Vallet et al., 2014). Lastly, the identification of stable and unstable events, on which the rainfall threshold definition is based, is difficult for continuously moving landslides. To the best of our knowledge, no attempts to define an empirical rainfall threshold to a deep-seated landslide (>100m) have been successfully undertaken (Zhang et al., 2006).

Most studies dealing with rainfall thresholds are biased since thresholds are usually determined visually or with poor mathematical or statistical bases (Guzzetti et al., 2007). In addition, the identification of the stable or unstable events as well as the associated rainfall conditions mainly resort to subjective decisions (Terlien, 1998; Segoni et al., 2014). An objective definition of the threshold, which minimizes false positive or negative occurrences, is fundamental to integrate rainfall thresholds as warning system tool.

The aim of this study is to develop an objective approach for the determination of a statistical rainfall threshold for deep-seated landslides. The determination is based on the estimation of recharge and on the definition of a multi-dimensional rainfall threshold definition. This new approach will be compared with precipitation and with a classical 'two-dimensional' rainfall threshold. The developed method is designed to be semi-automatic, ensuring an easy integration into a landslide warning system. It is based on a daily time step and consists in two independent parts which can be used together or separately, according to the user's requirements and according to the site constraints. These two parts are: (1) a semi-automatic identification of stable/unstable events based on displacement velocity time series and (2) a determination of multi-dimensional rainfall threshold based on support vector machines (SVM), a linear classifier related to the statistical learning theory (Fig. 36).

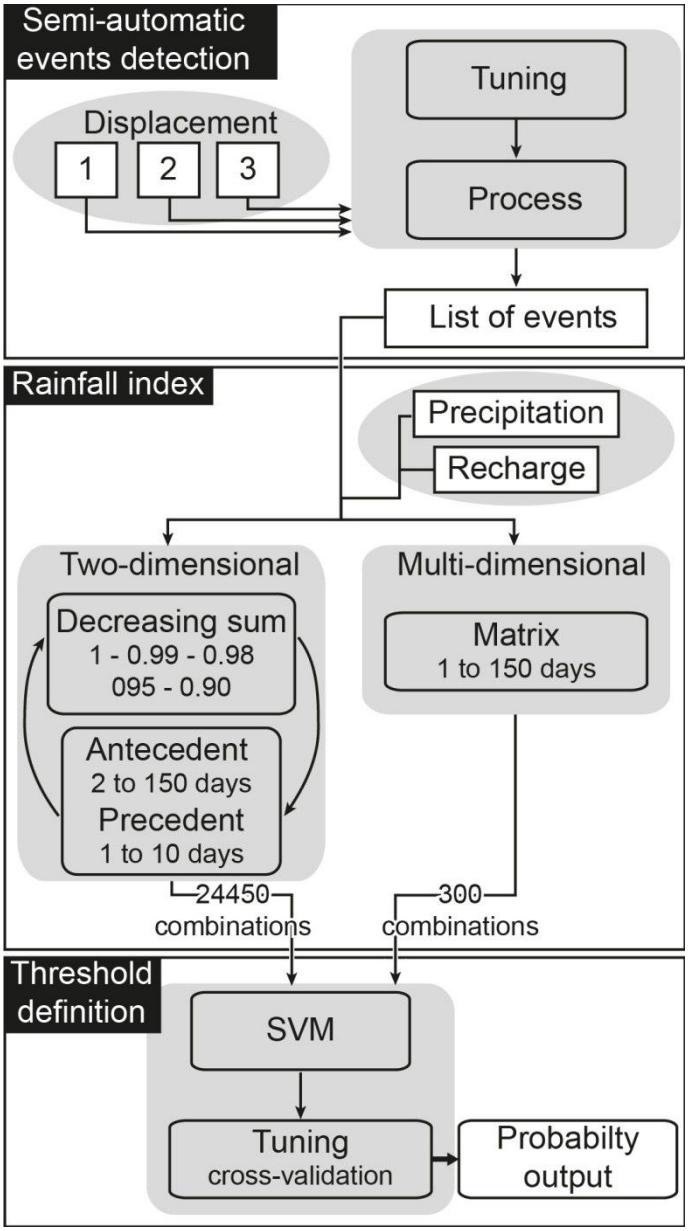

Fig. 36: Workflow of the method to determine the rainfall threshold for the two-dimensional (section 5.1) and the multi-dimensional (section 5.2) approaches, based on precipitation or recharge estimates. The rainfall threshold is defined using the Support Vector Machines (SVM) method (appendix A) of which the list of events is determined by a semi-automatic event detection method (section 4)

3 Strategy for the definition of an optimal and objective rainfall threshold suitable for deep-seated landslides

The rainfall threshold quantifies the minimal rainfall conditions that should trigger slope destabilization. The definition of the rainfall threshold is based on a historical inventory either of only unstable events (so-called one-class label threshold) or of both stable and unstable events (so-called two-class label threshold). For any event, the rainfall conditions, also referred to as the rainfall index, are classically based on two parameters. As such, the classical index is referred to as a two-dimensional index. The literature presents various combinations of indexes (Guzzetti et al., 2007, 2008), among which the most used are rainfall intensity and duration, or daily rainfall and antecedent rainfall. The selection of the rainfall index depends mainly on the landslide settings (landslide type, climate conditions, geomorphology, etc).

3.1 Rainfall threshold in the case of deep-seated landslides

The complex structural geology and the complex groundwater hydrodynamics of deep-seated landslides generally involve complicated hydro-mechanical relationships between precipitation and deformation (Terlien, 1998; Cappa et al., 2004; Binet et al., 2007a; Berti et al., 2012). For deep-seated landslides, threshold deterministic approaches based on hydro-mechanical models are difficult to implement and to calibrate due to the scarcity or absence of measured hydrodynamic parameters such as groundwater levels or spring flows in the disturbed areas (Guzzetti et al., 2007). Therefore, in the case of large amounts of available data, the definition of a statistical local threshold (specific to a landslide) is preferred since it can implicitly take into account these relationships (Guzzetti et al., 2007). The statistical threshold method is an efficient method in which the rainfall threshold can be simply and unambiguously determined from the data and does not require extensive investigations. In addition, there is no need for an *a priori* knowledge of the hydro-mechanical behaviour of the landslide to propose valid predictions. Using a statistical approach rather than a deterministic approach provides a truly objective method for the stakeholders managing the warning system.

Geomorphological, geological and hydrogeological characteristics play key roles in the destabilization of deep-seated landslides (Peruccacci et al., 2012). In addition, although the

deep-seated landslide destabilization is mainly controlled by a rainfall trigger (short-term component), site-specific time-dependent factors (long-term components) such as creep deformation or slope groundwater hydraulic connectivity modifications can also be significant (Rutqvist and Stephansson, 2003; Corominas et al., 2005; Berti et al., 2012). For these reasons, global thresholds are not suitable for landslides which are strongly influenced by site factors other than the rainfall trigger. In these cases, a local threshold which implicitly takes into account the landslide characteristics is more adequate (Guzzetti et al., 2008)

The inertia and the buffering hydraulic properties of the groundwater reservoir triggering the deep-seated landslide destabilisation can significantly smooth short-term fluctuations such as the intensity or the duration of rainfall events (Terlien, 1998; Van Asch et al., 1999; Nafarzadegan et al., 2012). The landslide aquifer hydrodynamical response is therefore more influenced by the antecedent rainfall which takes into account multiple rainfall events over a long period than by a single rainfall event (Martelloni et al., 2012). Therefore, the commonly used daily rainfall-antecedent rainfall index is more suitable for deep-seated landslide studies. The daily rainfall amount can be replaced by a period not necessarily limited to one day, named hereafter precedent rainfall amount (Fig. 37a). This choice is justified by the fact that a single rainfall day will not have a significant influence on destabilization for a large deep-seated landslide. Lastly, Vallet et al. (2014) showed that the recharge is a more suitable parameter than the precipitation to be considered for deep-seated landslides. The recharge is therefore a relevant parameter to take into account to establish a rainfall threshold.

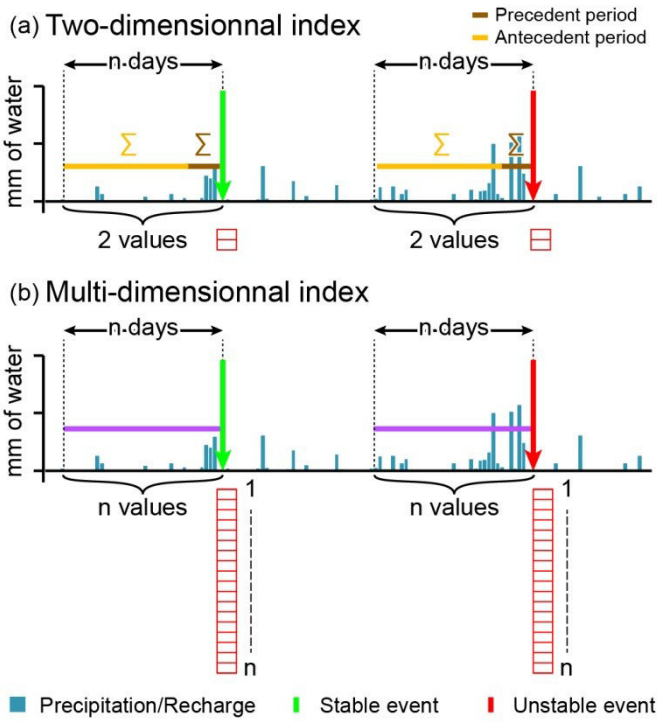

Fig. 37: Method of determination of the rainfall indexes in the case (a) of two-dimensional approach and (b) of multi-dimensional approach

3.2 Rainfall conditions: from two-dimensional to multi-dimensional rainfall index

Classically, rainfall threshold are determined with a two-dimensional rainfall index. For deep-seated landslide, the definition of the two-dimensional rainfall index requires the choices of the cumulative method (decreasing or conventional sum, decay method and decay factor) and of the period extent (Terlien, 1998). These choices are subjective and may depend on the actual knowledge of the landslide-rainfall relationship, with the possibility of missing the best combination (among the numerous possible combinations), that is the combination which maximizes the discrimination between stable and unstable events. The proposed multi-dimensional method is based on a multi-dimensional rainfall index (MDI). The MDI is built for each identified event, whatever stable or unstable. The index dimension is the number of days of the period preceding the event, the rainfall amount of each day being a dimension of the MDI (Fig. 37b). This approach allows an objective determination of the rainfall conditions associated to an event. It however requires a mathematical tool able to classify multi-dimensional datasets.

3.3 Mathematical classifier tool for an optimal definition of the rainfall threshold

Recent studies (Guzzetti et al., 2007; Brunetti et al., 2010; Berti et al., 2012; Peruccacci et al., 2012) have determined an optimal rainfall threshold using Bayesian statistical approaches or frequentist methods which, in addition to threshold identification, allow an estimation of landslide failure probabilities. The probability estimates are a great advantage for threshold definition where data quality and rainfall-displacement complex relationships can lead to significant uncertainties (Berti et al., 2012). Moreover, precipitation is not the only factor that causes destabilization or failure (Aleotti and Chowdhury, 1999). A probabilistic approach allows to take into account the uncertainties in the rainfall-destabilization relationship.

The Bayesian approach was tested in recent studies (Guzzetti et al., 2007; Brunetti et al., 2010; Berti et al., 2012). However the Support Vector Machines method (SVM classifier), a supervised learning method, is chosen here to determine the optimal rainfall threshold. The SVM classifier is characterized by a higher accuracy than other classifying methods (Ben-Yacoub, 1999; Huang et al., 2003). Furthermore, the SVM classifier is a widely available tool on various software platforms (Ivanciuc, 2007) and is easy to implement and to calibrate (Cristianini, 2000; Hsu et al., 2003; Ben-Hur and Weston, 2010). For studies where landslide probability assessment is important, even though it is a non-probabilistic binary linear classifier, SVM add-ins (complementary functionalities) have been developed for producing probabilistic estimates dependent on the SVM classifier (Platt, 1999; Lin et al., 2007). Most rainfall threshold mathematical studies (Brunetti et al., 2010; Martelloni et al., 2012; Peruccacci et al., 2012) are based only on unstable events (one-class rainfall threshold) and do not take into account stable events. Although the SVM classifier was initially designed to classify two-class datasets, a new SVM formulation for a one-class classification problem was developed (Schölkopf et al., 1999; Tax and Duin, 2004) and is suitable for such studies. Lastly, for the new threshold approach using a multi-dimensional rainfall index, the SVM classifier demonstrated a better performance for classification (Byvatov et al., 2003; Huang et al., 2003). For all these reasons, the SVM classifier is considered here as the best solution, being generic and being easily implemented as an objective tool by stakeholders in landslide warning systems.

3.4 Stable or unstable event detection

The use of a mathematical tool to define a rainfall threshold is not sufficient to warrant an operational applicability in an early warning system. Indeed, the identification of the stable/unstable events needs also to be based on an objective and reproducible method. For continuously moving landslides without historical acceleration crisis catalog, it is relevant to use a velocity criterion method based on displacement velocity time-series in order to detect acceleration crises (peaks) and periods of rest (troughs) accounting for unstable and stable events respectively.

Peak/trough identification is a classical task in signal processing and in time series analysis. A commonly used identification method is based on the derivative of the data series and seeks for downward-going zero-crossings. However, in a natural dataset, random noise can cause false zero-crossings, leading to incorrect peak/trough detections. To avoid this bias, data series are often smoothed to remove random noise resulting in signal information loss. Generally, the more generic the method, the more necessary it is to inform input parameters. Generic methods can be too general to fit to specific signal properties (non-periodic signal, trend, amplitude, etc) or to detect only given peak/trough patterns. On the contrary, methods which require few input parameters (Excoffier and Guiochon, 1982; Li et al., 1995; Jacobson, 2001) are usually restricted to a specific domain of application.

Generally, deep-seated landslide displacement velocities present random peak/trough location distributions and random peak/trough properties with a wide range of widths, amplitudes and shapes. Most of the peaks/troughs of the displacement velocity time series are asymmetrical. In addition, displacement velocity signals can be considered to be relatively noisy, considering that not all peaks/troughs match with an unstable landslide event and have to be filtered according to the definition of the events. None of the above mentioned methods are suitable to account for the displacement velocity signal characteristics and for the detection requirements. In this contribution, a method is specifically designed with the aim to be applicable to any other deep-seated landslide sites.

4 The semi-automatic event detection method

Most deep-seated landslides are continuously moving and it is not possible to identify stable or unstable events. Therefore, the choice is made here to define a critical statistical threshold defining the minimal amount of rainfall (precipitation or recharge) which results in a significant increase of slope destabilization. Based on the displacement velocity time series, two types of events are defined: low destabilization (LD) events and high destabilization (HD) events.

4.1 Definition of LD and HD events

In this study, LD and HD events are defined following a simple statistical indicator (quartile) and a data series pattern (peak or trough) based on the displacement velocity time series. The LD events must be inferior to the first quartile and must match a trough. The HD events must be superior to the third quartile and must match a peak. Because displacement velocity is measured locally, an event is considered as representative of landslide destabilization only if it is identified on a selected set of displacement measurement devices. In the cases for which several stations are required, an event is considered as representative only if it is identified on all selected stations within a 10-day margin (spatial and temporal coincidence). The event date is then defined as the barycentre of the various event dates identified on each displacement velocity time series.

4.2 Detection of events

The method to detect LD or HD events is based on two moving windows scanning the displacement velocity time series (Fig. 38). The peak or trough characteristics (width and amplitude) are first taken into account in the detection process by a moving window named the *event window*. The characteristics of the background signal neighbouring the considered event are defined by a second moving window named the *neighbour window*. This window consists in two parts (back part and front part) on either side of the event window. Since the patterns of the displacement velocity peaks and troughs are not symmetrical, both moving windows have the possibility to be asymmetrical with respect to the scanning increment date (Fig. 38). The neighbour window does not overlap with the event window. The detection,

within a 10-day time interval, of peaks and troughs on all selected displacement velocity time series allows the definition of LD/HD events.

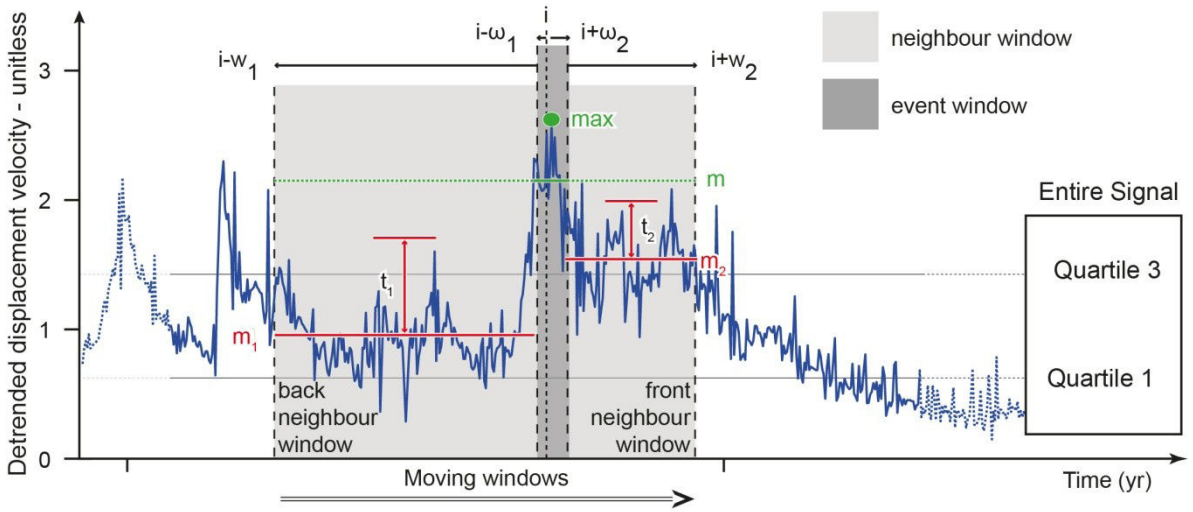

Fig. 38: Outline of the event detection method showing the two moving windows, a neighbour window separated in two parts (back and front) and an event window. This method needs the calibration of six parameters: (t_1, t_2), neighbour window half-width (w_1, w_2), event window half-width (ω_1, ω_1). The scanning increment date is denoted by i

For a given displacement velocity time series, the condition for a displacement event to be considered as a HD event peak is three-fold (Fig. 38). First, the mean value within the previously defined event window must be larger than the third quartile of the entire displacement velocity time series. Second, the mean value within the event window must be larger than the mean of the back part of the neighbour window to which a 'safety' margin is added. Third, the second condition also applies to the front part of the neighbour window, with a different safety margin value. Eventually, if the three above-mentioned conditions are fulfilled, then the date of the detected peak is defined as the date corresponding to the maximum value of displacement velocity within the event window (Fig. 38). The reverse procedure allows to detect a LD event trough: the mean value of the event window must be lower than the first quartile and it also must be lower than the mean values of the parts of the neighbour window (back and front) themselves lowered by 'safety' margins. Similarly, the date of the detected trough is defined as the date corresponding to the minimum value of displacement velocity within the event window.

A period of 20 days devoid of any LD/HD events is imposed after each identified LD/HD event, in order to reduce rainfall index information redundancy between successive events.

This condition is required to improve the SVM classifier. Ideally, the LD/HD event-free period should be equal to the maximum number of days covered by the rainfall index (150 days in this study). However, by doing so, the amount of detected events will be significantly reduced, leading to a loss of statistical meaning of the rainfall threshold. A 20-day period is an acceptable trade-off. The event detection method requires 6 parameters to be estimated (Fig. 38): (i) back and front neighbour window widths (w_1, w_2), (ii) the widths event window on either side of the scanning increment date (ω_1, ω_1) and (iii) 'safety' margin (t_1, t_2), (ii). These parameters are calibrated with an optimization algorithm.

4.3 Calibration of the parameters

A supervised learning method is implemented to calibrate the parameters of the event detection. This learning method uses a training interval where LD and HD events are identified manually on a set of selected displacement velocity time series. The training interval is a part of the whole study time interval. The event detection method parameters are tuned on this training interval with respect to manually identified events with the use of an optimization algorithm. Once the method is calibrated, it is applied to the whole study time interval in order to define a list of LD and HD events required for the rainfall index definition. Since this method mixes manual and automatic procedures, it is considered as a semi-automatic method.

An automatically identified event is considered as valid (true positive) if and only if it falls within a 10-day interval from a manually identified event. In the reverse case (more than 10 days), the automatically identified event is considered as a false positive. The optimization algorithm aims at minimizing the quantity $-\lambda_1 TPE + \lambda_2 D_{avg} + \lambda_3 FPE$ which is composed of three terms: (i) TPE, the proportion of true positive automatically identified events (Eq.(35)), (ii) D_{avg}, the average deviation of the time difference between manually and automatically identified matching events (Eq. (36)) and (iii) FPE, the proportion of false positive automatically identified events (Eq. (37)). A global optimization method, the simulated annealing (Kirkpatrick et al., 1983; Černý, 1985), is used in the minimization process. The weighting factors λ_1, λ_2 and λ_3 are applied to each of the terms in order to balance their relative influence in the optimization process. The weighting factors are adjusted manually (λ_1=1, λ_2=0.01 and λ_3=0.02).

The six parameters of the event detection method are calibrated separately for LD and for HD events. In order to avoid unrealistic values, the calibration algorithm seeks the parameters values within predefined ranges: w_1 and w_2 ranging from 2 to 200, ω_1 and ω_1 ranging from 1 to 20, t_1 and t_2 ranging from 0 to 4.

In summary:

$$\text{TPE} = \frac{Nb_a}{NbT_m} \tag{35}$$

$$\text{D}_{\text{avg}} = \frac{\sum_{i=1}^{Nb_a}\left(\sqrt[2]{\left(D_{a\,i} - D_{m_i}\right)^2}\right)}{Nb_a} \tag{36}$$

$$\text{FPE} = \frac{NbT_a - Nb_a}{NbT_a} \tag{37}$$

With:

NbT_a, NbT_m	total number of events automatically and manually identified respectively
Nb_a	number of events automatically identified which match with manual events
D_a, D_m	date of automatic and manual events respectively which match together.

5 Rainfall threshold definition method

The support vector machines (SVM) linear classifier is used to define an optimal and objective rainfall threshold by finding the best line separating two classes of n dimensions. A nonlinear classification can be achieved with the SVM classifier by using the so-called kernel trick. For the two-dimensional rainfall index only the linear kernel is used while for the multi-dimensional rainfall index the linear kernel and the radial basis function kernel are tested. The SVM calibration and threshold performance is assessed with the cross-validation method by computing an average misclassification error rate (MER). The SVM analysis is performed with the multiplatform package LIB-SVM© (Chang and Lin, 2011). The SVM classifier as well as the SVM classifier calibration and the kernel selection procedures are detailed in the appendix A.

5.1 The classical approach: the two-dimensional rainfall index (2DI)

Terlien (1998) showed the importance of selecting the proper time period extent for the definition of a failure threshold. In several studies, the choice of the period extent of the antecedent rainfall is explored empirically, with no optimization to find the best number of days which maximise the classification performance. In this study, the rainfall threshold is estimated for all combinations of antecedent and precedent periods varying from 2 to 150 days and from 1 to 10 days, respectively. The antecedent rainfall and the precedent rainfall match with the cumulated amount of rainfall over a specified number of days before an event (unstable or not). The precedent period and the antecedent period correspond to a short period and a long period respectively (see section 3.1 and Fig. 37a). The establishment of the threshold must be based on independent variables in order to be statistically true (Peruccacci et al., 2012). Consequently, the two periods, antecedent and precedent, do not overlap and are always adjacent. Groundwater hydrodynamic processes due to drainage are non-linear and an old rainfall event displays less impact than the most recent event on the aquifer saturation state (Canuti et al., 1985; Crozier, 1986). As a consequence, a decay weight factor α is applied to the cumulated rainfall amount to take into account this non-linearity (Eq. (38)). 15 weighted sum combinations based on 5 decay factors α equal to 1, 0.99, 0.98, 0.95 and 0.90 are tested (Fig. 36 and 39).

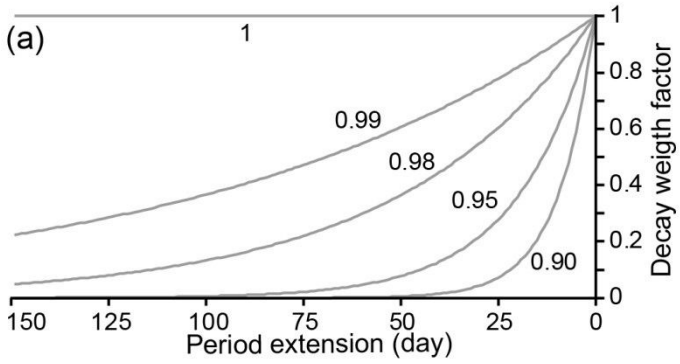

(b)

Combination	Decay weigth factor: Precedent period	Decay weigth factor: Antecedent period
1	1	1
2		0.99
3		0.98
4		0.95
5		0.90
6	0.99	0.99
7		0.98
8		0.95
9		0.90
10	0.98	0.98
11		0.95
12		0.90
13	0.95	0.95
14		0.90
15	0.90	0.90

Fig. 39: Determination of the rainfall index in the case of the two-dimensional approach with (a) plot of the 5 decay weight factors and (b) the set of 15 tested combinations coupling the 5 decay factors and the precedent and antecedent periods

For α equals one, the decreasing cumulated rainfall amount *WI* matches with a classical arithmetic sum.

$$WI = \sum_{i=1}^{n} \alpha^{(i-1)}\, y(i) \tag{38}$$

Where:

WI	decreasing cumulated rainfall amount of an event (mm)
n	cumulative period extent (day)
i	i^{th} day (i=1 match with event day)
y	recharge or rainfall (mm)
α_i	decay weight factor (α = 1 for i=1).

The two-dimensional rainfall index approach leads to 24450 combinations which are then evaluated with the SVM method. The SVM classifier performance (based on MER) is used to assess the best combination.

5.2 The new approach: the multi-dimensional rainfall index (MDI)

The maximum MDI dimension is set to 150 days that is the same as the maximum number of days allowed for the two-dimensional rainfall index (Fig. 37b). From a statistical point of view, it is important to find the most parcimonious model for the classification. It is well known that, when the amount of data is moderate, a too complicated model can lead to poor prediction due to the lack of data available to estimate that model (Hastie, 2009). This is known as the "bias variance trade-off". Furthermore, not all dimensions (also called features in this paper) are relevant in the event classification, i.e. the class labels can be predicted by only a few number (k) of features from the total available number p of features ($k << p$). In our case, the following question is a key question: how many days of precipitation/recharge are necessary to accurately predict whether an event is unstable or not?

Penalized SVM formulations (also called Least Absolute Shrinkage and Selection Operator or LASSO SVM penalty) have been developed to seek sparse solutions by removal of irrelevant and redundant dimensions (Knight and Fu, 2000; Hastie, 2009). For this study, the penalised SVM classifier analysis is tested with the Matlab© code NLPSVM (Fung and Mangasarian, 2004), but the results, which consist in scattered selected features, are not consistent with hydrogeological processes. Instead, in order to seek the shorter continuous interval minimizing MER, a sensitivity analysis is carried out by iterating precipitation and recharge MDIs from 1 to 150 days (Fig. 36). For each iteration, a traditional SVM model is performed and the corresponding MER is computed. The MDI solution having the minimum MER is selected as the best solution to separate stable events from unstable events. Therefore, the multi-dimensional rainfall index approach leads to evaluate only 300 combinations.

5.3 Validation procedure to test the forecast ability of the rainfall threshold

Most rainfall threshold studies are conducted only by determining a threshold based on a list of discrete rainfall events, but do not test their operational applicability with a validation

procedure performed against an independent continuous dataset recorded over a period different from the one used for the rainfall threshold definition (Martelloni et al., 2012; Bernardie et al., 2014). Landslide risk managers deal with continuously monitored rainfall datasets and also with weather forecasts. Even if a rainfall threshold defined with discrete historical stable/unstable events gives an acceptable classification performance, there is no guarantee that it can also give good classification performances on continuously monitored present-day or forecast rainfall datasets. In particular, it could lead to false positives or it could miss the detection of unstable events. In order to simulate hazard management requirements, the rainfall threshold forecast ability is tested against periods of high destabilization. These periods will be referred to as expected destabilization stages (EDS) which are arbitrarily defined as days during which the landslide velocity is larger than its third quartile. In other words, during EDS periods, the displacement velocity is greater than 75% of its recorded values. The forecast ability is evaluated with a sensitivity analysis based on SVM probability outputs over an independent period. Two performance criteria are computed on the validation interval and plotted for each threshold solution: (i) the proportion of detected EDS (number of automatically detected true positive unstable events divided by total number of EDS days) and (ii) the proportion of false positive events (number of automatically detected false positive unstable events divided by the total number of days of the independent validation time interval).

6 Geological and hydrogeological setting of the study area

The Séchilienne landslide is located to the south-east of Grenoble (France), on the right bank of the Romanche River on the southern slope of the Mont-Sec massif (Fig. 40). The landslide is located in the Belledonne crystalline range and is composed of micaschists. The micaschists are characterized by N-S trending vertical foliation. Carboniferous to Liassic sedimentary deposits unconformably cover the micaschists along the massif ridge line, above the unstable zone. Locally, glacio-fluvial deposits overlie both the micaschists and the sedimentary deposits.

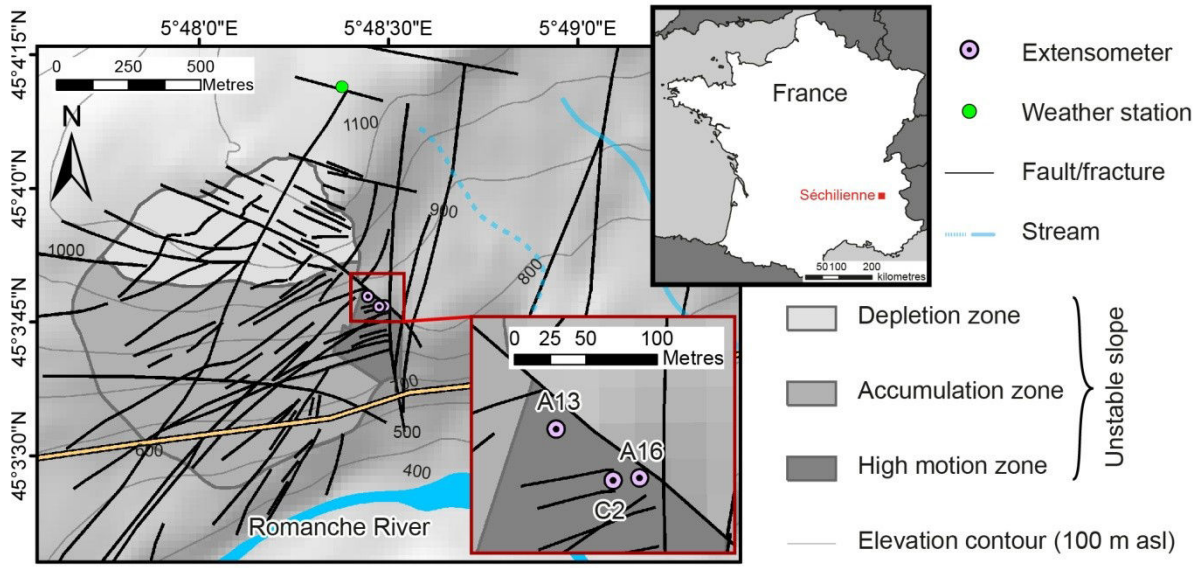

Fig. 40: Map of Séchilienne landslide with location of the monitoring network used in this study

The Séchilienne landslide is limited eastwards by a N-S fault scarp and northwards by a major head scarp of several hundred meters wide and tens of meters high below the Mont Sec. Rare geomorphological evidence allows to define precisely the western and southern boundaries of the unstable area. Below the head scarp, between 1100m and 950m asl, a low slope depletion zone shows an area in depression while between 950m and 450m asl, the slope becomes steeper (>40°) and is interpreted as an accumulation area (Vengeon, 1998; Le Roux et al., 2011). The slope is cut by a dense network of two sets of near-vertical open fractures trending N110° to N120° and N70°. The landslide Séchilienne is characterized by a deep progressive deformation controlled by the network of faults and fractures. A particularity of the Séchilienne landslide is the absence of a well-defined basal sliding surface. The landslide is

affected by a deeply rooted (about 100-150 m) toppling movement of the N50° to 70° slabs to the valley (accumulation zone) coupled with the sagging of the upper slope (depletion zone) beneath the Mont Sec (Vengeon, 1998; Durville et al., 2009; Lebrouc et al., 2013). The displacement monitoring shows displacement velocity vectors relatively homogeneous in direction (N140°) and in dip angles (10° to 20° toward the valley). Low displacement velocities (2 to 15 cm/yr) are observed for both the depletion and the accumulation zone (Le Roux et al., 2011). These velocities gradually decrease towards the west and the south, allowing to estimate the limits of the unstable area. A very actively moving zone with high displacement velocities about 150 cm/yr is distinguishable from the unstable slope.

6.1 Hydrogeology and rainfall triggering

The Séchilienne landslide, shows a higher hydraulic conductivity than the underlying stable bedrock (Vengeon, 1998; Meric et al., 2005; Le Roux et al., 2011) thus leading to a landslide perched aquifer (Guglielmi et al., 2002). The fractured metamorphic bedrock beneath the landslide contains a deep satured zone at the base of the slope and an overlying thick (about 100 m) vadose zone. The recharge of the landslide perched aquifer is essentially local, enhanced by the trenches and the counterscarps which tend to limit the runoff and to facilitate groundwater infiltration in the landslide area. However, the hydrochemical analyses of Guglielmi et al. (2002) shows that the sedimentary deposits distributed above the landslide hold a perched aquifer which can recharge the landslide perched aquifer. The groundwater flow of the entire massif is mainly controlled by the well developed network of fractures with high flow velocities (up to a few kilometre per day; Mudry and Etievant 2007). The triggering of the Séchilienne landslide is likely driven by a two-layer hydrosystem consisting of a landslide perched aquifer and a deep aquifer over the whole massif hosting the landslide (Cappa et al., 2014). As a result, the Séchilienne landslide is characterized by a good correlation between precipitations and displacement velocities (Rochet et al., 1994; Alfonsi, 1997; Durville et al., 2009; Chanut et al., 2013). Vallet et al. (2014) shows that the Séchilienne displacement rates are better correlated to the recharge than to the precipitation, reinforcing the significant role of groundwater flow in the Séchilienne destabilization.

6.2 Monitoring network and method implementation

The Séchilienne landslide is monitored by numerous displacement stations using a wide range of techniques (extensometer, radar, infra-red geodesy, inclinometer, GPS). A weather station is located at Mont-Sec, few hundred meters above the top of the disturbed zone (Fig. 40). Displacement and weather data are recorded at a daily rate. The daily displacement, identical to a velocity measurement in mm/day, is hereafter named displacement. The weather station is equipped with rain and snow gauges. Extensometer stations are selected for displacement data as they are the most reliable displacement recording devices on the site and also because they have been operating since the very beginning of displacement monitoring. For the semi-automatic detection event method, three extensometers, A13, A16 and C2, are selected. They are located on the most active moving zone, which is also the most reactive zone with regard to precipitation events (Fig. 40). The event detection method is calibrated on the testing interval from 1st January 2001 to 31 December 2004 (about 20% of the studied period), as displacement time series variations are representative of the overall time series for this period, and is then applied on the period from 1st January 1994 to 31 December 2011. The two rainfall threshold approaches are trained from 1st January 1994 to 31 December 2011 (same as for the event detection process interval), while the validation procedure implemented in the recent period, from 1st January 2012 to 31st August 2013. The training interval, which is longer than the test interval, is constrained by SVM classification accuracy which is enhanced with the number of LD/HD events identified. For the validation procedure, the SVM classifications are filtered, with isolated detected one-day LD or HD events disregarded since not being significant enough to lead to a destabilization event. The currently existing Séchilienne warning system, partly based on precipitation, in addition to displacement rate, micro-seismic, and rockfall monitoring, integrates an operational rainfall threshold (SWS threshold) defined as 80 mm of accumulated precipitation for a period of less than 3 days.

6.3 Recharge estimation

Evapotranspiration is estimated from temperature records by using the Penman-Monteith reduced-set equation (Allen et al., 1998) and Bristow-Campbell radiation equation (Bristow and Campbell, 1984), calibrated against the benchmark Penman-Monteith equation (Allen et al., 1998) and radiation measurements respectively. Calibration is performed with three

neighbouring weather stations, where all required parameters (temperature, wind, humidity and radiation) are measured. A soil water balance method is used to compute recharge with soil available water storage set at 105 mm and a runoff coefficient of 11%. Informations and details on the methodology adopted in this study can be found in Vallet et al. (2014).

6.4 Displacement detrending

The long-term displacement records of the three extensometers shows that displacement rate and amplitude exponentially increased with time (Fig. 41b). The rainfall data series does not show any trend over the year, meaning that the displacement trend is independent of the recharge amount (Fig. 41a). Consequently, on the Séchilienne landslide, for the same amount of rainfall, the displacement rate and magnitude responses increase steadily with time. The observed trend is the consequence of a progressive damaging of landslide mechanical properties due to long-term repetitive stresses which cause permanent deformation. This deformation can be assimilated to long-term creep (Brückl, 2001; Bonzanigo et al., 2007) and can lead to a decrease of the slope shear strength and/or to a modification of hydraulic properties (Rutqvist and Stephansson, 2003). In addition to the trend, the Séchilienne landslide is constantly moving and show large daily to seasonal variations. At Séchilienne, these variations are clearly linked to the recharge amount (Vallet et al., 2014). Consequently, the semi-automatic event detection and the determination of EDS periods are based on the detrended displacement time series which is the true response of the landslide to the rainfall trigger.

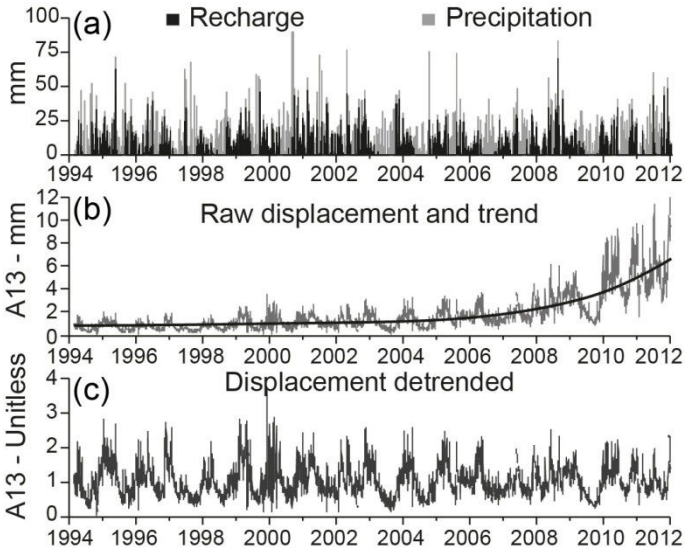

Fig. 41: Meteorological dataset and detrending of extensometer A13 records. (a) Precipitation and recharge dataset. (b) A13 daily displacement and parametric trend. (c) Detrended A13 daily displacement

The exponential trend is removed with the statistical multiplicative method ($y_t = T_t S_t I_t$) where the time series (y_t) is composed of three components (Madsen, 2007; Cowpertwait and Metcalfe, 2009; Aragon, 2011): trend (T_t), seasonal (S_t) and irregular (I_t). In this study, the irregular and seasonal components are both assumed to be linked to the rainfall triggering factor ($y_t = T_t R_t \; with \; R_t = S_t I_t$). The trend is determined by curve fitting of a fifth order polynomial (parametric detrending). The result is a detrended unitless time series (R_t) with both variance and mean trend removed. The time series decomposition process is illustrated with the A13 extensometer in the figure 41c.

7 Results

7.1 Semi-automatic event detection

The semi-automatic event detection results are plotted in the figure 42 and the calibrated parameters are presented in Table 13. Over the training interval (1st January 2001-31 December 2004), all the manually identified HD events are located in winter-spring seasons (high flow periods) whereas LD events take up the rest of the year. For HD events, 13 events are automatically detected among the 13 manually identified (100%) and 0 false positive is identified (Fig. 42a). For LD events, 10 events are automatically detected among the 13 manually identified (77%), and 3 false positives are identified (Table 13 and Fig. 42a). The calibration performance is better for HD events, as peak patterns are better constrained (sharp width, large amplitude, short wave length, one HD event per peak), while several LD events can be identified within the same trough (long wave length).

Table 13: Results of the calibration of the automatic event detection method for low destabilization (LD) events and high destabilization (HD) events

	Type	LD event	HD event
Calibrated parameters	Neighbour window (w_1, w_2) [day]	(123; 56)	(80; 16)
	Event window (ω_1, ω_2) [day]	(2; 3)	(2; 2)
	'Safety' margin: (t_1, t_2) [mm]	(0.0154; 0.0095)	(0.0524; 0.0649)
Performance	True positive events (TPE) [%]	77	100
	Average date deviation (D_{avg}) [day]	3.5	1.33
	False positive events (FPE) [%]	23	0

57 HD events and 55 LD events are identified for the whole studied interval (1st January 1994 - 31 December 2011) on the three detrended displacement times series, and are plotted on the raw displacement time series (Fig. 42b). Detections of events are regularly spread over the time series extent, although for some years only a few events are identified (1997, 1999, 2003 and 2006). LD and HD events mainly occur in summer-autumn and winter-spring, respectively, reflecting the seasonal pattern of manual events. The number of identified events is well balanced for each class and the total number of events is sufficient to perform SVM analysis.

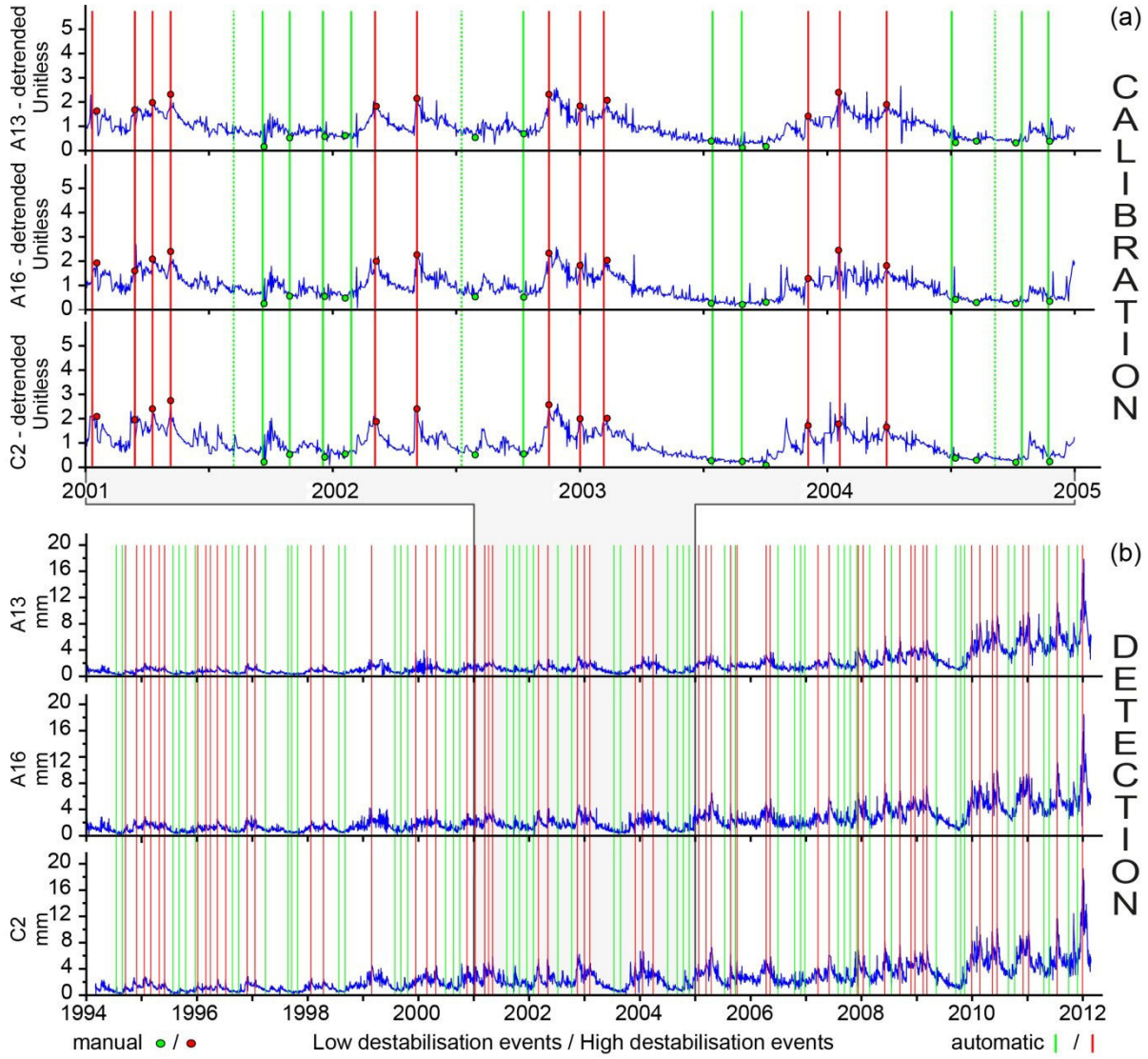

Fig. 42: Results of the semi-automatic event detection method for the A13, A16 and C2 extensometers. (a) Tuning results of the method with manual and automatic events detected relatively to detrended daily displacement. (b) Processing results of the calibrated method relatively to raw daily displacement on the whole studied interval. Dash lines stand for automatic false positive events relatively to the manual identified events

7.2 Rainfall threshold performances on the training interval

Among the combinations tested for the two-dimensional threshold (2DI threshold), the best rainfall threshold MER for precipitation (13.27%) is about two times larger than the best MER obtained with recharge (7.08%, Fig. 43a). The antecedent rainfall/precedent rainfall index involved in the two best threshold performance are 10 days/5 days for precipitation (short-term) and 34 days/8 days for recharge (long-term) with decay weight factors of 1 and 0.98 (identical for the two periods for the two cases), respectively.

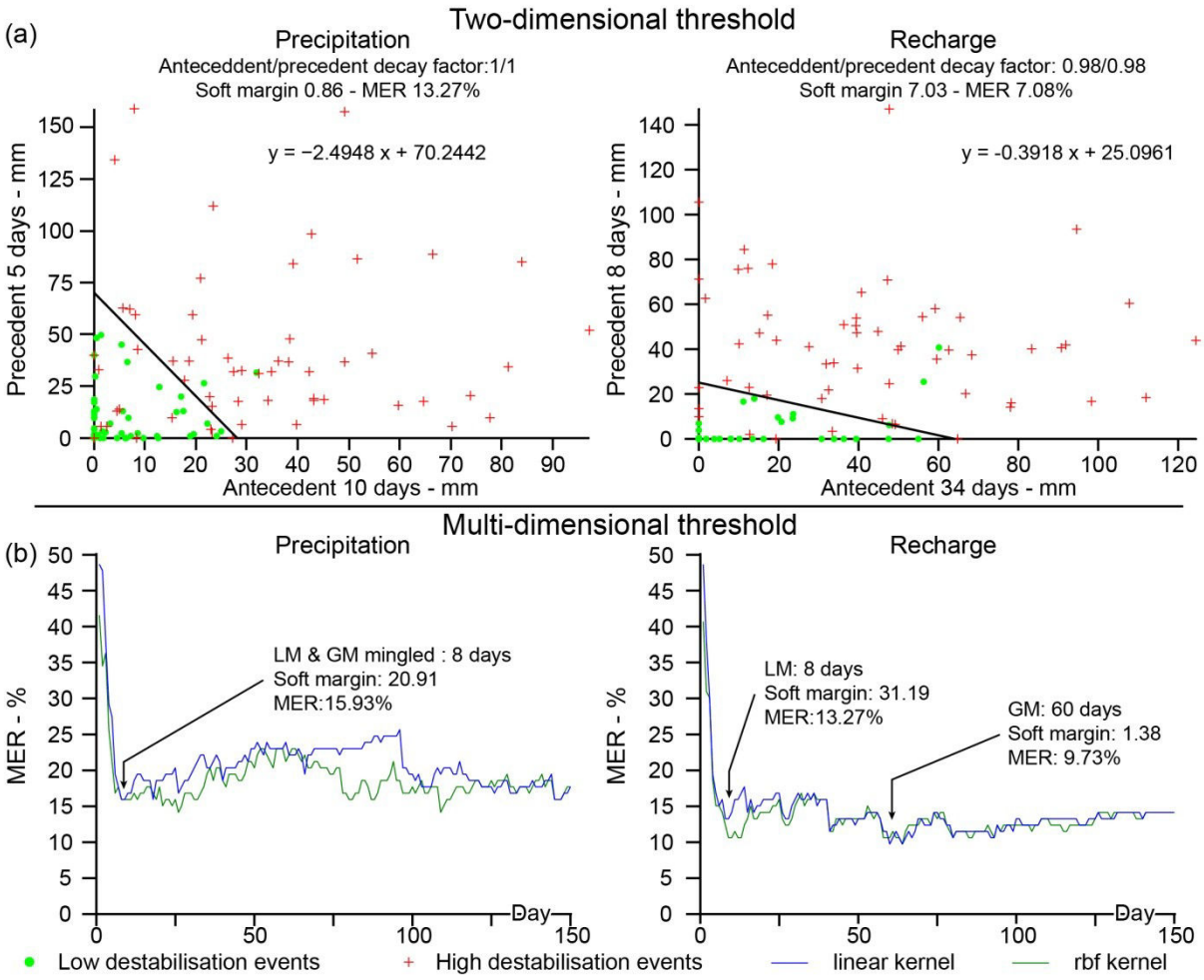

Fig. 43: Results of rainfall threshold classification on the training interval for the (a) two-dimensional and (b) multi-dimensional approaches. MER, LM and GM stand respectively for misclassification error rate, local minimum and global minimum

Regarding the multi-dimensional approach (MDI rainfall threshold), the two tested kernels (linear and RBF) show no significant differences in the MER performance for precipitation as well as for recharge (Fig. 43b). The linear kernel, which is much simpler than the RBF kernel, is chosen to determine the MDI rainfall threshold. The MDI number of days, from which MER is not significantly improved, is identified as a local minimum, whereas the MDI number of days having the minimum of MER is identified as a global minimum. Regarding precipitation, the local and the global MER minima are mingled (MER: 15.93%) for a rainfall MDI of 8 days. Regarding recharge, the local minimum (MER: 13.27%) is obtained at 8 days, whereas the global minimum (MER: 9.73%) is obtained at 60 days, both recharge MERs being lower than the MER derived from precipitation.

Both threshold approaches lead to short-term and long-term components. Recent studies (Guglielmi et al., 2002; Cappa et al., 2014) show that a two-layer hydrosystem may destabilize the Séchilienne landslide, with a shallow perched aquifer localized in the unstable area and a deep aquifer below the landslide. The perched aquifer behaviour is more reactive to short-term precipitation events, whereas the deeper aquifer is more sensitive to long-term seasonal recharge variations. In order to take into account the possible coupling of the two aquifers on the landslide destabilisation, a rainfall threshold is estimated for each threshold approach by averaging the probability of the short and long-term components (so-called composite threshold). The two-dimensional precipitation and recharge thresholds are combined while for the multi-dimensional threshold, only the recharge short-term and long-term MDI solutions are used. Although the precipitation is a more appropriate signal to characterise the landslide perched aquifer, the short-term component of the recharge is chosen for the multi-dimensional threshold. Indeed, the precipitation and recharge short-term optimal solutions of the multi-dimensional threshold occur within the 8th dimension, but recharge shows a slightly enhanced MER (see section 8.2 for process explanation).

7.3 Rainfall threshold performances on the forecast testing interval

The performances and the results of the thresholds estimated with the 2DI and the MDI approaches on the forecasting testing interval are plotted *versus* the time in the figure 44 whereas the figure 45 shows the performances of these thresholds according to the threshold SVM probability outputs.

The probability output signals show similar patterns between respective components of 2DI threshold and MDI threshold approaches, i.e. short-term, long-term and composite (Fig. 44b and 44c). For the SVM default classification (probability ≥ 0.5), regardless of the approach, short-term components show a more scattered HD event detection, sensitive to rainfall events, with several false positives in low flow periods. Conversely the long-term components show a more continuous HD event period in high flow periods, also leading to several false positives. The two-dimensional approach is characterized by a less noisy probability signal, which can be explained by the decreasing sum which acts as a smoothing function (Fig. 44b). The SWS threshold shows a low performance with an EDS detection at 1%.

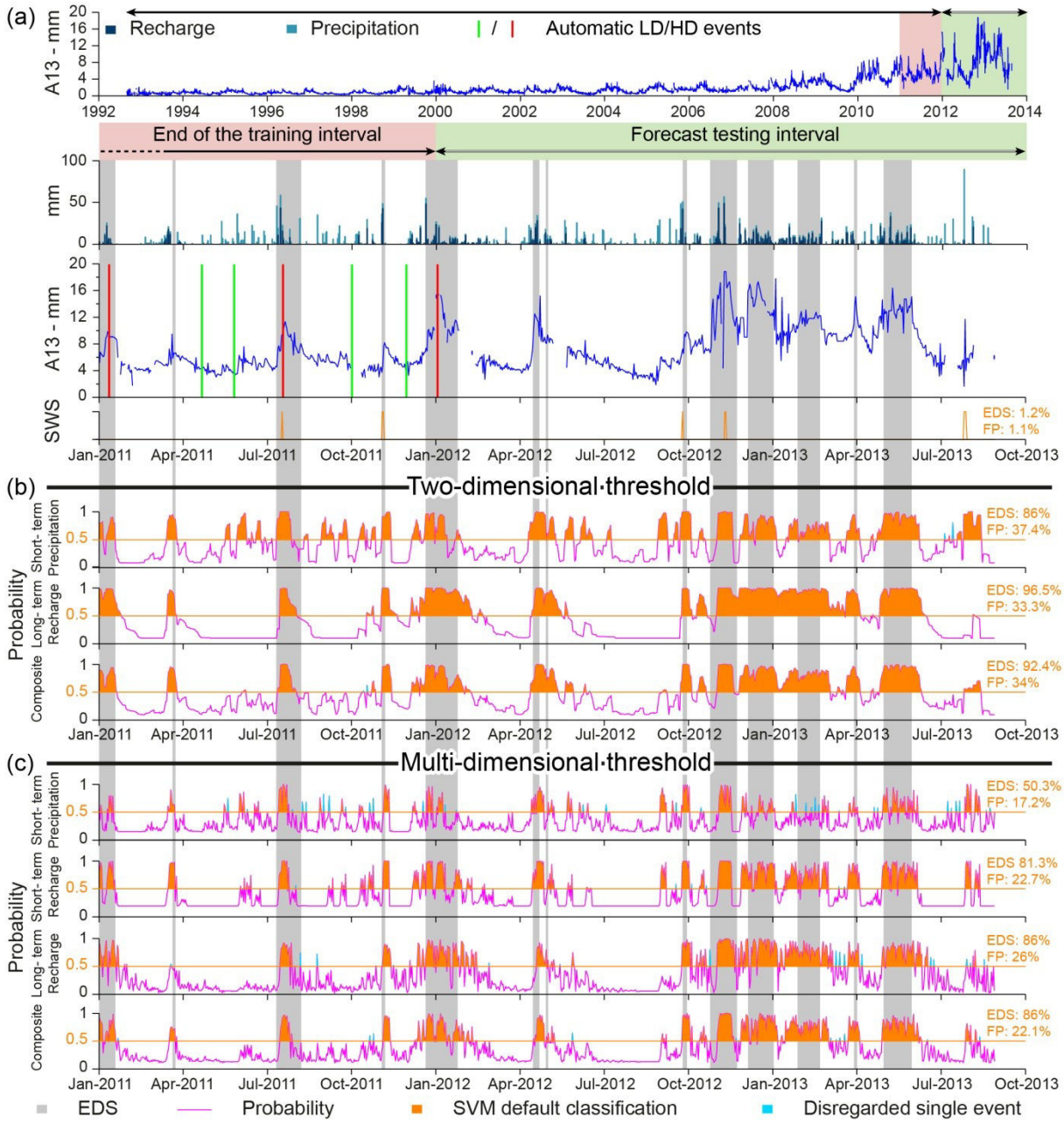

Fig. 44: Results of rainfall threshold classification on the forecast testing interval (a) A13 raw daily displacement and precipitation/recharge with the LD and HD automatic events. (b) Two-dimensional and (c) multi-dimensional threshold approaches. The short and long-term components as well as the resulting composite threshold are displayed for both approaches. For each component, the probability outputs and the SVM classification performances for probability ≥ 0.5 are plotted. Performance indicators are the proportion of EDS detected (EDS) and the proportion of false positives (FP). EDS, LD and HD stand for expected destabilization stages, low destabilization events and high destabilization events

For the 2DI and MDI approaches, the rainfall thresholds estimated with precipitation are always outperformed by those estimated from recharge, whatever the probability limits (Fig. 45). The composite 2DI threshold does not improve the classification performance, and the recharge 2DI threshold is clearly the best solution of the classical two-dimensional approach

(Fig. 44b and 45a). On the contrary, the composite MDI threshold slightly improves the classification performance, compared to the short-term and long-term components of the recharge MDI threshold, mostly for false positives in a proportion lower than 15% (Fig. 44c and 45b).

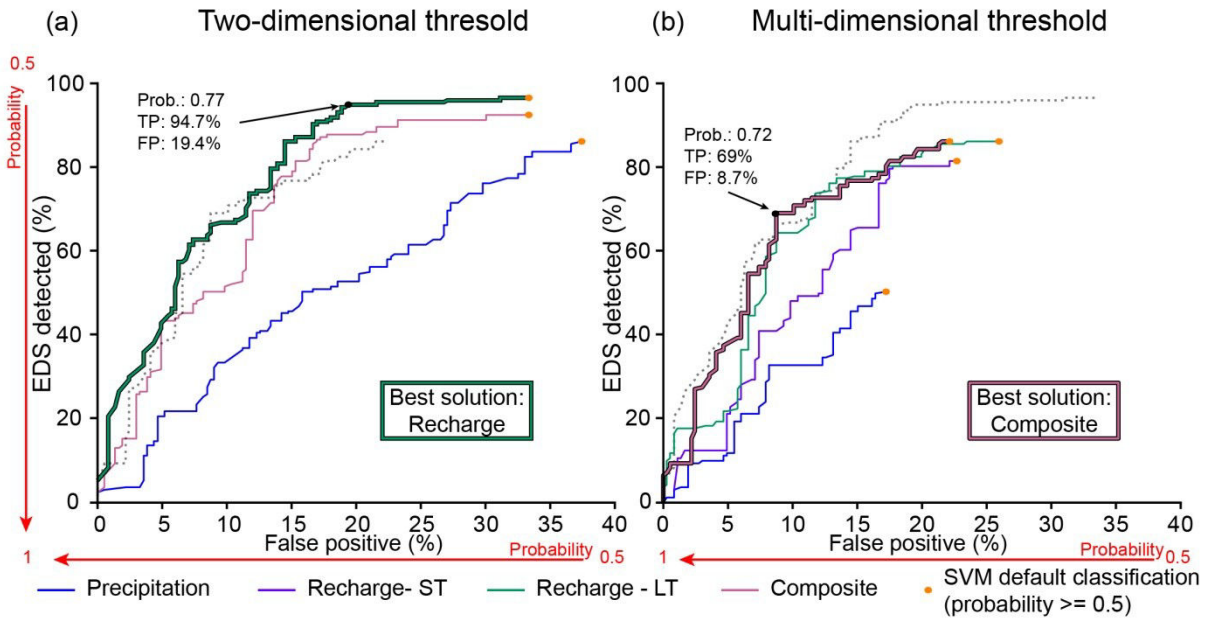

Fig. 45: Rainfall threshold performance comparison with proportion of false positives and EDS detected on the forecast testing interval for (a) the two-dimensional approach and (b) the multi-dimensional approach. ST: short-term; LT: long-term

8 Discussion on the event detection method and the rainfall threshold performances on the forecast testing interval

8.1 Event detection

The event detection method shows a very good performance and produces a large number of events to train SVM classification. Although the method is relatively robust and easy to implement, it requires a wide data interval with at least a daily time step to produce an enough number of events (statistical significance) for rainfall threshold classification. However, improvements of instrumental technology allow more and more cost-effective monitoring and nowadays, many landslides have been monitored daily for more than ten years. In addition, some landslide monitoring data are available with the open-access initiatives of the scientific community, such as the French OMIV observatory (Multidisciplinary Observatory of Versant Instabilities) in charge of the Séchilienne landslide. The proposed event identification should therefore be suitable for a large number of landslides, and this number should increase over the years.

8.2 Precipitation, recharge and composite rainfall threshold

Regardless of the approach (2DI or MDI), the recharge rainfall thresholds show the best performances. The use of precipitation leads to a poor performance/error ratio and is likely to produce an unreliable rainfall threshold. In addition, the best precipitation 2DI threshold does not require a decay factor in the decreasing cumulated rainfall amount computation (Fig. 43a), meaning that the short-term component does not involve a non-linear relationship with the displacement records. This reflects the fact that the key parameter to account for destabilisation of deep-seated landslides controlled by non-linear groundwater processes is not precipitation but recharge (Van Asch et al., 1999; Vallet et al., 2014).

The composite threshold shows the best performance for the MDI approach whereas the recharge threshold shows the best performance for the 2DI approach (Fig. 45). This difference can be explained by the fact that the composite MDI threshold is estimated only with the recharge component, whereas the composite 2DI threshold involves the precipitation component. The rainfall threshold takes only interest in classifying extremely low or high destabilisation events resulting from extremely high or low precipitation events.

Consequently, the soil-water balance which acts as a filter by removing numerous precipitation events of low magnitude (soil water storage cut-off) enables to define a better rainfall threshold identifying fewer false positives. This is another advantage to use the recharge signal rather than the precipitation signal. Lastly, the good performance of the composite threshold agrees with a landslide destabilisation triggered by a two-layer hydrosystem.

8.3 Two-dimensional vs. multi-dimensional rainfall threshold

The similarity of the probability output signals between the two methods (2DI and MDI) indicates that the weight applied by the SVM classifier to the dimensions of the MDI successfully reproduces the non-linear relationship between precipitation/recharge input and landslide destabilisation (Fig. 44). Unlike the 2DI rainfall threshold determination, there is no need to introduce parameters such as decay factors in order to adjust for the non-linearity. The multi-dimensional approach (MDI) fulfils the requirement of the method to adhere to the concept of requisite simplicity (Stirzaker et al., 2010), balancing technical accuracy with utility for operational implementation. For all these reasons, although 2DI threshold globally shows a slightly better performance, a composite MDI threshold is an efficient alternative method. Indeed, it has the benefit of having a truly objective and cost-effective computation method. From an implementation point of view, although the two-dimensional approach requires numerous hypotheses and extended computation time, it nevertheless has the advantage of defining the rainfall threshold by a simple linear equation which can be used regardless of the SVM model from which it originates (Fig. 43a). Conversely, the MDI rainfall threshold method does not require any hypothesis or extended computation time. It however requires the use of the SVM established model to discriminate between events.

8.4 Relevancy of the SVM probability output

The SVM probability outputs are investigated in figure 45 with a sensitivity analysis in relation to the proportion of detected EDS and false positive events. Whatever the approach (2DI and MDI), the probability outputs allow a finer and more flexible classification than the SVM default classification (probability ≥ 0.5). In the case of the recharge 2DI threshold (Fig. 45a), the default SVM classification identifies 33.3% of false positive events for a 96.5% proportion of detected EDS. The modification of the probability limit to 0.77 allows, for a

similar proportion (94.7%) of detected EDS, to decrease the proportion of false positive events to 19.4%, that is an improvement of about 40%. The sensitivity analysis shows that the higher the probability, the fewer the EDS events detected and the fewer the false positive events (Fig. 45).

A method to select the probability limit which maximizes the proportion of detected EDS with respect to the proportion of false positive events is to identify the break-point on the detected EDS *vs.* false positive plot above which the EDS proportions do not significantly increase compared to the false positive proportion (highlighted by arrows in Fig. 45).

The composite MDI threshold probability outputs and the A13 displacement time series are plotted for seven limits from 0.5 to 0.99 for illustration purposes (Fig. 46). These results highlight the relevance of using a validation procedure, in order to assess the forecast ability of the rainfall threshold (Martelloni et al., 2012; Bernardie et al., 2014). Indeed, it allows to choose the appropriate probability limit according to the threshold purpose and to assess whether the accuracy of the threshold is sufficient to be integrated or not into a warning system. Time series signal patterns of displacement and SVM probability outputs (Fig. 44 and 46) suggest that the SVM probability outputs might be linked to hydraulic stress levels triggering the landslide destabilization, but this has still to be proven.

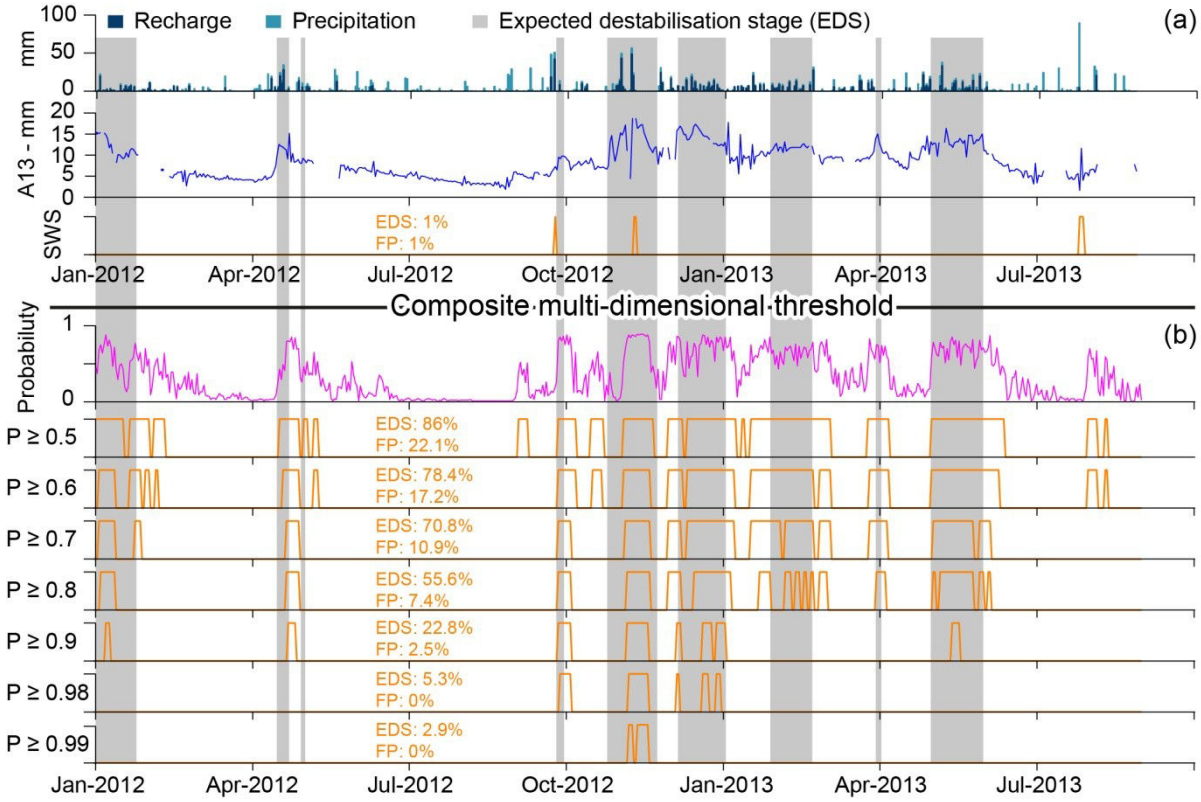

Fig. 46: Illustration of probability output versatility from the composite multi-dimensional threshold. (a) A13 raw daily displacement and precipitation/recharge. (b) Seven different limits corresponding to increasing probabilities from 0.5 to 0.99 associated with the proportion of expected destabilization stages (EDS) detected and of false positives (FP)

8.5 Operational applicability of the rainfall threshold in the Séchilienne warning system

The low performance of the present-day SWS threshold can be partly explained by the fact that the identified periods for EDS do not match the detection requirement of the rainfall threshold in the Séchilienne warning system. However, the SWS threshold misses numerous high-destabilisation events, demonstrating that the SWS threshold does not consistently link rainfall input with landslide destabilisation (Fig. 44). The composite MDI threshold outperforms the presently used SWS threshold whose probability output flexibility makes it suitable to be integrated in the Séchilienne warning system (Fig. 46).

9 Conclusion and perspectives

The aim of this study is to develop a new operational objective method to determine statistical rainfall thresholds for deep-seated landslides. Combining the SVM multi-dimensional rainfall threshold with the semi-automatic event detection method described in this study produces very good results and constitutes an appropriate tool to define an objective and optimal rainfall threshold. In addition to shortened computation times, to the non-necessity of pre-requisite hypotheses and to a fully automatic implementation, the newly introduced multi-dimensional (MDI) approach shows performances similar to the classical two-dimensional approach. This shows its relevance and its suitability for defining a rainfall threshold. Moreover, the multi-dimensional approach allows to find the best period combination which maximizes the separation of stable and unstable events. Lastly, this study shows that the recharge is a relevant parameter to be taken into account for deep-seated landslide triggering by aquifer pore water pressure. Using the recharge rather than the precipitation significantly improves the delineation of a rainfall threshold separating stable and unstable events. The performance and accuracy of the multi-dimensional composite threshold make it an appropriate method for integration into the Séchilienne landslide warning system. Probability outputs allow to design an adjustable rainfall threshold adapted to early warning system requirements, especially for those having multi-step crisis alerts.

The outcomes of these results are numerous. It would be worth testing the proposed method for other deep-seated or shallow landslides in order to evaluate its application and performances. As well, it would worth comparing performances of the proposed method to frequentist and Bayesian studies. Indeed, the intensity–duration thresholds are often defined resorting to subjective decisions mainly for the identification of the triggering rainfall conditions (Segoni et al., 2014). For shallow landslides, it may be necessary to adjust the method by defining a multi-dimensional index at an infra-hourly time step, in order to characterise intensity and duration of rainfall events. Another application would be to define a rainfall threshold with the proposed method for micro-seismic and rockfall events, linked to landslide destabilization mechanisms. Lastly, in order to improve threshold accuracy, it will be of interest to evaluate rainfall threshold biases induced by meteorological forecast uncertainties.

Acknowledgments

This research was fund by the program SLAMS (Séchilienne Land movement: Multidisciplinary Studies) of the Agence Nationale de la Recherche. The meteorological and displacement data were supplied by CEREMA Lyon. The authors acknowledge the support of Jean-Pierre Duranthon and Marie-Aurélie Chanut from the CEREMA Lyon.

10 Appendix A : Application of the Support Vector Machines for the determination of rainfall threshold

10.1 The SVM classifier tool

The support vector machines (SVM) method is a widely used two-class linear classifier, belonging to supervised learning models and kernel methods (Hastie, 2009). The purpose of a supervised learning method is to produce an inferred function from a set of training data (with known properties). The inferred function is then used to classify new data for prediction. The SVM classifier can be used to find the best hyperplane separating two classes of n dimensions by maximizing the margin between the two classes (Fig. 47). The margin can be defined as the width between data points (called support vectors) of the two classes that are closest to the separating hyperplane with no points within the margin (Cristianini, 2000). Data scaling or normalization are strongly recommended to enhance the SVM classifier performance (Hsu et al., 2003; Ben-Hur and Weston, 2010). For this study, all data are scaled to the [0, 1] range.

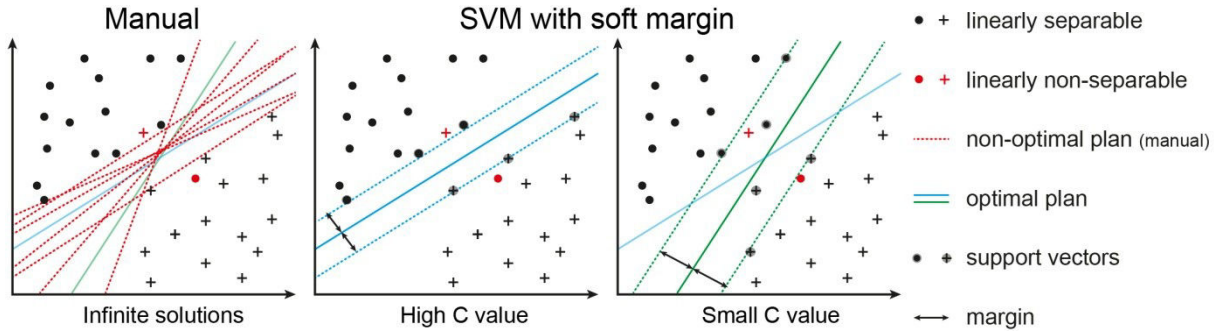

Fig. 47: Schematic illustration of the SVM classifier principle and the soft margin formulation

The SVM classifier assumes that the data are linearly separable and requires that the best hyperplane classifies each point correctly. However, a rainfall threshold classification presents possible nonlinear separable data. In order to achieve a larger margin, the soft margin SVM formulation (Cortes and Vapnik, 1995) allows some points to be in the margin or even to be misclassified. This is achieved by introducing slack variables ε_i in the minimization program (Eq. (39)). A soft margin cost parameter C must be specified by the user. The C parameter controls the trade-off between errors of the SVM on training data and the margin maximization. Small values of C will produce a classifier with larger margins and will allow a higher proportion of misclassified sample data. The optimal hyperplane is obtained by solving

the optimization problem in equation (39). The optimisation function is built-in for the SVM packages used. More details and an introduction to the SVM classifier can be found in Hsu et al. (2003) and Ben-Hur and Weston (2010).

$$\underset{w,b,\varepsilon}{minimize}\ \frac{1}{2}\|w\|^2 + C\sum_{i=1}^{n}\varepsilon_i \text{ with } \|w\|^2 = \sum_{j=1}^{p} {w_j}^2$$
$$subject\ to\ y_i(w^T x_i + b) \geq 1 - \varepsilon_i, \varepsilon_i \geq 0 \quad (39)$$

With:

w	normal vector of the classifier
p	number of dimensions
b	intercept of the separating hyperplane (also called bias)
C	soft margin cost
y_i	labels +1 or -1
x_i	i^{th} sample dataset (p dimensional row)
ε_i	slack variable
n	number of sample (observations)

10.2 SVM kernel selection

The efficiency of the SVM classification depends on the soft margin parameter, the selected kernel function and kernel parameters. The kernel function allows to map data from the input space to a higher dimensional space where the SVM classifier can find a linear separating hyperplane (kernel trick). A non-linear kernel can handle the cases for which the separation between class labels is non-linear in the input space. In order to do so, the non-linear kernel finds a linear solution in the feature space. In this study, the kernel is selected from the four commonly used kernel functions: linear, polynomial, radial basis function (RBF) and sigmoid.

10.3 Two-dimensional rainfall index

Although the RBF kernel is recommended by default for classification with a number of instances larger than the number of features (Hsu et al., 2003), the linear kernel is selected for the classical rainfall threshold. The choice of the linear kernel is justified as the non-linearity is already taken into account by the decreasing cumulated rainfall amount. In addition, the linear kernel does not require the input of any parameter, so only the soft margin parameter

(C) need to be tuned. This allows a cost-effectiveness computation given that the large amount (24,450) of combinations to explore.

10.4 Multi-dimensional rainfall index

For the multi-dimensional approach, the number of features involved in the classification varies from 1 to 150, whereas the number of instances (events) is constant. The linear and RBF kernels are tested and compared for each iteration. The linear kernel is selected for its cost-effectiveness and simplicity in tuning computation. Among the non-linear kernels, the RBF kernel (Eq. (40)) is chosen for the reasons mentioned by Hsu et al. (2003) and Ben-Hur and Weston (2010): having only one parameter γ to calibrate, generally out-performs other non-linear kernels and presents less numerical difficulties.

$$K(X_i X_j) = exp\left(-\gamma \left\| X_i X_j \right\|^2\right), \gamma > 0 \quad (40)$$

10.5 SVM calibration and threshold performance: cross-validation

The cross-validation is a statistical method which evaluates a model performance, and is especially adapted to a learning predictive model such as the SVM classifier (Hsu et al., 2003; Refaeilzadeh et al., 2009; Ben-Hur and Weston, 2010). The cross-validation consists in successive rounds where the dataset is randomly partitioned into two subsets; one will be used for training the model (learning) with known properties and the other will be used for validating the model with unknown properties (testing). The method ensures that all data are used both for training and validation. The cross-validation assesses the accuracy of the model to predict new data by estimating the average misclassification error rate (MER). The cross-validation is recommended for SVM calibration. It can also avoid model overfitting (Hsu et al., 2003). There are several methods to partition the data according to the goals of the study. In this study, a 'leave-one-out' cross-validation is chosen as it allows unbiased performance estimation. The leave-one-out is a particular case of k-folds cross-validation where k equals the number of observations. The k-folds method consists of dividing the dataset into k equal subsets (folds). Each fold in turn is used for validation, while the remaining k-1 folds are used for SVM training for k iterations.

The built-in Matlab® function *fminsearch*, which is an unconstrained nonlinear optimization, is used to search for the best soft margin cost parameter C and the RBF parameter γ which minimizes MER of the cross-validation (calibration process). Because *fminsearch* is dependent of an initial estimate of the parameter to calibrate, an exponential grid-search of C solutions from -4 to 8 (with an increment of 0.01 rounds) is performed for each SVM model. The *fminsearch* function is then applied to the model with the best performance. The calibration is performed for each tested combination. The MER obtained after SVM calibration from the leave-one out cross-validation is used to assess the classification performance for each tested combination for both the classical and new approaches. The MER is the ratio between the number of erroneous predictions and the total number of predictions produced.

CONCLUSION GÉNÉRALE

1 Synthèse des principaux résultats et apports du travail de recherche à la compréhension des mouvements de terrain profonds en milieu fissuré

Ce travail de thèse a permis de produire un schéma conceptuel d'écoulement et de caractériser la relation pluie-déplacement du mouvement de terrain de Séchilienne. Un outil d'alerte des phases d'accélérations a pu en être déduit. En s'appuyant sur ces résultats, ce travail de recherche permet un nouvel éclairage scientifique sur la compréhension des mouvements de terrain profonds en milieu fissuré (Fig. 48).

1.1 Schéma d'écoulement des eaux souterraines – Figure 48a

Les milieux fissurés en contexte montagneux présentent généralement un gradient vertical de perméabilité en direction des zones de surfaces décomprimées qui peut générer des aquifères perchés. Dans le cas des versants instables, ce contraste est amplifié par la zone instable déstructurée, ce qui conduit généralement à un système à double-aquifère, avec un aquifère perché peu profond, principalement situé dans la zone instable, et un aquifère profond, étendu sur l'ensemble du massif.

L'aquifère perché de la zone instable est temporaire, discontinu, et son étendue ainsi que sa connectivité fluctuent en fonction des variations journalières à saisonnières des précipitations. La zone de recharge de cet aquifère est essentiellement locale et est principalement alimentée par l'infiltration de précipitations brutes qui est favorisée par les nombreuses zones d'infiltration préférentielles (zones en contre-pentes, crevasses et autres fractures ouvertes). Dans certains cas, le bassin d'alimentation de l'aquifère perché de la zone instable peut comprendre une zone plus large que le mouvement de terrain lui-même, à la faveur d'aquifères perchés présents dans la zone stable (couverture sédimentaire, zone décomprimée…). L'aquifère perché de la zone instable est marqué par une importante

perméabilité où l'eau souterraine s'écoule principalement à travers le réseau dense de fractures largement ouvertes. Cette propriété confère à cet aquifère un comportement hydrodynamique réactif avec des variations à haute fréquence de la pression hydraulique.

Les milieux fissurés de la zone stable montrent un écoulement préférentiel et rapide de l'eau souterraine dans les principales fractures et un écoulement plus lent dans les zones moins fracturées. Le sol et la végétation du versant stable peuvent être très développés, ce qui conduit à une influence significative de l'évapotranspiration sur le signal de recharge de l'aquifère profond stable. De plus les pentes du massif de la zone stable peuvent être importantes et engendrer un ruissellement conséquent. L'aquifère profond est donc alimenté par une recharge très différente des précipitations brutes. Les propriétés de l'aquifère profond, moins perméable, couplées au signal de recharge, confèrent à cet aquifère un comportement hydrodynamique plus inertiel que l'aquifère perché, avec des variations de hauteur d'eau à basse fréquence.

1.2 Relation précipitations-déplacement et précipitations-déformation par fluage - Figure 48b

Les chroniques de vitesses de déplacement présentent des variations périodiques ainsi qu'une tendance pluriannuelle alors que les précipitations montrent uniquement des variations périodiques.

Les variations périodiques de la vitesse de déplacement sont contrôlées par les fluctuations des niveaux piézométriques de l'aquifère perché du mouvement de terrain ainsi que par celles de l'aquifère profond. L'aquifère profond explique la majorité de la variabilité périodique des vitesses de déplacement, alors que l'aquifère perché du mouvement de terrain explique les accélérations à haute fréquence.

Le mécanisme de déformation par fluage, matérialisé par la tendance exponentielle des vitesses de déplacement, ne peut être directement lié aux chroniques de précipitations ou de recharge. Cette déformation n'est cependant pas la conséquence d'un auto-emballement de la déstabilisation du versant contrôlé par son propre poids comme en témoignent les fortes diminutions de vitesse de déplacement durant les périodes de basses-eaux. Ces périodes attestent que la pression de fluides est toujours le moteur de la déstabilisation. La tendance exponentielle est la conséquence de la détérioration des propriétés mécaniques du versant, en

raison des actions répétées des variations de pression de fluides des deux aquifères (couplage hydro-mécanique indirect).

L'amplitude des variations périodiques du déplacement augmente en même temps que la tendance sur la moyenne. Le modèle multiplicatif de décomposition des chroniques de déplacement suggère que l'endommagement du versant agit comme un amplificateur de l'impact périodique de la pression de fluides sur l'accélération du massif. Les fluctuations du niveau piézométrique de l'aquifère perché et de l'aquifère profond peuvent donc expliquer les variations périodiques ainsi que la tendance exponentielle des déplacements de surface.

1.3 Outil opérationnel de prévision des phases d'accélération - Figure 48c

Un seuil d'activation pluviométrique peut être défini pour les mouvements de terrain profonds, à condition d'utiliser le signal de recharge plutôt que celui des précipitations. Pour les sites où la déstabilisation est contrôlée par un hydrosystème à double aquifère, une approche composite intégrant ces deux systèmes est pertinente en tenant compte de deux composantes, une à court terme représentative de l'aquifère perché et une à long terme représentative de l'aquifère profond. Bien que les précipitations soient représentatives de l'alimentation de l'aquifère perché, la recharge s'avère être un signal plus pertinent même pour ce compartiment. En effet, le calcul du bilan hydrique montre que le sol agit comme un filtre, en supprimant de nombreux épisodes de précipitations de faible ampleur. Ce processus de filtre permet d'améliorer les performances du seuil, qui s'attache à caractériser uniquement les événements extrêmes de déstabilisation, en diminuant la détection de faux positifs. L'approche multi-dimensionnelle combinée avec la méthode semi-automatique de détection d'événements permet une définition objective et optimale d'un seuil d'activation, facilitant son intégration opérationnelle dans un système d'alerte.

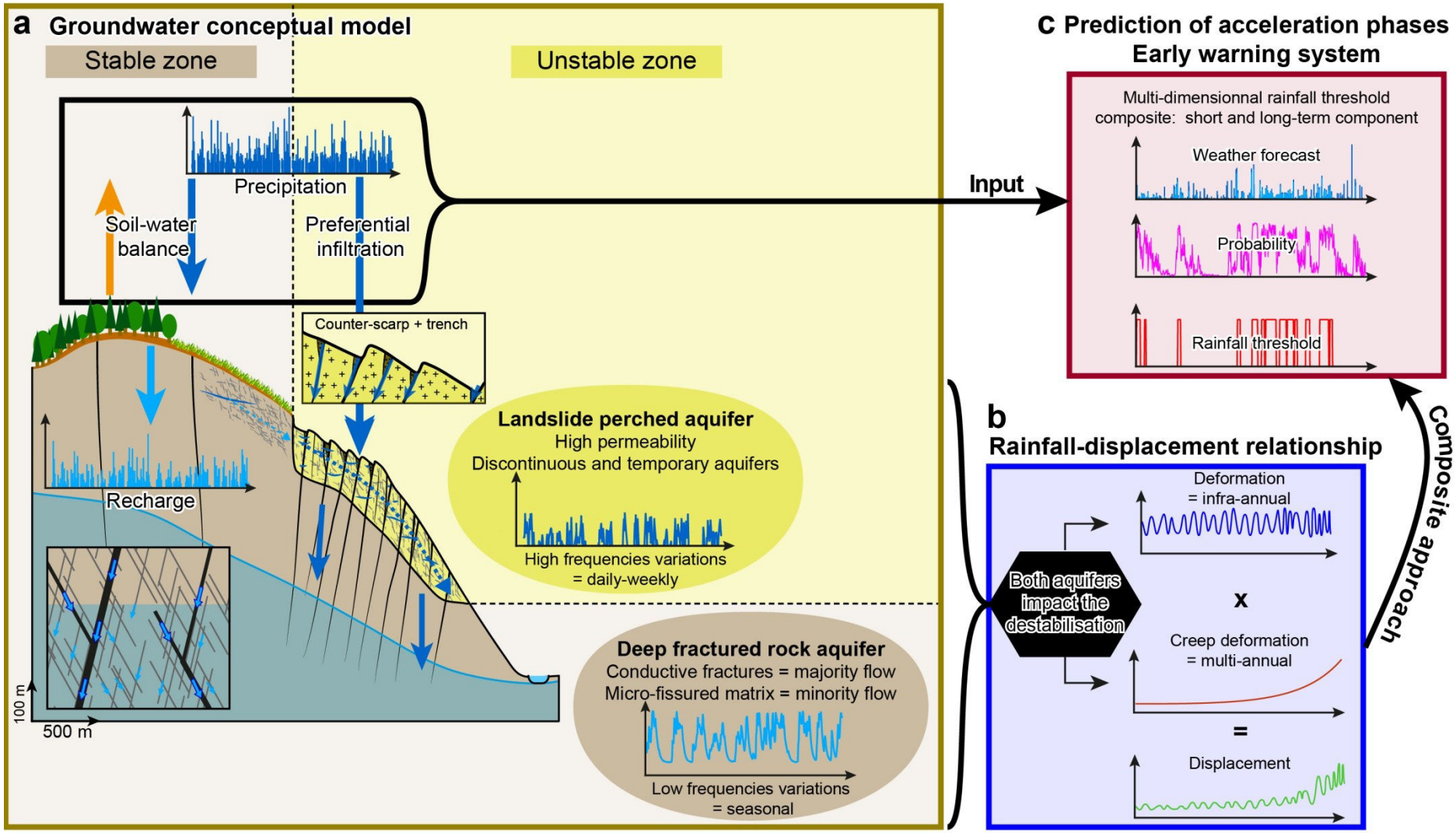

Fig. 48: Fonctionnent hydrogéologique et couplages hydromécaniques des mouvements de terrain profonds en milieu fissuré

2 Perspectives transversales d'application des méthodes développées

Ce travail de thèse s'est attaché au travers des processus et mécanismes caractérisés, à développer des méthodes innovantes et adaptées aux mouvements de terrain:

- une méthode d'élaboration du modèle conceptuel d'écoulement des eaux souterraines basée sur un suivi temporel de traceurs naturels et artificiels ;
- une méthode de calcul quotidien de la recharge basée sur un bilan hydrique au niveau du sol impliquant l'évapotranspiration et le ruissellement ;
- une méthode d'analyse de la relation pluie-déplacement basée sur les ondelettes et un nouveau modèle numérique ;
- une méthode de détermination d'un seuil d'activation pluviométrique basée sur la recharge et une approche multi-dimensionnelle des conditions pluviométriques.

Ces méthodes, bien que basées sur l'étude du versant instable de Séchilienne, ont été conçues dans une démarche universelle, c'est-à-dire dans l'optique d'être appliquées à d'autres sites ayant un contexte équivalent ou différent de celui de Séchilienne. Afin d'évaluer leur applicabilité et leur pertinence, ces méthodes peuvent être testées dans un premier temps sur les sites du réseau OMIV (Observatoire Multidisciplinaire des Instabilités de Versant). Ces sites ont l'avantage de présenter des mécanismes de déformation différents et de posséder une base de données significative. Dans cette optique, la recharge pourrait constituer un nouvel 'observable' proposé par cet observatoire.

Les méthodes ont été développées dans un contexte de caractérisation de la relation précipitations-déplacement. Cependant, ces méthodes peuvent aussi s'appliquer à d'autres paramètres des mouvements de terrain. La caractérisation et la compréhension de la relation entre la pluie et les événements d'éboulements rocheux (Helmstetter and Garambois, 2010) pourraient notamment être améliorées en tenant compte de la composante recharge. De même, l'utilisation du seuil d'activation multi-dimensionnel peut servir à caractériser le seuil d'activation pluviométrique de ces éboulements. Enfin, en dehors du contexte des mouvements de terrain, il serait pertinent de tester et d'évaluer la méthode des seuils d'activations multi-dimensionnels dans le cadre de prédictions des crues (Reichenbach et al.,

1998; Martina et al., 2006) et dans une moindre mesure dans la détermination d'un seuil d'activation des séismes induits par les précipitions (Hainzl et al., 2006).

3 Perspectives du signal chimique de l'eau souterraine comme paramètre de suivi global de la déformation

Binet et al. (2009) ont mis en évidence l'existence d'interactions hydro-mécano-chimiques dans les mouvements de terrain. Ces travaux montrent que les variations de concentration en sulfate sont corrélées avec les variations de la déstabilisation pour le mouvement de terrain de la Clapière (Alpes-Maritimes, France), même pour de faibles vitesses de déplacement. La corrélation entre les variations de concentrations en sulfates et la déstabilisation est expliquée par la réactivation de nouvelles surfaces minérales de la pyrite lors du déplacement du versant instable, qui génère un endommagement de la roche.

Le signal chimique, qui, contrairement aux mesures de déplacement locales, intègre des informations sur l'ensemble de l'aquifère, donc de la zone instable, est un signal pertinent et complémentaire à prendre en compte dans la surveillance des mouvements de terrain. Bien que les processus liant les sulfates aux phases de déstabilisation aient été caractérisés, la corrélation entre les deux séries temporelles n'a été établie que qualitativement et aucune analyse statistique quantitative n'a été encore entreprise pour caractériser et vérifier la significativité de cette corrélation.

A Séchilienne, un suivi continu de la conductivité électrique (linéairement proportionnelle à la concentration en sulfate) et un suivi ponctuel de la concentration chimique de l'eau en deux points de la zone instable et en un point de la zone stable a été mis en place depuis Septembre 2010. Les premiers résultats montrent que les eaux circulant dans le mouvement de terrain de Séchilienne présentent également de fortes concentrations en sulfate liées aux phases de déstabilisation (Bertrand et al., 2014).

La quantification de la relation entre la chimie et la déstabilisation est complexe, car ces deux variables sont toutes deux influencées par le comportement hydrodynamique de l'aquifère (Fig. 49). La quantification de cette relation nécessite donc des outils statistiques élaborés, capables d'isoler le lien entre la déstabilisation et la chimie indépendamment de l'influence de l'aquifère. Cette analyse s'est pour l'instant heurtée au nombre insuffisant de données collectées qui ne permettaient pas d'identifier significativement cette relation. Nous disposons

maintenant de 4 années de chroniques continues et nous envisageons différents tests statistiques (travail sur les résidus, modèles statistiques de séries temporelles, test de causalité de Granger, …).

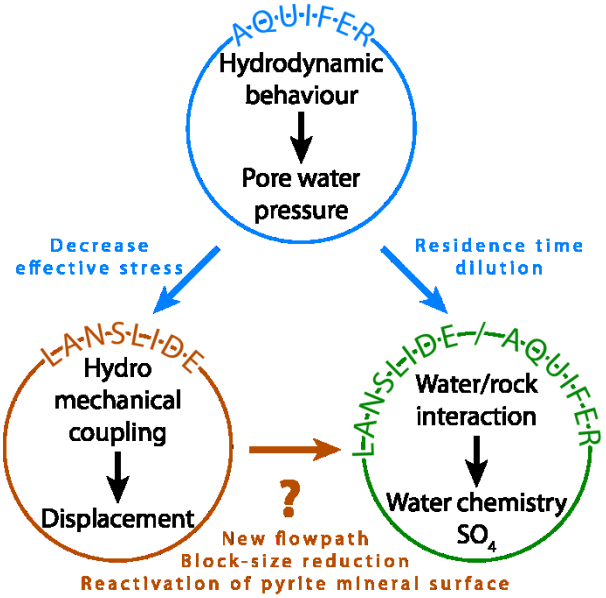

Fig. 49: Interactions hydro-mécano-chimiques des mouvements de terrain. Les couplages hydro-mécaniques indirects ne sont pas explicités

4 Perspectives de l'hydrogéophysique pour le suivi des fluctuations des pressions de fluides

L'étude des mouvements de terrain profonds se heurte généralement à une instrumentation faible ou inexistante du site d'étude permettant de mesurer les fluctuations temporelles du niveau piézométrique. Ces données sont pourtant cruciales pour la caractérisation des couplages hydro-mécaniques contrôlant la déstabilisation. Bien que ce travail de thèse se soit attaché à mieux caractériser la relation précipitations-déplacement, la localisation et les variations des pressions de fluides responsables de la déstabilisation n'ont pu être caractérisées qu'indirectement et relativement (absence d'eau dans les galeries, pondération de la recharge, modélisation numérique…).

Les méthodes hydrogéophysiques non-invasives intégrant le facteur temps, présentent une perspective majeure pour localiser et suivre les fluctuations des hydrosystèmes des versants instables et ainsi améliorer la compréhension des processus de déstabilisation. Cependant, la caractérisation du niveau d'eau et des écoulements souterrains, ainsi que des variations

temporelles à partir d'investigations géophysiques est complexe (Rubin and Hubbard, 2006). La détection de la présence d'eau dans les mouvements de terrain s'est pour l'instant le plus souvent faite grâce aux investigations électriques (Bruno and Martillier, 2000; Lapenna et al., 2005; Jomard et al., 2007; Lebourg et al., 2010), électromagnétiques (Caris and Van Asch, 1991; Mauritsch et al., 2000) et par polarisation spontanée (Bruno and Martillier, 2000; Giano et al., 2000; Meric et al., 2005).

Cependant, les mesures physiques de ces méthodes n'ont pas un lien univoque avec la présence d'eau. De plus, la forte hétérogénéité des mouvements de terrain, qui peuvent présenter de nombreux filons minéralisés ainsi que des remplissages de fractures par des produits de l'altération (matériels argileux par exemple), complique l'interprétation des données géophysiques. Par exemple, dans le cas de Séchilienne, Meric et al (2005) n'ont pas pu discriminer si la source des anomalies de polarisation spontanées avait pour origine les écoulements souterrains ou les objets géologiques. De plus, très peu d'études hydrogéophysiques sur les mouvements de terrain ont eu pour objectif de caractériser les fluctuations temporelles des aquifères.

D'autres méthodes d'hydrogéophysiques prometteuses n'ont pas encore été appliquées de façon approfondie aux contextes des mouvements de terrain, telles que la méthode de géoradar (ground penatrating radar) et la méthode par résonance magnétique protonique (magnetic resonnance sounding). Le géoradar est basé sur la propagation des ondes électromagnétiques (propagation des ondes contrôlée par la permittivité diélectrique, principalement liée à l'eau) alors que la méthode par résonance magnétique protonique a l'avantage d'être directement dépendante de la molécule d'eau (moment magnétique du noyau d'hydrogène). Ces deux méthodes permettent de localiser la profondeur et l'épaisseur de la nappe ainsi que les teneurs d'eau et les propriétés hydrauliques de l'aquifère (Legchenko et al., 2002, 2004; Doolittle et al., 2006; Mahmoudzadeh et al., 2012).

Une expérimentation approfondie de méthodes hydrogéophysiques intégrant le facteur temps, couplées à des mesures directes du niveau d'eau ou à des suivis de traceurs naturels ou artificiels est un enjeu majeur des prochaines années pour l'amélioration de la compréhension des processus hydro-mécaniques.

RÉFÉRENCES BIBLIOGRAPHIQUES

Abellán, A., Michoud, C., Jaboyedoff, M., Baillifard, F., Demierre, J., Carrea, D., Derron, M.-H., 2014. Predicting rates of displacement in continuously-moving mass movements, in: Proceedings of International Association Engineering Geology Conference. Presented at the International Association Engineering Geology Conference, Springer, Torino (Italy).

Agliardi, F., Crosta, G., Zanchi, A., 2001. Structural constraints on deep-seated slope deformation kinematics. Engineering Geology 59, 83–102. doi:10.1016/S0013-7952(00)00066-1

Aleotti, P., 2004. A warning system for rainfall-induced shallow failures. Engineering Geology, Rainfall-triggered landslides and debris flows 73, 247–265. doi:10.1016/j.enggeo.2004.01.007

Aleotti, P., Chowdhury, R., 1999. Landslide hazard assessment: summary review and new perspectives. Bull Eng Geol Env 58, 21–44. doi:10.1007/s100640050066

Alexandris, S., Stricevic, R., Petkovic, S., 2008. Comparative analysis of reference evapotranspiration from the surface of rainfed grass in central Serbia, calculated with six empirical methods against the Penman–Monteith formula. European Water 21/22, 17–28.

Alfonsi, P., 1997. Relation entre les paramètres hydrologiques et la vitesse dans les glissements de terrains. Exemples de La Clapière et de Séchilienne. Revue Française de Géotechnique 3–12.

Alkaeed, O.A., Flores, C., Jinno, K., Tsutsumi, A., 2006. Comparison of Several Reference Evapotranspiration Methods for Itoshima Peninsula Area, Fukuoka, Japan. Memoirs of the Faculty of Engineering, Kyushu University 66, 1–14.

Allen, R.E., Pereira, L.S., Raes, D., Smith, M., 1998. Crop evapotranspiration : guidelines for computing crop water requirements, FAO Irrigation and drainage paper 56. ed. Food and Agriculture Organization of the United Nations, Rome.

Allen, R.G., Smith, M., Pereira, L.S., Perrier, A., 1994. An Update for the Definition of Reference Evapotranspiration. ICID Bulletin of the International Commission on Irrigation and Drainage 43, 1–34.

Almorox, J., 2011. Estimating global solar radiation from common meteorological data in Aranjuez, Spain. Turkish Journal of Physics, Tübitak 35, 53–64.

Angeli, M.G., Buma, J., Gasparetto, P., Pasuto, A., 1998. A combined hillslope hydrology/stability model for low-gradient clay slopes in the Italian Dolomites. Engineering Geology 49, 1–13. doi:10.1016/S0013-7952(97)00033-1

Angeli, M.G., Gasparetto, P., Bromhead, E., 2004. Strength-regain mechanisms in intermittently moving landslides, in: Proceedings of the 9th International Symposium on Landslides. Presented at the 9th International Symposium on Landslides, Taylor & Francis, London, Rio de Janeiro, pp. 689–696.

Aragon, Y., 2011. Séries temporelles avec R: Méthodes et cas. Springer Science & Business Media.

Atteia, O., 1994. Major and trace elements in precipitation on Western Switzerland. Atmospheric Environment 28, 3617–3624. doi:10.1016/1352-2310(94)00193-O

Barféty, J.-C., Bordet, P., Carme, J., Debelmas, J., Meloux, M., Montjuvent, G., Mouterde, R., Sarrotreynauld, J., 1972. Notice et carte géologique de la France au 1/50000, feuille de Vizille numéro 797. Bureau de recherches géologiques et minières.

Barla, G., Chiriotti, E., 1995. Insights into the behaviour of the large deep-seated gravitational slope deformation of Rosone, in the Piemonte Region (Italy), in: Proceedings 44th Geomechanics Colloquim. Presented at the 44th Geomechanics Colloquim, Salzburg, pp. 425–432.

Belle, P., Aunay, B., Bernardie, S., Grandjean, G., Ladouche, B., Mazué, R., Join, J.-L., 2013. The application of an innovative inverse model for understanding and predicting landslide movements (Salazie cirque landslides, Reunion Island). Landslides 1–13. doi:10.1007/s10346-013-0393-5

Ben-Hur, A., Weston, J., 2010. A User's Guide to Support Vector Machines, in: Carugo, O., Eisenhaber, F. (Eds.), Data Mining Techniques for the Life Sciences, Methods in Molecular Biology. Humana Press, pp. 223–239.

Ben-Yacoub, S., 1999. Multi-modal data fusion for person authentication using SVM, in: Proceedings of 2nd International Conference on Audio and Video Based Person Authentication. Presented at the Conference on Audio and Video based Person Authentication, Washington D.C., pp. 25–30.

Bernardie, S., Desramaut, N., Malet, J.-P., Gourlay, M., Grandjean, G., 2014. Prediction of changes in landslide rates induced by rainfall. Landslides 1–14. doi:10.1007/s10346-014-0495-8

Berti, M., Martina, M.L.V., Franceschini, S., Pignone, S., Simoni, A., Pizziolo, M., 2012. Probabilistic rainfall thresholds for landslide occurrence using a Bayesian approach. Journal of Geophysical Research: Earth Surface 117, n/a–n/a. doi:10.1029/2012JF002367

Bertrand, C., Vallet, A., Mudry, J., 2014. Hydrochemical Approach of Mechanical Degradation of the Séchilienne Unstable Slope, in: Lollino, G., Giordan, D., Crosta, G.B., Corominas, J., Azzam, R., Wasowski, J., Sciarra, N. (Eds.), Engineering

Geology for Society and Territory - Volume 2. Springer International Publishing, pp. 2137–2141.

Bièvre, G., Jongmans, D., Winiarski, T., Zumbo, V., 2012. Application of geophysical measurements for assessing the role of fissures in water infiltration within a clay landslide (Trièves area, French Alps). Hydrol. Process. 26, 2128–2142. doi:10.1002/hyp.7986

Binet, S., 2006. L'hydrochimie, marqueur de l'évolution à long terme des versants montagneux fracturés vers de grands mouvements de terrain Application à plusieurs échelles sur la haute vallée de la Tinée (Mercantour, France) et sur le versant de Rosone (Gran Paradiso, Italie) (PhD thesis). Université de Franche-Comté, Besançon.

Binet, S., Guglielmi, Y., Bertrand, C., Mudry, J., 2007a. Unstable rock slope hydrogeology: insights from the large-scale study of western Argentera-Mercantour hillslopes (South-East France). Bulletin de la Société Géologique de France 178, 159–168. doi:10.2113/gssgfbull.178.2.159

Binet, S., Jomard, H., Lebourg, T., Guglielmi, Y., Tric, E., Bertrand, C., Mudry, J., 2007b. Experimental analysis of groundwater flow through a landslide slip surface using natural and artificial water chemical tracers. Hydrol. Process. 21, 3463–3472. doi:10.1002/hyp.6579

Binet, S., Mudry, J., Scavia, C., Campus, S., Bertrand, C., Guglielmi, Y., 2007c. In situ characterization of flows in a fractured unstable slope. Geomorphology 86, 193–203. doi:10.1016/j.geomorph.2006.08.013

Binet, S., Spadini, L., Bertrand, C., Guglielmi, Y., Mudry, J., Scavia, C., 2009. Variability of the groundwater sulfate concentration in fractured rock slopes: a tool to identify active unstable areas. Hydrol. Earth Syst. Sci. 13, 2315–2327. doi:10.5194/hess-13-2315-2009

Blasio, F.V. de, 2011. Introduction To The Physics of Landslides: Lecture Notes On The Dynamics of Mass Wasting. Springer, New York.

Bogaard, T., Guglielmi, Y., Marc, V., Emblanch, C., Bertrand, C., Mudry, J., 2007. Hydrogeochemistry in landslide research: a review. Bulletin de la Société Géologique de France 178, 113–126. doi:10.2113/gssgfbull.178.2.113

Bogaard, T., Maharjan, L.D., Maquaire, O., Lissak, C., Malet, J.-P., 2013. Identification of Hydro-Meteorological Triggers for Villerville Coastal Landslide, in: Margottini, C., Canuti, P., Sassa, K. (Eds.), Landslide Science and Practice. Springer Berlin Heidelberg, pp. 141–145.

Bonzanigo, L., Eberhardt, E., Loew, S., 2007. Long-term investigation of a deep-seated creeping landslide in crystalline rock. Part I. Geological and hydromechanical factors controlling the Campo Vallemaggia landslide. Can. Geotech. J. 44, 1157–1180. doi:10.1139/T07-043

Bristow, K.L., Campbell, G.S., 1984. On the relationship between incoming solar radiation and daily maximum and minimum temperature. Agricultural and Forest Meteorology 31, 159–166. doi:10.1016/0168-1923(84)90017-0

Brocca, L., Ponziani, F., Moramarco, T., Melone, F., Berni, N., Wagner, W., 2012. Improving Landslide Forecasting Using ASCAT-Derived Soil Moisture Data: A Case Study of the Torgiovannetto Landslide in Central Italy. Remote Sensing 4, 1232–1244. doi:10.3390/rs4051232

Bruand, A., Duval, O., Cousin, I., 2004. Estimation des propriétés de rétention en eau des sols à partir de la base de données SOLHYDRO : Une première proposition combinant le type d'horizon, sa texture et sa densité apparente. Etude et Gestion des Sols 11, 3, 323–334.

Brückl, E.P., 2001. Cause-Effect Models of Large Landslides. Natural Hazards 23, 291–314. doi:10.1023/A:1011160810423

Brunetti, M.T., Peruccacci, S., Rossi, M., Luciani, S., Valigi, D., Guzzetti, F., 2010. Rainfall thresholds for the possible occurrence of landslides in Italy. Nat. Hazards Earth Syst. Sci. 10, 447–458. doi:10.5194/nhess-10-447-2010

Bruno, F., Martillier, F., 2000. Test Of High-Resolution Seismic Reflection And Other Geophysical Techniques On The Boup Landslide In The Swiss Alps. Surveys in Geophysics 21, 335–350. doi:10.1023/A:1006736824075

Brunsden, D., 1999. Some geomorphological considerations for the future development of landslide models. Geomorphology 30, 13–24. doi:10.1016/S0169-555X(99)00041-0

Brunsden, D., 2001. A critical assessment of the sensitivity concept in geomorphology. CATENA, Landscape sensitivity: principles and applications in Northern 42, 99–123. doi:10.1016/S0341-8162(00)00134-X

Byvatov, E., Fechner, U., Sadowski, J., Schneider, G., 2003. Comparison of support vector machine and artificial neural network systems for drug/nondrug classification. J Chem Inf Comput Sci 43, 1882–1889. doi:10.1021/ci0341161

Caine, N., 1980. The Rainfall Intensity: Duration Control of Shallow Landslides and Debris Flows. Geografiska Annaler. Series A, Physical Geography 62, 23–27. doi:10.2307/520449

Calmels, D., Gaillardet, J., Brenot, A., France-Lanord, C., 2007. Sustained sulfide oxidation by physical erosion processes in the Mackenzie River basin: Climatic perspectives. Geology 35, 1003–1006. doi:10.1130/G24132A.1

Canuti, P., Focardi, P., Garzonio, C., 1985. Correlation between rainfall and landslides. Bulletin of Engineering Geology and the Environment 32, 49–54. doi:10.1007/BF02594765

Cappa, F., Guglielmi, Y., Rutqvist, J., Tsang, C.-F., Thoraval, A., 2006. Hydromechanical modelling of pulse tests that measure fluid pressure and fracture normal displacement

at the Coaraze Laboratory site, France. International Journal of Rock Mechanics and Mining Sciences 43, 1062–1082. doi:10.1016/j.ijrmms.2006.03.006

Cappa, F., Guglielmi, Y., Soukatchoff, V.M., Mudry, J., Bertrand, C., Charmoille, A., 2004. Hydromechanical modeling of a large moving rock slope inferred from slope levelling coupled to spring long-term hydrochemical monitoring: example of the La Clapière landslide (Southern Alps, France). Journal of Hydrology 291, 67–90. doi:10.1016/j.jhydrol.2003.12.013

Cappa, F., Guglielmi, Y., Viseur, S., Garambois, S., 2014. Deep fluids can facilitate rupture of slow-moving giant landslides as a result of stress transfer and frictional weakening. Geophys. Res. Lett. 41, 61–66. doi:10.1002/2013GL058566

Caris, J.P.T., Van Asch, T.W.J., 1991. Geophysical, geotechnical and hydrological investigations of a small landslide in the French Alps. Engineering Geology 31, 249–276. doi:10.1016/0013-7952(1)90011-9

Cartier, G., Pouget, P., 1987. Corrélation entre la pluviométrie et les déplacements de pentes instables, in: 9th European Conference on Soil Mechanics and Foundation Engineering. Presented at the 9th European conference on soil mechanics and foundation engineering, CRC Press, Dublin.

Castellvi, F., 2001. A new simple method for estimating monthly and daily solar radiation. Performance and comparison with other methods at Lleida (NE Spain); a semiarid climate. Theoretical and Applied Climatology 69, 231–238. doi:10.1007/s007040170028

Černý, V., 1985. Thermodynamical approach to the traveling salesman problem: An efficient simulation algorithm. J Optim Theory Appl 45, 41–51. doi:10.1007/BF00940812

Cervi, F., Ronchetti, F., Martinelli, G., Bogaard, T.A., Corsini, A., 2012. Origin and assessment of deep groundwater inflow in the Ca' Lita landslide using hydrochemistry and in situ monitoring. Hydrol. Earth Syst. Sci. 16, 4205–4221. doi:10.5194/hess-16-4205-2012

Chang, C.-C., Lin, C.-J., 2011. LIBSVM: A library for support vector machines. ACM Transactions on Intelligent Systems and Technology 2, 1–27. doi:10.1145/1961189.1961199

Chanut, M.-A., Vallet, A., Dubois, L., Duranthon, J.-P., 2013. Mouvement de versant de Séchilienne : relations entre déplacements de surface et précipitations – analyse statistique, in: Journées Aléa Gravitaire 2013. Presented at the Journées Aléa Gravitaire, Grenoble, France.

Charlier, J.-B., Bertrand, C., Binet, S., Mudry, J., Bouillier, N., 2010. Use of continuous measurements of dissolved organic matter fluorescence in groundwater to characterize fast infiltration through an unstable fractured hillslope (Valabres rockfall, French Alps). Hydrogeol J 18, 1963–1969. doi:10.1007/s10040-010-0670-5

Charlier, J.-B., Bertrand, C., Mudry, J., 2012. Conceptual hydrogeological model of flow and transport of dissolved organic carbon in a small Jura karst system. Journal of Hydrology 460–461, 52–64. doi:10.1016/j.jhydrol.2012.06.043

Chernick, M.R., 2008. Bootstrap methods: A guide for practitioners and researchers. Wiley-Interscience, Hoboken, N.J.

Chigira, M., 1992. Long-term gravitational deformation of rocks by mass rock creep. Engineering Geology 32, 157–184. doi:10.1016/0013-7952(92)90043-X

Clark, I.D., Fritz, P., 1997. Environmental Isotopes in Hydrogeology. CRC Press, Boca Raton, FL.

Clauser, C., 1992. Permeability of crystalline rocks. Eos, Transactions American Geophysical Union 73, 233–238. doi:10.1029/91EO00190

Cordeiro, C., Neves, M., 2006. The Bootstrap methodology in time series forecasting, in: COMPSTAT 2006 - Proceedings in Computational Statistics. Presented at the COMPSTAT 2006 - 17th Symposium of IASC, Springer, Italy, Rome, pp. 1067–1073.

Corominas, J., Moya, J., Ledesma, A., Lloret, A., Gili, J.A., 2005. Prediction of ground displacements and velocities from groundwater level changes at the Vallcebre landslide (Eastern Pyrenees, Spain). Landslides 2, 83–96. doi:10.1007/s10346-005-0049-1

Cortes, C., Vapnik, V., 1995. Support-vector networks. Mach Learn 20, 273–297. doi:10.1007/BF00994018

Cowpertwait, P.S.P., Metcalfe, A., 2009. Introductory Time Series with R, Édition : 2009. ed. Springer-Verlag New York Inc., Dordrecht ; New York.

Cristianini, N., 2000. An Introduction to Support Vector Machines and Other Kernel-based Learning Methods. Cambridge University Press, Cambridge; New York.

Crozier, M.J., 1986. Landslides: Causes, consequences et environment. Croom Helm, London ; Dover, N.H.

Debieche, T.-H., Bogaard, T., Marc, V., Emblanch, C., Krzeminska, D.M., Malet, J.-P., 2012. Hydrological and hydrochemical processes observed during a large-scale infiltration experiment at the Super-Sauze mudslide (France). Hydrological Processes 26, 2157–2170. doi:10.1002/hyp.7843

Decrop, G., 2012. Le risque des Ruines de Séchilienne, 1985-2012, l'histoire de sa construction scientifique et technique, de sa gestion opérationnelle et du sort des populations concernées (ANR Risknat - SLAMS).

Delmas, P., Cartier, G., Pouget, G., 1987. Méthodes d'analyse des risques liés aux glissements de terrain. Bulletin Liaison Laboratoire Ponts et Chaussées 150/151, 29–38.

Diodato, N., Guerriero, L., Fiorillo, F., Esposito, L., Revellino, P., Grelle, G., Guadagno, F.M., 2014. Predicting Monthly Spring Discharges Using a Simple Statistical Model. Water Resources Management 28, 969–978. doi:10.1007/s11269-014-0527-0

Dongarrà, G., Manno, E., Sabatino, G., Varrica, D., 2009. Geochemical characteristics of waters in mineralised area of Peloritani Mountains (Sicily, Italy). Applied Geochemistry 24, 900–914. doi:10.1016/j.apgeochem.2009.02.002

Doolittle, J.A., Jenkinson, B., Hopkins, D., Ulmer, M., Tuttle, W., 2006. Hydropedological investigations with ground-penetrating radar (GPR): Estimating water-table depths and local ground-water flow pattern in areas of coarse-textured soils. Geoderma, Hydropedology: Bridging disciplines, scales and data 131, 317–329. doi:10.1016/j.geoderma.2005.03.027

Dramis, F., Sorriso-Valvo, M., 1994. Deep-seated gravitational slope deformations, related landslides and tectonics. Engineering Geology, Deep-seated Landslides and Large-scale Rock Avalanches 38, 231–243. doi:10.1016/0013-7952(94)90040-X

Du, J., Yin, K., Lacasse, S., 2013. Displacement prediction in colluvial landslides, Three Gorges Reservoir, China. Landslides 10, 203–218. doi:10.1007/s10346-012-0326-8

Duranthon, J.-P., Effendiaz, L., Memier, M., Previtali, I., 2003. Apport des méthodes topographiques et topométriques au suivi du versant rocheux instable des ruines de Séchilienne. Association Francaise de Topographie 31–38.

Durville, J.-L., Bonnard, C., Potherat, P., 2011. The Séchilienne (France) landslide: a non-typical progressive failure implying major risks. Journal of Mountain Science 8, 117–123. doi:10.1007/s11629-011-2086-7

Durville, J.-L., Kasperki, J., Duranthon, J.-P., 2009. The Séchilienne landslide: monitoring and kinematics, in: First Italian Workshop on Landslides. Presented at the First Italian Workshop on Landslides, Napoli, Italia, pp. 174–180.

Excoffier, J.L., Guiochon, G., 1982. Automatic peak detection in chromatography. Chromatographia 15, 543–545. doi:10.1007/BF02280372

Federico, A., Popescu, M., Elia, G., Fidelibus, C., Internò, G., Murianni, A., 2012. Prediction of time to slope failure: a general framework. Environ Earth Sci 66, 245–256. doi:10.1007/s12665-011-1231-5

Frattini, P., Crosta, G., Sosio, R., 2009. Approaches for defining thresholds and return periods for rainfall-triggered shallow landslides. Hydrological Processes 23, 1444–1460. doi:10.1002/hyp.7269

Fung, G.M., Mangasarian, O.L., 2004. A Feature Selection Newton Method for Support Vector Machine Classification. Comput. Optim. Appl. 28, 185–202. doi:10.1023/B:COAP.0000026884.66338.df

Gaillardet, J., Dupré, B., Louvat, P., Allègre, C.J., 1999. Global silicate weathering and CO2 consumption rates deduced from the chemistry of large rivers. Chemical Geology 159, 3–30. doi:10.1016/S0009-2541(99)00031-5

Garel, E., Marc, V., Ruy, S., Cognard-Plancq, A.-L., Klotz, S., Emblanch, C., Simler, R., 2012. Large scale rainfall simulation to investigate infiltration processes in a small landslide under dry initial conditions: the Draix hillslope experiment. Hydrological Processes 26, 2171–2186.

Gat, J.R., 1996. Oxygen and Hydrogen Isotopes in the Hydrologic Cycle. Annual Review of Earth and Planetary Sciences 24, 225–262. doi:10.1146/annurev.earth.24.1.225

Giano, S.I., Lapenna, V., Piscitelli, S., Schiattarella, M., 2000. Electrical imaging and self-potential survayes to study the geological setting of the Quaternary, slope depositsin the Agri high valley (Southern Italy). Ann. Geophys. 43. doi:10.4401/ag-3642

Gochis, D., Cuenca, R., 2000. Plant Water Use and Crop Curves for Hybrid Poplars. Journal of Irrigation and Drainage Engineering 126, 206–214. doi:10.1061/(ASCE)0733-9437(2000)126:4(206)

Godt, J.W., Baum, R.L., Chleborad, A.F., 2006. Rainfall characteristics for shallow landsliding in Seattle, Washington, USA. Earth Surf. Process. Landforms 31, 97–110. doi:10.1002/esp.1237

Grandjean, G., Hibert, C., Mathieu, F., Garel, E., Malet, J.-P., 2009. Monitoring water flow in a clay-shale hillslope from geophysical data fusion based on a fuzzy logic approach. Comptes Rendus Geoscience, Hydrogéophysique Hydrogeophysics 341, 937–948. doi:10.1016/j.crte.2009.08.003

Grinsted, A., Moore, J.C., Jevrejeva, S., 2004. Application of the cross wavelet transform and wavelet coherence to geophysical time series. Nonlin. Processes Geophys. 11, 561–566. doi:10.5194/npg-11-561-2004

Guglielmi, Y., Cappa, F., Binet, S., 2005. Coupling between hydrogeology and deformation of mountainous rock slopes: Insights from La Clapière area (southern Alps, France). Comptes Rendus Geoscience 337, 1154–1163. doi:10.1016/j.crte.2005.04.016

Guglielmi, Y., Vengeon, J.M., Bertrand, C., Mudry, J., Follacci, J.P., Giraud, A., 2002. Hydrogeochemistry: an investigation tool to evaluate infiltration into large moving rock masses (case study of La Clapière and Séchilienne alpine landslides). Bulletin of Engineering Geology and the Environment 61, 311 – 324.

Guzzetti, F., Peruccacci, S., Rossi, M., Stark, C.P., 2007. Rainfall thresholds for the initiation of landslides in central and southern Europe. Meteorol. Atmos. Phys. 98, 239–267. doi:10.1007/s00703-007-0262-7

Guzzetti, F., Peruccacci, S., Rossi, M., Stark, C.P., 2008. The rainfall intensity–duration control of shallow landslides and debris flows: an update. Landslides 5, 3–17. doi:10.1007/s10346-007-0112-1

Hainzl, S., Kraft, T., Wassermann, J., Igel, H., Schmedes, E., 2006. Evidence for rainfall-triggered earthquake activity. Geophys. Res. Lett. 33, L19303. doi:10.1029/2006GL027642

Hargreaves, G.H., Allen, R.G., 2003. History and Evaluation of Hargreaves Evapotranspiration Equation. Journal of Irrigation and Drainage Engineering 129, 53–63. doi:10.1061/(ASCE)0733-9437(2003)129:1(53)

Hargreaves, G., Samani, Z., 1985. Reference Crop Evapotranspiration from Temperature. Applied Engineering in Agriculture 1, 96–99.

Hastie, T., 2009. The elements of statistical learning: data mining, inference, and prediction, 2nd ed. ed, Springer series in statistics. Springer, New York, NY.

Helmstetter, A., Garambois, S., 2010. Seismic monitoring of Séchilienne rockslide (French Alps): Analysis of seismic signals and their correlation with rainfalls. Journal of Geophysical Research 115, F03016. doi:10.1029/2009JF001532

Hilley, G.E., Chamberlain, C.P., Moon, S., Porder, S., Willett, S.D., 2010. Competition between erosion and reaction kinetics in controlling silicate-weathering rates. Earth and Planetary Science Letters 293, 191–199. doi:10.1016/j.epsl.2010.01.008

Hong, Y., Hiura, H., Shino, K., Sassa, K., Suemine, A., Fukuoka, H., Wang, G., 2005. The influence of intense rainfall on the activity of large-scale crystalline schist landslides in Shikoku Island, Japan. Landslides 2, 97–105. doi:10.1007/s10346-004-0043-z

Hou, L.G., Xiao, H.L., Si, J.H., Xiao, S.C., Zhou, M.X., Yang, Y.G., 2010. Evapotranspiration and crop coefficient of Populus euphratica Oliv forest during the growing season in the extreme arid region northwest China. Agricultural Water Management 97, 351–356. doi:10.1016/j.agwat.2009.09.022

Hsu, C.-W., Chang, C.-C., Lin, C.-J., 2003. A Practical Guide to Support Vector Classification. Department of Computer Science, National Taiwan University.

Huang, A.-B., Lee, J.-T., Ho, Y.-T., Chiu, Y.-F., Cheng, S.-Y., 2012. Stability monitoring of rainfall-induced deep landslides through pore pressure profile measurements. Soils and Foundations 52, 737–747. doi:10.1016/j.sandf.2012.07.013

Huang, J., Lu, J., Ling, L.C.X., 2003. Comparing Naive Bayes, decision trees, and SVM with AUC and accuracy, in: Proceedings of the Third IEEE International Conference on Data Mining. Presented at the Third IEEE International Conference on Data Mining, IEEE Computer Society, pp. 553–556.

Igbadun, H., Mahoo, H., Tarimo, A., Salim, B., 2006. Performance of Two Temperature-Based Reference Evapotranspiration Models in the Mkoji Sub-Catchment in Tanzania. Agricultural Engineering International: the CIGR Ejournal, Manuscript LW 05 008 VIII.

Itenfisu, D., Elliott, R.L., Allen, R.G., Walter, I.A., 2003. Comparison of Reference Evapotranspiration Calculations as Part of the ASCE Standardization Effort. Journal

of Irrigation and Drainage Engineering 129, 440–448. doi:10.1061/(ASCE)0733-9437(2003)129:6(440)

Ivanciuc, O., 2007. Applications of support vector machines in chemistry. Reviews in computational chemistry 23, 291–400.

Iverson, R.M., 2000. Landslide triggering by rain infiltration. Water Resources Research 36, 1897–1910. doi:10.1029/2000WR900090

Jabiol, B., Baize, D., 2011. Guide pour la description des sols. Quae éditions.

Jacobson, M.L., 2001. Auto-threshold peak detection in physiological signals, in: Proceedings of the 23rd Annual International Conference of the IEEE Engineering in Medicine and Biology Society, 2001. Presented at the Proceedings of the 23rd Annual International Conference of the IEEE Engineering in Medicine and Biology Society, 2001, pp. 2194–2195. doi:10.1109/IEMBS.2001.1017206

Jacobson, P.M.Z., 2005. Fundamentals of Atmospheric Modeling, Édition : 2. ed. Cambridge University Press, Cambridge, UK; New York.

Jamagne, M., Bétrémieux, R., Bégon, J.C., Mori, A., 1977. Quelques données sur la variabilité dans le milieu naturel de la réserve en eau des sols. Bulletin Technique d'Information du Ministère de l'Agriculture 627–641.

Jensen, M.E., Burman, R.D., Allen, R.G., 1990. Evapotranspiration and irrigation water requirements : a manual, ASCE manuals and reports on engineering practice. American Society of Civil Engineers, New York.

Jevrejeva, S., Moore, J.C., Grinsted, A., 2003. Influence of the Arctic Oscillation and El Niño-Southern Oscillation (ENSO) on ice conditions in the Baltic Sea: The wavelet approach. J. Geophys. Res. 108, 4677. doi:10.1029/2003JD003417

Jomard, H., Lebourg, T., Binet, S., Tric, E., Hernandez, M., 2007. Characterization of an internal slope movement structure by hydrogeophysical surveying. Terra Nova 19, 48–57. doi:10.1111/j.1365-3121.2006.00712.x

Jongmans, D., Garambois, S., 2007. Geophysical investigation of landslides : a review. Bulletin de la Societe Geologique de France 178, 101–112. doi:10.2113/gssgfbull.178.2.101

Julian, M., Anthony, E., 1996. Aspects of landslide activity in the Mercantour Massif and the French Riviera, southeastern France. Geomorphology, Landslides in the European Union 15, 275–289. doi:10.1016/0169-555X(95)00075-G

Kirkpatrick, S., Gelatt, C.D., Vecchi, M.P., 1983. Optimization by Simulated Annealing. Science 220, 671–680. doi:10.1126/science.220.4598.671

Klemeš, V., 1986. Operational testing of hydrological simulation models. Hydrological Sciences Journal 31, 13–24. doi:10.1080/02626668609491024

Knight, K., Fu, W., 2000. Asymptotics for Lasso-type estimators. Ann. Statist. 28, 1356–1378. doi:10.1214/aos/1015957397

Krause, P., Boyle, D.P., Bäse, F., 2005. Comparison of different efficiency criteria for hydrological model assessment. Adv. Geosci. 5, 89–97. doi:10.5194/adgeo-5-89-2005

Kumar, P., Foufoula-Georgiou, E., 1997. Wavelet analysis for geophysical applications. Rev. Geophys. 35, 385–412. doi:10.1029/97RG00427

Labat, D., Ababou, R., Mangin, A., 2000. Rainfall–runoff relations for karstic springs. Part II: continuous wavelet and discrete orthogonal multiresolution analyses. Journal of Hydrology 238, 149–178. doi:10.1016/S0022-1694(00)00322-X

Lapenna, V., Lorenzo, P., Perrone, A., Piscitelli, S., Rizzo, E., Sdao, F., 2005. 2D electrical resistivity imaging of some complex landslides in the Lucanian Apennine chain, southern Italy. Geophysics 70, B11–B18. doi:10.1190/1.1926571

Lebourg, T., Binet, S., Tric, E., Jomard, H., El Bedoui, S., 2005. Geophysical survey to estimate the 3D sliding surface and the 4D evolution of the water pressure on part of a deep seated landslide. Terra Nova 17, 399–406. doi:10.1111/j.1365-3121.2005.00623.x

Lebourg, T., Hernandez, M., Zerathe, S., El Bedoui, S., Jomard, H., Fresia, B., 2010. Landslides triggered factors analysed by time lapse electrical survey and multidimensional statistical approach. Engineering Geology 114, 238–250. doi:10.1016/j.enggeo.2010.05.001

Lebrouc, V., Schwartz, S., Baillet, L., Jongmans, D., Gamond, J.F., 2013. Modeling permafrost extension in a rock slope since the Last Glacial Maximum: Application to the large Séchilienne landslide (French Alps). Geomorphology 198, 189–200. doi:10.1016/j.geomorph.2013.06.001

Legchenko, A., Baltassat, J.-M., Beauce, A., Bernard, J., 2002. Nuclear magnetic resonance as a geophysical tool for hydrogeologists. Journal of Applied Geophysics, Surface Nuclear Magnetic Resonance: What is Possible? 50, 21–46. doi:10.1016/S0926-9851(02)00128-3

Legchenko, A., Baltassat, J.-M., Bobachev, A., Martin, C., Robain, H., Vouillamoz, J.-M., 2004. Magnetic Resonance Sounding Applied to Aquifer Characterization. Ground Water 42, 363–373. doi:10.1111/j.1745-6584.2004.tb02684.x

Leibundgut, C., Maloszewski, P., Külls, C., 2011. Tracers in Hydrology. John Wiley & Sons.

Le Roux, O., 2009. Caractérisation de l'évolution géomorphologique de la basse vallée de la Romanche en relation avec les instabilités gravitaires de ses versants rocheux. Université Joseph-Fourier - Grenoble I.

Le Roux, O., Jongmans, D., Kasperski, J., Schwartz, S., Potherat, P., Lebrouc, V., Lagabrielle, R., Meric, O., 2011. Deep geophysical investigation of the large

Séchilienne landslide (Western Alps, France) and calibration with geological data. Engineering Geology 120, 18–31. doi:10.1016/j.enggeo.2011.03.004

Le Roux, O., Schwartz, S., Gamond, J.F., Jongmans, D., Bourles, D., Braucher, R., Mahaney, W., Carcaillet, J., Leanni, L., 2009. CRE dating on the head scarp of a major landslide (Séchilienne, French Alps), age constraints on Holocene kinematics. Earth and Planetary Science Letters 280, 236–245. doi:10.1016/j.epsl.2009.01.034

Le Roux, O., Schwartz, S., Gamond, J.F., Jongmans, D., Tricart, P., Sebrier, M., 2010. Interaction between tectonic and erosion processes on the morphogenesis of an Alpine valley: geological and geophysical investigations in the lower Romanche valley (Belledonne massif, western Alps). Int J Earth Sci (Geol Rundsch) 99, 427–441. doi:10.1007/s00531-008-0393-1

Li, C., Zheng, C., Tai, C., 1995. Detection of ECG characteristic points using wavelet transforms. IEEE Transactions on Biomedical Engineering 42, 21–28. doi:10.1109/10.362922

Lin, H.-T., Lin, C.-J., Weng, R.C., 2007. A note on Platt's probabilistic outputs for support vector machines. Mach Learn 68, 267–276. doi:10.1007/s10994-007-5018-6

Lin, P.-Y., Tsai, L.L.-Y., 2012. A hydrochemical study of Hungtsaiping landslide area, Nantou, Taiwan. Environ Earth Sci 67, 1045–1060. doi:10.1007/s12665-012-1564-8

Lis, G., Wassenaar, L.I., Hendry, M.J., 2008. High-Precision Laser Spectroscopy D/H and 18O/16O Measurements of Microliter Natural Water Samples. Anal. Chem. 80, 287–293. doi:10.1021/ac701716q

Li, T., Chen, M., Wang, L., Zhou, Y., 1996. Time prediction of landslides using Verhulst inverse-function model, in: Proceedings of the 7th International Symposium on Landslides. Presented at the 7th International Symposium on landslides, Trondheim, pp. 1289–1293.

Liu, X., Zeng, X.-H., Liu, C.-Y., 2005. Research on artificial neural network-time series analysis of slope nonlinear displacement. Yanshilixue Yu Gongcheng Xuebao/Chinese Journal of Rock Mechanics and Engineering 24, 3499–3504.

López-Moreno, J.I., Hess, T.M., White, S.M., 2009. Estimation of reference evapotranspiration in a mountainous mediterranean site using the Penman-Monteith equation with limited meteorological data. Pirineos 164, 7–31.

Lu, J., Sun, G., McNulty, S.G., Amatya, D.M., 2005. A comparison of six potential evapotranspiration methods for regional use in the Southeastern United States. JAWRA Journal of the American Water Resources Association 41, 621–633. doi:10.1111/j.1752-1688.2005.tb03759.x

Madsen, H., 2007. Time Series Analysis, 1 edition. ed. Chapman and Hall/CRC, Boca Raton.

Mahmoudzadeh, M.R., Francés, A.P., Lubczynski, M., Lambot, S., 2012. Using ground penetrating radar to investigate the water table depth in weathered granites — Sardon

case study, Spain. Journal of Applied Geophysics 79, 17–26. doi:10.1016/j.jappgeo.2011.12.009

Makkink, G.., 1957. Testing the Penman formula by means of lysimeters. Journal of the Institution of Water Engineers 11, 277–288.

Malet, J.P., Maquaire, O., Vanash, T.W., 2003. Hydrological behaviour of earthflows developed in clay-shales: investigation, concept and modelling. The Occurrence and Mechanisms of Flows in Natural Slopes and Earthfills, Patron Editore, Bologna 175–193.

Malet, J.-P., van Asch, T.W.J., van Beek, R., Maquaire, O., 2005. Forecasting the behaviour of complex landslides with a spatially distributed hydrological model. Nat. Hazards Earth Syst. Sci. 5, 71–85. doi:10.5194/nhess-5-71-2005

Maquaire, O., 2000. Effects of Groundwater on the Villerville-Cricqueboeuf Landslides , Sixteen Year Survey (Calvados, France), in: 8th Landslides International Symposium. Presented at the 8th Landslides International symposium, Cardiff, pp. 1005–1010.

Maraun, D., Kurths, J., 2004. Cross wavelet analysis: significance testing and pitfalls. Nonlin. Processes Geophys. 11, 505–514. doi:10.5194/npg-11-505-2004

Maréchal, J.-C., 1998. Les circulations d'eau dans les massifs cristallins alpins et leurs relations avec les ouvrages souterrains (PhD thesis). Ecole Polytechnique Fédérale de Lausanne (EPFL), Lausanne.

Maréchal, J.-C., Etcheverry, D., 2003. The use of 3H and delta18O tracers to characterize water inflows in Alpine tunnels. Applied Geochemistry 18, 339–351.

Martelloni, G., Segoni, S., Fanti, R., Catani, F., 2012. Rainfall thresholds for the forecasting of landslide occurrence at regional scale. Landslides 9, 485–495. doi:10.1007/s10346-011-0308-2

Martina, M.L.V., Todini, E., Libralon, A., 2006. A Bayesian decision approach to rainfall thresholds based flood warning. Hydrol. Earth Syst. Sci. 10, 413–426. doi:10.5194/hess-10-413-2006

Massei, N., Dupont, J.P., Mahler, B.J., Laignel, B., Fournier, M., Valdes, D., Ogier, S., 2006. Investigating transport properties and turbidity dynamics of a karst aquifer using correlation, spectral, and wavelet analyses. Journal of Hydrology 329, 244–257. doi:10.1016/j.jhydrol.2006.02.021

Matichard, Y., Pouget, P., 1988. Pluviométrie et comportement de versants instables, in: Landslides : Proceedings of the Fifth International Symposium on Landslides. Presented at the Fifth International Symposium on Landslides, Lausanne, Switzerland, pp. 725–730.

Matsuura, S., Asano, S., Okamoto, T., 2008. Relationship between rain and/or meltwater, pore-water pressure and displacement of a reactivated landslide. Engineering Geology 101, 49–59. doi:10.1016/j.enggeo.2008.03.007

Mauritsch, H.J., Seiberl, W., Arndt, R., Römer, A., Schneiderbauer, K., Sendlhofer, G.P., 2000. Geophysical investigations of large landslides in the Carnic Region of southern Austria. Engineering Geology 56, 373–388. doi:10.1016/S0013-7952(99)00120-9

McCuen, R.H., 2005. Hydrologic analysis and design. Pearson Prentice Hall, Upper Saddle River, N.J.

Meric, O., Garambois, S., Jongmans, D., Wathelet, M., Chatelain, J.L., Vengeon, J.M., 2005. Application of geophysical methods for the investigation of the large gravitational mass movement of Séchilienne, France. Can. Geotech. J. 42, 1105–1115. doi:10.1139/t05-034

Meric, O., Garambois, S., Orengo, Y., 2006. Large Gravitational Movement Monitoring Using a Spontaneous Potential Network, in: Proc. 19th Annual Symposium on the Application of Geophysics to Engineering and Environmental Problems. EEGS, Seattle, USA, pp. 202–209. doi:10.4133/1.2923649

Mudry, J., Etievant, K., 2007. Synthèse hydrogéologique du versant instable des Ruines de Séchilienne (Unpublished report). UMR Chrono-Environnement, University of Franche-Comté.

Musy, A., Higy, C., 2011. Hydrology: A Science of Nature, English ed. ed. CRC Press ; Science Publishers, Boca Raton, FL. : Enfield, N.H.

Nafarzadegan, A.R., Talebi, A., Malekinezhad, H., Emami, N., 2012. Antecedent Rainfall Thresholds for the Triggering of Deep-Seated Landslides (Case study: Chaharmahal & Bakhtiari Province, Iran). ECOPERSIA 1, 23–39.

Nash, J.E., Sutcliffe, J.V., 1970. River flow forecasting through conceptual models part I — A discussion of principles. Journal of Hydrology 10, 282–290. doi:10.1016/0022-1694(70)90255-6

Nieuwenhuis, J.D., 1991. Variations in Stability and Displacements of a Shallow Seasonal Landslide in Varved Clays. Utrecht University, Utrecht.

Noverraz, F., Bonnard, C., Dupraz, H., Huguenin, L., 1998. Grands glissements de terrain et climat, VERSINCLIM - Comportement passé, présent et futur des grands versants instables subactifs en fonction de l'évolution climatique, et évolution en continu des mouvements en profondeur (Rapport final PNR31 (Programme National de Recherche) No. PNR31). vdf Hochschulverlag AG an der ETH Zürich, Zürich, Switzerland.

Pachepsky, Y., Rawls, W.J., 2004. Development of pedotransfer functions in soil hydrology. Elsevier, Amsterdam; New York.

Panet, M., Bonnard, C., Degoutte, G., Desvarreux, P., Durville, J.-L., Rochet, L., 2009. Scenarios d'évolution du versant des Ruines de Séchiliennes (Rapport du Collège des experts).

Patwardhan, A., Nieber, J., Johns, E., 1990. Effective Rainfall Estimation Methods. Journal of Irrigation and Drainage Engineering 116, 182–193. doi:10.1061/(ASCE)0733-9437(1990)116:2(182)

Penna, D., Stenni, B., Šanda, M., Wrede, S., Bogaard, T.A., Gobbi, A., Borga, M., Fischer, B.M.C., Bonazza, M., Chárová, Z., 2010. On the reproducibility and repeatability of laser absorption spectroscopy measurements for δ2H and δ18O isotopic analysis. Hydrol. Earth Syst. Sci. 14, 1551–1566. doi:10.5194/hess-14-1551-2010

Peruccacci, S., Brunetti, M.T., Luciani, S., Vennari, C., Guzzetti, F., 2012. Lithological and seasonal control on rainfall thresholds for the possible initiation of landslides in central Italy. Geomorphology 139–140, 79–90. doi:10.1016/j.geomorph.2011.10.005

Pili, É., Perrier, F., Richon, P., 2004. Dual porosity mechanism for transient groundwater and gas anomalies induced by external forcing. Earth and Planetary Science Letters 227, 473–480. doi:10.1016/j.epsl.2004.07.043

Pisani, G., Castelli, M., Scavia, C., 2010. Hydrogeological model and hydraulic behaviour of a large landslide in the Italian Western Alps. Nat. Hazards Earth Syst. Sci. 10, 2391–2406. doi:10.5194/nhess-10-2391-2010

Platt, J.C., 1999. Probabilistic Outputs for Support Vector Machines and Comparisons to Regularized Likelihood Methods, in: Advances in Large Margin Classifiers. MIT Press, pp. 61–74.

Ponziani, F., Pandolfo, C., Stelluti, M., Berni, N., Brocca, L., Moramarco, T., 2012. Assessment of rainfall thresholds and soil moisture modeling for operational hydrogeological risk prevention in the Umbria region (central Italy). Landslides 9, 229–237. doi:10.1007/s10346-011-0287-3

Priestley, C.H.B., Taylor, R.J., 1972. On the Assessment of Surface Heat Flux and Evaporation Using Large-Scale Parameters. Monthly Weather Review 100, 81–92. doi:10.1175/1520-0493(1972)100<0081:OTAOSH>2.3.CO;2

Prokešová, R., Medveďová, A., Tábořík, P., Snopková, Z., 2013. Towards hydrological triggering mechanisms of large deep-seated landslides. Landslides 10, 239–254. doi:10.1007/s10346-012-0330-z

Refaeilzadeh, P., Tang, L., Liu, H., 2009. Cross-validation. Encyclopedia of Database Systems 3, 532–538.

Reichenbach, P., Cardinali, M., Vita, P.D., Guzzetti, F., 1998. Regional hydrological thresholds for landslides and floods in the Tiber River Basin (central Italy). Environmental Geology 35, 146–159. doi:10.1007/s002540050301

Rochet, L., Giraud, A., Antoine, P., Évrard, H., 1994. La déformation du versant sud du Mont-Sec dans le secteur des ruines de Séchilienne (Isère). Bulletin of the International Association of Engineering Geology 50, 75–87. doi:10.1007/BF02594959

Rubin, Y., Hubbard, S.S., 2006. Hydrogeophysics. Springer Science & Business Media.

Rutqvist, J., Stephansson, O., 2003. The role of hydromechanical coupling in fractured rock engineering. Hydrogeology Journal 11, 7–40. doi:10.1007/s10040-002-0241-5

Saito, M., 1969. RESEARCH ON FORECASTING THE TIME OF OCCURRENCE OF SLOPE FAILURE. Railway Technical Research Institute, Quarterly Reports 10.

Sanchez, G., Rolland, Y., Corsini, M., Braucher, R., Bourlès, D., Arnold, M., Aumaître, G., 2010. Relationships between tectonics, slope instability and climate change: Cosmic ray exposure dating of active faults, landslides and glacial surfaces in the SW Alps. Geomorphology 117, 1–13. doi:10.1016/j.geomorph.2009.10.019

Schölkopf, B., Williamson, R.C., Smola, A.J., Shawe-Taylor, J., Platt, J.C., 1999. Support Vector Method for Novelty Detection., in: NIPS. pp. 582–588.

Segoni, S., Rossi, G., Rosi, A., Catani, F., 2014. Landslides triggered by rainfall: A semi-automated procedure to define consistent intensity–duration thresholds. Computers & Geosciences 63, 123–131. doi:10.1016/j.cageo.2013.10.009

Shahidian, S., Serralheiro, R., Serrano, J., Teixeira, J., Haie, N., Santos, F., 2012. Hargreaves and Other Reduced-Set Methods for Calculating Evapotranspiration, in: Irmak, A. (Ed.), Evapotranspiration - Remote Sensing and Modeling. InTech, Rijeka, Croatia, pp. 60–80.

Sivaprakasam, S., Murugappan, A., Mohan, S., 2011. Modified Hargreaves equation for estimation of ETo in a Hot and Humid Location in Tamilnadu State, India. Int. Journal of Engineering Science and Technology 3, 592–600.

Statham, I., Finlayson, B., 1980. Hillslope Analysis, 1st ed. edition. ed. Butterworth-Heinemann, London; Boston.

Stirzaker, R., Biggs, H., Roux, D., Cilliers, P., 2010. Requisite Simplicities to Help Negotiate Complex Problems. Ambio 39, 600–607. doi:10.1007/s13280-010-0075-7

Sun, J., Liu, Q., Li, J., An, Y., 2009. Effects of rainfall infiltration on deep slope failure. Science in China Series G: Physics Mechanics and Astronomy 52, 108–114. doi:10.1007/s11433-009-0004-6

Tabari, H., Grismer, M.E., Trajkovic, S., 2013. Comparative analysis of 31 reference evapotranspiration methods under humid conditions. Irrigation Science 31, 107–117. doi:10.1007/s00271-011-0295-z

Tabari, H., Talaee, P.H., 2011. Local Calibration of the Hargreaves and Priestley-Taylor Equations for Estimating Reference Evapotranspiration in Arid and Cold Climates of Iran Based on the Penman-Monteith Model. Journal of Hydrologic Engineering 16, 837–845. doi:10.1061/(ASCE)HE.1943-5584.0000366

Tacher, L., Bonnard, C., Laloui, L., Parriaux, A., 2005. Modelling the behaviour of a large landslide with respect to hydrogeological and geomechanical parameter heterogeneity. Landslides 2, 3–14. doi:10.1007/s10346-004-0038-9

Tax, D.M.J., Duin, R.P.W., 2004. Support Vector Data Description. Machine Learning 54, 45–66. doi:10.1023/B:MACH.0000008084.60811.49

Terlien, M.T.J., 1998. The determination of statistical and deterministic hydrological landslide-triggering thresholds. Environmental Geology 35, 124–130. doi:10.1007/s002540050299

Torrence, C., Compo, G.P., 1998. A Practical Guide to Wavelet Analysis. Bulletin of the American Meteorological Society 79, 61–78. doi:10.1175/1520-0477(1998)079<0061:APGTWA>2.0.CO;2

Trajkovic, S., 2005. Temperature-Based Approaches for Estimating Reference Evapotranspiration. Journal of Irrigation and Drainage Engineering 131, 316–323. doi:10.1061/(ASCE)0733-9437(2005)131:4(316)

Trajkovic, S., 2007. Hargreaves versus Penman-Monteith under Humid Conditions. Journal of Irrigation and Drainage Engineering 133, 38–42. doi:10.1061/(ASCE)0733-9437(2007)133:1(38)

Trajkovic, S., Stojnic, V., 2007. Effect of wind speed on accuracy of Turc method in a humid climate. Facta universitatis - series: Architecture and Civil Engineering 5, 107–113. doi:10.2298/FUACE0702107T

Tullen, P., 2002. Méthodes d'analyse du fonctionnement hydrogéologique des versants instables (PhD thesis). EPFL, Lausanne.

Turc, L., 1961. Evaluation des besoins en eau d'irrigation, évapotranspiration potentielle, formule simplifiée et mise à jour. Annales Agronomiques 12, 13–49.

Vallet, A., Bertrand, C., Fabbri, O., Mudry, J., 2014. A new method to compute the groundwater recharge for the study of rainfall-triggered deep-seated landslides. Application to the Séchilienne unstable slope (western Alps). Hydrol. Earth Syst. Sci. Discuss. 11, 6343–6403. doi:10.5194/hessd-11-6343-2014

Van Asch, T.W.J., Buma, J., van Beek, L.P.., 1999. A view on some hydrological triggering systems in landslides. Geomorphology 30, 25–32. doi:10.1016/S0169-555X(99)00042-2

Van Asch, T.W.J., Van Beek, L.P.H., Bogaard, T.A., 2007. Problems in predicting the mobility of slow-moving landslides. Engineering Geology, Slope Transport Processes and Hydrology. A tribute to Jan Nieuwenhuis 91, 46–55. doi:10.1016/j.enggeo.2006.12.012

Vengeon, J.M., 1998. Déformation et rupture des versants en terrain métamorphique anisotrope: Apport de l'étude des Ruines de Séchilienne (PhD thesis). Université Joseph Fourier I, Grenoble.

Verstraeten, W.W., Muys, B., Feyen, J., Veroustraete, F., Minnaert, M., Meiresonne, L., De Schrijver, A., 2005. Comparative analysis of the actual evapotranspiration of Flemish forest and cropland, using the soil water balance model WAVE. Hydrol. Earth Syst. Sci. 9, 225–241. doi:10.5194/hess-9-225-2005

Vita, P.D., Reichenbach, P., Bathurst, J.C., Borga, M., Crosta, G., Crozier, M., Glade, T., Guzzetti, F., Hansen, A., Wasowski, J., 1998. Rainfall-triggered landslides: a reference list. Environmental Geology 35, 219–233. doi:10.1007/s002540050308

Wieczorek, G.F., Guzzetti, F., 1999. A review of rainfall thresholds for triggering landslides, in: Proc. of the EGS Plinius Conference, Maratea, Italy. pp. 407–414.

Wilson, R.C., Wieczorek, G.F., 1995. Rainfall thresholds for the initiation of debris flows at La Honda, California. Environmental & Engineering Geoscience 1, 11–27.

Yoder, R.E., Odhiambo, L.O., Wright, W.C., 2005. Evaluation of methods for estimating daily reference crop evapotranspiration at a site in the humid Southeast United States. Applied Engineering in Agriculture 21, 197–202.

Zêzere, J.L., Trigo, R.M., Trigo, I.F., 2005. Shallow and deep landslides induced by rainfall in the Lisbon region (Portugal): assessment of relationships with the North Atlantic Oscillation. Natural Hazards and Earth System Sciences 5, 331–344. doi:10.5194/nhess-5-331-2005

Zhang, W.J., Chen, Y.M., Zhan, L.T., 2006. Loading/Unloading response ratio theory applied in predicting deep-seated landslides triggering. Engineering Geology 82, 234–240. doi:10.1016/j.enggeo.2005.11.005

RÉSUMÉ- ABSTRACT

MOUVEMENTS DE FLUIDES ET PROCESSUS DE DÉSTABILISATION DES VERSANTS ALPINS

Apport de l'étude de l'instabilité de Séchilienne

L'eau, par l'intermédiaire de la pression de fluides, est un phénomène déclencheur majeur de la déstabilisation des mouvements de terrain profonds. En conséquence, la caractérisation des mécanismes de déformation nécessite une bonne compréhension des processus hydrogéologiques contrôlant la déstabilisation. Les milieux fissurés et de surcroit les milieux instables présentent de fortes hétérogénéités, ce qui rend les études hydrogéologiques classiques peu adaptées. De plus, les mouvements de terrain profonds présentent des relations hydromécaniques complexes avec des évolutions significatives dépendantes du temps (déformation de type fluage). Cette thèse s'attache à caractériser les relations précipitations-déplacement du mouvement de terrain profond de Séchilienne. Un suivi saisonnier de traceurs naturels et artificiels a permis de définir un schéma conceptuel d'écoulement de l'eau souterraine sur l'ensemble du massif malgré un nombre limité de points d'intérêt hydrogéologiques. Les données de pression de fluides étant rarement mesurées, les paramètres indirects, tels que la recharge, sont souvent les seules données hydrogéologiques qui permettent de caractériser la relation précipitations-déstabilisation. Une méthode d'estimation de la recharge basée sur un calcul de bilan du sol a été développée afin d'estimer la recharge avec précision. En se basant sur le schéma conceptuel d'écoulement et le calcul de la recharge, une analyse en ondelettes couplée à un modèle numérique a permis de caractériser la relation précipitations-vitesse de déplacement. Cette modélisation tient compte de paramètres dépendant du temps et permet de simuler une déformation de type fluage (tendance pluriannuelle des vitesses de déplacement), conséquence des couplages hydro-mécaniques indirects. La caractérisation des processus hydrogéologiques contrôlant la déstabilisation a permis de définir un seuil statistique d'activation de la déstabilisation, basé sur une approche multi-dimensionnelle innovante.

Mots clés : mouvement de terrain profond, hydrogéologie, milieu fissuré, hydrochimie, hydromécanique, recharge, seuil d'activation

FLUIDS MOVEMENTS AND DESTABILSATION PROCESSES OF ALPINES LANDSLIDES

Contribution to the study of the unstable slope of Séchilienne

Pore water pressure build-up by recharge of underground hydrosystems is one of the main triggering factors of deep-seated landslides. Consequently, the characterization of landslide deformation mechanisms requires a thorough knowledge of the hydrogeological processes triggering the destabilization. Anisotropic and heterogeneous media combined with landslide deformation render classical hydrogeological investigations unsuitable. Hydro-mechanical processes which lead to slope failure of deep-seated landslides are complex and are influenced by the evolution of the landslide deformation through time. This thesis aims at improving the understanding of the relationships between precipitation and displacement velocity based on the study of the Séchilienne deep-seated landslide. A time-related monitoring of natural and artificial tracers allows to define a conceptual groundwater flow model despite a limited number of hydrogeological points of interest. Fluid pore pressures are rarely measured on landslide sites and, instead the groundwater recharge is generally used as the most relevant parameter. A parsimonious, yet robust, guideline workflow to calculate time series of groundwater recharge is developed. Based on the conceptual groundwater flow model and the recharge calculation, a wavelet analysis coupled to a numerical model integrating time-dependent parameters allows to characterize the relationship between precipitation and displacement velocity and to simulate the creep deformation resulting of indirect hydro-mechanical coupling (multi-year trend of displacement velocities). The characterization of the hydrogeological processes controlling the destabilization allowed to define a statistical rainfall threshold based on an innovative multi-dimensional approach.

Key words : deep-seated landslide, hydrogeology, fractured rock, hydrochemistry, hydromechanic, recharge, rainfall threshold